Low Frequency Microscale Energy Harvesting

by

Daniel Jolomi Apo

Dissertation submitted to the faculty of the
Virginia Polytechnic Institute and State University
in partial fulfillment of the requirements for the degree of

Doctor of Philosophy

in

Mechanical Engineering

Shashank Priya, *Chair*
Muhammad R. Hajj
Jean J. Heremans
Scott T. Huxtable
Mark R. Paul

June 20, 2014
Blacksburg, Virginia

Keywords: energy harvesting, MEMS, low frequency, electromagnetic, piezoelectric, magnetoelectric

Low Frequency Microscale Energy Harvesting

Daniel Jolomi Apo
Virginia Polytechnic Institute and State University, 2014
Advisor: Shashank Priya, Ph.D

Abstract

The rapid advancement in complimentary metal-oxide-semiconductor (CMOS) electronics has led to a reduction in the sizes of wireless sensor networks (WSN) and a subsequent decrease in their power requirements. To meet these power requirements for long time of operation, energy harvesters have been developed at the micro scale which can convert vibration energy into electrical energy. Recent studies have shown that for mechanical-to-electrical conversion at the mm-scale (or micro scale), piezoelectric mechanism provides the best output power density at low frequencies as compared to the other possible mechanisms for vibration energy harvesting (VEH). However, piezoelectric-based VEH presents a fundamental challenge at the micro scale since the resonance frequency of the structure increases as the dimension decreases. Electromagnetic induction is another voltage generation mechanism that has been utilized for VEH. However, the electromagnetic induction based VEH is limited by the magnet and coil size and the decrease in power density at the micro scale. Hybrid energy harvesting is a novel concept that allows for increased power response and increased optimization of the generated voltage. The work in this field is currently limited due to integration challenges at small dimensions.

An effective design for low frequency piezoelectric VEH is presented in this work. A unique cantilever design called arc-based cantilever (ABC) is presented which exhibits low

natural frequencies as compared to traditional cantilevers. A general out-of-plane vibration model for ABCs was developed that incorporated the effects of bending, torsion, transverse shear deformation and rotary inertia. Different configurations of micro ABCs were investigated through analytical modeling and validation experiments. ABC structures were fabricated for dual-phase energy harvesting from vibrations and magnetic fields.

Next, a levitation-induced electromagnetic VEH concept based on double-repulsion configuration in the moving magnet composite was studied. Computational modeling clearly illustrated the advantages of the double-repulsion configuration over the single-repulsion and no-repulsion configurations. Based on the modeling results, an AA battery-sized harvester with the double-repulsion configuration was fabricated, experimentally characterized and demonstrated to charge a cell phone. The scaling analysis of electromagnetic energy harvesters was conducted to understand the performance across different length scales. A micro electromagnetic harvester was developed that exhibited softening nonlinear spring behavior, thus leading to the finding of nonlinear inflection in magnetically-levitated electromagnetic harvesters. The nonlinear inflection theory was developed to show its causal parameters.

Lastly, a coupled harvester is presented that combines the piezoelectric and electromagnetic voltage mechanisms. The advantages of each mechanism were shown to positively contribute to the performance of hybrid harvester. The cantilever provided low stiffness, low frequency, and pure bending, while the magnetic system provided nonlinearity, broadband response, and increased strain (and thus voltage).

Dedication

To my lovely wife Rebecca for her unwavering love and for the joy she brings to my life

Acknowledgements

I would like to thank my advisor, Dr. Shashank Priya, for his guidance during my PhD program. His advice, encouragement, and overall belief in my ability proved invaluable for my success in research. My gratitude also goes to my PhD committee members (Dr. Muhammad Hajj, Dr. Jean Heremans, Dr. Scott Huxtable, and Dr. Mark Paul) for their support and recommendations. I would also like to extend my gratitude to my research colleagues who made my work so much smoother than it would otherwise have been. Their advice and help with experiments proved to be indispensable. These colleagues include Yuan Zhou, Nathan Sharpes, Christian Odafin, Cary Baur (UT Dallas), Dr. Dragan Avirovik, Dr. Anthony Marin, Dr. Ronnie Varghese, Dr. Bo Chen, Dr. Su Chul Yang, Dr. Deepam Murya, Dr. Yongke Yan, and Dr. Jungho Ryu (Korea Institute of Material Science).

My special thanks go to my research sponsors and industry contacts that ensured the financial aspect of my research was always taken proper care of. My sponsors were the Center for Energy Harvesting Materials and Systems (CEHMS), the National Science Foundation (NSF), the United States Army Research Development and Engineering Command (USA RDECOM), and OptiXtal. My industry contacts were Dr. Mohan Sanghadasa (US Army RDECOM), and Dr. Sagar Venkateswaran (OptiXtal).

I'm indebted to my wife Rebecca for her unwavering love and for the joy she brings to my life. My gratitude also goes to my mom and sisters who have provided an indispensable support system for my journey through graduate school. I am the man I am today because of my dad. I wish he was alive to see that I finally achieved my educational goal. Finally, all thanks go to the almighty God in heaven, for his mercies endureth forever.

Contents

List of Tables

List of Figures

Nomenclature

Abbreviations

VEH	vibration energy harvesting
ABC	arc-based cantilever
LIVE	levitation-induced vibration energy
CEHMS	center for energy harvesting materials and systems (at Virginia Tech)
MEMS	microelectromechanical system
NEMS	nanoelectromechanical system
WSN	wireless sensor network
CMOS	complimentary metal-oxide-semiconductor
PVDF	polyvinylidene flouride
PZT	lead zirconate titanate
AIN	aluminium nitride
PMN-PT	lead magnesium niobate-lead titanate
KNN	potassium sodium niobate
LDPE	low-density polyethylene
CYTOP	a trade name for an amorphous flouropolymer
FEP	fluorinated ethylene propylene
ME	magnetoelectric
DC	direct current
AC	alternating current
RMS	root-mean-square

IDE	interdigitated electrode
od	outer diameter
id	inner diameter

Symbols

$\theta =$ angular coordinate

$t =$ time

$M(\theta, t) =$ bending moment

$T(\theta, t) =$ twist torque

$Y =$ Young's modulus

$I =$ area moment of inertia in the bending plane

$R \; or \; r =$ radius (R is also used as 'resistance')

$G =$ modulus of rigidity

$J =$ polar moment of inertia

$\varphi(\theta, t) =$ angle of twist

$\psi(\theta, t) =$ slope of the deflection curve in the absence of shear

$z(\theta, t) =$ vertical displacement (or deflection)

$\alpha =$ angle of shear at the neutral axis

$Q(\theta, t) =$ shear force **or** electric charge

$A =$ cross sectional area

$\eta =$ shear coefficient

$\rho =$ mass density

$k =$ dimensionless stiffness parameter (GJ/YI) **or** stiffness constant (in N/m)

ω = natural frequency

j = imaginary unit $\left(\sqrt{-1}\right)$

n = distance from neutral axis

h = beam/layer/magnet thickness **or** height

W = beam width

m = mass

c = damping term

G *or* g = acceleration due to gravity ($1g = 9.8\text{ms}^{-2}$)

F = force

σ = stress **or** surface charge density (for electrets)

μ = permeability

ε = permittivity

d = distance **or** piezoelectric strain constant

M = magnetization

ζ = damping ratio

B = magnetic flux density

l = length

V = voltage

P = power

E = electric field strength

1 Chapter 1:

Introduction

The term “vibration-based energy harvester” describes the devices that scavenge energy from vibration sources or devices that can convert mechanical energy to electrical power. The optimum magnitude of power generated from the energy harvester is dependent on the difference between the operating frequency and resonance frequency. The best performance is obtained when the operational frequency is matched to the resonance frequency. Since most of the naturally available vibration sources operate at low frequencies (< 100Hz), it is important to design energy harvesters with low resonance frequencies. Vibration sources are ubiquitous and they include:

- human motion (e.g. running, and walking),
- stationary vibrating equipment (e.g. heavy industrial machinery), and
- moving equipment (e.g. cars, ships, and trains).

Sources which can induce vibration in energy harvesters include

- magnetic fields (abundant in the environment),
- environments with thermal gradients, and
- dynamic fluids-based systems/environments (e.g. ocean and wind)

For the purpose of this thesis, a micro (or MEMS) energy harvester must fit into a form factor of 10 mm × 10 mm × 10 mm. The concerns with the energy harvesters at small sizes include:

- high resonance frequencies
- narrow bandwidth
- poor structural stability (mostly cantilever-based harvesters)
- packaging and handling issues, and
- low output power

1.1 MEMS Energy Harvesting Mechanisms

Energy harvesting systems can be broadly classified based on the transduction mechanism such as piezoelectric, electromagnetic, magnetoelectric, dielectric elastomers and electrets (or electrostatic devices). The output power ($P = U^2/R$, where U is the output voltage and R is the load resistance) is dependent on the voltage generated and the impedance of the energy harvesting device.

The most common forms of vibration-based energy harvesting at the micro scale are piezoelectric, electromagnetic and electrostatic. The scaling of magnetoelectric harvesters is limited by the very low voltage output observed when placed under low AC magnetic field. Dielectric elastomers are limited in performance at the MEMS scale since they require large surface areas and constant application of cyclic pressure. For magnetoelectric harvesters the output voltage can be expressed as:

$$\frac{\partial U}{\partial H} = \frac{\partial \sigma_m}{\partial H} g_{ij} t_p \tag{1}$$

where σ_m is the stress generated by the magnetostrictive material, H is the applied magnetic field, and t_p is the thickness of piezoelectric material. For dielectric elastomers the output voltage is expressed as:

$$U^2 \propto \frac{\varepsilon_r \varepsilon_0}{C_p} * V * E_{\max}^2 * \left[1 - \frac{A_{\min}^2}{A_{\max}^2}\right] \tag{2}$$

where C_p is the capacity of generator, A is the surface area, V is the material volume , E_{max} is the maximum electric field strength, ε_r is the relative permittivity, and ε_0 is the permittivity of vacuum.

1.2 Modeling and Characterization of Energy Harvesters

1.2.1 Experimental Characterization

The experimental characterization of a piezoelectric, electromagnetic, or electrostatic harvester is usually conducted in a vibration testing setup. Usually, the harvester is attached to a vibrating base which actuates the harvester at arbitrary frequencies and accelerations. As shown in Figure 1, the harvester is clamped to a shaker and a laser vibrometer is used to detect the motion relative to the shaker. The relative motion can be subtracted from the induced acceleration results recorded from an accelerometer attached to the shaker or

clamp. A central digital signal processor can be used to supply the output voltage signal to the shaker and receive input voltage signals during testing.

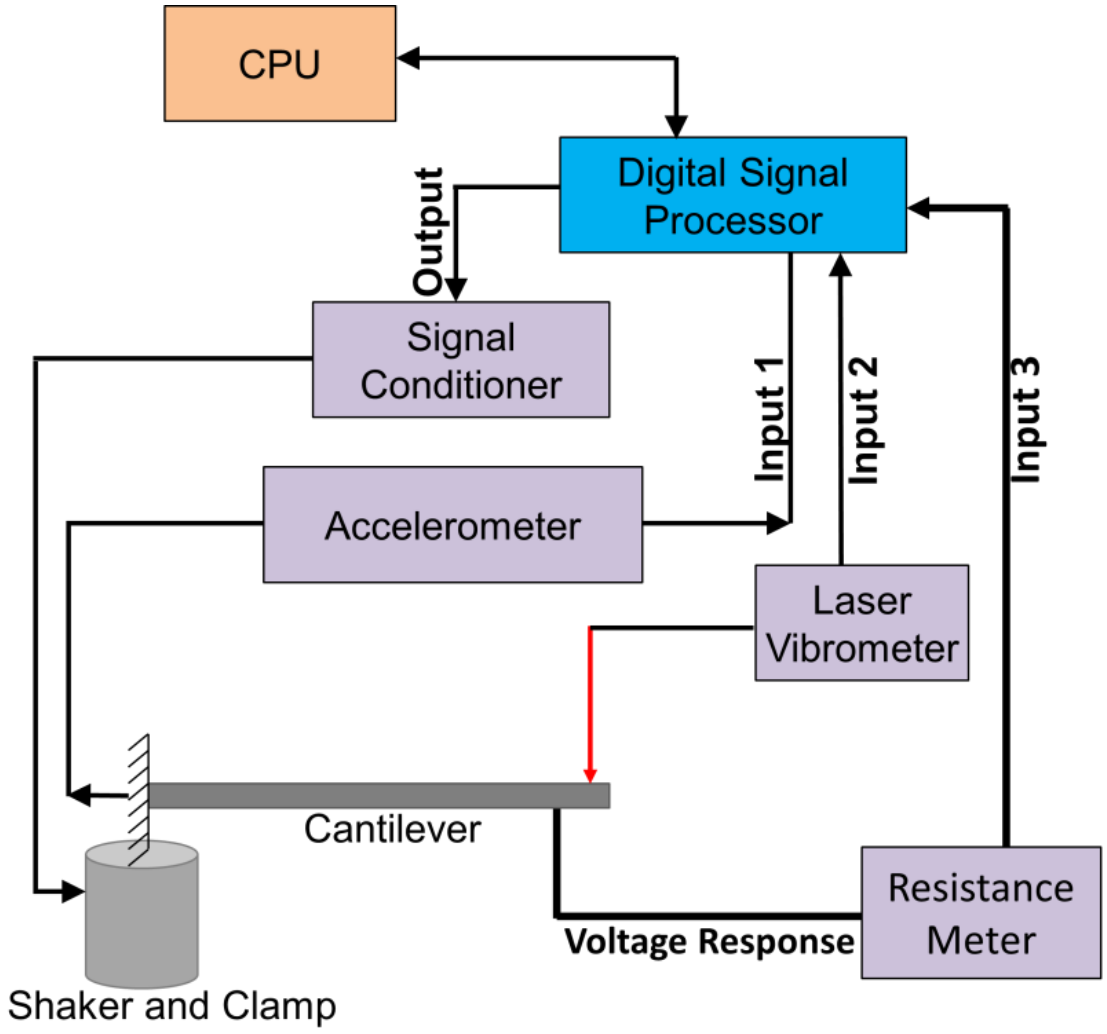

Figure 1: Typical vibration testing schematic for piezoelectric, electromagnetic and electrostatic energy harvesters.

1.2.2 Piezoelectric harvester modeling

Most piezoelectric harvesters are designed in the form of a simple cantilever (with more than one material layer) having a tip mass to tune the operating frequency as depicted in Figure 2. Piezoelectric harvesters can consist of unimorph or bimorph design. Unimorph

harvesters are composed of one layer of piezoelectric material (e.g. PZT) laminated on a flexible support layer (e.g. brass) while bimorph harvesters are composed of two layers of piezoelectric material laminated on either side of a flexible support layer. The most commonly used piezoelectric material is lead zirconate titanate (PZT) because of its significantly high piezoelectric properties (e.g. piezoelectric strain constant) when compared to the other piezoelectric materials. Piezoelectric harvesting systems tend to exhibit linear behavior in their dynamic and voltage responses, and as such are heavily reliant on cantilever resonance frequencies for appreciable power output. In some cases, electromagnetic harvesters can be used as the tip mass (placed at the end of a cantilever beam) where a magnet moves through the stationary coil. In such instances, the positions of the magnetic mass and coil within the electromagnetic harvester may also be switched [1]. These electromagnetic systems can be modeled for their vibration characteristics similar to the piezoelectric cantilevers. Similar vibration modeling approach can be applied to cantilever-based electrostatic harvesters [2].

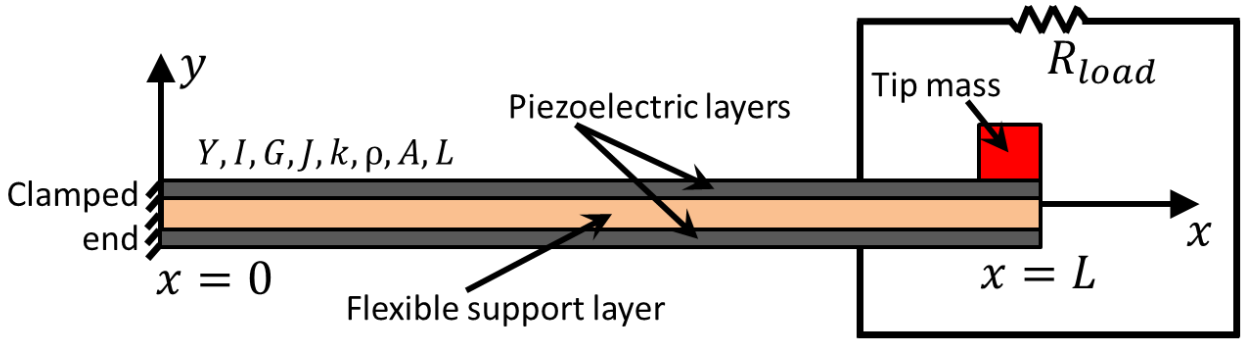

Figure 2: Bimorph piezoelectric energy harvester

A simplified derivation of the fundamental frequency (first mode) of a simple cantilever is based on the lumped mass approximation given as:

$$\omega_1 = \sqrt{\frac{k}{m_{beam} + 2.3m_{tip}}} \tag{3}$$

where ω_1 is the fundamental frequency, k is the beam stiffness, m_{beam} is the mass of the beam, and m_{tip} is the tip mass at the free end. A more accurate model for obtaining natural frequencies is based the Euler-Bernoulli theory. The equation of motion for free out-of-plane vibration is [3]:

$$YI\frac{\partial^4 w(x,t)}{\partial x^4} + \rho A\frac{\partial^2 w(x,t)}{\partial t^2} = 0 \tag{4}$$

where Y, I, ρ, and A are the Young's modulus, area moment of inertia, density, and surface area of the beam respectively. The symbol w represents the out-of-plane displacement of the beam as a function of distance along the beam length (x) and time (t). By using a separation of variables approach, we can express the beam displacement (w) and twist (β) as:

$$w(x,t) = W(x)\eta(t) \tag{5}$$

$$\beta(x,t) = B(x)\eta(t)$$

leading to spatial general solutions of the form

$$W(x) = \sum_{i=1}^{4} a_i e^{\gamma_i x}$$
$$B(x) = \sum_{i=5}^{6} a_i e^{\gamma_i x} \tag{6}$$

where

$$\gamma_i = \pm\left(\frac{\omega_n^2 \rho A}{YI}\right)^{\frac{1}{4}} \tag{7}$$

and the values of a_i are numerical constants. The values of the numerical constants, natural frequencies (ω_n), and mode shapes ($W(x)$), can be obtained by applying the following boundary conditions:

$$\begin{gathered} W(x=0) = 0 \\ W'(x=0) = 0 \\ B(x=0) = 0 \\ M(x=l) = -YIW''(x=l) = 0 \\ Q(x=l) = -YIW'''(x=l) = m_{tip}\omega_n W(x=l) \\ T(x=l) = -GJB'(x=l) = 0 \end{gathered} \tag{8}$$

to equation (6) and solving computationally. In equation (8), W', M, Q, T, G, and J represent the beam slope, bending moment, transverse shear force, twist torque, shear modulus, and polar moment of inertia respectively.

The piezoelectric harvester response to external excitation can be derived based on the Timoshenko beam theory [4, 5]. The electrically coupled governing equation of motion for a simple bimorph piezoelectric harvester with tip mass in response to external sinusoidal excitation is given as [6]:

$$YI\frac{\partial^4 w_{rel}(x,t)}{\partial x^4} + c_s I\frac{\partial^5 w_{rel}(x,t)}{\partial x^4 \partial t} + c_a\frac{\partial w_{rel}(x,t)}{\partial t} + \rho A\frac{\partial^2 w_{rel}(x,t)}{\partial t^2} + \vartheta V(t) \times\left(\frac{d\delta(x)}{dx} - \frac{d\delta(x-L)}{dx}\right) = -(\rho A + m_{tip}\delta(x-L))\frac{\partial^2 w_b(x,t)}{\partial t^2} \quad (9)$$

from which the time-dependent voltage responses for on- and off-resonance condition can be obtained. In equation (9), $c_s, c_a, w_{rel}, w_b, \delta, \vartheta$, and V denote the coefficient of strain rate damping, coefficient of viscous air damping, displacement of the beam relative to its base, displacement of the base, Dirac delta function, coupling constant, and voltage respectively. The coupling constant is dependent on the type of electrical connection (series or parallel) applied to the piezoelectric layers.

The steady state voltage response from a bimorph piezoelectric cantilever when excited transversely at resonance, is given as:

$$V = \frac{j2\omega R_{load}\kappa_r F_r e^{jwt}}{\left(2 + jwR_{load}C_p\right)(\omega_r^2 - \omega^2 + j2\zeta_r\omega_r\omega) + j2\omega R_{load}\kappa_r\chi_r} \quad (10)$$

where $\omega, \omega_r, \kappa_r, F_r, \zeta_r, \chi_r^s, C_p, R_{load}$, and j are the forcing frequency, resonance frequency, modal electrical circuit coupling term, amplitude of the modal forcing function, mechanical

damping ratio, modal electromechanical coupling term, internal capacitance of the piezoelectric layer, load resistance, and unit imaginary number ($\sqrt{-1}$) respectively. The equations of motion and voltage response can be further simplified for unimorph harvesters and harvesters without tip mass [7].

Some piezoelectric materials (mostly polymers), such as polyvinylideneflouride (PVDF), have been found to be promising for vibration energy harvesting in off resonance conditions that involve the application of alternating or uniform force (or stresses) directly to the harvester. In this mode, the harvester functions like a capacitor.

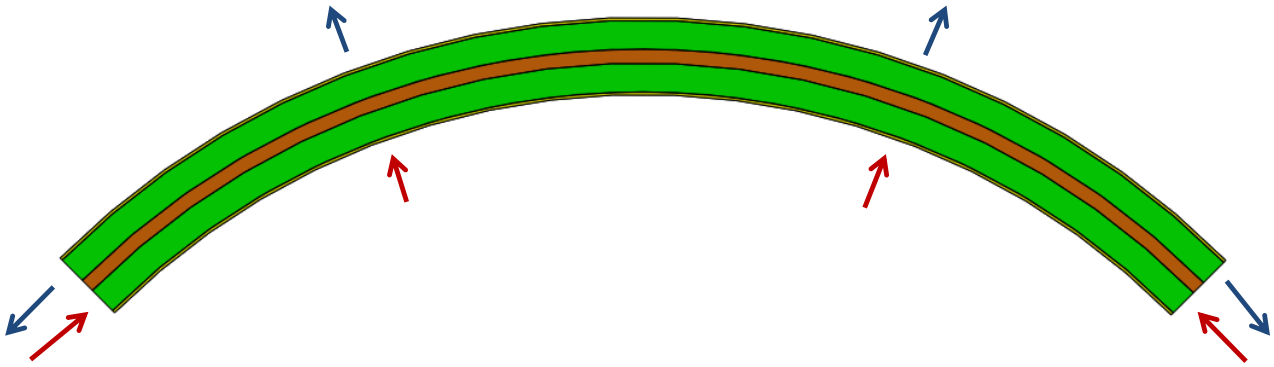

Figure 3: Forces applied to the flexible piezoelectric bimorph harvester. Red arrow = compressive force, blue arrow = tensile force.

The electric energy available under ac stress excitation from a parallel plate capacitor is given as:

$$U = \frac{1}{2}CV^2 \qquad \textbf{or} \qquad \text{energy per unit volume, } u = \frac{1}{2}d.g.\sigma^2 \tag{11}$$

where U is the energy, C is the capacitance, V is the voltage, and σ is the applied stress. A piezoelectric material with high energy density is characterized by a high product of

piezoelectric voltage constant (g) and piezoelectric strain constant (d), given as ($d \times g$). There are two extreme cases to the high energy density material, PVDF piezoelectric polymer (d_{33} = 33 pC/N, $\varepsilon_{33}/\varepsilon_o$ = 13, g_{33} = 286.7 x10^{-3} m^2/C) and relaxor piezoelectric single crystals such as PZN – 7%PT (d_{33} = 2500 pC/N, $\varepsilon_{33}/\varepsilon_o$ = 6700, g_{33} = 42.1 x10^{-3} m^2/C). It can be seen from this data that piezoelectric polymer has the highest piezoelectric voltage constant, g_{33}, of 286.7 x10^{-3} m^2/C and relaxor-based single crystals have the highest product ($d_{33} \times g_{33}$) of the order of 105250 x 10^{-15} m^2/N.

1.2.3 Electromagnetic harvester modeling

Electromagnetic harvesters consist of magnets, coils, and in some cases springs. The modus operandi involves the passage of magnetic flux field through a coil of wire, thus inducing current in the coil. The modeling of such systems depends on the spring force(s) present. When a return spring is attached to the magnet, the response of the system is mostly linear (just like piezoelectric cantilevers), and the vibration characteristics can be modeled using a simple lumped mass approach thus:

$$\omega_1 = \sqrt{\frac{k_{sp}}{m_{mag}}} \tag{12}$$

where ω_1 is the fundamental frequency, k_{sp} is the spring stiffness, m_{mag} is the mass of the beam. However, some electromagnetic systems incorporate abstract spring systems based on magnetic repulsion. For such systems, the dynamic voltage responses typically exhibit

nonlinear and broadband behavior [8]. An efficient design for electromagnetic energy harvesters involves the levitation of a magnet between two stationary magnets. Finite element analysis can be used to obtain the force field (F) and magnetic flux field (B) while a computational model can be used to simulate the dynamics and voltage response of the harvester. The electromagnetic harvester in this case is modeled as a moving mass restricted by two nonlinear springs and two dampers. As shown in Figure 4, the model can be simplified to one mass, one nonlinear spring, and one damper since the two springs are based on magnetic repulsion forces which are similar.

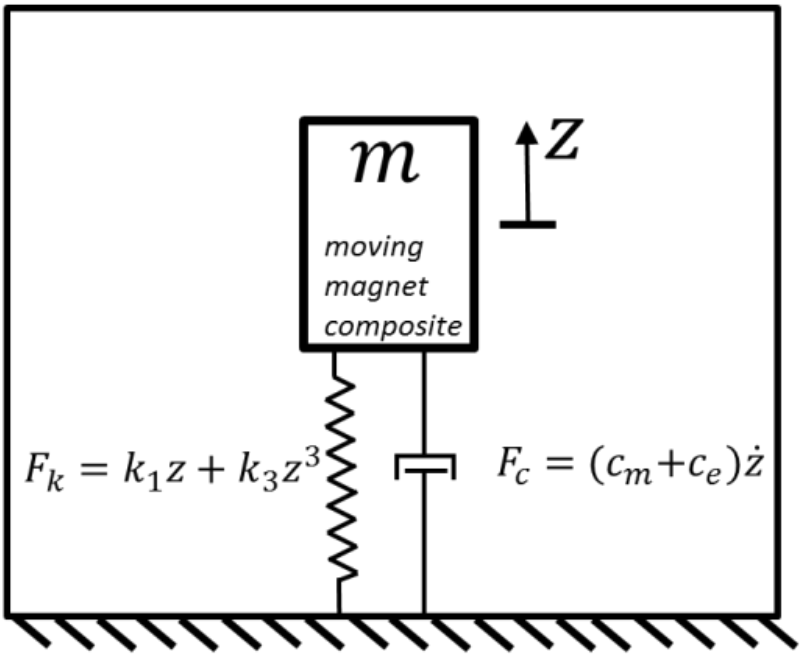

Figure 4: Schematic representation of the dynamic modeling for electromagnetic harvesters

Thus the dynamics of the oscillating moving magnet composite can be mathematically modeled by using a nonlinear spring-mass-damper mechanical system with an externally applied base excitation given as:

$$m\ddot{z}(t) + c_m\dot{z}(t) + c_e(t)\dot{z}(t) + kz(t) + k_3z(t)^3 = -m\ddot{y}(t) - mg \tag{13}$$

where m is the moving magnet composite mass, c_m is the mechanical damping constant, $c_e(t)$ is the instantaneous electrical damping, k is the linear stiffness constant of the spring, k_3 is the nonlinear stiffness constant of the spring, z̈(t) is the relative acceleration between the base of the structure ÿ(t) and the vibrating mass ẍ(t), g is the gravitational constant, $\dot{z}$ and z are the velocity and displacement of the moving magnet composite respectively. The acceleration of the vibrating mass ẍ(t) includes the moving magnet and the base of the structure, i.e. $z(t) = x(t) - y(t)$. Thus the value of z defines the vibration of the moving magnet only. The nonlinear mathematical spring represents the repulsion between the moving magnet composite and the stationary magnets and it is related to the instantaneous magnetic repulsion force (F) and the moving magnet displacement by $F(t) = kz(t) + k_3z(t)^3$. The instantaneous voltage response of the harvester can be obtained from $V = \frac{Bl\dot{z}}{R_L+R_e}R_L$, where n is the number of discrete points applied.

1.2.4 Electrostatic/Electret harvester modeling

Electrostatic energy harvesters are based on a capacitive design (two charged electrodes spaced by an air gap). Vibrations induce changes in the geometry of the capacitor and a circulation of charges between the electrodes through the electrical load as shown in Figure 5. The total charge induced in the electret is a sum of the charges in the electrode and counter-electrode ($Q_{total} = Q_e + Q_{ce}$). The most common method for electret manufacturing is via the 'corona discharge'. This involves subjecting a point-grid-plane structure to a strong electric field leading to the implantation of charges at the electret surface. The most commonly used electret material is CYTOP polymer because of its capacity for significantly large surface charge density [9-12].

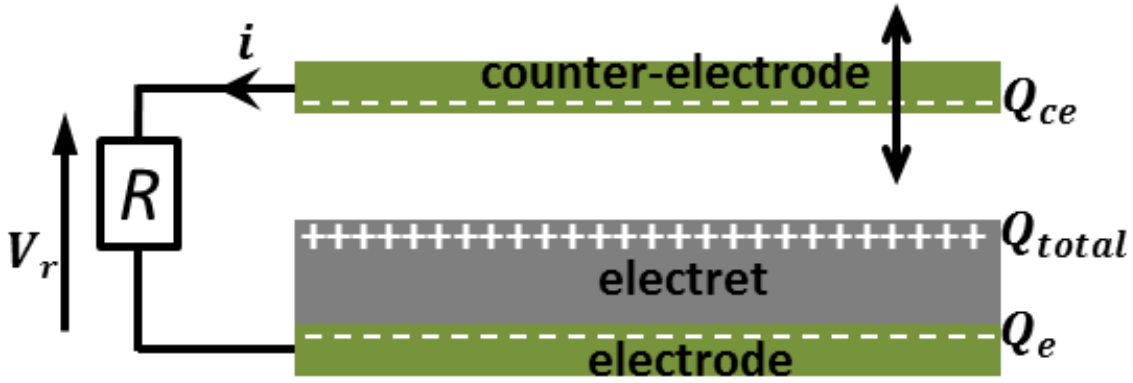

Figure 5: Configuration of an operational electret (variable out-of-plane gap configuration) in which the counterelectrode vibrates relative to the electret and electrode ($Q_{total} = Q_e + Q_{ce}$).

Electrostatic power generators can be classified into three types: variable in-plane overlap, variable in-plane gap and variable out-of-plane gap. The most commonly used configurations at the micro scale are the variable in-plane gap and variable in-plane gap. The

maximum power output from a micro electret power generator can be estimated from Eq. (14):

$$P = \left(\left[\frac{4\varepsilon_0 \varepsilon_E}{t_E} \left(\frac{\varepsilon_E d}{\varepsilon_A t_E} + 1 \right) \right]^{-1} * \sigma^2 * \frac{dA(t)}{dt} \right) \propto t_E^2 \tag{14}$$

where σ is the surface charge density, $A(t)$ is the variable overlap area between the top and bottom electrodes, ε_E is the dielectric constant of the electret, ε_0 is the permittivity of vacuum, ε_A is the dielectric constant of air (i.e. ~1), d is the distance between the top electrode and electret surface, and t_E is the electret thickness.

As seen in equation (14), the power output of a micro electret power generator is dependent on the geometric parameters such as the gap distance, *d*, and the thickness of the electret material, t_E [13]. Since typical values of ε_E, the dielectric constant of polymer electrets, are around 2 (2.2 for parylene HTR, 2.1 for CYTOP, 1.9 for Teflon AF and 2.1 for PTFE), we can estimate the effect of variations in the gap distance and electret thickness. When the gap distance is larger than two times the electret thickness ($d > 2t_E$), the gap distance becomes a limiting factor for the power response of the electret harvester. Therefore, a small gap-to-thickness ratio is important if the power response is to be maximized. Since the largest state-of-the-art thickness of electrets is 20 μm of CYTOP, the gap distance has to be controlled within around 50 μm for appreciable energy harvesting response.

1.3 Trends in Low Frequency MEMS Energy Harvesting

Tables 1-3 and Figures 1 & 2 provide a summary of experimental MEMS energy harvesters reported in literature.

Table 1: Summary of Low Frequency Piezoelectric MEMS Harvesters

No.		Author (Ref.)	Year	Piezo Material	Operating Frequency, f (Hz)	Base Excitation (g)	Max. Average Power (μW)	Bandwidth (Hz)	Device Volume (mm^3)	NPD ($\mu W mm^{-3} g^{-2}$)
1		Choi [14]	2006	PZT	150	n/p	1.01	n/p	2.50E-03	n/p
2		Liu [15]	2008	PZT	229	0.5	3.98	8	n/p	n/p
3	i	Aktakka [16]	2011	PZT	154	1.5	205	n/p	26.95	3.4
	ii				167	0.1	2.74			10.1
4		Hajati [17]	2011	PZT	1300	n/p	45	171	2.10E-02	n/p
5		Liu [18]	2011	PZT	20 – 50[a]	1	5.13E-02	17	16	3.21E-03
6	i	Tang [19]	2012	PMN-PT	237.4	1	2.7	n/p	0.6	4.5
	ii						5.93			1.48
7		Xu [20]	2012	PZT	243	1	37.1	4.3	54.7	0.69
8		Jackson [21]	2013	AIN	149	0.2	3	4	30.71	2.55
9		Kim [22]	2013	PZT	243	0.5	2.15	n/p	1.5	5.73
10		Tsujiura [23]	2013	KNN	393	1	1.6	6	17	9.40E-02
11		Tsujiura [24]	2013	PZT	75	1	1.1	3	5.4	0.2
12	i	Jackson [25]	2014	AIN	149	0.2	3.5	1.2	35	2.5
	ii				118	0.4	1.27	0.9	10.2	0.78
	iii				97		0.43	0.82	4.13	0.65
13	i	Janphuang [26]	2014	PZT	100	0.1	1.6	n/p	47.82	3.35
	ii					1	82.4	5.5		1.72
14		Liu [27]	2014	PVDF	20	0.2	8.1	7	10	2.03E-02

n/p = not provided

[a] Broadband device with 10 PZT elements.

Table 2: Summary of Low Frequency Electromagnetic MEMS Harvesters

No.		Author (Ref.)	Year	Operating Frequency, f (Hz)	Base Excitation (g)	Max. Average Power (μW)	Bandwidth (Hz)	Device Volume (mm^3)	NPD ($\mu W mm^{-3} g^{-2}$)
1		Ching [28]	2002	70	n/p	830	1	1000	n/p
2		Beeby [29]	2007	52	0.06	46	2	150	85
3		Wang [30]	2011	242	0.5	0.55	20	660	3.30E-03
4	i	Cepnik [31]	2011	342	0.1	0.62	4	460	0.135
	ii				0.05	0.25	3.5		0.217
5	i	Liu [32]	2012	1285	1	1.60E-02	8	36	4.44E-04
	ii			1470		8.70E-03	12		2.42E-04
	iii			1550		4.50E-03	13		1.25E-04
6	i	Bang [33]	2013	36	0.3	29.02	0.4	600	0.537
	ii			63		24.2	0.6		0.448
7		Li [34]	2013	48	1.2	1.50E-02	n/p	2.72	3.83E-03
8	i	Liu [35]	2013	840	1	5.50E-03	9	35	1.57E-04
	ii			1070		5.00E-04			1.40E-05
	iii			1490		4.10E-03	16		1.17E-04
9	i	Zorlu [1]	2013	2100	n/p	0.363	n/p	3.12	n/p
	ii			1950		0.364			
11	i	Chen [36]	2014	211	1.42	7.66E-03	8.5	1.988	1.91E-03
	ii			274	1.23	7.43E-03	5		2.47E-03
12		Han [37]	2014	27	0.5	0.75	5	1000	3.00E-03
13		Lei [38]	2014	124.2	0.5	205.38	1.7	1800	0.457

n/p = *not provided*

Table 3: Summary of Low Frequency Electrostatic/Electret MEMS Harvesters

No.		Author (Ref.)	Year	Dielectric Material	Operating Frequency, f (Hz)	Base Excitation (g)	Max. Average Power (μW)
1		Tsutsumino [9]	2006	CYTOP	20	n/p	38
2	i	Lo [13]	2008	Parylene HT	50	n/p	17.98
	ii				20		8.23
	iii				10		7.7
3		Miki [39]	2010	CYTOP	63	2	1
4		Boisseau [2]	2011	FEP	50	0.1	50
5		Triches [40]	2012	CYTOP	75	1.40E-02	1.17
6		Crovetto [41]	2013	CYTOP	179	3.00E-02	32.5
7	i	Jia [42]	2013	n/p	1380[a]	0.43	1.56E-01
	ii				342.5[b]		1.27E-01
	iii				700[c]		1.10E-02
8		Minakawa [43]	2013	CYTOP	28	0.5	1.50E+00
9		Wang [44]	2013	CYTOP	96	1	1.50E-01
10		Cottone [45]	2014	n/p	50	0.3	4.50E-01
11		Tao [46]	2014	LDPE	66	5.00E-02	4.80E-03

[a]First-order parametric resonance, [b]fourth-order parametric resonance, and [c]fundamental resonance mode.

From the tables 1 – 3, it can be seen that significant progress has been made in miniaturizing energy harvesters. Piezoelectric MEMS harvesters produce the highest power outputs and power densities when compared to the electromagnetic MEMS and electrostatic MEMS harvesters. Electromagnetic MEMS harvesters exhibit lower power output because of the reduced magnet and coil sizes.

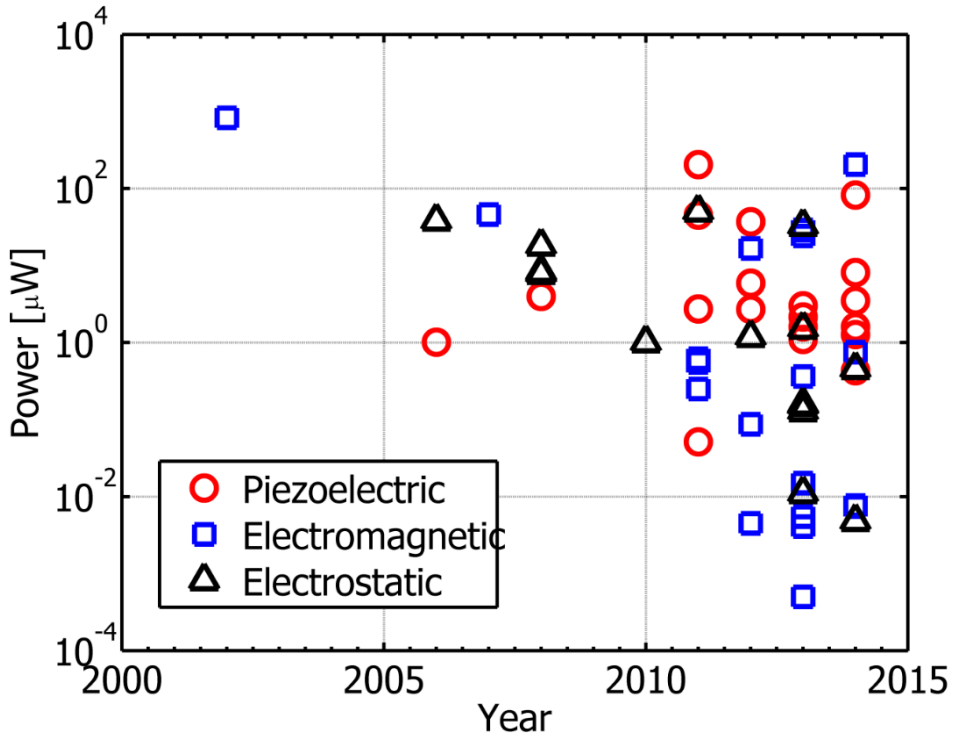

Figure 6: Performance of MEMS harvesters as a function of time.

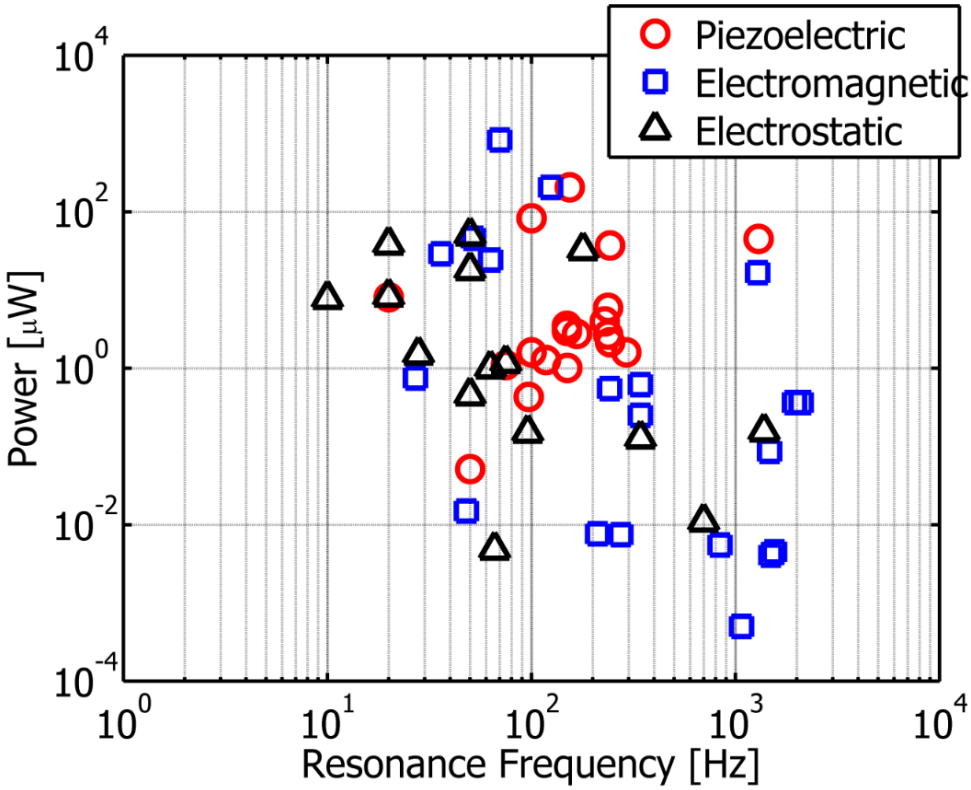

Figure 7: Performance of MEMS harvesters as a function of resonance frequency

Most fully characterized MEMS harvesters were developed and reported within the last three years (since 2011) as shown in Figure 6. The power responses reported are typically in the μW range. As seen from Figure 7, low frequency has been achieved mostly with piezoelectric MEMS and electrostatic MEMS harvesters due to the addition of tip masses which increase the effective mass. However, the addition of tip masses severely limits the structural integrity and durability of the harvesters.

1.4 Thesis Focus

Overall, the goal of this thesis is the development (via modeling and experiments) of five unique MEMS harvester structures which overcome most of the problems associated with the state of the art. The harvesters exhibit low resonance frequency (< 35 Hz), are structurally stable, can be easily handled without mechanical damage occurring, and produce significant power response (0.1 – 100mW range). The overall thesis breakdown is as following:

- Magnetoelectric cantilever MEMS energy harvesters (chapters 2 & 3),
- MEMS electromagnetic energy harvesters (chapters 4 & 5), and
- Coupled MEMS energy harvester which incorporates piezoelectric cantilever and electromagnetic mechanisms (chapter 6).

Chapter 1 presents the state of the art in low frequency micro energy harvesting. It covers the basics of the modeling and characterization for piezoelectric, electromagnetic, and electrostatic harvesters. A literature review of the reported properties for low frequency MEMS harvesters is presented.

Chapter 2 introduces the unique design for micro cantilever harvesters. This design is called 'arc-based cantilever' or 'ABC'. The ABC design ensures low resonance frequency and pure bending in the first mode. The mathematical vibration modeling of the cantilever is thoroughly discussed. The model is based on the classical Timoshenko beam theory and includes the effects of bending, torsion, transverse shear deformation and rotary inertia. It was also developed with a provision for multilayered beam modeling. An example beam model is provided as well as experimental verification using an aluminium arc based cantilever.

Chapter 3 introduces various designs of ABCs characterized via modeling and experiments, and shows the application of the arc-based cantilever to harvest energy from vibrations and magnetic fields. Micro arc-based cantilevers developed as variations of simple and zigzag cantilvers are presented to show their potential for frequency reduction. Also, micro arc-based cantilever designs (S-shaped and C-shaped) were modeled, fabricated, and tested. Finally, two PVDF-based magnetoelectric harvesters based on the C-shaped arc-based cantilever design were fabricated and experimentally characterized for dual-phase energy harvesting from vibrations and magnetic fields.

Chapter 4 introduces the modeling concepts for electromagnetic energy harvesters that consist of the magnetic levitation of a magnet (or magnet composite) between two stationary magnets. These harevsters are refered to as levitation-induced vibration energy (LIVE) harvesters. The double-repulsion configuration is computationally modeled and

characterized to show its advantages over the other moving magnet configurations (increased dynamics, reduced electrical damping, and significantly increased output power response). An AA battery-sized device was then fabricated based on the double-repulsion configuration and experimentally characterized. The device was shown to exhibit significantly higher normalized power density when compared to the other reported electromagnetic harvesters. An external charging circuit was designed and shown to enable the charging of a cell phone when shaken by hand.

Chapter 5 shows the scaling analysis of the electromagnetic LIVE harvesters and introduces the development of a MEMS electromagnetic energy harvester which exhibits a unique nonlinear inflection profile. The power scaling of LIVE harvesters is presented to show the effects of dynamics on the output response. A MEMS LIVE harvester with metglas guides (to increase the magnetic flux field) was also modeled and experimentally characterized. The harvester was shown to exhibit a softening spring and a nonlinear inflection profile. The analysis of nonlinear inflection causal parameters in magnetically-levitated electromagnetic energy harvesters is presented.

Chapter 6 presents a coupled MEMS harvester which incorporates piezoelectric cantilever and electromagnetic mechanisms. The positive attributes of each component (low frequency and increased velocity attributes of the arc-based cantilever as well as the broadband nature and nonlinearity of the electromagnetic part) are shown to be positively transferred from one component to another. A novel PIEZOCAP concept is introduced for increased voltage

induction in the piezoelectric membranes due to pressure generated from magnetic repulsion.

Chapter 7 provides the summary of the thesis and conclusions which have been derived for the work performed. Lastly, a performance evaluation of the harvesters is presented thereby providing context for future outlook.

2 Chapter 2:

Arc-Based Cantilever Vibration Modeling and Experimental Verification

The performance, capabilities, and deployment of wireless sensor networks (WSNs) continue to rise. One of the reasons for the rapid proliferation of the WSNs is related to the significant progress being made in CMOS electronics that has brought down the power requirements considerably. At the same time, there has been significant progress in development of energy harvesters that can meet the power requirements of the electronics, and enhance the lifetime and limitations of a conventional battery. Among these varieties of energy harvesting approaches, vibration energy harvesting has been pursued both as an alternative and as a supplement to batteries, and in recent years there has been a surge in the number of publications in this area. In order for vibration energy harvesting (VEH) to become practical, the size and weight of the harvester should be compatible with the mm-scale electronics and sensors. Recent study by Mitcheson *et al.* [47] has shown that at the mm-scale, piezoelectric mechanism provides the best output power density at low frequencies as compared to other possible mechanisms for VEH. However, piezoelectric based VEH presents a fundamental challenge at the small dimensions since the resonance frequency of the structure increases as the dimension decreases. This challenge should be overcome in order for this technology to become compatible with the applications.

Vibration analysis of curved beams has been extensively investigated in literature. Ojalvo [48] has presented an analysis of coupled twist-bending vibrations of incomplete circular rings by applying the classical Euler-Bernoulli beam theory. A two-span curved girder was modeled by Culver *et al.* [49] for use in the bridge structures. Some of the early literature in this field has utilized Timoshenko beam theory [4] and investigated the effects of transverse shear and rotary inertia on circular beam vibration [50-53]. Rao *et al*. [53] have shown that the modeling of circular arc beams without incorporation of both rotary inertia and shear deformation leads to errors in the calculation of natural frequencies. Over the past four decades, there have been other reports that have incorporated the Timoshenko beam theory in modeling of circular arc or ring beams. Wang et al. [54, 55] have studied the out-of-plane vibrations of continuous unidirectional circular beams with and without shear and rotary inertia consideration. Their study provided the detailed development of a dynamic circular beam stiffness matrix. Howson *et al.* [56] have also studied out-of-plane vibrations of continuous unidirectional circular beams and introduced parameters that can be modified to gauge the effects of shear and rotary inertia. More recently, Lee *et al.*[57] presented the theory for non-uniform circular arc beams with constant radius. However, the exact modeling of continuous circular arc beams which are multilayered and multidirectional has been absent in literature.

Cantilever beams have been used widely in low frequency energy harvesting applications at the micro scale[3]. However the increase in natural frequency as cantilevers become smaller limits the low frequency potential of standalone micro cantilevers. Several researchers have attempted to resolve this problem by adding a tip mass to the end of the cantilever. However, a more effective method lies in developing uniquely shaped cantilevers,

such as arc-based cantilevers, which exhibit low natural frequencies. In this chapter, a general out-of-plane vibration model for single and continuous circular arc beams is presented. The effects of bending, torsion, transverse shear deformation and rotary inertia have been incorporated in the development of the model. The model can be applied for multilayered beams with different beam boundary conditions (e.g. clamped, pinned and free). To demonstrate the application of model, an example of a multilayered multi-directional continuous beam with three circular arcs is included. The beam was designed for piezoelectric energy harvesting application. To verify the accuracy of the numerical model, experimental results of an arc-based cantilever are compared with numerical results. The theory presented in this chapter can be applied to the modeling of microscale or macroscale beams which can be divided into any number of circular arcs (such as S-shaped beams).

2.1 Theoretical Development of the Model

2.1.1 Governing Equations

Consider the circular arc beam shown in Figure 8. The expressions for the bending moment, M, and twist torque, T, of the beam can be written as [48, 54-56, 58]:

$$M(\theta,t) = \frac{YI}{R}\left(\varphi - \frac{\partial\psi}{\partial\theta}\right) \tag{15}$$

$$T(\theta,t) = \frac{GJ}{R}\left(\psi + \frac{\partial\varphi}{\partial\theta}\right) \tag{16}$$

where Y is the Young's modulus, I is the area moment of inertia in the bending plane, G is the modulus of rigidity, J is the polar moment of inertia, R is the radius, φ is the angle of twist, ψ is the slope of the deflection curve when shearing is neglected, θ is the angular coordinate, and t is the time.

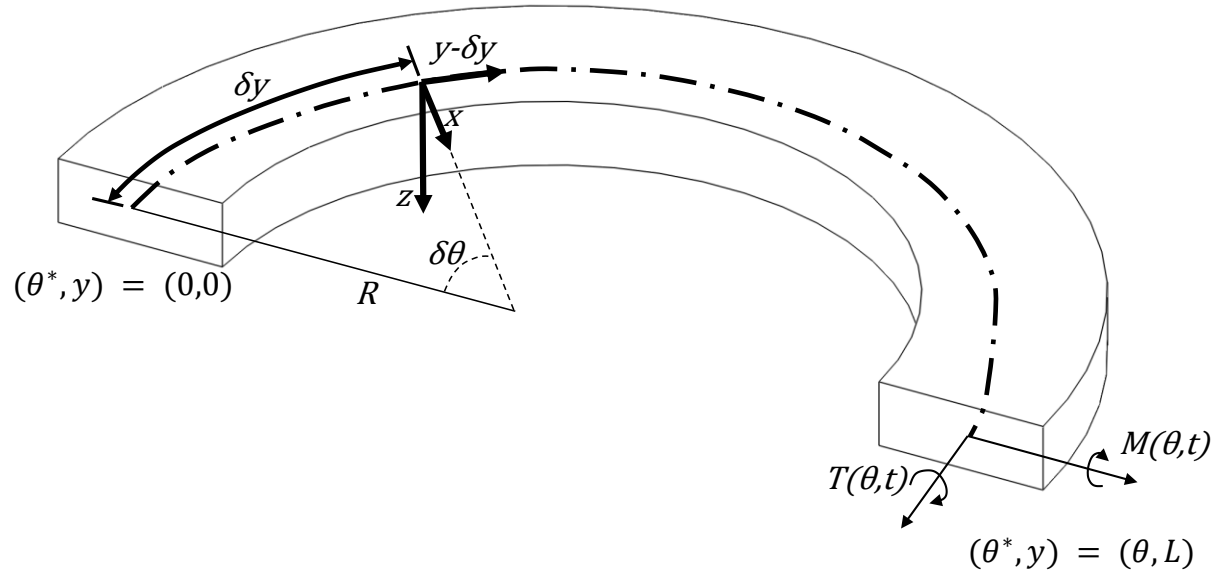

Figure 8: Schematic representation of a circular arc beam.

In the presence of shearing force, the slope of the transverse deflection curve is expressed as:

$$\frac{1}{R}\frac{\partial z}{\partial \theta} = \psi + \alpha \tag{17}$$

where z is the vertical displacement (deflection) of the beam, and α is the angle of shear at the neutral axis. We can express the shear force in the transverse direction (Q) as:

$$Q(\theta, t) = \eta \alpha A G \tag{18}$$

where A is the cross-sectional area of the beam and η is the shear coefficient. The parameter η is an indication of the variation of α through the cross-section. For rectangular cross sections, η can be expressed as [59]:

$$\eta = \frac{10(1+\nu)}{12+11\nu} \tag{19}$$

where ν is the Poisson's ratio. From Eqns. (17) and (18), we can express Q as:

$$Q(\theta, t) = \eta A G \left(\frac{1}{R}\frac{\partial z}{\partial \theta} - \psi\right) \tag{20}$$

For free vibrations, external force and torque distributions are neglected, and the equations of motion for the rotation of a circular arc about the radial and tangential axes can be written as:

$$\frac{\partial M}{\partial \theta} + T - QR = -\rho I R \frac{\partial^2 \psi}{\partial t^2} \tag{21}$$

$$M - \frac{\partial T}{\partial \theta} = -\rho J R \frac{\partial^2 \varphi}{\partial t^2} \tag{22}$$

where ρ is the mass density of the beam. The equation governing the translation of a differential element of the beam in the transverse direction is given as:

$$\frac{\partial Q}{\partial \theta} = \rho AR \frac{\partial^2 z}{\partial t^2} \tag{23}$$

Using input from equations (15) – (20), the equations (21) - (23) can be re-written as:

$$\frac{\partial z}{\partial \theta} = \frac{YI}{\eta ARG}\left(\frac{\partial \varphi}{\partial \theta} - \frac{\partial^2 \psi}{\partial \theta^2}\right) + \psi R + \frac{J}{\eta AR}\left(\psi + \frac{\partial \varphi}{\partial \theta}\right) + \frac{\rho IR}{\eta AG}\frac{\partial^2 \psi}{\partial t^2} \tag{24}$$

$$GJ\frac{\partial^2 \varphi}{\partial \theta^2} - YI\varphi - \rho JR^2\frac{\partial^2 \varphi}{\partial t^2} = -\frac{\partial \psi}{\partial \theta}(GJ + YI) \tag{25}$$

$$\frac{\partial \psi}{\partial \theta} = \frac{1}{R}\frac{\partial^2 z}{\partial \theta^2} - \frac{\rho R}{\eta G}\frac{\partial^2 z}{\partial t^2} \tag{26}$$

From equations (24) - (26), we can obtain a single equation of the form:

$$\begin{aligned}
&\frac{\partial^6 z}{\partial \theta^6} + 2\frac{\partial^4 z}{\partial \theta^4} + \frac{\partial^2 z}{\partial \theta^2} \\
&\quad = \frac{\rho R^2}{G}\left(1 + \frac{1}{\eta} + \frac{G}{Y}\right)\frac{\partial^6 z}{\partial \theta^4 \partial t^2} - \frac{\rho^2 R^4}{G^2}\left(\frac{1}{\eta} + \frac{G}{Y} + \frac{G}{\eta Y}\right)\frac{\partial^6 z}{\partial \theta^2 \partial t^4} \\
&\quad - \frac{\rho R^2}{G}\left(\frac{AR^2 k}{J} - \frac{2}{\eta} + \frac{I}{\eta J} + k\right)\frac{\partial^4 z}{\partial \theta^2 \partial t^2} + \frac{\rho^3 R^6}{G^2 Y \eta}\frac{\partial^6 z}{\partial t^6} \\
&\quad + \frac{\rho^2 R^4}{G^2}\left(\frac{AR^2 k}{J} + \frac{I}{\eta J} + \frac{k}{\eta}\right)\frac{\partial^4 z}{\partial t^4} + \frac{\rho R^2}{G}\left(\frac{AR^2}{J} + \frac{1}{\eta}\right)\frac{\partial^2 z}{\partial t^2}
\end{aligned} \tag{27}$$

where k is the stiffness parameter ($k = GJ/YI$). We can assume solutions for the transverse deflection, slope, and twist of the beam as:

$$\begin{aligned} z &= Z(\theta)e^{j\omega t}, \\ \psi &= \Psi(\theta)e^{j\omega t}, \\ \varphi &= \Phi(\theta)e^{j\omega t} \end{aligned} \tag{28a-c}$$

where ω is the natural frequency and $j = \sqrt{-1}$. Applying the assumed solutions to equations (25), (26), and (27) we obtain the spatial form of the equations as:

$$k\Phi'' + (ku - 1)\Phi = -\Psi'(k + 1) \tag{29}$$

$$\Psi' = \frac{1}{R}\left(Z'' + \frac{u}{\eta}Z\right) \tag{30}$$

$$Z^{VI} + mZ^{IV} + nZ'' + qZ = 0 \tag{31}$$

where

$$\begin{aligned} u &= \frac{\rho R^2 \omega^2}{G} \\ m &= 2 + u\left(1 + \frac{1}{\eta} + \frac{G}{Y}\right) \\ n &= 1 - u\left(\frac{AR^2 k}{J} - \frac{2}{\eta} + \frac{I}{\eta J} + k\right) + u^2\left(\frac{1}{\eta} + \frac{G}{Y} + \frac{G}{\eta Y}\right) \end{aligned} \tag{32}$$

$$q = u\left\{\frac{AR^2}{J} + \frac{1}{\eta} - u\left(\frac{AR^2k}{J} + \frac{I}{\eta J} + \frac{k}{\eta}\right) + u^2\left(\frac{G}{\eta Y}\right)\right\}$$

We can further assume spatial solutions of the form:

$$\begin{aligned} Z(\theta) &= \sum_{n=1}^{6} a_n e^{\gamma_n \theta}, \\ \Psi(\theta) &= \sum_{n=1}^{6} a_n b_n e^{\gamma_n \theta}, \\ \Phi(\theta) &= \sum_{n=1}^{6} a_n c_n e^{\gamma_n \theta} \end{aligned} \tag{33a-c}$$

where the values of a_n are numerical constants, and the values of γ_n are the roots of the characteristic equation:

$$\gamma^6 + m\gamma^4 + n\gamma^2 + q\gamma = 0 \tag{34}$$

Plugging the assumed spatial solutions into equations (29), we obtain the values of b_n and c_n as:

$$\begin{aligned} b_n &= \frac{1}{R}\left(\gamma_n + \frac{u}{\eta\gamma_n}\right), \\ c_n &= b_n\gamma_n\left(\frac{1+k}{1-ku-\gamma_n^2 k}\right) \end{aligned} \tag{35a-b}$$

2.1.2 Boundary and Continuity Matrices

In order to calculate the natural frequencies, we consider six properties. These properties include the deflection, slope and twist as expressed in equation 33a-c. The other three properties are the bending moment (M), twist torque (T), and transverse shear force (Q). They are determined from equations 15, 16, 20, and 33a-c, and expressed as:

$$M(\theta) = \frac{YI}{R}\sum_{n=1}^{6}\left[a_n(c_n - b_n\gamma_n)e^{\gamma_n\theta}\right]$$

$$T(\theta) = \frac{GJ}{R}\sum_{n=1}^{6}\left[a_n(b_n + c_n\gamma_n)e^{\gamma_n\theta}\right] \qquad \text{(36a-c)}$$

$$Q(\theta) = \eta AG\sum_{n=1}^{6}\left[a_n\left(\frac{\gamma_n}{R} - b_n\right)e^{\gamma_n\theta}\right]$$

Therefore for any circular arc beam defined with θ in the clockwise direction, we can define the continuity conditions by the beam properties at its ends. We can represent the beam properties at the start of the arc (AS) in matrix form as:

$$AS = \begin{bmatrix} 1 & 1 & 1 & 1 & 1 & 1 \\ b_1 & b_2 & b_3 & b_4 & b_5 & b_6 \\ c_1 & c_2 & c_3 & c_4 & c_5 & c_6 \\ \frac{c_1 - b_1\gamma_1}{R} & \frac{c_2 - b_2\gamma_2}{R} & \frac{c_3 - b_3\gamma_3}{R} & \frac{c_4 - b_4\gamma_4}{R} & \frac{c_5 - b_5\gamma_5}{R} & \frac{c_6 - b_6\gamma_6}{R} \\ \frac{b_1 + c_1\gamma_1}{R} & \frac{b_2 + c_2\gamma_2}{R} & \frac{b_3 + c_3\gamma_3}{R} & \frac{b_4 + c_4\gamma_4}{R} & \frac{b_5 + c_5\gamma_5}{R} & \frac{b_6 + c_6\gamma_6}{R} \\ \frac{\gamma_1}{R} - b_1 & \frac{\gamma_2}{R} - b_2 & \frac{\gamma_3}{R} - b_3 & \frac{\gamma_4}{R} - b_4 & \frac{\gamma_{15}}{R} - b_5 & \frac{\gamma_6}{R} - b_6 \end{bmatrix} \qquad (37)$$

while the beam properties at the end of the arc (AE) can be written as:

$$AE = \begin{bmatrix} e^{\gamma_1\theta} & e^{\gamma_2\theta} & e^{\gamma_3\theta} & e^{\gamma_4\theta} & e^{\gamma_5\theta} & e^{\gamma_6\theta} \\ b_1 e^{\gamma_1\theta} & b_2 e^{\gamma_2\theta} & b_3 e^{\gamma_3\theta} & b_4 e^{\gamma_4\theta} & b_5 e^{\gamma_5\theta} & b_6 e^{\gamma_6\theta} \\ c_1 e^{\gamma_1\theta} & c_2 e^{\gamma_2\theta} & c_3 e^{\gamma_3\theta} & c_4 e^{\gamma_4\theta} & c_5 e^{\gamma_5\theta} & c_6 e^{\gamma_6\theta} \\ \left(\frac{c_1 - b_1\gamma_1}{R}\right) e^{\gamma_1\theta} & \left(\frac{c_2 - b_2\gamma_2}{R}\right) e^{\gamma_2\theta} & \left(\frac{c_3 - b_3\gamma_3}{R}\right) e^{\gamma_3\theta} & \left(\frac{c_4 - b_4\gamma_4}{R}\right) e^{\gamma_4\theta} & \left(\frac{c_5 - b_5\gamma_5}{R}\right) e^{\gamma_5\theta} & \left(\frac{c_6 - b_6\gamma_6}{R}\right) e^{\gamma_6\theta} \\ \left(\frac{b_1 + c_1\gamma_1}{R}\right) e^{\gamma_1\theta} & \left(\frac{b_2 + c_2\gamma_2}{R}\right) e^{\gamma_2\theta} & \left(\frac{b_3 + c_3\gamma_3}{R}\right) e^{\gamma_3\theta} & \left(\frac{b_4 + c_4\gamma_4}{R}\right) e^{\gamma_4\theta} & \left(\frac{b_5 + c_5\gamma_5}{R}\right) e^{\gamma_5\theta} & \left(\frac{b_6 + c_6\gamma_6}{R}\right) e^{\gamma_6\theta} \\ \left(\frac{\gamma_1}{R} - b_1\right) e^{\gamma_1\theta} & \left(\frac{\gamma_2}{R} - b_2\right) e^{\gamma_2\theta} & \left(\frac{\gamma_3}{R} - b_3\right) e^{\gamma_3\theta} & \left(\frac{\gamma_4}{R} - b_4\right) e^{\gamma_4\theta} & \left(\frac{\gamma_5}{R} - b_5\right) e^{\gamma_5\theta} & \left(\frac{\gamma_6}{R} - b_6\right) e^{\gamma_6\theta} \end{bmatrix} \tag{38}$$

The matrices AS and AE serve as the continuity conditions for beams comprising of more than one circular arc.

For any circular arc beam or combination of circular arc beams, we can write the known boundary conditions at the two ends, $BE_{(3\times6)}$, in matrix form. For a beam clamped at one end and free on the other end, and consisting of i number of circular arcs, the known boundary conditions are [59]:

$$\begin{aligned} Z_1(\theta^*) &= 0, \\ \Psi_1(\theta^*) &= 0, \\ \Phi_1(\theta^*) &= 0, \\ M_i(\theta^*) &= 0, \\ T_i(\theta^*) &= 0, \text{ and} \\ Q_i(\theta^*) &= 0 \end{aligned} \tag{39a-f}$$

where θ^* represents the angular location (0 or θ) on the arc to which the boundary condition is applied. Therefore, we can obtain the boundary condition matrices as:

$$BE_a = \begin{bmatrix} e^{\gamma_{11}\theta_1^*} & e^{\gamma_{12}\theta_1^*} & e^{\gamma_{13}\theta_1^*} & e^{\gamma_{14}\theta_1^*} & e^{\gamma_{15}\theta_1^*} & e^{\gamma_{16}\theta_1^*} \\ b_{11}e^{\gamma_{11}\theta_1^*} & b_{12}e^{\gamma_{12}\theta_1^*} & b_{13}e^{\gamma_{13}\theta_1^*} & b_{14}e^{\gamma_{14}\theta_1^*} & b_{15}e^{\gamma_{15}\theta_1^*} & b_{16}e^{\gamma_{16}\theta_1^*} \\ c_{11}e^{\gamma_{11}\theta_1^*} & c_{12}e^{\gamma_{12}\theta_1^*} & c_{13}e^{\gamma_{13}\theta_1^*} & c_{14}e^{\gamma_{14}\theta_1^*} & c_{15}e^{\gamma_{15}\theta_1^*} & c_{16}e^{\gamma_{16}\theta_1^*} \end{bmatrix} \tag{40}$$

$$BE_b = \begin{bmatrix} \left(\frac{c_{i1}-b_{i1}\gamma_{i1}}{R_i}\right)e^{\gamma_{i1}\theta_i^*} & \left(\frac{c_{i2}-b_{i2}\gamma_{i2}}{R_i}\right)e^{\gamma_{i2}\theta_i^*} & \left(\frac{c_{i3}-b_{i3}\gamma_{i3}}{R_i}\right)e^{\gamma_{i3}\theta_i^*} & \left(\frac{c_{i4}-b_{i4}\gamma_{i4}}{R_i}\right)e^{\gamma_{i4}\theta_i^*} & \left(\frac{c_{i5}-b_{i5}\gamma_{i5}}{R_i}\right)e^{\gamma_{i5}\theta_i^*} & \left(\frac{c_{i6}-b_{i6}\gamma_{i6}}{R_i}\right)e^{\gamma_{i6}\theta_i^*} \\ \left(\frac{b_{i1}+c_{i1}\gamma_{i1}}{R_i}\right)e^{\gamma_{i1}\theta_i^*} & \left(\frac{b_{i2}+c_{i2}\gamma_{i2}}{R_i}\right)e^{\gamma_{i2}\theta_i^*} & \left(\frac{b_{i3}+c_{i3}\gamma_{i3}}{R_i}\right)e^{\gamma_{i3}\theta_i^*} & \left(\frac{b_{i4}+c_{i4}\gamma_{i4}}{R_i}\right)e^{\gamma_{i4}\theta_i^*} & \left(\frac{b_{i5}+c_{i5}\gamma_{i5}}{R_i}\right)e^{\gamma_{i5}\theta_i^*} & \left(\frac{b_{i6}+c_{i6}\gamma_{i6}}{R_i}\right)e^{\gamma_{i6}\theta_i^*} \\ \left(\frac{\gamma_{i1}}{R_i}+b_{i1}\right)e^{\gamma_{i1}\theta_i^*} & \left(\frac{\gamma_{i2}}{R_i}+b_{i2}\right)e^{\gamma_{i2}\theta_i^*} & \left(\frac{\gamma_{i3}}{R_i}+b_{i3}\right)e^{\gamma_{i3}\theta_i^*} & \left(\frac{\gamma_{i4}}{R_i}+b_{i4}\right)e^{\gamma_{i4}\theta_i^*} & \left(\frac{\gamma_{i5}}{R_i}+b_{i5}\right)e^{\gamma_{i5}\theta_i^*} & \left(\frac{\gamma_{i6}}{R_i}+b_{i6}\right)e^{\gamma_{i6}\theta_i^*} \end{bmatrix} \tag{41}$$

2.1.3 Natural Frequencies and Mode Shapes

The boundary and continuity conditions described so far result in an eigenvalue problem for continuous beams with circular arcs. To obtain the natural frequencies for a single arc beam, we can write the expression as:

$$[H]_{6\times6}[a]_{6\times1} = [0]_{6\times1} \tag{42}$$

where

$$[H]_{6\times6} = \begin{bmatrix} BE_a \\ BE_b \end{bmatrix} \tag{43}$$

and

$$[a]_{6\times1} = [a_1, a_2, \dots, a_6\ ]^{\mathrm{T}} \tag{44}$$

with known values of beam material properties and geometry for the arc, $[H]_{6\times6}$ is only dependent on ω. The values of ω which satisfies $det(H) = 0$ are the natural frequencies of the beam. The numerical constants can be obtained thereafter by setting a_6 to an arbitrary value and solving for a_1 to a_5 from equation (42). Thereafter, the mode shapes can be obtained by plugging the numerical constants into equation 33a-c. For a beam consisting of i number of arcs, we can write:

$$[H]_{6i\times6i}[a]_{6i\times1} = [0]_{6i\times1} \tag{45}$$

where $[H]_{6i\times6i}$ is a combination of the beam boundary and continuity matrices and $[a]_{6i\times1}$ is a combination of the numerical constants of the circular arcs which can be expressed as:

$$[a]_{6i\times1} = [a_{11}, .., a_{16}, \dots, a_{i1}, \dots, a_{i6}\ ]^{\mathrm{T}} \tag{46}$$

Again, with known values of beam material properties and geometry for each arc, $[H]_{6i\times6i}$ is only dependent on ω. Therefore the values of ω which satisfy $det(H) = 0$ are the natural frequencies of the beam. The numerical constants can be obtained thereafter by setting a_{i6} to an arbitrary value and solving for a_{11} to a_{i5} from equation (45). Thereafter, the mode shapes can be obtained by plugging the numerical constants into equation 33a-c.

In order to reduce numerical errors and time, we can reduce the sizes of matrices in equation (45). If CS and CE represent the start and end continuity matrices respectively of an arc in

the direction of the full beam (e.g. clamped end to free end), continuity conditions require that [3]:

$$\begin{bmatrix} a_{i1} \\ a_{i2} \\ \vdots \\ a_{i6} \end{bmatrix} = CS_i^{-1} CE_{i-1} \begin{bmatrix} a_{(i-1)1} \\ a_{(i-1)2} \\ \vdots \\ a_{(i-1)6} \end{bmatrix} \tag{47}$$

Note that CS and CE are determined by the direction of the whole beam and either of CS and CE could therefore occur at $\theta^* = 0$ (i. e matrix AS) *or* $\theta^* = \theta$ (i. e matrix AE) of the specified arc. Also, the bottom three rows of the CS matrix for each beam must be multiplied by -1 to account for the equilibrium conditions from one arc to the next. The equilibrium conditions are:

$$\begin{aligned} Z_{i-1}(\theta^*) &= Z_i(\theta^*), \\ \Psi_{i-1}(\theta^*) &= \Psi_i(\theta^*), \\ \Phi_{i-1}(\theta^*) &= \Phi_i(\theta^*), \\ M_{i-1}(\theta^*) &= -M_i(\theta^*), \\ T_{i-1}(\theta^*) &= -T_i(\theta^*), \text{ and} \\ Q_{i-1}(\theta^*) &= -Q_i(\theta^*) \end{aligned} \tag{48a-f}$$

Therefore, we can write

$$\begin{bmatrix} a_{i1} \\ a_{i2} \\ \vdots \\ a_{i6} \end{bmatrix} = CSE \begin{bmatrix} a_{11} \\ a_{12} \\ \vdots \\ a_{16} \end{bmatrix} \tag{49}$$

where

$$CSE = CS_i^{-1} CE_{i-1} CS_{i-1}^{-1} CE_{i-2}, \dots, CS_2^{-1} CE_1 \tag{50}$$

The eigenvalue problem now becomes

$$[N]_{6\times6}[a_1]_{6\times1} = [0]_{6\times1} \tag{51}$$

where

$$[N]_{6\times6} = \begin{bmatrix} BE_a \\ BE_b \times CSE \end{bmatrix} \tag{52}$$

and

$$[a_1]_{6\times1} = [a_{11}, a_{12}, \dots, a_{16}]^{\mathrm{T}} \tag{53}$$

As with matrices $[H]_{6\times6}$ and $[H]_{6i\times6i}$, the values of ω which satisfy $det(N) = 0$ are the natural frequencies of the beam. Thereafter, the numerical constants for the first arc can be obtained by setting a_{16} to an arbitrary value and solving for a_{11} to a_{15} from equation (51). The numerical constants for the remaining arcs can then be obtained by applying equation (47). The mode shapes can be obtained by plugging the numerical constants into equation 33a-c

2.1.4 Effective mechanical properties for multilayered beams

In many applications of micro-cantilever beams, a number of layers of different materials are bonded to each other to provide the desired effect.

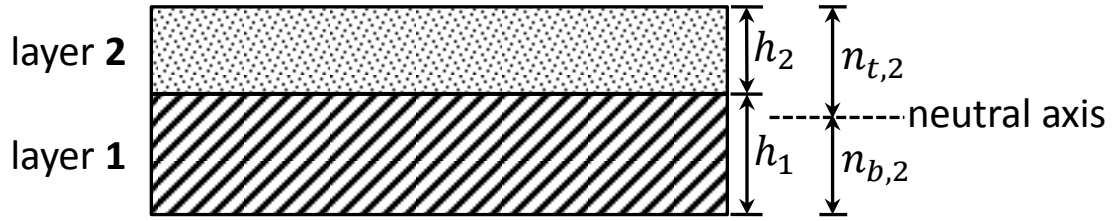

(a)

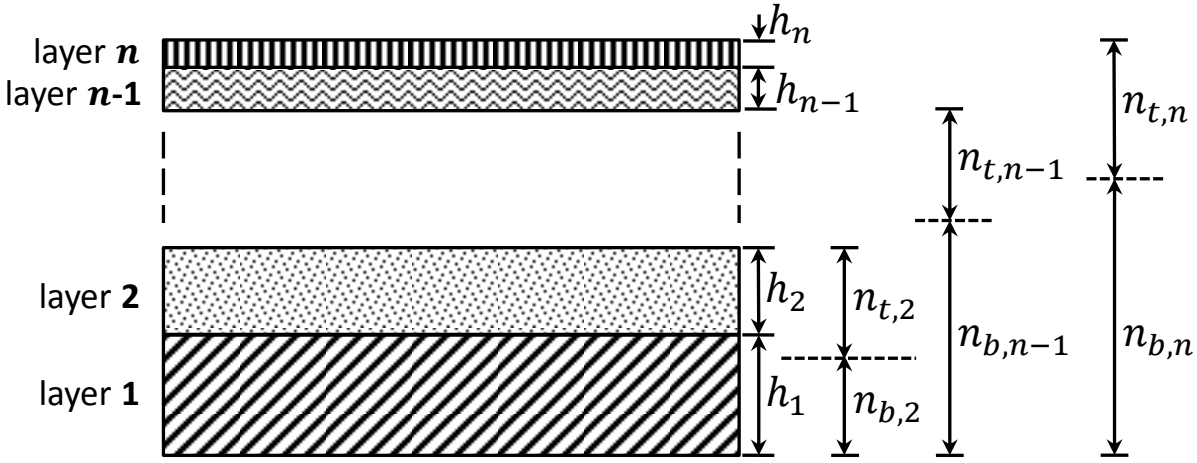

(b)

Figure 9: Schematic depiction of multilayered beam cross-sections with the layers arranged in order of decreasing thickness (from bottom to top): (a) Cross section of a beam with two layers; and (b) cross section of a beam with *n* layers.

For multilayered beams with rectangular cross-sections, we can determine approximate effective properties needed for calculating the natural frequencies and mode shapes. The theory presented here is based on the following assumptions:

(1) The beam is in uniform torsion;

(2) The beam layers as well as the composite beam are elastic, homogeneous, and isotropic;

(3) The beam layers are perfectly bonded to prevent in-plane shearing; and

(4) The overall thickness of the composite beam is small compared with its width and length.

The effective properties required for calculating the natural frequencies of circular arc beams are the effective flexural rigidity, YI, the effective shear modulus, G, the effective mass per unit length, ρA, and the effective Poisson's ratio, ν. Consider the beam cross-section shown in Figure 9a where the bottom layer is the thicker of the two layers. The distances from the neutral axis can be expressed as [5, 7]:

$$n_{b,2} = \frac{h_2^2 + 2h_2h_1 + \frac{Y_1}{Y_2}h_1^2}{2\left(h_2 + \frac{Y_1}{Y_2}h_1\right)}$$
$$n_{t,2} = \frac{h_2^2 + 2\frac{Y_1}{Y_2}h_2h_1 + \frac{Y_1}{Y_2}h_1^2}{2\left(h_2 + \frac{Y_1}{Y_2}h_1\right)} \quad (54)$$

where $n_{b,2}$ represents the distance from the end of the bottom layer to the neutral axis (for 2 layers), $n_{u,2}$ represents the distance from the top of the top layer to the neutral axis (for 2 layers), h_1 is the thickness of the bottom layer, and h_2 is the thickness of the top layer. Therefore, we can write the effective flexural rigidity for a beam with two layers and width W as:

$$(YI)_2 = \frac{W}{3}\left[Y_1\left(n_{b,2}^3 + \left(n_{t,2} - h_2\right)^3\right) + Y_2\left(n_{t,2}^3 - \left(n_{t,2} - h_2\right)^3\right)\right] \tag{55}$$

Now consider a beam with more than two layers. If we rearrange the layers (from bottom to top) in descending order of their thicknesses, we can obtain a well-defined cross-section as shown in Figure 9b. The effective flexural rigidity for a beam with n layers can be written as:

$$YI = (YI)_n = \frac{W}{3}\left[Y_{\mathrm{e},n-1}\left(n_{b,n}^3 + \left(n_{t,n} - h_n\right)^3\right) + Y_n\left(n_{t,n}^3 - \left(n_{t,n} - h_n\right)^3\right)\right] \tag{56}$$

where

$$\begin{aligned} Y_{e,n-1} = \frac{W}{3I_{e,n-1}}\Big[&Y_{e,n-2}\left(n_{b,n-1}^3 + \left(n_{t,n-1} - h_{n-1}\right)^3\right) \\ &+ Y_{n-1}\left(n_{t,n-1}^3 - \left(n_{t,n-1} - h_{n-1}\right)^3\right)\Big] \end{aligned} \tag{57}$$

and this is solved further until Y_1. Therefore for n layers, there are $n-1$ flexural rigidity equations to be solved in order to obtain the overall effective flexural rigidity. Note that any term with subscript e indicates an effective property and not the property of a single layer. For example, $Y_{\mathrm{e},n-1}$ denotes the effective Young's modulus for layers 1 to $n-1$ while Y_{n-1} denotes the Young's modulus for layer $n-1$ only. The effective thickness for n layers is simply a sum of the thicknesses of all the n layers, while the effective area moment of inertia

for n layers is calculated assuming the n layers comprise a single beam. We can also write the distances from the neutral axis for any number of layers. For n layers, the equations for the distance to the neutral axis can be written as:

$$n_{b,n} = \frac{h_n^2 + 2h_n h_{e,n-1} + \frac{Y_{e,n-1}}{Y_n} h_{e,n-1}^2}{2\left(h_n + \frac{Y_{e,n-1}}{Y_n} h_{e,n-1}\right)}$$
$$n_{t,n} = \frac{h_n^2 + 2\frac{Y_{e,n-1}}{Y_n} h_n h_{e,n-1} + \frac{Y_{n-1}}{Y_n} h_{e,n-1}^2}{2\left(h_n + \frac{Y_{e,n-1}}{Y_n} h_{e,n-1}\right)} \quad (58)$$

The effective mass per unit length and Poisson's ratio for a beam with n layers can be calculated from rule of mixtures and expressed as (respectively):

$$\rho A = W \sum_{i=1}^{n} \rho_i h_i \quad (59)$$

and

$$\nu = \frac{1}{\sum_i^n h_i} \sum_{i=1}^{n} \nu_i h_i \quad (60)$$

The effective shear modulus, G, can be obtained from:

$$G = \frac{Y}{2(1+\nu)} \tag{61}$$

2.2 Cantilever Beam Example

2.2.1 Modeling Analysis

A multilayered cantilever beam with constant cross-section is shown in Figure 10. It is clamped at one end and free at the other. The beam has been designed for piezoelectric energy harvesting. The beam is layered with different materials which have different material properties and thicknesses are described in Table 4. The boundary condition matrices for the cantilever are:

BE_a(fixed end)

$$= \begin{bmatrix} e^{\gamma_{11}\pi/2} & e^{\gamma_{12}\pi/2} & e^{\gamma_{13}\pi/2} & e^{\gamma_{14}\pi/2} & e^{\gamma_{15}\pi/2} & e^{\gamma_{16}\pi/2} \\ b_{11}e^{\gamma_{11}\pi/2} & b_{12}e^{\gamma_{12}\pi/2} & b_{13}e^{\gamma_{13}\pi/2} & b_{14}e^{\gamma_{14}\pi/2} & b_{15}e^{\gamma_{15}\pi/2} & b_{16}e^{\gamma_{16}\pi/2} \\ c_{11}e^{\gamma_{11}\pi/2} & c_{12}e^{\gamma_{12}\pi/2} & c_{13}e^{\gamma_{13}\pi/2} & c_{14}e^{\gamma_{14}\pi/2} & c_{15}e^{\gamma_{15}\pi/2} & c_{16}e^{\gamma_{16}\pi/2} \end{bmatrix} \tag{62}$$

BE_b(free end)

$$= \begin{bmatrix} \frac{c_{31}-b_{31}\gamma_{31}}{R_3} & \frac{c_{32}-b_{32}\gamma_{32}}{R_3} & \frac{c_{33}-b_{33}\gamma_{33}}{R_3} & \frac{c_{34}-b_{34}\gamma_{34}}{R_3} & \frac{c_{35}-b_{35}\gamma_{35}}{R_3} & \frac{c_{36}-b_{36}\gamma_{36}}{R_3} \\ \frac{b_{31}+c_{31}\gamma_{31}}{R_3} & \frac{b_{32}+c_{32}\gamma_{32}}{R_3} & \frac{b_{33}+c_{33}\gamma_{33}}{R_3} & \frac{b_{34}+c_{34}\gamma_{34}}{R_3} & \frac{b_{35}+c_{35}\gamma_{35}}{R_3} & \frac{b_{36}+c_{36}\gamma_{36}}{R_3} \\ \frac{\gamma_{31}}{R_3}-b_{31} & \frac{\gamma_{32}}{R_3}-b_{32} & \frac{\gamma_{33}}{R_3}-b_{33} & \frac{\gamma_{34}}{R_3}-b_{34} & \frac{\gamma_{35}}{R_3}-b_{35} & \frac{\gamma_{36}}{R_3}-b_{36} \end{bmatrix} \tag{63}$$

The continuity matrices are:

$$CE_1$$

$$= \begin{bmatrix} 1 & 1 & 1 & 1 & 1 & 1 \\ b_{11} & b_{12} & b_{13} & b_{14} & b_{15} & b_{16} \\ c_{11} & c_{12} & c_{13} & c_{14} & c_{15} & c_{16} \\ \frac{c_{11} - b_{11}\gamma_{11}}{R_1} & \frac{c_{12} - b_{12}\gamma_{12}}{R_1} & \frac{c_{13} - b_{13}\gamma_{13}}{R_1} & \frac{c_{14} - b_{14}\gamma_{14}}{R_1} & \frac{c_{15} - b_{15}\gamma_{15}}{R_1} & \frac{c_{16} - b_{16}\gamma_{16}}{R_1} \\ \frac{b_{11} + c_{11}\gamma_{11}}{R_1} & \frac{b_{12} + c_{12}\gamma_{12}}{R_1} & \frac{b_{13} + c_{13}\gamma_{13}}{R_1} & \frac{b_{14} + c_{14}\gamma_{14}}{R_1} & \frac{b_{15} + c_{15}\gamma_{15}}{R_1} & \frac{b_{16} + c_{16}\gamma_{16}}{R_1} \\ \frac{\gamma_{11}}{R_1} - b_{11} & \frac{\gamma_{12}}{R_1} - b_{12} & \frac{\gamma_{13}}{R_1} - b_{13} & \frac{\gamma_{14}}{R_1} - b_{14} & \frac{\gamma_{15}}{R_1} - b_{15} & \frac{\gamma_{16}}{R_1} - b_{16} \end{bmatrix}$$

(64)

$$CS_2 = \begin{bmatrix} 1 & 1 & 1 & 1 & 1 & 1 \\ b_{21} & b_{22} & b_{23} & b_{24} & b_{25} & b_{26} \\ c_{21} & c_{22} & c_{23} & c_{24} & c_{25} & c_{26} \\ -\frac{c_{21} - b_{21}\gamma_{21}}{R_2} & -\frac{c_{22} - b_{22}\gamma_{22}}{R_2} & -\frac{c_{23} - b_{23}\gamma_{23}}{R_2} & -\frac{c_{24} - b_{24}\gamma_{24}}{R_2} & -\frac{c_{25} - b_{25}\gamma_{25}}{R_2} & -\frac{c_{26} - b_{26}\gamma_{26}}{R_2} \\ -\frac{b_{21} + c_{21}\gamma_{21}}{R_2} & -\frac{b_{22} + c_{22}\gamma_{22}}{R_2} & -\frac{b_{23} + c_{23}\gamma_{23}}{R_2} & -\frac{b_{24} + c_{24}\gamma_{24}}{R_2} & -\frac{b_{25} + c_{25}\gamma_{25}}{R_2} & -\frac{b_{26} + c_{26}\gamma_{26}}{R_2} \\ -\left(\frac{\gamma_{21}}{R_2} - b_{21}\right) & -\left(\frac{\gamma_{22}}{R_2} - b_{22}\right) & -\left(\frac{\gamma_{23}}{R_2} - b_{23}\right) & -\left(\frac{\gamma_{24}}{R_2} - b_{24}\right) & -\left(\frac{\gamma_{25}}{R_2} - b_{25}\right) & -\left(\frac{\gamma_{26}}{R_2} - b_{26}\right) \end{bmatrix}$$

(65)

CE_2

$$= \begin{bmatrix} e^{\gamma_{21}\pi} & e^{\gamma_{22}\pi} & e^{\gamma_{23}\pi} & e^{\gamma_{24}\pi} & e^{\gamma_{25}\pi} & e^{\gamma_{26}\pi} \\ b_{21}e^{\gamma_{21}\pi} & b_{22}e^{\gamma_{22}\pi} & b_{23}e^{\gamma_{23}\pi} & b_{24}e^{\gamma_{24}\pi} & b_{25}e^{\gamma_{25}\pi} & b_{26}e^{\gamma_{26}\pi} \\ c_{21}e^{\gamma_{21}\pi} & c_{22}e^{\gamma_{22}\pi} & c_{23}e^{\gamma_{23}\pi} & c_{24}e^{\gamma_{24}\pi} & c_{25}e^{\gamma_{25}\pi} & c_{26}e^{\gamma_{26}\pi} \\ \left(\frac{c_{21} - b_{21}\gamma_{21}}{R_2}\right)e^{\gamma_{21}\pi} & \left(\frac{c_{22} - b_{22}\gamma_{22}}{R_2}\right)e^{\gamma_{22}\pi} & \left(\frac{c_{23} - b_{23}\gamma_{23}}{R_2}\right)e^{\gamma_{23}\pi} & \left(\frac{c_{24} - b_{24}\gamma_{24}}{R_2}\right)e^{\gamma_{24}\pi} & \left(\frac{c_{25} - b_{25}\gamma_{25}}{R_2}\right)e^{\gamma_{25}\pi} & \left(\frac{c_{26} - b_{26}\gamma_{26}}{R_2}\right)e^{\gamma_{26}\pi} \\ \left(\frac{b_{21} + c_{21}\gamma_{21}}{R_2}\right)e^{\gamma_{21}\pi} & \left(\frac{b_{22} + c_{22}\gamma_{22}}{R_2}\right)e^{\gamma_{22}\pi} & \left(\frac{b_{23} + c_{23}\gamma_{23}}{R_2}\right)e^{\gamma_{23}\pi} & \left(\frac{b_{24} + c_{24}\gamma_{24}}{R_2}\right)e^{\gamma_{24}\pi} & \left(\frac{b_{25} + c_{25}\gamma_{25}}{R_2}\right)e^{\gamma_{25}\pi} & \left(\frac{b_{26} + c_{26}\gamma_{26}}{R_2}\right)e^{\gamma_{26}\pi} \\ \left(\frac{\gamma_{21}}{R_2} - b_{21}\right)e^{\gamma_{21}\pi} & \left(\frac{\gamma_{22}}{R_2} - b_{22}\right)e^{\gamma_{22}\pi} & \left(\frac{\gamma_{23}}{R_2} - b_{23}\right)e^{\gamma_{23}\pi} & \left(\frac{\gamma_{24}}{R_2} - b_{24}\right)e^{\gamma_{24}\pi} & \left(\frac{\gamma_{25}}{R_2} - b_{25}\right)e^{\gamma_{25}\pi} & \left(\frac{\gamma_{26}}{R_2} - b_{26}\right)e^{\gamma_{26}\pi} \end{bmatrix}$$

(66)

$$CS_3$$

$$= \begin{bmatrix} e^{\gamma_{31}3\pi/4} & e^{\gamma_{32}3\pi/4} & e^{\gamma_{33}3\pi/4} & e^{\gamma_{34}3\pi/4} & e^{\gamma_{35}3\pi/4} & e^{\gamma_{36}3\pi/4} \\ b_{31}e^{\gamma_{31}3\pi/4} & b_{32}e^{\gamma_{32}3\pi/4} & b_{33}e^{\gamma_{33}3\pi/4} & b_{34}e^{\gamma_{34}3\pi/4} & b_{35}e^{\gamma_{35}3\pi/4} & b_{36}e^{\gamma_{36}3\pi/4} \\ c_{31}e^{\gamma_{31}3\pi/4} & c_{32}e^{\gamma_{32}3\pi/4} & c_{33}e^{\gamma_{33}3\pi/4} & c_{34}e^{\gamma_{34}3\pi/4} & c_{35}e^{\gamma_{35}3\pi/4} & c_{36}e^{\gamma_{36}3\pi/4} \\ -\left(\frac{c_{31}-b_{31}\gamma_{31}}{R_3}\right)e^{\gamma_{31}3\pi/4} & -\left(\frac{c_{32}-b_{32}\gamma_{32}}{R_3}\right)e^{\gamma_{32}3\pi/3} & -\left(\frac{c_{33}-b_{33}\gamma_{33}}{R_3}\right)e^{\gamma_{33}3\pi/4} & -\left(\frac{c_{34}-b_{34}\gamma_{24}}{R_3}\right)e^{\gamma_{34}3\pi/4} & -\left(\frac{c_{35}-b_{35}\gamma_{35}}{R_3}\right)e^{\gamma_{35}3\pi/4} & -\left(\frac{c_{36}-b_{36}\gamma_{36}}{R_3}\right)e^{\gamma_{36}3\pi/4} \\ -\left(\frac{b_{31}+c_{31}\gamma_{31}}{R_3}\right)e^{\gamma_{31}3\pi/4} & -\left(\frac{b_{32}+c_{32}\gamma_{32}}{R_3}\right)e^{\gamma_{32}3\pi/4} & -\left(\frac{b_{33}+c_{33}\gamma_{33}}{R_3}\right)e^{\gamma_{33}3\pi/4} & -\left(\frac{b_{34}+c_{34}\gamma_{34}}{R_3}\right)e^{\gamma_{34}3\pi/4} & -\left(\frac{b_{35}+c_{35}\gamma_{35}}{R_3}\right)e^{\gamma_{35}3\pi/4} & -\left(\frac{b_{36}+c_{36}\gamma_{26}}{R_3}\right)e^{\gamma_{36}3\pi/4} \\ -\left(\frac{\gamma_{31}}{R_3}-b_{31}\right)e^{\gamma_{31}3\pi/4} & -\left(\frac{\gamma_{32}}{R_3}-b_{32}\right)e^{\gamma_{32}3\pi/4} & -\left(\frac{\gamma_{33}}{R_3}-b_{33}\right)e^{\gamma_{33}3\pi/4} & -\left(\frac{\gamma_{34}}{R_3}-b_{34}\right)e^{\gamma_{34}3\pi/4} & -\left(\frac{\gamma_{35}}{R_3}-b_{35}\right)e^{\gamma_{35}3\pi/4} & -\left(\frac{\gamma_{36}}{3}-b_{36}\right)e^{\gamma_{36}3\pi/4} \end{bmatrix} \quad (67)$$

The eigenvalue problem for the beam was solved by combining the beam continuity and boundary matrices according to equation (52) for the values of ω which satisfy $det(N) = 0$. The numerical constants for arc 1 were obtained by setting a_{16} to 1 and solving for a_{11} to a_{15} from equation (51). Thereafter, the numerical constants for arcs 2 and 3 were obtained by applying equation (47). The mode shapes were obtained by plugging the numerical constants into equation 33a-c.

Figure 11 shows the effect of varying the thickness of the silicon substrate layer of the beam on the variable u for first four modes (also see equation 15). The variable u is useful for determining the effect of arc geometry (e.g. thickness and arc radius) on the natural frequency. When u is varied as a function of silicon layer thickness, it behaves nonlinearly, and the nonlinearity increases with mode number.

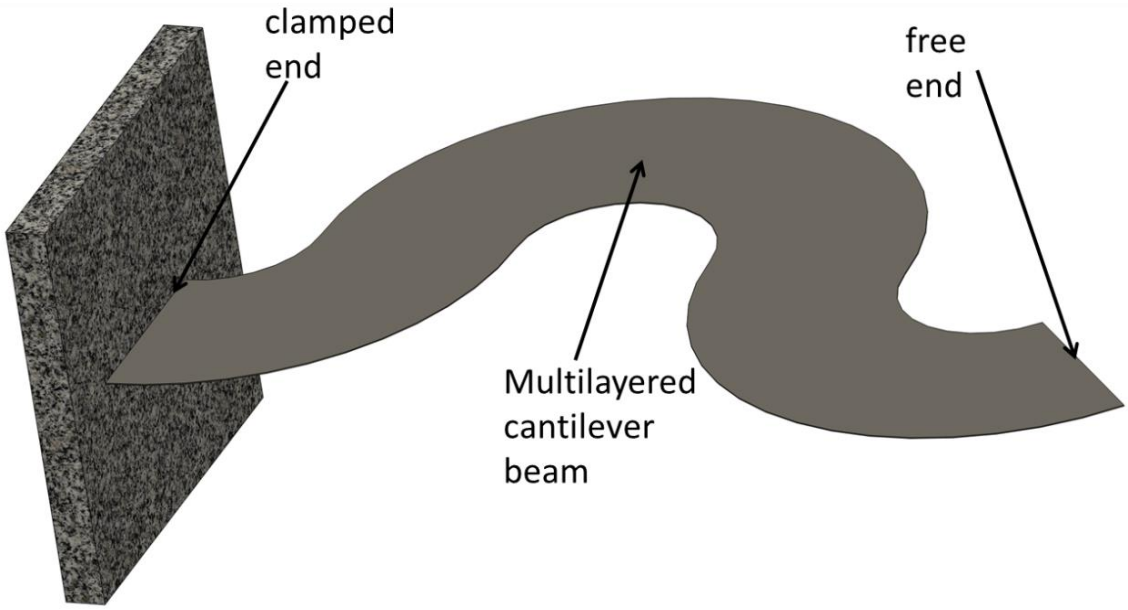

(a)

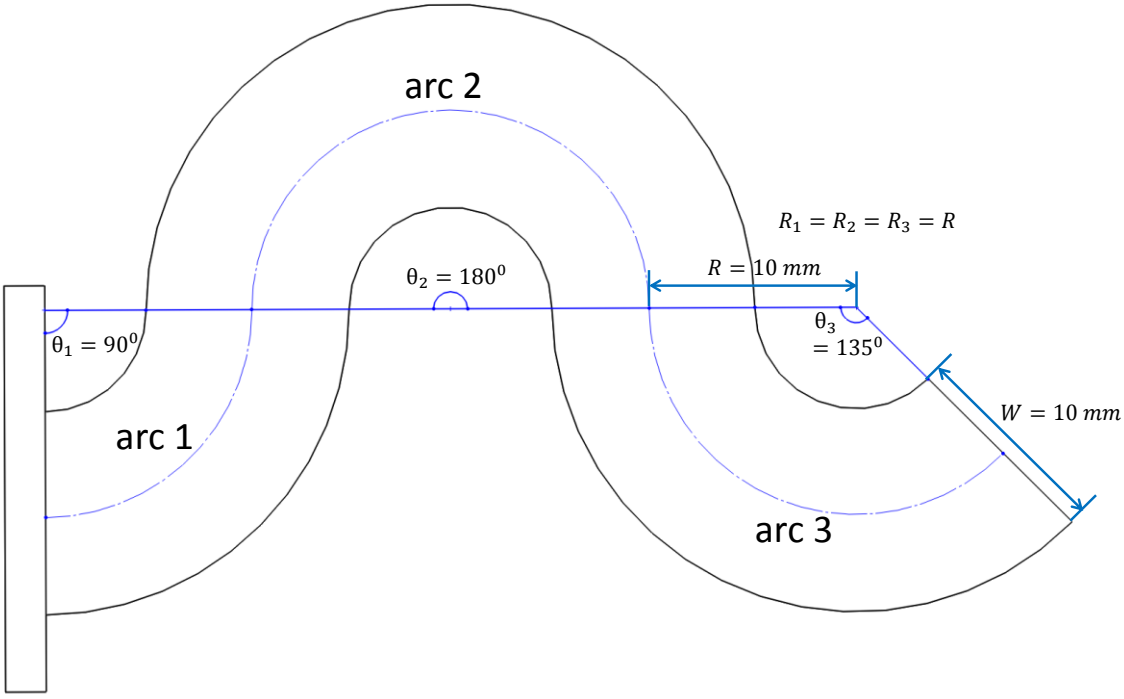

(b)

Figure 10: Example of a micro-cantilever beam with three circular arcs: (a) 3D view of the beam; and (b) 2-D view of the beam showing its dimensions.

Table 4: Properties of the materials used for the micro-cantilever layers

Material	Layer no. (effective no.)*	Thickness [μm]	Young's modulus [GPa]	Density [g/cm^3]	Poisson's Ratio
Pt	5 (6)	0.2	168	21.45	0.38
PZT	4 (2)	1	66	7.8	0.35
Pt	5 (5)	0.2	168	21.45	0.38
TiO_2	3 (4)	0.25	230	4	0.27
SiO_2	2 (3)	0.5	73	2.2	0.17
Si	1 (1)	100 - 200	112	2.329	0.28

*The layer number indicates the actual position of the layer numbering from bottom to top. The effective number indicates the re-ordered position of the layer (from bottom to top) for calculating effective properties.

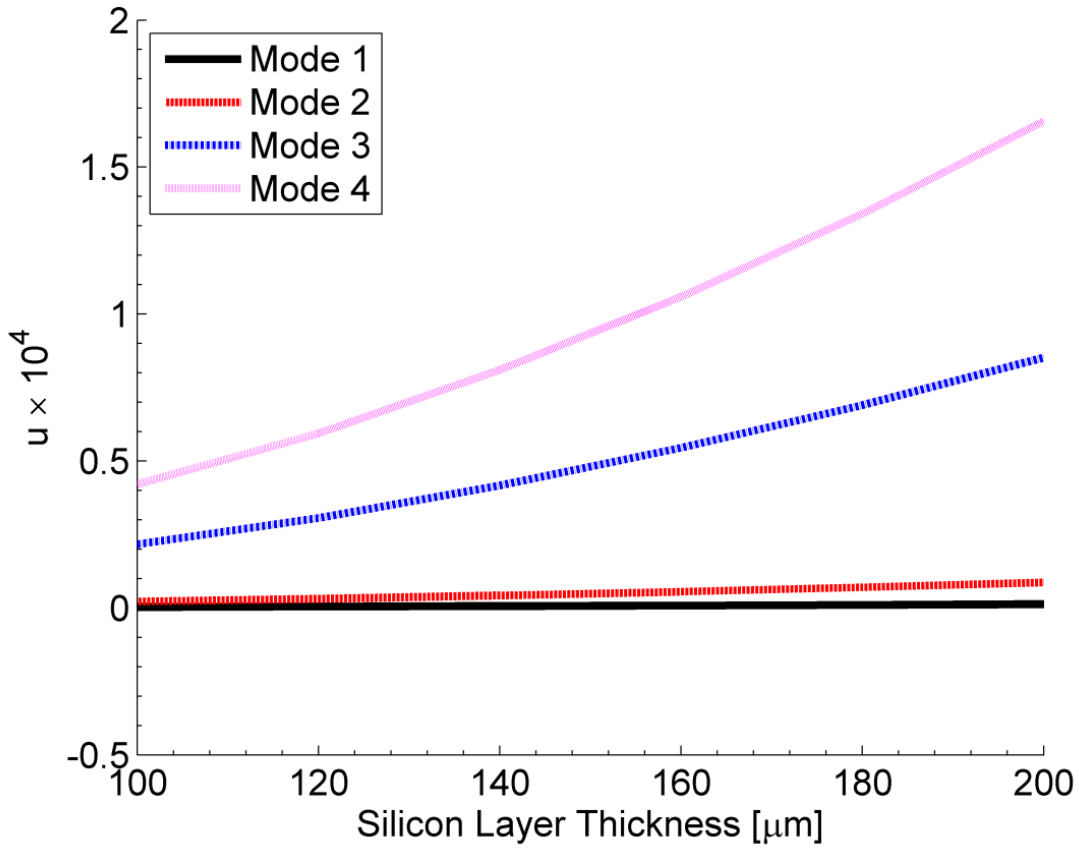

Figure 11: Variation of *u* with silicon layer thickness for the arc-based cantilever with three arcs.

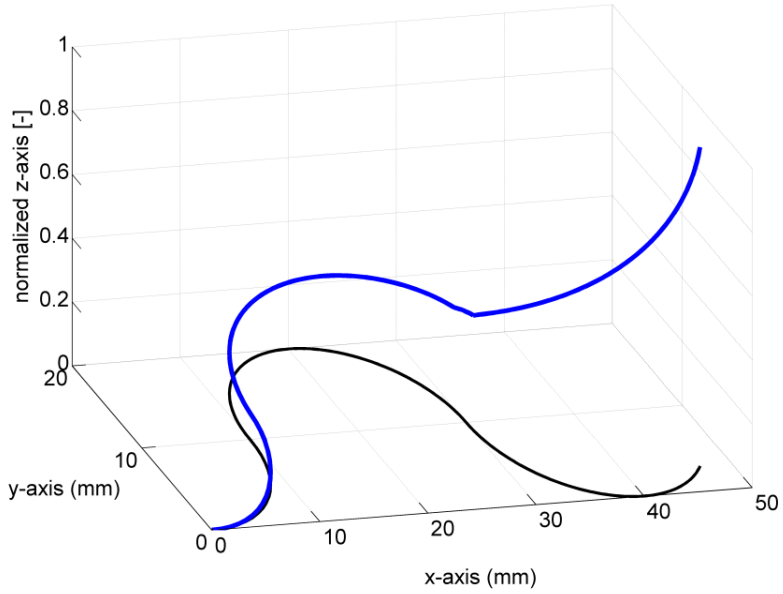

(a)

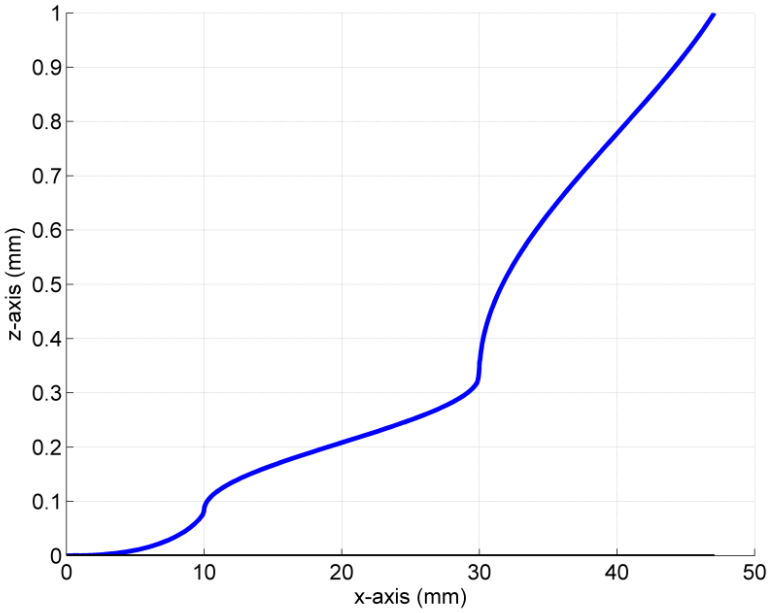

(b)

Figure 12: Mode shape for the fundamental frequency (38Hz) of the arc-based cantilever beam with 100µm thick silicon layer: (a) 3D view; (b) Side view of showing the displacement profile relative to the clamped end. Blue line = mode shape, black line = undeformed shape.

The normalized fundamental mode shape of the beam centerline for the beam described in Figure 10 and Table 4 is shown in Figure 12a & Figure 12b. In this case, the silicon layer thickness is 100μm. The fundamental mode occurs at 38Hz and it exhibits dominant bending behavior. The fundamental bending mode is advantageous for applications which rely on uniform cantilever straining such as piezoelectric energy harvesting. The steps required for modeling the multilayered arc-based cantilever beams are summarized in a modeling flow chart in Figure 13.

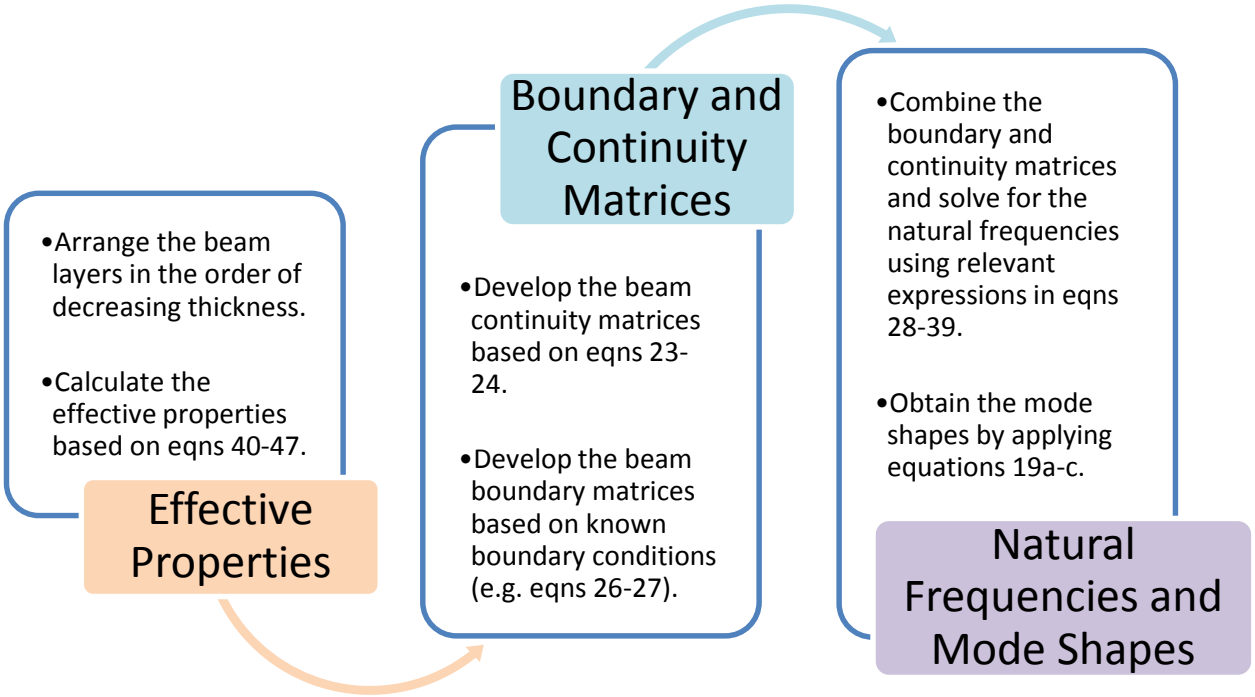

Figure 13: Modeling flow chart for obtaining the natural frequencies and mode shapes of multilayered arc-based cantilever beams.

2.2.2 Experimental Verification of the Numerical Model

Modal experimental verification was performed on the cantilever. The geometry of the beam (except thickness) is same as in Figure 10 and it is made up of 0.4064mm thick aluminum.

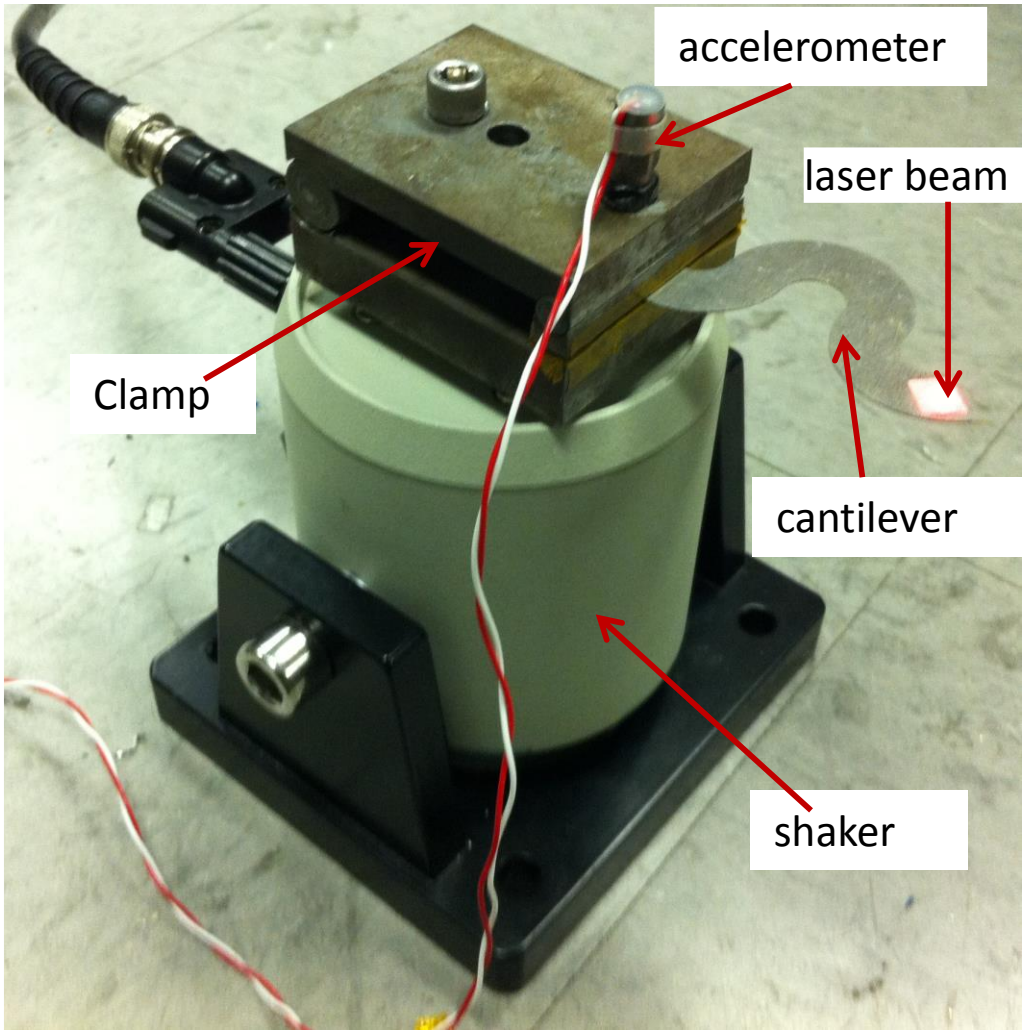

Figure 14: Experimental setup for modal analysis of the aluminum cantilever beam.

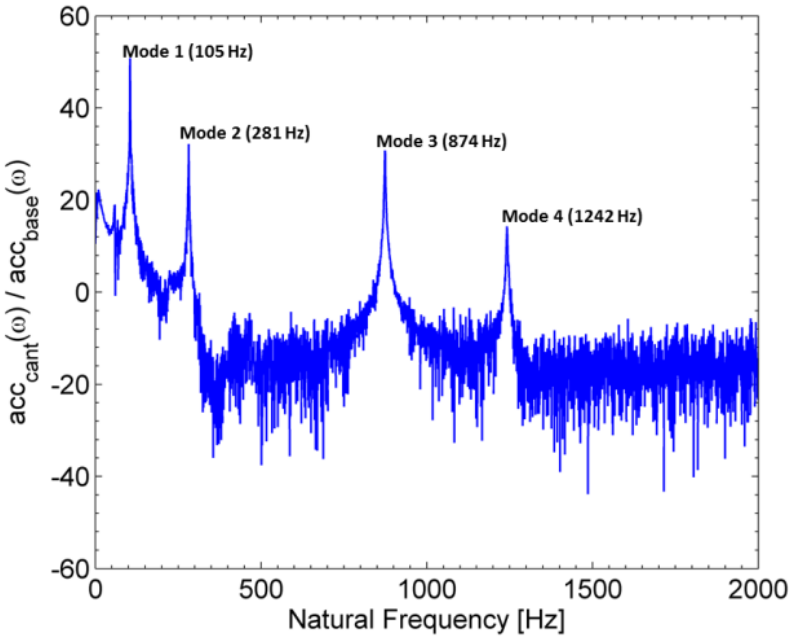

(a)

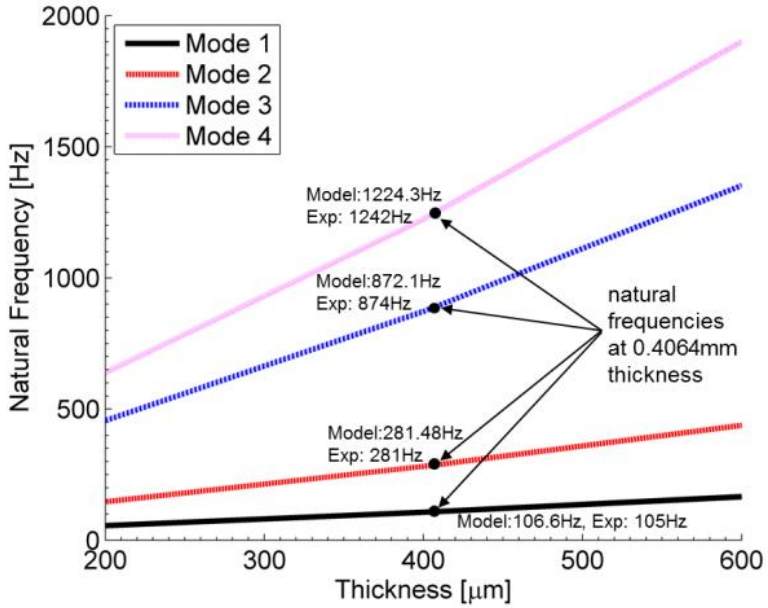

(b)

Figure 15: Experimental verification of the numerical model using a single-layer aluminum cantilever: (a) experimental results showing the first four modes of the cantilever; (b) Numerical results for the first four modes as a function of beam thickness

The experimental setup is shown in Figure 14. The shaker was used to provide a base acceleration to the cantilever which was measured by the accelerometer while the acceleration of the cantilever was measured by using a laser beam. The peak values of the cantilever acceleration (relative to the shaker acceleration) denote the natural frequencies of the cantilever. The first four modes of the experimental cantilever are shown in Figure 15. It can be seen that the results from the numerical model are in close agreement for the first four modes (< 2% error). Euler-Bernoulli equation (Blevins, 1979) for a straight cantilever beam with same width (10mm), thickness (0.4064mm) and length distance (50mm) as the experimental cantilever produces 144.27, 902.43, 1359.6, and 2533 Hz for the first four modes. Therefore, the straight cantilever exibits 37 to 204 percent increase in natural frequency (from mode 1-4) when compared with the experimental arc-based cantilever.

2.3 Chapter Conclusion

A general out-of-plane vibration model for continuous arc based cantilevers which includes the effects of shear and rotary inertia and also considers the multiple layers of different materials has been developed for the determining the natural frequency and mode shapes. Based on the Timoshenko beam theory, an eigenvalue problem was developed which enables the analysis of multidirectional continuous beams. Expressions for effective properties of multilayered beams were obtained based on calculation of the distances of the layers from the neutral axes and reordering of the layers by decreasing thicknesses. An example cantilever beam was analyzed to illustrate the application of the model and the potential for achieving low frequency resonance in arc-based beams at the micro scale. As

indicated by the results, the fundamental mode was 38Hz for 100μm thick silicon substrate. The mode shapes showed the behavior of the centerline of the beams and indicated that the important fundamental mode exhibited a dominant bending behavior which is favorable for many micro-scale applications. Modal experiments were performed on an aluminum arc-based cantilever and the results showed close agreement with the numerical model.

3 Chapter 3:

Arc-Based Microcantilevers for Low Frequency Applications and Dual-Phase Energy Harvesting

3.1 Vibration Characteristics of Low Frequency Arc-Based Microcantilevers

Cantilevers have been developed in literature for a variety of actuation and transduction applications. However, recently the cantilever beam structure utilizing smart materials has been widely investigated for the vibration energy harvesting (VEH) [60, 61]. This involves voltage transduction via strain induced in the piezoelectric layer of the cantilever when exposed to external vibration. Cantilever-based vibration energy harvesting requires the development of structures with low natural frequencies (below 100Hz) to match the frequencies observed in most common natural sources of vibrations. However, the increase in natural frequency of cantilevers as the length scale is reduced, limits the low frequency potential of standalone microcantilevers [60]. The most commonly used approach for reducing the natural frequency involves the addition of a huge tip mass to the free end of a simple cantilever [14-20, 23, 62, 63]. Other methods involve the use of increased effective surface area cantilevers such as spirals [14, 62, 64]. However, the use of tip masses severely affects the structural integrity and durability of the harvesters while the increased effective surface area designs exhibit torsion (causing voltage cancellation effects) in the very important first vibration mode. A more effective approach lies in developing specially shaped

microcantilevers, such as purely arc-based cantilevers, which exhibit low natural frequencies and pure bending behavior in the first vibration mode thus making them suitable for a wide range of low frequency applications at the microscale.

This section details the modeling and experimental analysis of arc-based microcantilevers which have either been specially designed (S-shaped and C-shaped) or have been designed as modifications of widely known designs (ArcSimple and ArcZigzag). The ArcSimple and ArcZigzag cantilevers were designed based on linear (Simple and Zigzag) profiles, to showcase the low frequency potential of arcs in comparison with their linear counterparts. The modeling of the arc-based cantilevers was based on a previously reported model for multidirectional and multilayered arc-based cantilevers [60]. All the arc-based cantilevers were shown to resonate below 200Hz and they exhibited dominant bending behavior in the fundamental mode. Furthermore, the free end tip displacement amplitudes of the ArcSimple and ArcZigzag microcantilevers were shown to be higher than those of their linear counterparts due to the decrease in mass and stiffness. The analysis presented here therefore provides a foundation for the development of standalone arc-based microcantilevers which can be used for energy harvesting, actuation, and sensing applications.

3.1.1 Design and Experiments

The design of the microcantilevers in this study follows the arc-based concept introduced in a previous study to evaluate the low frequency behavior in the absence of the widely used frequency-reduction tip mass [60, 65]. An arc-based cantilever is a continuous cantilever that can be divided into purely circular arc segments, thereby making it a low

frequency structure with dominant bending characteristic in the first (or fundamental) frequency mode. As shown in Figure 16a, two arc-based microcantilevers (ArcSimple and ArcZigzag) were designed based on the well-known linear configurations (Simple and Zigzag). Two specially defined microcantilevers (S-shaped and C-shaped) are also presented. The S-shaped cantilever is defined by

$$W = \frac{L + S}{n + 1} - S \tag{68}$$

while the C-shaped cantilever is defined by

$$W = \frac{L}{n + 1} - S \tag{69}$$

where W is the width of the cantilever arcs, L is the longest side length (measured in a straight line) occupied by the cantilever, n is the minimum number of pure circular arcs into which the cantilever can be divided, and S is the spacing between arcs. Therefore, the special microcantilevers can be modified and optimized to fit desired configurations based on the number of arcs, longest side length, spacing and width. The S-shaped and C-shaped microcantilevers in Figure 16a can be divided into a minimum of 8 and 9 circular arcs respectively.

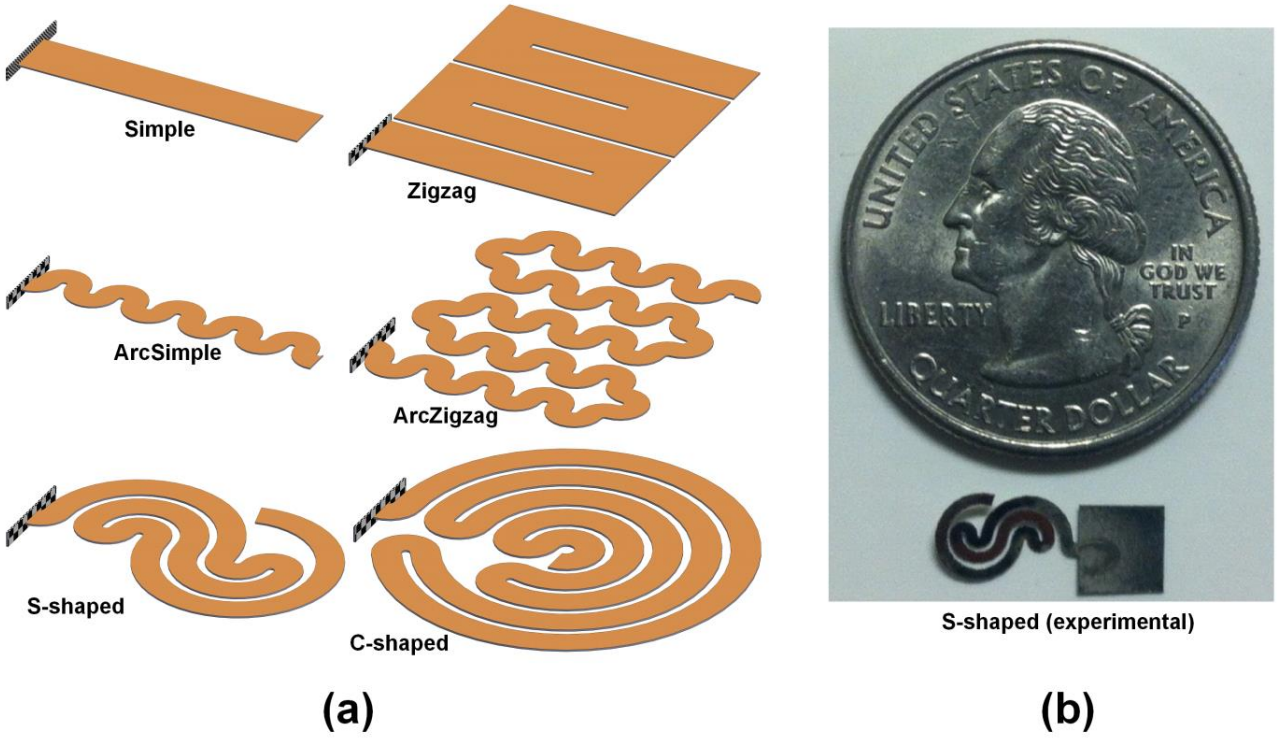

Figure 16: Arc-based microcantilevers: (a) design of the cantilevers, (b) fabricated S-shaped cantilever (N.B: the square section is for clamping only).

All the cantilevers shown in Figure 16a are fixed-free, and they were designed, modeled, fabricated and tested for free vibration analysis. As seen in Figure 16b, the fabricated S-shaped microcantilever features the arc-based cantilever and clamping (square) sections. All the microcantilevers analyzed in this study were micromilled using a milling bit of 150μm cutting diameter. Table 5 provides the properties of the microcantilevers. The cantilevers were fabricated from low carbon steel material and were limited to a top maximum surface area of 9mm x 9mm (i.e. Length × Width). The parameters common to all the arc-based microcantilevers were arc width (W), spacing between the arcs (S), and thickness of the arcs (h). The linear cantilevers (Simple and Zigzag) occupied higher

surface area in comparison to their arc-based counterparts (ArcSimple and ArcZigzag). The linear cantilevers have member widths (W_l) equal to

$$W_l = 2W + S \tag{70}$$

Out of all the arc-based cantilevers analyzed in this study, the C-shaped cantilever utilizes the highest surface area within the given top surface area limitations.

Table 5: Properties of all analyzed microcantilevers

Property	Value
Material	Low carbon steel
Material elastic modulus (GPa)	202
Material shear modulus (GPa)	79.8
Material Poisson's ratio	0.29
Material density (g/cm^3)	7.86
Top surface area limitation, L(mm) x B(mm)	9 x 9
*Largest length dimension of the Zigzag and ArcZigzag cantilevers (mm)	8.8
*Largest length dimension of the S-shaped cantilever (mm)	7.9
*Largest length dimension of the other cantilevers (mm)	9
Arc width ($R_o - R_i$) for ABCs (mm)	0.7
Member width for non-ABCs (mm)	1.6
Minimum spacing or via (mm)	0.2
Thickness of all cantilevers (mm)	0.0254

*this is a straight length measurement of the longest side of the cantilever

All the microcantilevers were tested in a simple vibration testing setup to obtain the resonance frequencies and tip amplitude response. The square sections of the cantilevers were clamped and a laser vibrometer (PDV 100, Polytec, Inc.) [66] was used to detect the motion of each cantilever free end during testing. An accelerometer (PCB U352C22) [67] was

used to detect the applied base acceleration to the shaker and clamp, while a digital signal processor (SigLab, Model 20-42) [68] was used to supply the output voltage signal to the shaker and receive input voltage signal during testing controlled by a computer. The peak values of cantilever end tip displacement amplitude were obtained via full integral of the obtained tip velocities corresponding to natural (or resonance) frequencies of the free vibrations of the cantilevers.

3.1.2 Modeling

The modeling of the arc-based cantilevers in this study is based on the out-of-plane vibration model as previously reported in our study [60]. The model is based on Timoshenko beam theory and includes the effects of bending, torsion, transverse shear deformation and rotary inertia [4]. It involves the development of eigenvalue matrices and can be applied to single or continuous (multidirectional) beams with different boundary conditions (e.g. clamped, pinned and free). The arc-based microcantilevers were modeled with fixed-free boundary conditions and thus included two boundary matrices each. The number of continuity matrices for any arc-based cantilever corresponds to $2n - 2$. The ArcSimple microcantilever was modeled with 10 arcs and 18 continuity matrices while the ArcZigzag microcantilever was modeled with 44 arcs and 86 continuity matrices. The S-shaped and C-shaped microcantilevers have 14 and 16 continuity matrices respectively.

The continuity matrices for an arc-based cantilever with a minimum of n distinct circular arcs can be combined into a single continuity matrix (*CSE*) thus [60]:

$$CSE = CS_n^{-1} CE_{n-1} CS_{n-1}^{-1} CE_{n-2}, \ldots, CS_2^{-1} CE_1 \tag{71}$$

where *CS* and *CE* are start and end continuity matrices respectively. Therefore, the eigenvalue problem becomes:

$$[N]_{6\times6}[a_1]_{6\times1} = [0]_{6\times1} \tag{72}$$

where

$$[N]_{6\times6} = \begin{bmatrix} BE_a \\ BE_b \times CSE \end{bmatrix} \tag{73}$$

and

$$[a_1]_{6\times1} = [a_{11}, a_{12}, \ldots, a_{16}]^{\mathrm{T}} \tag{74}$$

BE_{a} and BE_{b} are the boundary matrices of the cantilever at its fixed and free ends respectively. The continuity and boundary matrices were developed as a function of the as-yet-unknown natural frequency of the cantilever (ω) in rad/s. The values of ω which satisfy $det(N) = 0$ are the natural frequencies of the cantilever. The model was implemented in, and solved computationally with matlab [69].

The linear microcantilevers (Simple and Zigzag) were modeled using finite element analysis in ANSYS 15.0 [70] to obtain their natural frequencies. ANSYS was also used to obtain 3D mass-normalized mode shapes for all the analyzed microcantilevers. The finite element model was based on modal and harmonic structural analysis using fine meshes with a minimum of 100,000 elements for each cantilever.

3.1.3 Natural Frequencies and Mode Shapes

In order to obtain a fair comparison between the microcantilevers, a lumped mass approximation based on

$$2\pi f = \sqrt{\frac{k}{m}} = c\frac{H}{L^2} \tag{75}$$

was applied to the actual frequencies obtained via experiments and modeling to derive the normalized natural frequencies given as:

$$2\pi f_n = \frac{L_m^2}{H_m} \times \frac{H}{L^2} \tag{76}$$

where f and f_n represent the actual and normalized natural frequencies respectively (in Hz), H and H_m are the actual and maximum allowed cantilever thicknesses respectively, L and L_m denote the actual and maximum allowed side length of the microcantilever (i.e. a straight line measurement of the longest side of the cantilever) respectively, and c is a constant dependent solely on the mechanical properties of the cantilever. This approximation is accurate especially in the fundamental frequency mode since the frequencies of linear and arc-based cantilevers have been shown to vary linearly with thickness [65].

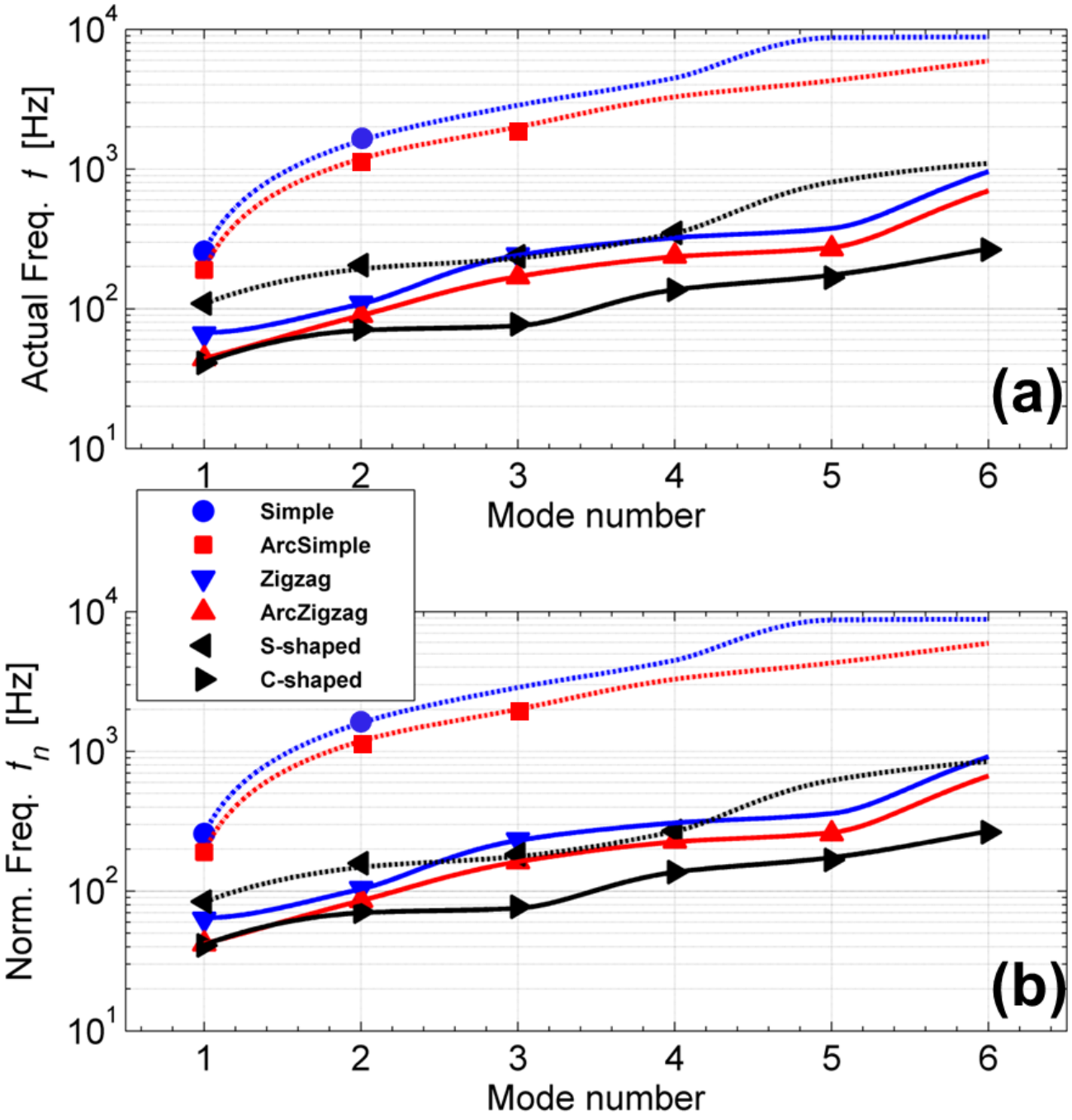

Figure 17: (a) Actual natural frequencies and (b) normalized natural frequencies of the analyzed microcantilevers as a function of mode number. N.B: The symbols represent experimental values while the lines represent modeling results (for both plots).

The actual natural frequencies of all analyzed microcantilevers obtained via modeling and experiments are shown in Figure 17a. However, a fairer comparison is shown in Figure 17b where the experimental and modeling results of normalized natural frequencies are plotted as a function of mode number. The experimental and modeling results were consistently within 1% agreement. The analysis of the natural frequencies in this section is based on the modeling results since the experimental results were limited to 2000 Hz. As seen in Figure 17b, the ArcSimple microcantilever exhibited consistently lower natural frequencies for the first six modes when compared with the Simple cantilever. The frequency reduction in the first mode was 26%, making the ArcSimple microcantilever vibrate experimentally at a frequency of 190 Hz ($f_n = f$ = 190 Hz) when compared with the Simple microcantilever at 258 Hz ($f_n = f$ = 258 Hz). The first six modes of the ArcSimple microcantilever were all less than 6000 Hz, while the sixth mode of the Simple cantilever occurred at 8818 Hz. The largest percentage difference occurred in the fifth mode (49% reduction) and the lowest percentage difference occurred in the first mode (26% reduction). As shown in Figure 18, an added benefit of modifying a Simple cantilever into an ArcSimple microcantilever is the ability to predict free vibration mode shapes. The ArcSimple microcantilever exhibited the same mode shapes as the Simple cantilever for the first three modes. The first two modes were dominantly bending, while the third mode was dominantly torsional.

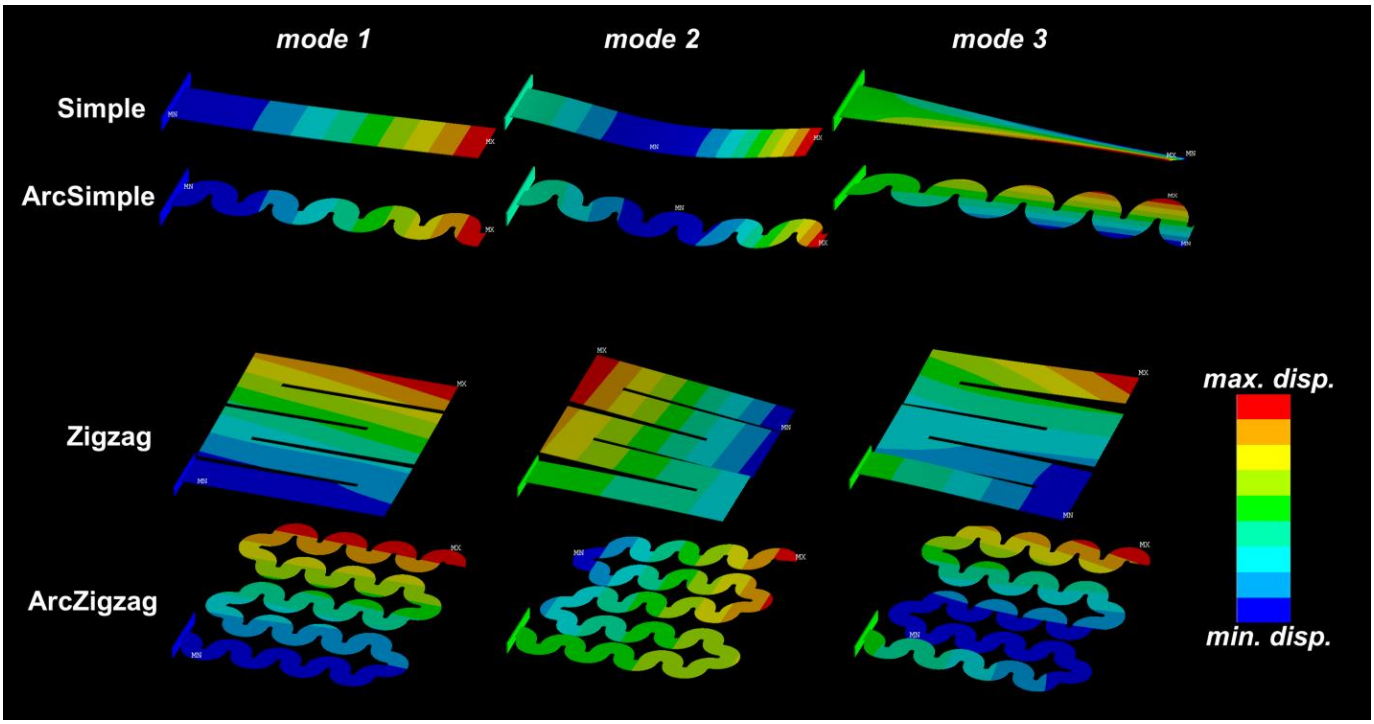

Figure 18: Mode shapes for the first three natural frequencies of the ArcSimple and ArcZigzag microcantilevers and their linear counterparts.

Figure 17b also shows a comparison between the ArcZigzag and Zigzag microcantilevers. The actual fundamental frequency of the ArcZizag microcantilever was 44Hz (f = 44 Hz, f_n = 42 Hz) while that of the Zigzag microcantilever was 68Hz (f = 68 Hz, f_n = 65 Hz) causing a reduction of 35% in the first mode. Again, just like the ArcSimple microcantilever case, the first six modes of the ArcZigzag microcantilever were consistently lower than their corresponding modes in the Zigzag microcantilever. The largest and lowest percentage differences occurred in the first (35% reduction) and second (18% reduction) modes respectively. It should be noted that based on the lumped mass approximation in Equation (75), the decreases in natural frequencies observed in the Simple (to ArcSimple) and Zigzag (to ArcZizag) microcantilevers would have been higher if the arc-based cantilevers had

equivalent surface area (and thus mass) as their linear counterparts. As with the Simple microcantilever case, Figure 18 shows that the ArcZigzag microcantilever exhibits similar free vibration mode shapes as its linear counterpart for the first three modes, making it easy to approximately predict the vibration characteristics ahead of design (as long as the Zigzag microcantilever characteristics are already known). However, for the first mode, there is less torsion and more bending exhibited by ArcZigzag microcantilever when compared with the Zigzag microcantilever. This behavior has also been reported for an ArcZigzag microcantilever which was designed based on a three-member Zigzag microcantilever [65].

In the case of the specially shaped microcantilevers, the C-shaped microcantilever ($f_n = f$ = 41 Hz in the first mode) exhibited lower natural frequencies than the S-shaped microcantilever (f = 108 Hz and f_n = 83 Hz in the first mode). The C-shaped microcantilever also exhibited the lowest frequencies across all first six modes when compared with the other analyzed cantilevers. The first six modes of the C-shaped microcantilever were all less than 270 Hz.

Figure 19 shows the free vibration mode shapes of the C- and S-shaped microcantilevers. Both microcantilevers exhibited dominant bending behavior in the first mode, but dominant torsional behavior in the second and third modes.

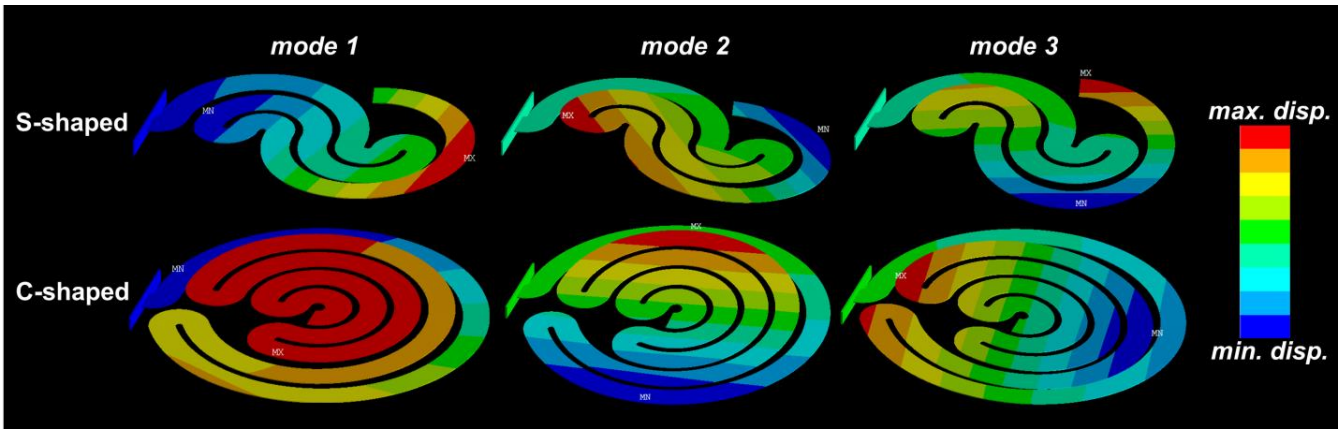

Figure 19: Mode shapes for the first three natural frequencies of the S-shaped and C-shaped microcantilevers.

For the ArcSimple and ArcZigzag microcantilevers and their linear counterparts, approximate effective stiffness constants can be obtained based on the lumped mass approximation in Equation (75) which would be accurate for determining the fundamental frequencies. The vibration characteristics of these cantilevers are shown in Table 6. It can be seen that the percentage decrease in stiffness is larger than the percentage decrease in mass when the arc-based microcantilevers are compared with their linear counterparts. This is the main reason for the significant reduction in the natural frequencies observed.

Table 6: Vibration characteristics of the ArcSimple and ArcZigzag microcantilevers and their linear counterparts

Cantilever	Mass [mg]	Stiffness [10^{-9}N/m]	Actual Natural Frequency [Hz]
Simple	2.875	13.4	258
ArcSimple	1.877	4.206	190
Zigzag	14.06	83.78	68
ArcZigzag	7.804	16.84	44

3.1.4 Response to External Excitation

The fabricated microcantilevers were analyzed in a vibration test setup for their response to externally applied forces/accelerations. Values of end tip velocities obtained via a laser vibrometer were converted via integration as a function of time to obtain the end tip displacement amplitudes. The tests were carried out at frequencies between 20 to 300 Hz and each test was repeated three times in response to an externally applied base acceleration of 0.1g, where g = 9.8 m/s^2. The results plotted with error bars showed less than 0.1% variation as seen in Figure 20 & Figure 21.

In Figure 20, the ArcSimple and ArcZigzag microcantilevers are compared with their linear counterparts. As expected, the resonance frequencies were consistently lower in the arc-based microcantilevers. Due to the reduced mass and stiffness, the values of tip displacement amplitudes (and thus velocity amplitudes) were also higher when comparing the arc-based microcantilevers with their linear counterparts. The ArcZigzag microcantilever exhibited the largest tip displacement amplitude of all tested cantilevers (z_{tip} = 1.24 mm). The tip displacement amplitudes of the specially shaped arc-based microcantilevers are shown in Figure 21. The S-shaped microcantilever exhibited higher tip displacement in the second and third modes only. The C-shaped microcantilever exhibited large first mode tip displacement amplitude (z_{tip} = 1.2 mm) mainly due to its saucer-like vibration mode shape in the first mode.

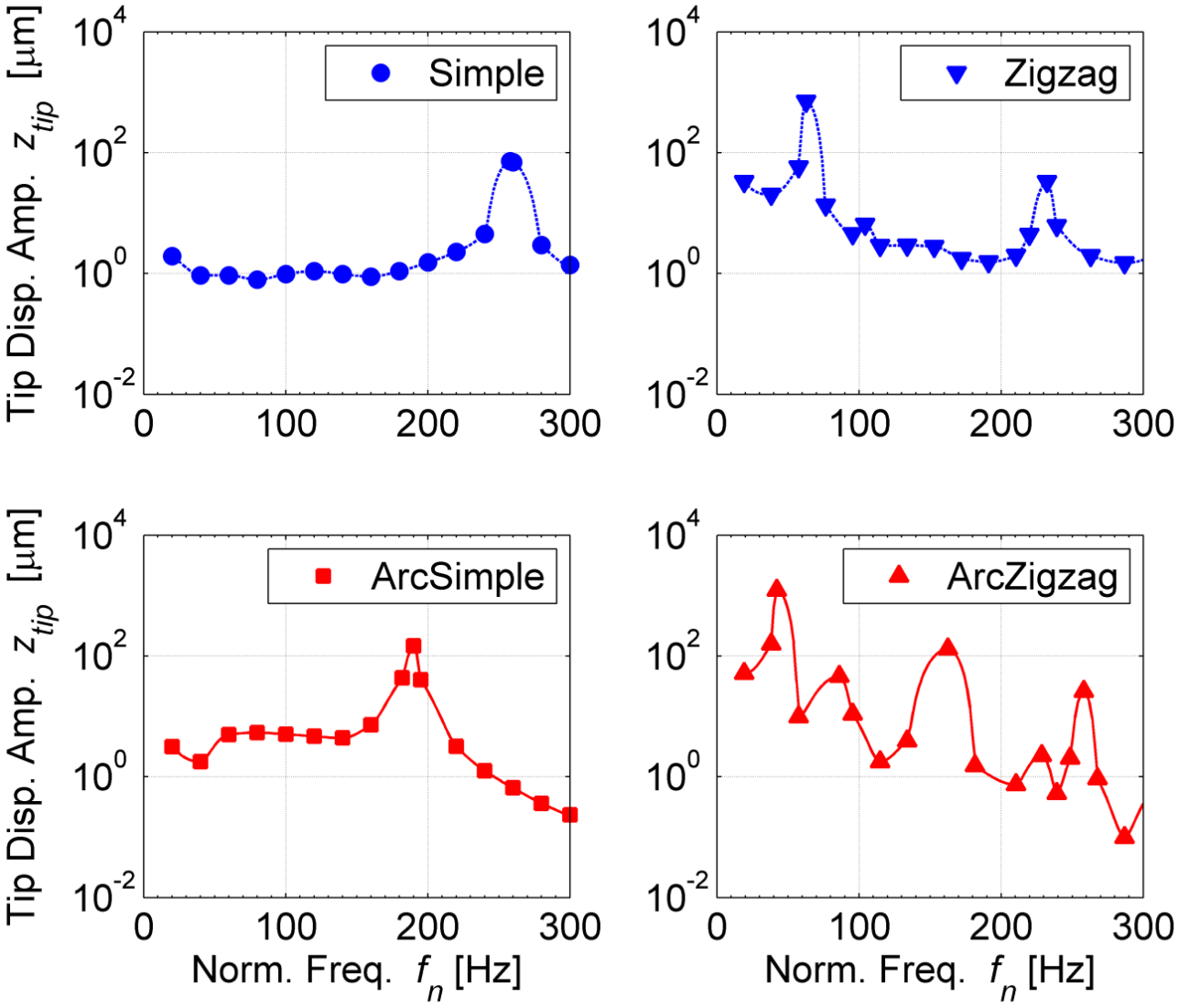

Figure 20: Free end tip displacement amplitudes of the experimental ArcSimple and ArcZigzag microcantilevers and their linear counterparts as a function of normalized frequency under an applied sinusoidal base acceleration of 0.1g (1g = 9.8m/s^2).

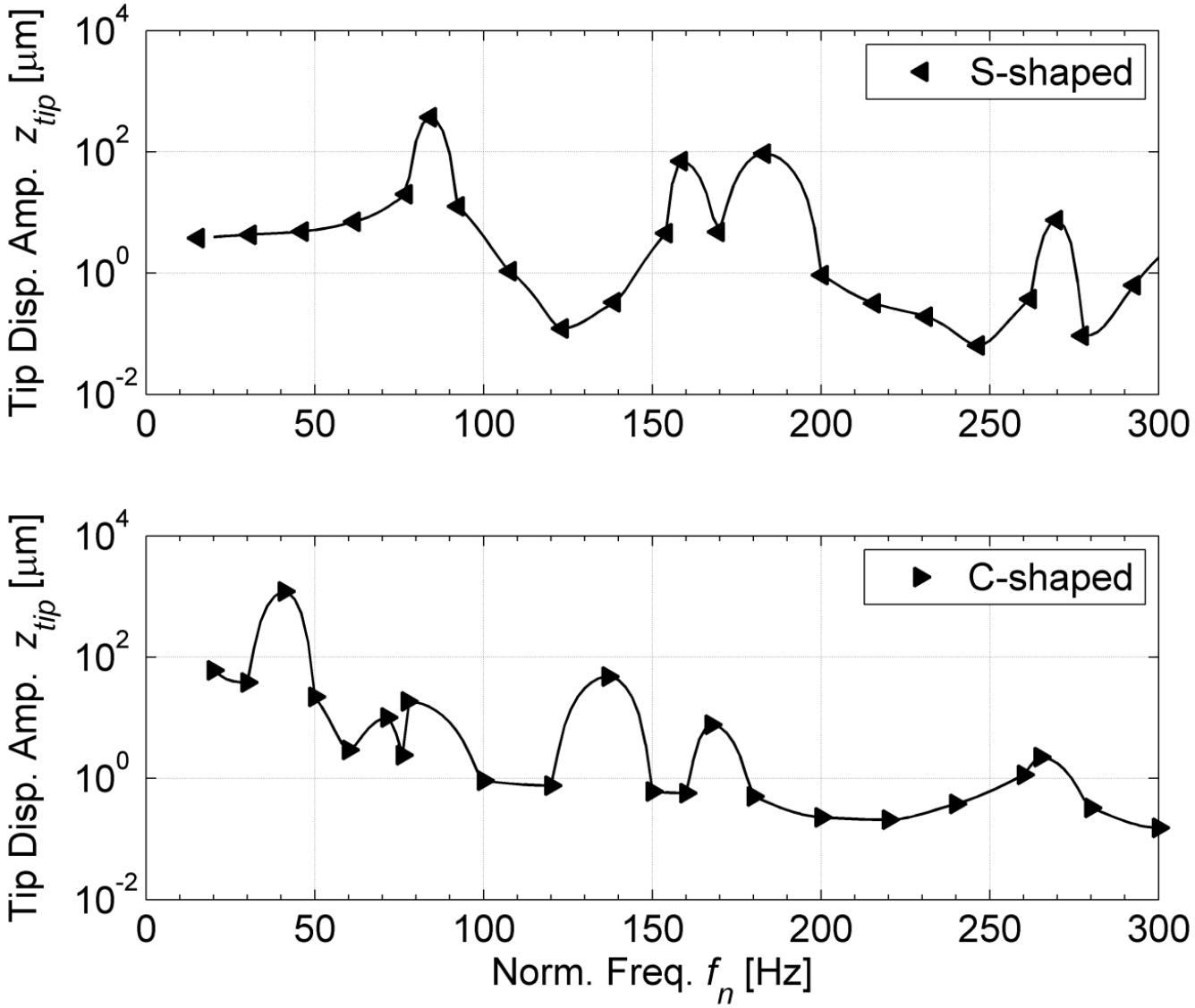

Figure 21: Free end tip displacement amplitudes of the experimental S-shaped and C-shaped microcantilevers as a function of normalized frequency under an applied sinusoidal base acceleration of $0.1g$ ($1g = 9.8\text{m/s}^2$).

3.1.5 Low Frequency Applications for Arc-Based Microcantilevers

The arc-based microcantilevers discussed in this section were designed in view of broad low frequency applications such as transduction (strain to voltage) and actuation (voltage to strain). However, a promising application for arc-based microcantilevers is in the

field of energy harvesting since all analyzed microcantilevers exhibited dominant bending behavior in the first mode. Furthermore, the low fundamental frequencies observed (especially for the ArcZigag and C-shaped microcantilevers) make the microcantilevers suitable for resonating with most vibration sources (e.g. vehicles, heavy machinery, and bridges), thus increasing the ability to harvest energy at their peak point. The arc-based microcantilevers also have the added advantage of functioning without a tip mass which would affect the mode shapes negatively (more torsion) and reduce structural integrity.

Of all the analyzed arc-based microcantilevers, the C-shaped cantilever is most suitable for energy harvesting due to its low fundamental frequency and saucer-like pure bending behavior in the first mode. The ArcSimple and ArcZigag microcantilevers can be designed when the natural frequencies of Simple and Zigzag cantilevers or structures need to be reduced. Other well-known cantilever or structural shapes can also be modified into arc-based shapes to obtain this low frequency effect.

3.2 Magnetoelectric MEMS Device for Low-Frequency Dual-Phase Energy Harvesting

This section introduces the use of modified MEMS arc-based cantilevers for vibration, magnetic field, and dual-phase (vibration and magnetic field) energy harvesting. Two harvester designs are presented as following:

- C-shaped harvester with piezoelectric (PVDF) bimorph present only at the center area
- C-shaped harvester with piezoelectric (PVDF) unimorph across the entire area

It should be noted that the modification was done to increase the surface area available for voltage generation

3.2.1 Design and Fabrication

The harvesters in this section were designed as modifications of the 9-arc C-shaped cantilever as shown in Figure 23a. As seen in the finite element mode shapes obtained from ANSYS modal simulations, the modification does not appreciably affect the fundamental frequency nor the mode shape of the harvester. The modification increases the surface area available for energy harvesting and reduces the fabrication cost and time.

Table 7: Properties of both MEMS magnetoelectric harvesters

Property	Value
Piezoelectric material	PVDF
Magnetostrictive material	metglas
Harvester overall diameter (mm)	9
Width of each arc ($R_o - R_i$) (mm)	0.7
Spacing or via (mm)	0.2
PVDF or metglas thickness (μm)	25
Electrode thickness (μm)	1.5

The process of harvester fabrication involved epoxy bonding, material micromilling and laser processing of the micromilled material as depicted in Figure 22. Firstly, metglas (Hitachi Metals Ltd. [71]) was cut into a square shape of 2" x 2". Then, a tool path was designed in NX Unigraphics software mimicking the intended harvester shape. This tool path was fed into a computer-controlled CNC machine that resulted in the fabrication of the desired shape.

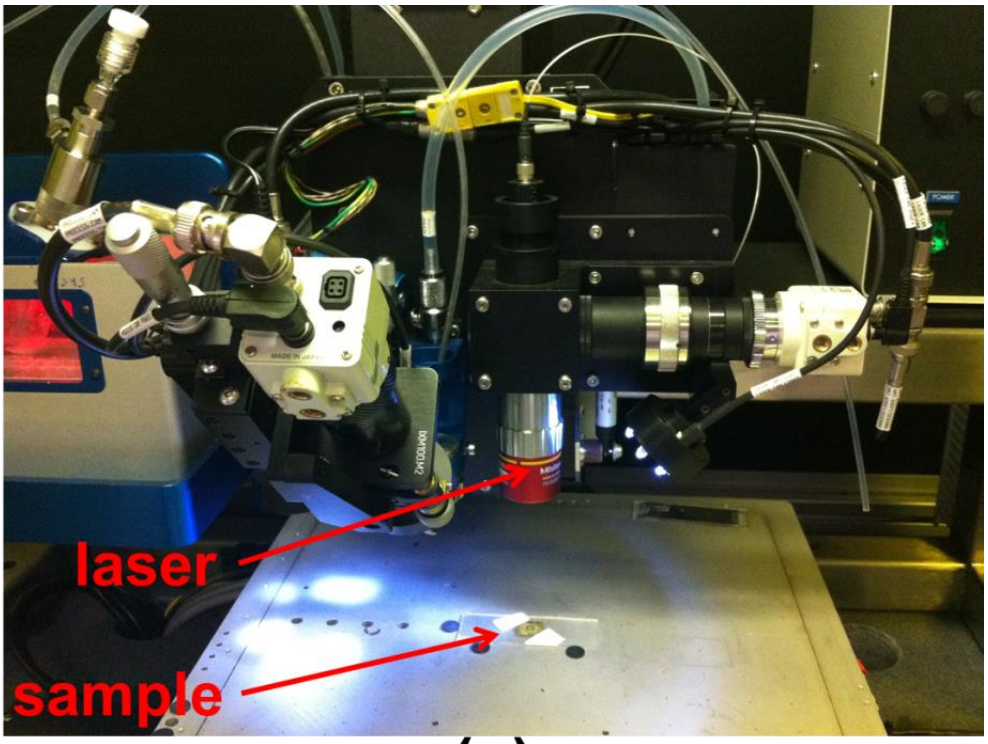

(a)

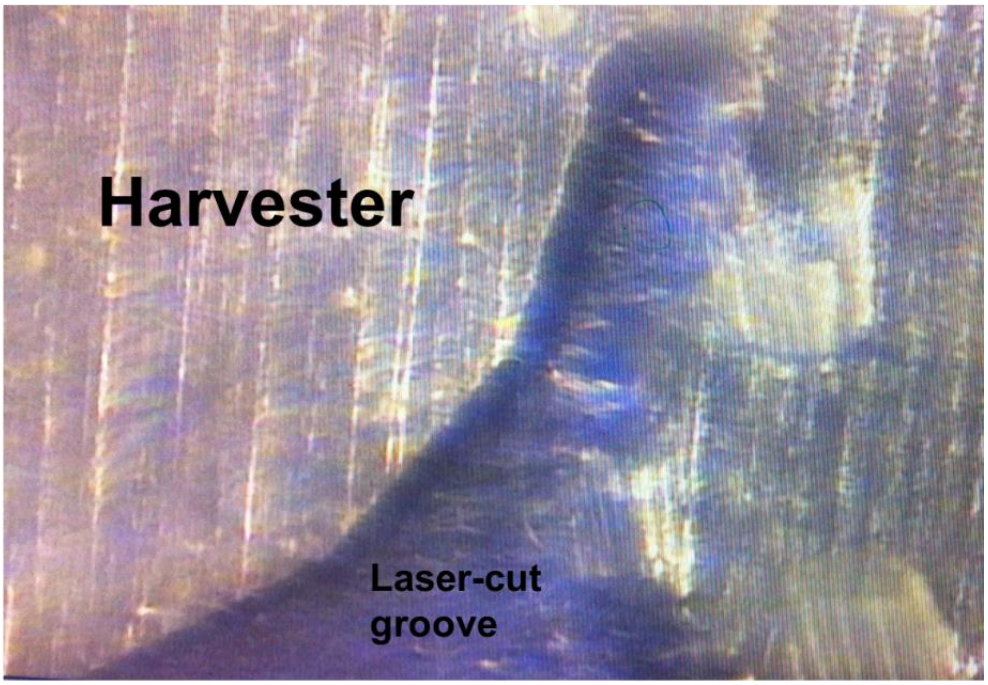

(b)

Figure 22: (a) Harvester in laser-cutting chamber, (b) Microscopic view of a laser-cut grove within the harvester

Next, the polymer piezoelectric – PVDF (Measurement Specialties Inc. [72]) of dimension 2" x 2" was bonded onto the top of the machined structure. The machined shape was used as a guide for the PVDF during the next step (laser cutting). An Aerosol Jet printing system (Optomec) [73] equipped with an 830 nm continuous wave Yb-fiber laser was used to make the desired pattern on the PVDF attached on the already machined structure. The current in the laser source can be varied in the range 0.2-2 A. The PVDF sample was kept on a stage capable of moving in XYZ directions with speed in the range of 0.01-15 mm/s. The speed and current were also optimized to achieve nice clean patterned surface of PVDF as shown in Figure 23b.

Figure 23c & d show the dual-phase testing setup with a Helmholtz coil clamp which allows the application of vibration and magnetic field simultaneously. The Helmholtz coil equation in this case is:

$$H\,[oe] = \frac{B}{\mu_{r,air}} = \frac{\left(\frac{4}{5}\right)^{\frac{3}{2}} \mu_0 nV}{rR\mu_{r,air}} \tag{77}$$

where

$\mu_{r,air}$ = relative permeability of air $\approx$ 1

μ_0 = permeaability of free space = $4\pi \times 10^{-7}$ Hm^{-1}

n = number of wire loops in one coil segment = 30

Resistance of coil (R) = 6.3Ω

Center radius of coil (r) $\approx$ 53 mm

V = applied voltage

Voltage needed to obtain $1oe$ of H field or B field = 2.5V

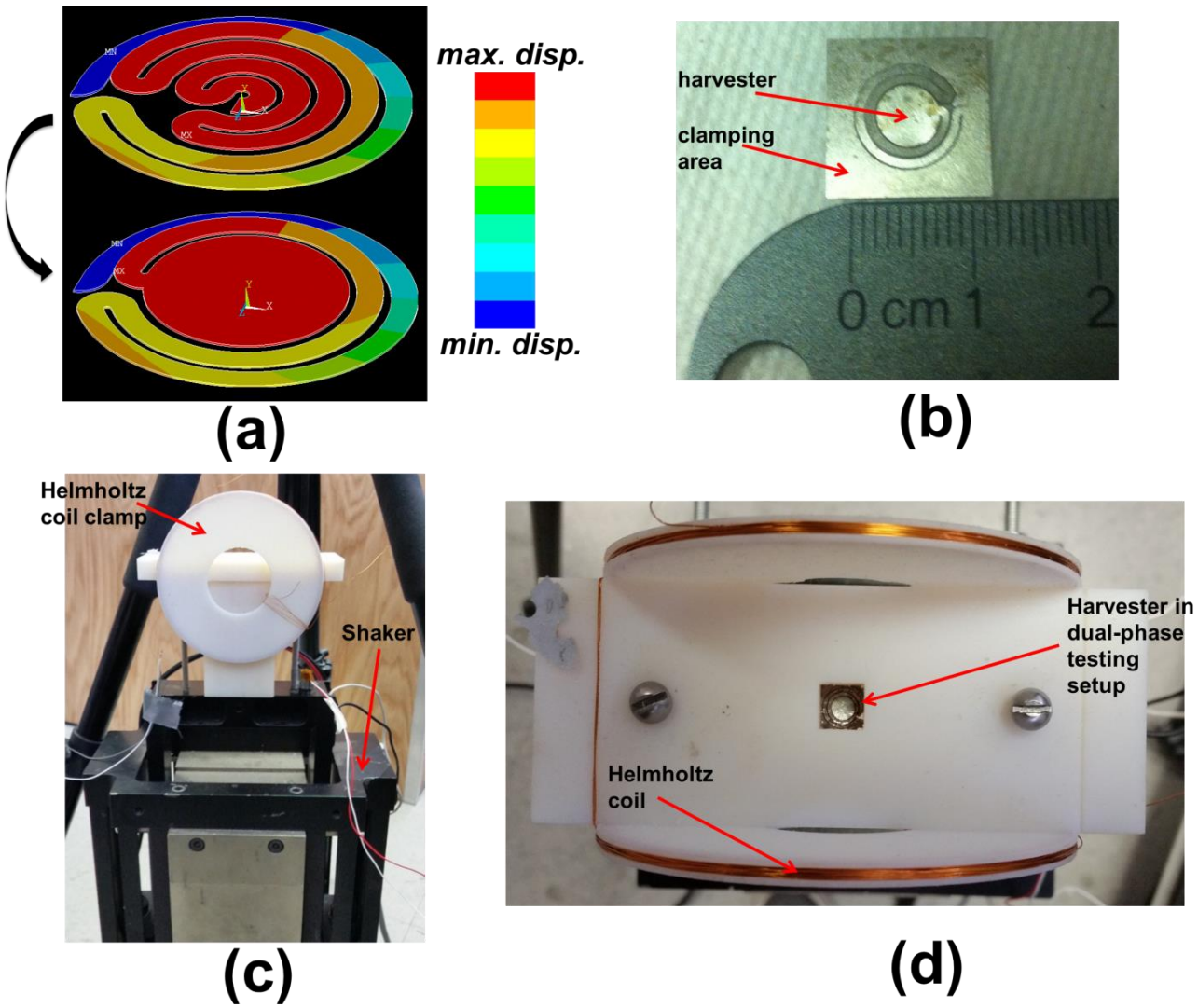

Figure 23: (a) Fundamental frequency mode shapes of the arc-based and modified arc-based cantilevers, (b) Fabricated harvester, (c) Dual-phase testing setup with Helmholtz coil clamp, and (d) Harvester in dual-phase testing.

The detailed harvester designs are shown in Figure 24 to provide a depiction of the three-dimensional and layer views. Configuration 1 harvester is a center bimorph with the PVDF piezoelectric placed on the circular center section while configuration 2 harvester is a unimorph with the PVDF piezoelectric covering the entire harvester. For the second

configuration, an extra metglas-only cantilever is attached to provide more amplitude (and thus strain) during vibration.

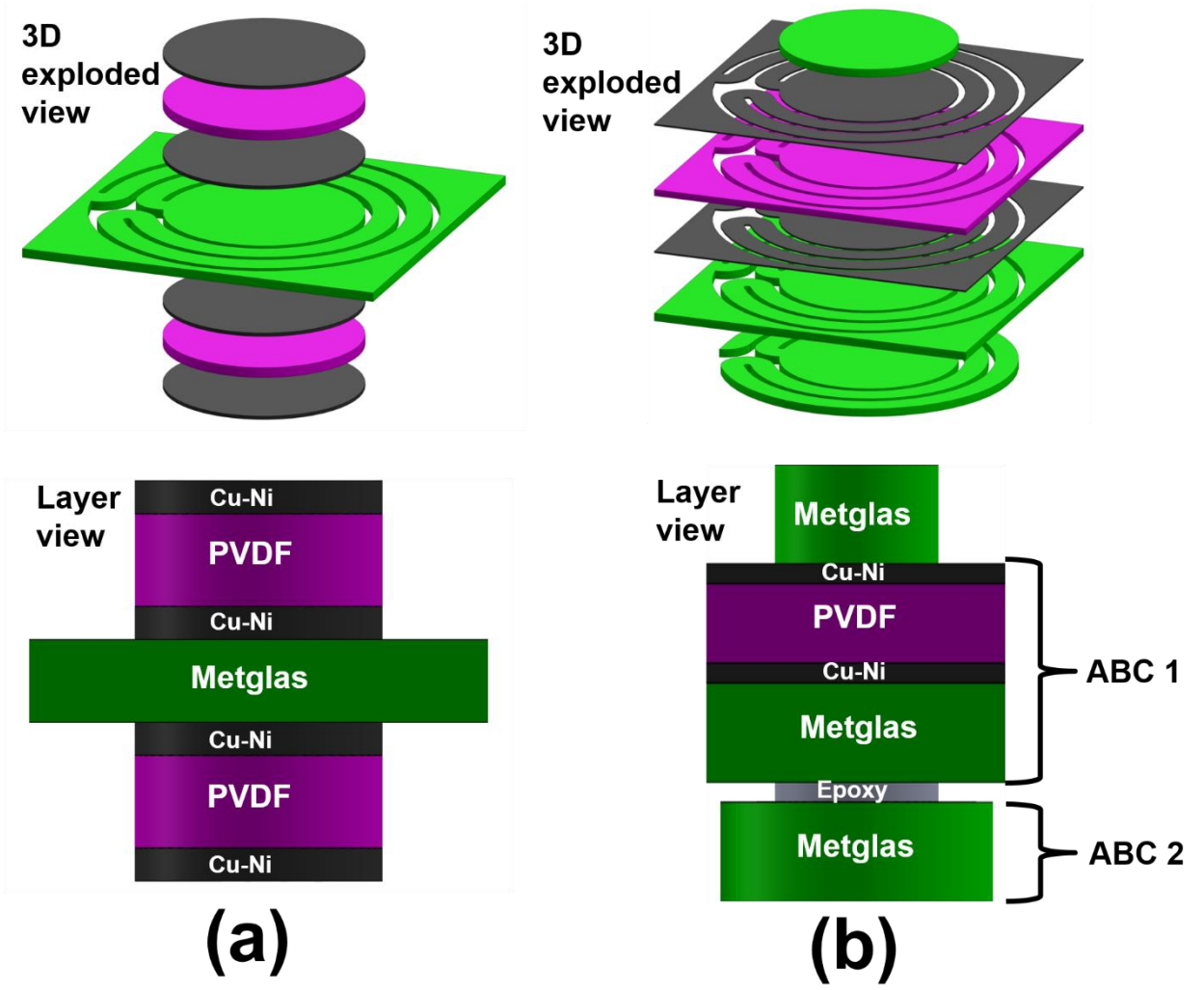

Figure 24: Design of the experimental dual-phase harvesters (a) Configuration 1 with PVDF bimorph on circular section only, and (b) Configuration 2 with PVDF unimorph on a metglas arc-based cantilever (ABC) which is bonded to another metglas ABC by its circular section only.

3.2.2 Harvesters in Magnetic Field Environment

When tested in a magnetic field setup, the two harvesters performed independent of DC magnetic field as shown in Figure 25a with harvester 2 exhibiting about 6 times the magnetoelectric coefficient of harvester 1 (14.1 V/cmOe vs. 2.3 V/cmOe) due to the larger piezoelectric surface area in harvester 2. The harvester behavior with DC magnetic field variation is a positive effect which implies that a DC magnetic field (placement of a stationary magnet closeby) is not needed for harvester operation as long as an alternating (AC) magnetic field is present.

Another interesting phenomenon is the increase in magnetoelectric coefficient with increasing frequency as shown in Figure 25b. This trend almost peaks around 200Hz leading to only minor increase in the magnetoelectric coefficient beyond 200Hz. As expected in Figure 25c, the magnetoelectric voltage increases linearly with increasing AC magnetic field for both harvesters. Using finite element modeling with ANSYS, the strain profiles for the harvesters at different frequencies were simulated to provide an explanation for the unexpected responses to DC magnetic field and frequency as shown in Figure 26. The resonance-independent uniform strain in the center of the harvester is one reason for the harvester's unique response to frequency and DC magnetic field.

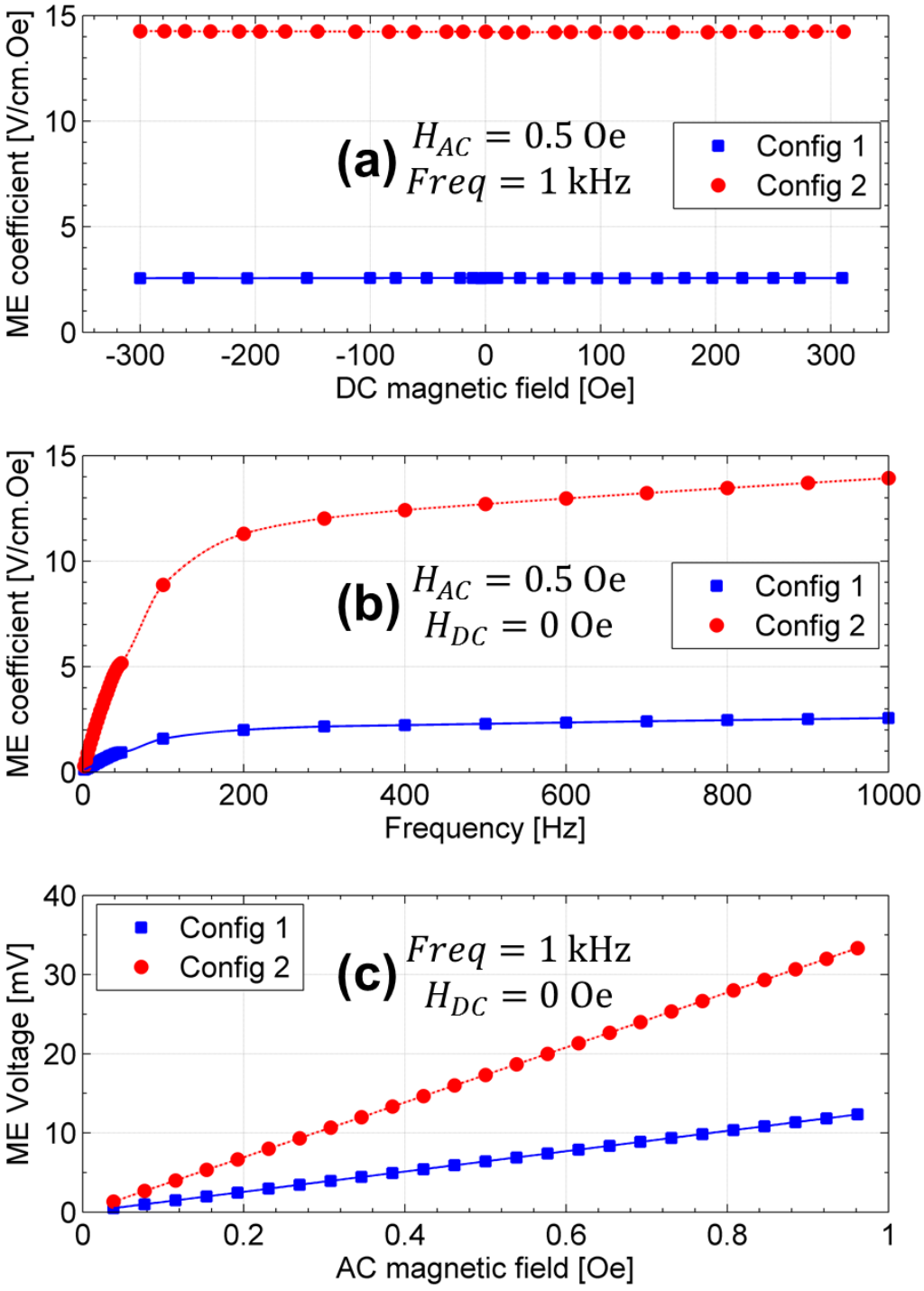

Figure 25: Experimental results from magnetoelectric testing of the harvesters: (a) Magnetoelectric coefficient as a function of applied DC magnetic field, (b) Magnetoelectric coefficient as a function of frequency, and (c) Magnetoelectric voltage as a function of applied AC magnetic field.

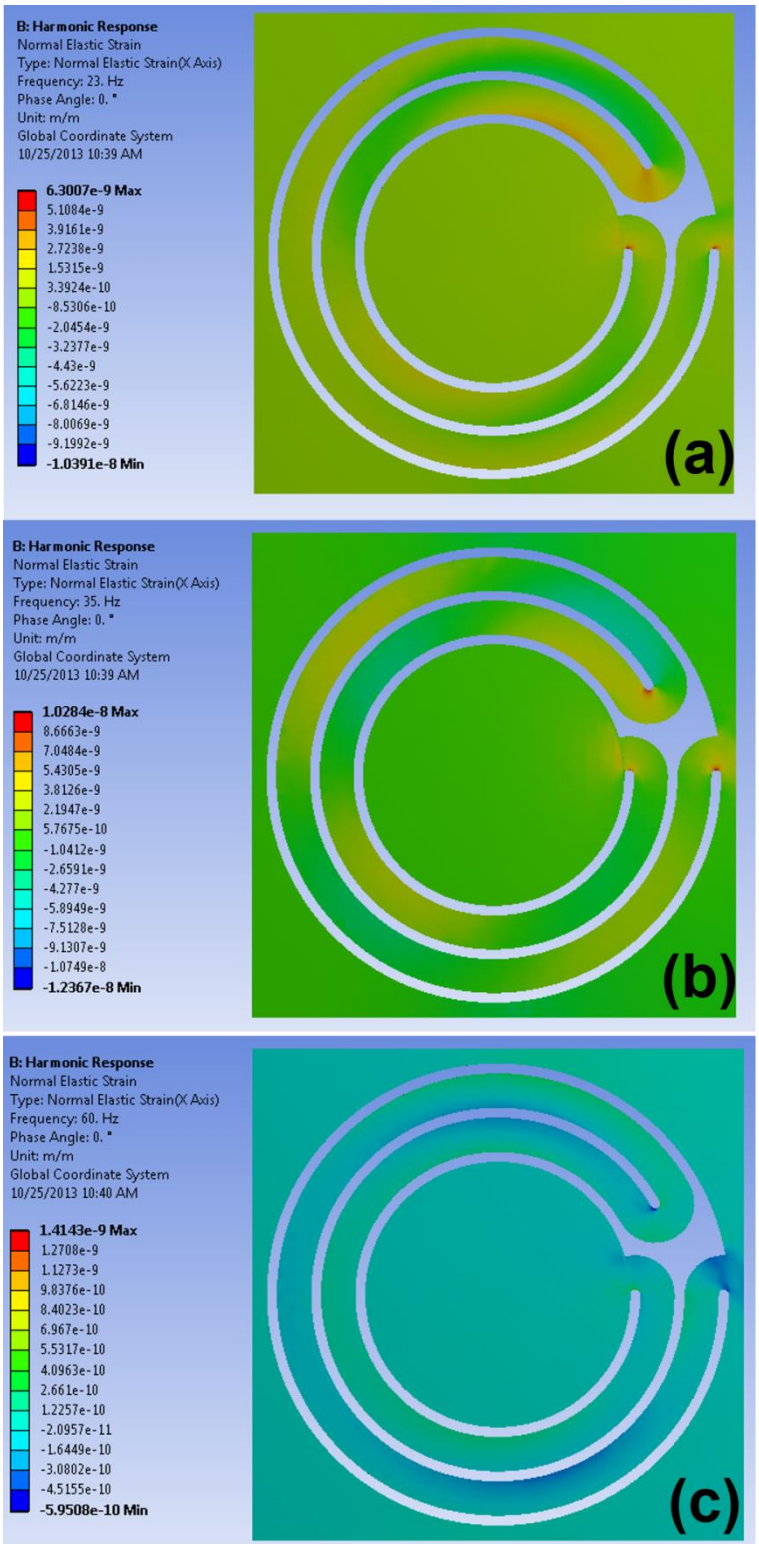

Figure 26: Strain profiles for harvester 1 (bimorph) at different frequencies with an applied external acceleration of 0.6*g* (5.83m/s²): (a) 23Hz (vibration resonance), (b) 35 Hz off-resonance, and (c) 60 Hz off resonance. The uniform strain in the center is one reason for the harvester's unique response to frequency and DC magnetic field

3.2.3 Harvesters in Vibration and Dual-Phase Environments

When harvester 1 & 2 were tested in a vibration-only setup, the optimum electrical loads were observed at 1.05 MΩ and 1 MΩ respectively. Also, the fundamental resonance frequencies for harvesters 1 & 2 were 23Hz and 33Hz respectively.

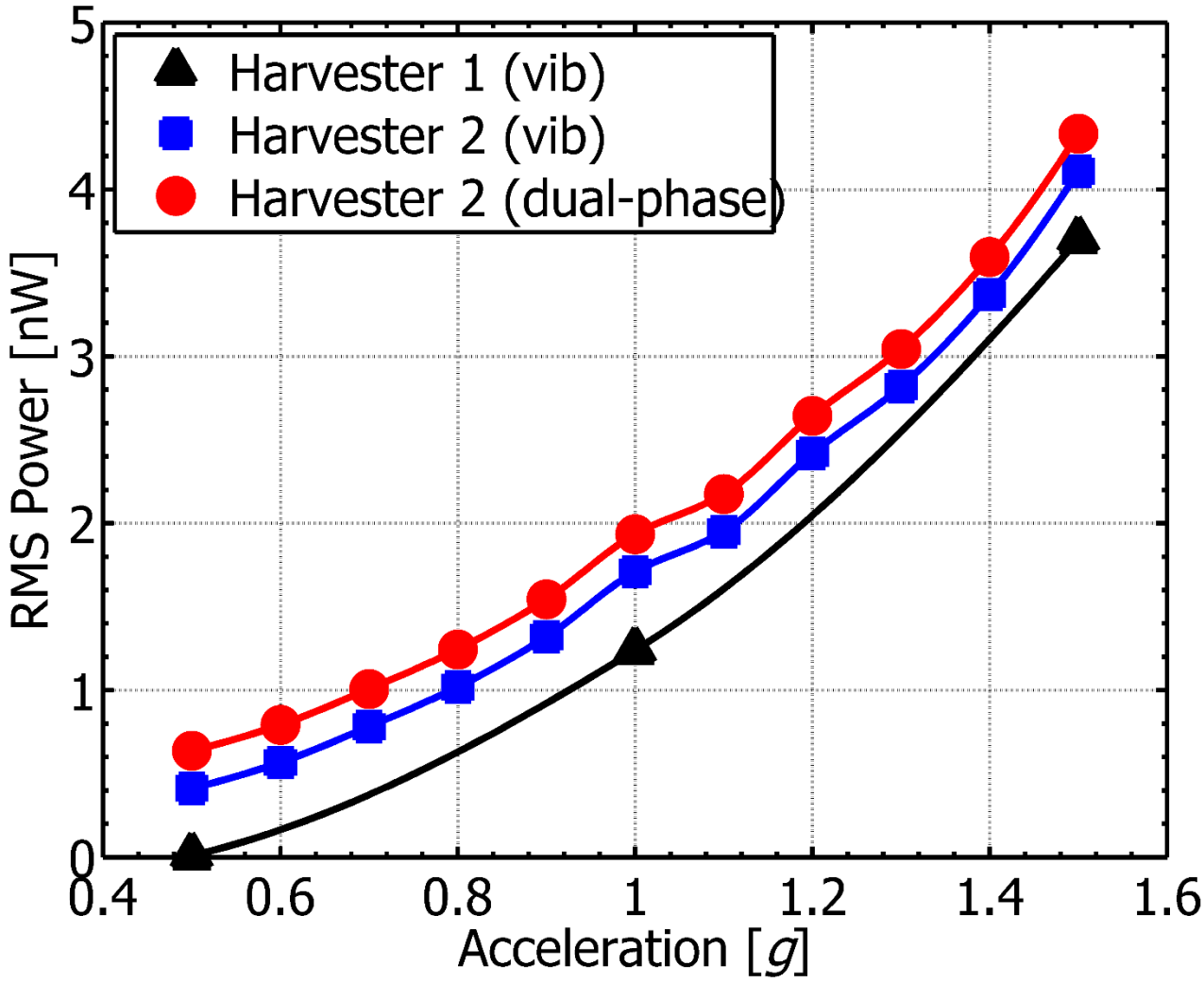

Figure 27: Vibration-only and dual-phase testing results at resonance for both harvester configurations (harvester 1 at 23Hz, and harvester 2 at 33Hz).

From the power response results in vibration testing in Figure 27, harvester 2 consistently produced higher output values than harvester 1. The tests were conducted at the resonance frequencies of the harvesters as a function of the applied sinusoidal base acceleration. At an acceleration amplitude of 1*g*, harvester 1 produced RMS voltage of 36mV (RMS power = 1.24nW) while harvester 1 produced RMS voltage of 41mV (RMS power = 1.71nW). Finally, when tested within the helmoltz coil clamp (dual-phase testing), harvester 2 was shown to exhibit an additive effect and the output value of RMS voltage at 1*g* was 44mV (RMS power = 1.94nW). Based on the reported vibration-only and magnetic-only voltage values for harvester 2, the loss due to combining the vibration and magnetic field testing environments was < 1%.

3.3 Chapter Conclusion

The free vibration characteristics of four standalone arc-based microcantilevers were modeled and experimentally validated. The arc-based microcantilevers were modeled as a pure combination of circular arcs, tested in a simple vibration setup, analyzed for their natural vibration characteristics, and quantified for their response to externally applied forces/accelerations. In comparison to their linear counterparts, the ArcSimple and ArcZigzag exhibited up to 49% and 35% reductions in natural frequencies respectively, and they exhibited higher tip displacement amplitudes (due to lower masses and stiffnesses). All the analyzed arc-based microcantilevers exhibited dominant bending behavior in the first mode and were shown to resonate below 200 Hz. The C-shaped microcantilever was shown to exhibit the lowest fundamental frequency (41 Hz), thus making it suitable for most cantilever-based applications at the microscale.

Furthermore, two arc-based harvester designs were utilized for dual-phase energy harvesting from vibrations and magnetic fields. Harvester 1 provided 36mV at low frequency of 23 Hz and acceleration of 1*g*, while harvester 2 provided 41mV also at a low frequency (33 Hz) and acceleration of 1*g*. Also, both harvesters performed independently of DC magnetic field and exhibited significant magnetoelectric coefficient (up to 14.1 V/cmOe). Harvester 2 was then shown to exhibit an additive effect during dual-phase testing with voltage losses below 1%.

4 Chapter 4:

High Power Density Levitation-Induced Vibration Energy (LIVE) Harvester

Vibration-based energy harvesting devices are typically designed to scavenge mechanical energy from sources such as heavy machinery, railways, trucks, bridges, and ships. However, these natural sources typically vibrate at low excitations, below 0.5G (where 1G = 9.8m/s^2), and low frequencies, below 20Hz [74]. Piezoelectric cantilever-based devices have become popular for harvesting energy from vibrations. However, these devices present a fundamental challenge when designed for small scale applications since the resonance frequency of the structure increases as the dimension decreases. Thus, most currently reported cantilevers operate at frequencies higher than 50Hz [75]. Furthermore, cantilever-based devices are generally devoid of broadband behavior at their resonance frequencies, therefore limiting their capability outside the resonance region.

A promising solution for low frequency – low excitation energy harvesting is the development of magnetic levitation systems. These systems exhibit nonlinear stiffness profile due to the repulsive force between magnetic poles that varies as the square of the distance between them. The non-linear stiffness profile in turn results in non-linear frequency response which allows harvesting more power in a broader range of frequencies when compared with the linear frequency response observed for most of the piezoelectric devices. Several studies have identified broadband response and high power response from

different forms of nonlinear magnet-based energy harvesters. A small subset of these studies [8, 76, 77] have reported a more direct method of harvesting energy by magnetic levitation of a magnet (or magnet composite) between two stationary magnets placed in a repelling direction to the magnet composite. Tornincasa *et al*. [78] analyzed this configuration for energy scavenging in automotive tires. Marin *et al.* have conducted considerable work in this field with the development of a pen harvester [79] and multi mechanism devices [80, 81].

The literature on magnetically-levitated energy harvesters has not addressed the design of efficient magnet and coil configurations which would maximize the power output at low frequencies. In this chapter, we present a levitation induced vibration energy (LIVE) harvester that incorporates a double-repulsion magnet composite levitated between two stationary magnets. The coil configuration was designed to target the regions of high magnetic flux density around the moving magnet composite. Finite element modeling and mathematical modeling were used to analyze the force field, magnetic flux, dynamics, and output response of the harvester. The models were also used to identify the advantages of the double-repulsion configuration over other possible configurations. Lastly, an AA battery-sized harvester was designed, fabricated and tested based on the modeling results. The harvester was found to exhibit significantly high power density across different frequencies and base excitations. The harvester was also used to supply charge to a cellphone via an external circuit.

4.1 Design, Fabrication and Testing

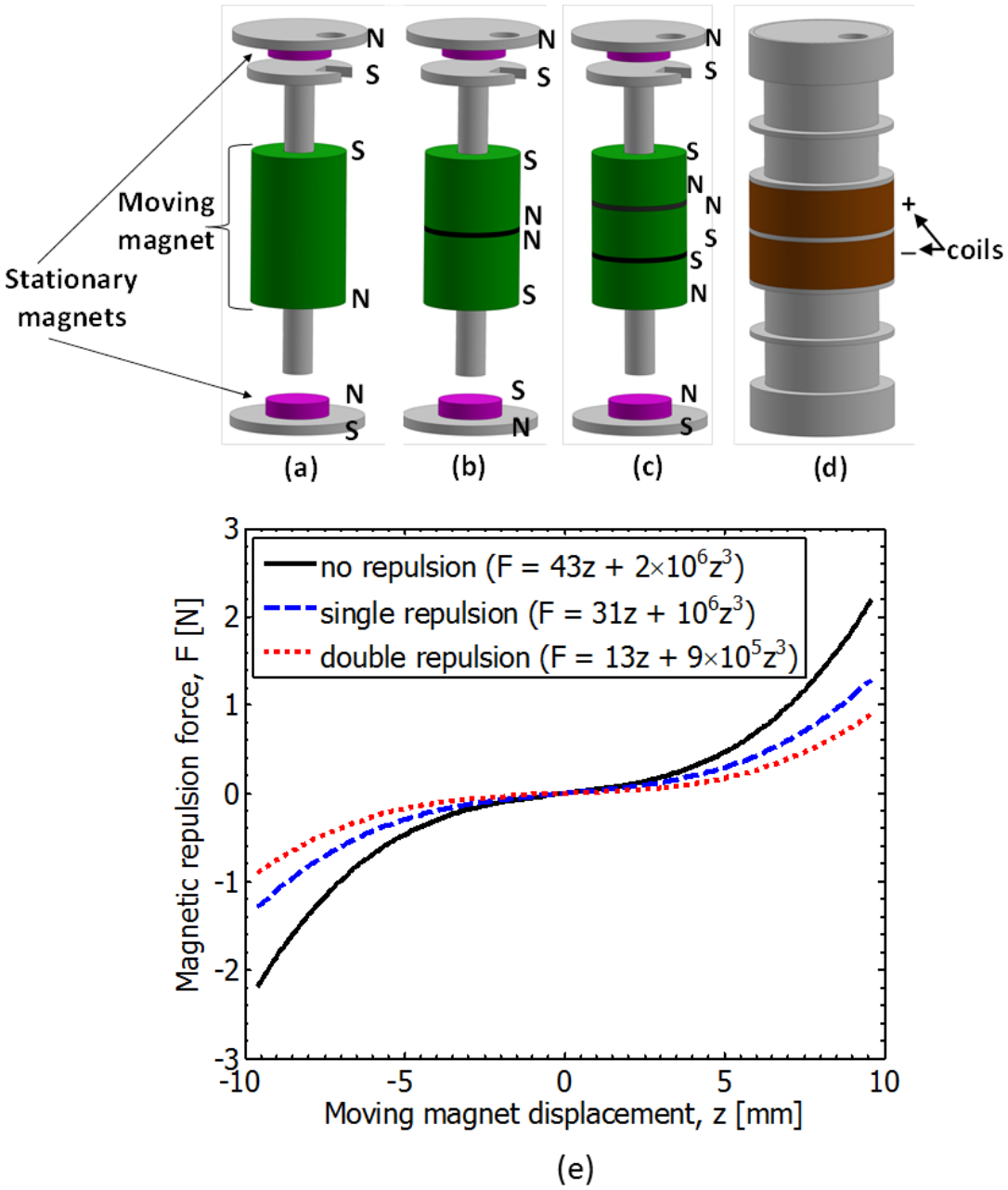

Figure 28: Design configurations of the harvester: (a) single moving magnet (no-repulsion) configuration, (b) two moving magnets (single-repulsion) configuration, (c) the fabricated three moving magnets (double-repulsion) configuration, and (d) coil and casing design for the fabricated double-repulsion configuration, (e) Predicted magnetic repulsion force vs. moving magnet displacement relationship for all three configurations.

Table 8: Properties of the LIVE harvester components (all configurations)

Component	Properties
Harvester casing dimensions (mm)	14 od x 10.5 id x 40 long
Magnet material	NdFeB N42
Moving magnet composite dimensions (mm)	9.5 od x 3.2 id x 15.3 thick
Moving magnet composite mass (grams)	7.29
Carbon steel ring dimensions (mm)	9.5 od x 3.2 id x 0.5 thick
Carbon steel ring mass (grams)	0.25
Stationary magnet dimensions (mm)	6.4 od x 0.8 thick
Stationary magnet mass (grams)	0.2
Coil material	copper
Each coil segment (mm)	14 od x 11 id x 4.8 thick
Coil resistance	14.43 ohm/m
Coil diameter (mm)	44μm
No. of coil turns per segment	2800

The harvester configurations modeled in this study are shown in Figure 28. The design of the harvester fabricated and characterized is shown in Figure 28c & d. As shown in this figure, a magnetic ring composite was levitated by placing it in a repelling configuration between two stationary disc magnets in a tube with 14mm outer diameter (od), 10.5mm inner diameter (id) and 40mm height. The properties of the harvester components are listed in Table 8. The magnets were designed from NdFeB N42 type material and were obtained commercially (K&J Magnetics, USA). It was important to ensure that the stationary magnet diameter was greater than the inside diameter of the moving magnet composite to prevent the magnetic attraction at high displacement amplitudes where the moving magnet composite comes in close vicinity to the stationary magnets.

As shown in Figure 28c, the fabricated moving magnet composite was composed of a unique double-repulsion configuration in which three magnets (each with dimensions

9.5mm od x 3.2 id x 4.8 mm height) were assembled with repelling poles and separated with carbon steel rings (dimensions 9.5mm od x 3.2 id x 0.5mm height). The reason for the double-repulsion design was to create two strong regions of high magnetic flux density (B-field). Two coil segments, each with dimensions of 14mm od x 11mm id x 4.8mm height, were wound around the tube in opposite directions and aligned with the regions of high B-field around the moving magnet composite. This magnet and coil configuration ensures effective use of the coils and the absence of constant zero voltage regions (magnet outside the coil area, or cancellation effects) during operation since the coils have the same height as one of the magnet in the levitating composite and the coils were wound in opposite directions. Also, the spacing between the coils equals the height of one carbon steel ring in the moving magnet composite. The center pole which guides the moving magnet composite is essential for limiting the friction. Reduction in friction can be obtained by ensuring the moving magnet composite is always concentrically located within the device thus longitudinally aligning its axis with those of the coils and stationary magnets.

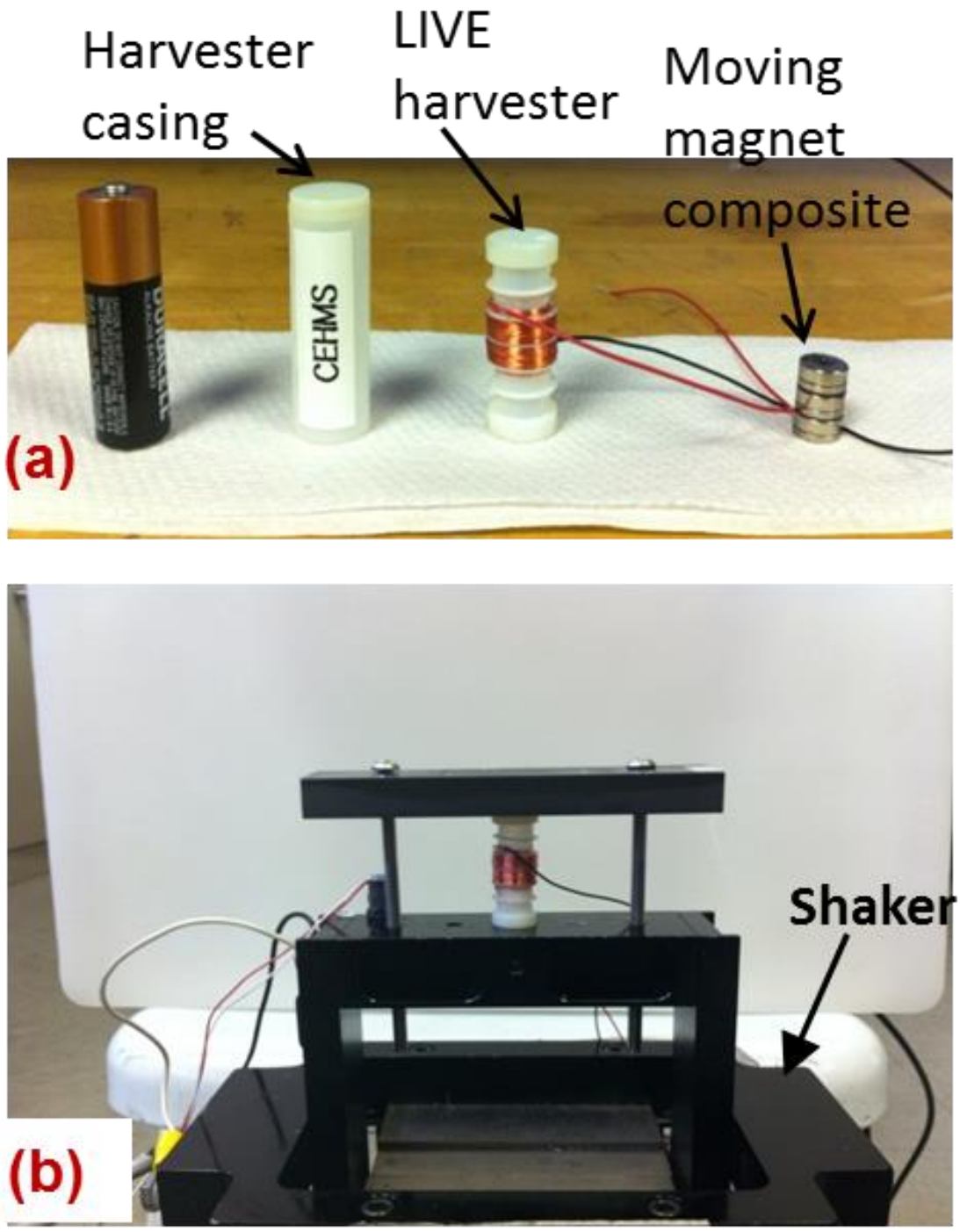

Figure 29: The fabricated LIVE harvester with double-repulsion configuration: (a) beside an AA battery, and (b) in a vibration testing setup

The moving magnet composite was assembled using Loctite® epoxy (Henkel Corp, USA) and clamped together for two days to allow the epoxy set properly. The copper coils were wound in two segments with each segment being wound in a direction different from the other and each having 2800 turns of coil. The total coil resistance was measured to be 2800Ω implying an average of 0.5Ω per turn. The coil wire had a resistance of 14.43Ω/m and a diameter of 44μm. The moving magnet composite was assembled by bonding the stationary magnets to the tube caps using epoxy. The LIVE harvester was tested with a standard energy harvesting setup as shown in Figure 29. A SigLab box was connected to a computer and was used as an input for an accelerometer (attached to the shaker), a laser vibrometer (pointed at the moving magnet composite) and a resistance box (to supply load resistance). The SigLab also provided the voltage response recordings from the harvester.

4.2 Modeling

A finite element model (ANSYS v14) was used to obtain the force field (solid 236 elements) and magnetic flux (solid 96 elements) while a mathematical model was used to simulate the dynamics and voltage response of the harvester. The dynamics of the oscillating moving magnet composites in the three different configurations were mathematically modeled by using a nonlinear spring-mass-damper mechanical system with an external applied base excitation given as:

$$m\ddot{z}(t) + c_m\dot{z}(t) + c_e(t)\dot{z}(t) + kz(t) + k_3z(t)^3 = -m\ddot{y}(t) - mg \tag{78}$$

where m is the moving magnet composite mass, c_m is the mechanical damping constant, $c_e(t)$ is the instantaneous electrical damping, k is the linear stiffness constant of the spring, k_3 is the nonlinear stiffness constant of the spring, z̈(t) is the relative acceleration between the base of the structure ÿ(t) and the vibrating mass ẍ(t), g is the gravitational constant, $\dot{z}$ and z are the velocity and displacement of the moving magnet composite respectively. The acceleration of the vibrating mass ẍ(t) includes the moving magnet and the base of the structure also, i.e. $z(t) = x(t) - y(t)$. Thus the value of z defines the vibration of the moving magnet only. Gravitational force is normally included in the analysis of vibrating nonlinear systems (unlike linear systems) to account for the nonlinear stiffness constant [82]. The nonlinear mathematical spring refers to the repulsion between the moving magnet composite and the stationary magnets and it is related to the instantaneous magnetic repulsion force (F) and the moving magnet displacement by:

$$F(t) = kz(t) + k_3 z(t)^3 \tag{79}$$

This relationship is shown for all three moving magnet configurations in Figure 28e. It can be seen that the double-repulsion configuration is the least stiff of all the three configurations, and that the stiffness of the system (value of k) decreases as the number of magnets in the moving magnet composite increases (with the overall moving magnet height remaining the same). The stiffness terms were estimated by fitting the computational data with a 3rd order non-linear polynomial curve as described by Equation (79). Furthermore, it is clear from the stiffness relations that the configuration of the moving magnet composite

contributes significantly to the stiffness of the entire system. This can be seen from the static magnetic force relation between two repelling cylindrical magnets which is estimated as:

$$F(d) = \frac{\mu_0 M^2 A^2 (h+r)^2}{4\pi h^2}\left[\frac{1}{d^2} + \frac{1}{(d+2h)^2} + \frac{2}{(d+h)^2}\right] \tag{80}$$

where $F(d)$ is the static repulsion force between the magnets, μ_0 is the permeability of the medium between the magnets, M is the magnetization of the magnets, A is the surface area common to both magnets, r is the radius of the magnet with the smaller diameter, h is the average height of the two magnets (or magnet composites) involved, and d is the distance between the magnets. Therefore the repulsion force of the moving magnet composite towards the stationary magnets is smallest in the double-repulsion configuration since the limiting factor as shown in Eq. 3 is the magnetization (M) between the two magnets involved (and magnetization varies with size). For example, the magnetization of the top stationary magnet in the double-repulsion configuration is caused mainly by the top magnet in the moving magnet composite.

In order to solve the dynamic system, the damping terms, c_m and c_e, were obtained and added to the model. The mechanical damping constant is defined by:

$$c_m = 2\zeta_m\sqrt{km} \tag{81}$$

where ζ_m is mechanical damping ratio. The damping ratio can be empirically determined by measuring the amplitude of displacement decay after the moving magnet composite was

initially displaced from its rest position. This approach assumes a linear decay and therefore allows the damping ratio to be obtained from:

$$\ln\left|\frac{A_0}{A_n}\right| = \frac{2\pi n\zeta_m}{\sqrt{\left(1-{\zeta_m}^2\right)}} \tag{82}$$

where A_0 is the first amplitude of motion, n is the decaying cycle. The damping ratio was calculated as 0.047. The electrical damping was estimated from:

$$c_e(t) = \frac{(B(t)\times l)^2}{R_e + R_l} \tag{83}$$

where $B(t)$ is the instantaneous magnetic flux density, l is the length of coil, R_e is the total coil resistance, and R_l is the optimum coil resistance. The B-field values apply to the instantaneous B-field region cutting through the coil. The values of coil length and resistance for the model were based on the configuration in Figure 28d using a coil factor of 0.54. The coil factor is the volume fraction of the coil compartment that is actually occupied by the coil. The total load resistance obtained was 2900Ω and the optimum coil resistance applied was 4000Ω.

The mathematical model was also used to predict the output response of the harvester by discretizing the coil volume and applying looping forms of the equations below:

$$V = \frac{Bl\dot{z}}{R_L+R_e} R_L, \qquad V_{rms} = \sqrt{\frac{1}{n}\sum_{i=1}^{n} V_i^2} \tag{84}$$

$$P = \left(\frac{Bl\dot{z}}{R_L+R_e}\right)^2 R_L \qquad P_{rms} = \sqrt{\frac{1}{n}\sum_{i=1}^{n} P_i^2} \tag{85}$$

where n is the number of discrete points applied.

4.3 Results

4.3.1 Modeling Results

The predicted displacement amplitudes across different frequencies at $0.25g$ base excitation are shown in Figure 30. As shown, the effects of gravity and stiffness were evident in the rest position (mean displacement) of the moving magnet composites. The rest position increased downward as the moving magnet composite was modified from no-repulsion to double-repulsion. However, the maximum amplitude of displacement at resonance was less in the downward direction when compared with the upward direction across all configurations.

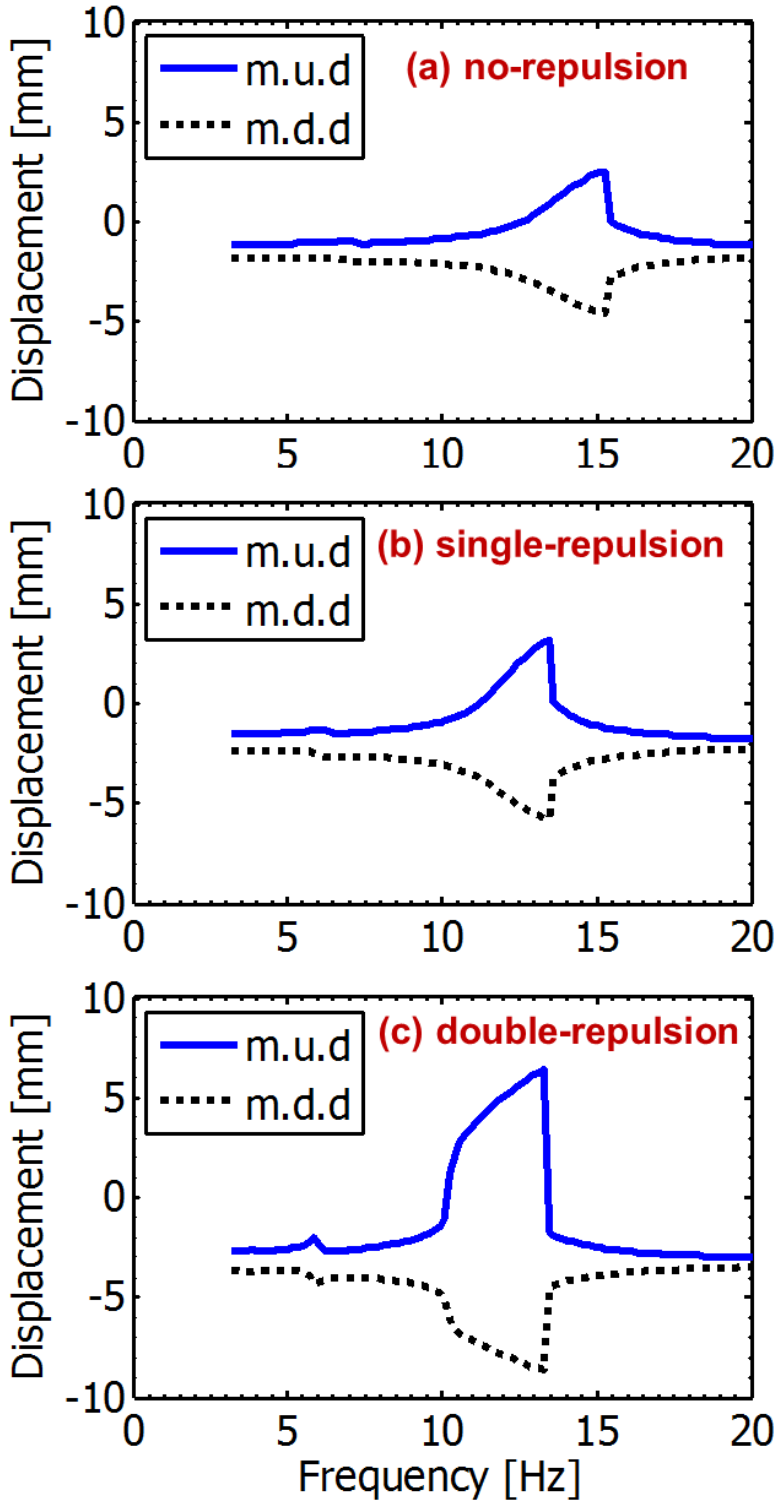

Figure 30: Predicted displacement of the three moving magnet composites at base excitation of 0.25g. m.u.d = maximum upward displacement, and m.d.d = maximum downward displacement. (a) no-repulsion within the moving magnet composite, (b) single-repulsion within the moving magnet composite, and (c) double-repulsion within the moving magnet composite.

This was more pronounced in the double-repulsion configuration, and it was due to the difference in the instantaneous repulsion force between the moving magnet composite and the stationary magnets as described in Equation (80) (because of the rest position of the moving magnet composite). Overall, the double-repulsion configuration exhibited the highest displacement amplitude at resonance.

The predicted resonance frequencies across all configurations showed a decreasing pattern from no-repulsion to double-repulsion as shown from their velocity profiles (at 0.25g base excitation) in Figure 31a. The decrease was more pronounced between the no-repulsion and single-repulsion configurations. The average values of radial magnetic flux (*B*-field) around the moving magnet composites are shown in Figure 31c. The sampled cross-sectional area was between 14mm od and 11mm id to specifically target the 'shedding' region of the magnetic flux, and the radial *B*-field was analyzed across 24mm height. The location of the coil was limited by the fact that the moving magnet composite required radial spacing to vibrate vertically without significant friction from the tube. As seen from the figure, the no-repulsion configuration has the weakest *B*-field profile. The single-repulsion configuration has one strong *B*-field region, but the most efficient (or optimized) height of the coil compartment for the single-repulsion configuration cannot be as easily determined as in the double-repulsion case. This is because the height of each coil segment in the double repulsion case must equal the height of one magnet in the moving magnet composite to avoid voltage cancellation effects. The double-repulsion configuration has two strong *B*-field regions which can be targeted by two coil segments placed close to each other (and wound in opposite directions) thus creating an efficient coil/magnet configuration. Small-sized LIVE harvesters require small magnet thicknesses and can be difficult to fabricate, thus imposing

a limitation on the number of magnets in the moving magnet composite. It is possible to increase the number of magnets in the moving magnet composite (for large harvesters), but such increase would cause a decrease in the magnetic flux density and shift the regions of strong magnetic field (due to repulsion) toward the moving composite and away from the coils, thus severely decreasing the energy harvesting potential of the device.

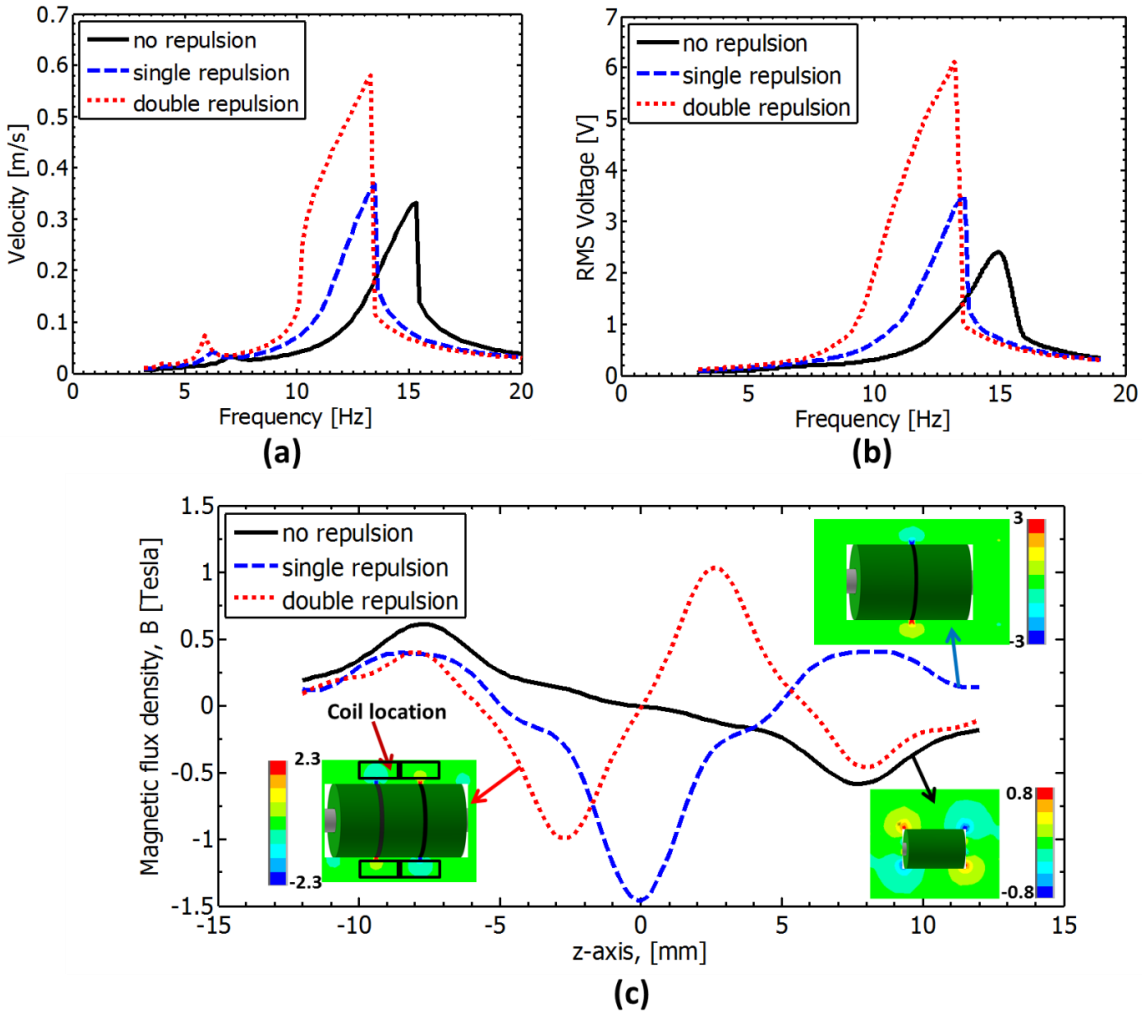

Figure 31: (a) Predicted velocity profiles across all three moving magnet configurations at base excitation of 0.25g, (b) Predicted RMS voltage response across all three moving magnet configurations at base excitation of 0.25g, and (c) Predicted average radial magnetic flux density around the moving magnet composites. Sampled cross sectional area was between 14mm od and 11mm id.

As seen in the magnetic flux profile, the summation of the magnetic flux values (when the moving magnet is at its rest position) produced a net value only in the single-repulsion case. As a result, the electrical damping term (as outlined in Equation (87)) impacted the single-repulsion configuration significantly more than the no-repulsion and double-repulsion configurations. Moving magnet composites with an even number of magnets will be affected by a higher electrical damping than those with an odd number of magnets. However, the electrical damping effect reduces as the number of magnets in the moving magnet composite increases (for odd number composites). The negative impact of the electrical damping is shown in the velocity profile (Figure 31a). The resonance frequency of the single-repulsion configuration was significantly reduced but the velocity was also negatively impacted by the electrical damping. The velocity was thus highest in the double-repulsion configuration therefore suggesting a higher voltage response for the same amount of coil around the magnets.

The velocity was crucial in estimating the voltage (V) and power (P) response as expressed in Equations (89) & (90). The voltage increases with velocity while the power response varies with the square of the velocity. Again, the B-field values used to obtain the voltage and power response applies to the instantaneous B-field region cutting through the coil. The predicted values of the root-mean-square (RMS) voltage show similar trends when compared with the velocity profile, therefore validating the effect of the electrical damping term, and the linear relationship between velocity and the B-field.

From the modeling results, some important factors for optimum LIVE harvester performance (for a given tube size) were observed as listed in Table **8**. Low frequency, increased displacement and velocity can all be attained by increasing the repulsion

configuration (to double-repulsion) in the moving magnet composite. Also, decreasing the ratio of moving magnet size to stationary magnet size would positively impact the dynamics of the harvester. For the voltage and power response, the coil should be placed strategically to target the regions of high *B*-field and also adjusted for the rest position of the moving magnet composite. Limiting the friction on the outer and inner regions of the moving magnet composite positively impacts the electrical response. Furthermore, the use of a center pole in the tube to longitudinally align the axis of the moving magnet with the stationary magnets ensures that the radial magnetic flux lines are properly aligned with the coils.

Table 9: Important factors for optimum LIVE harvester performance

Criteria	Important factor
Improved dynamics (low frequency, increased displacement amplitude and increased velocity)	1. Increase repulsion configuration. 2. Decrease moving-to-stationary magnet size ratio.
Improved output response (voltage and power)	1. Centralize coil location with moving magnet rest position. 2. Target regions of high *B*-field with coils. 3. Reduce friction on the outer and inner regions of the moving magnet. 4. Use a center pole (in the tube) to longitudinally align the axis of the moving magnet to the stationary magnets.

4.3.2 Experimental Results

A load optimization test was conducted by applying a varying load resistance to the coil and monitoring the RMS voltage and power response as shown in Figure 32a & b. The optimum load resistance was approximately 3800Ω and it was applied via a resistor for the output response experiments.

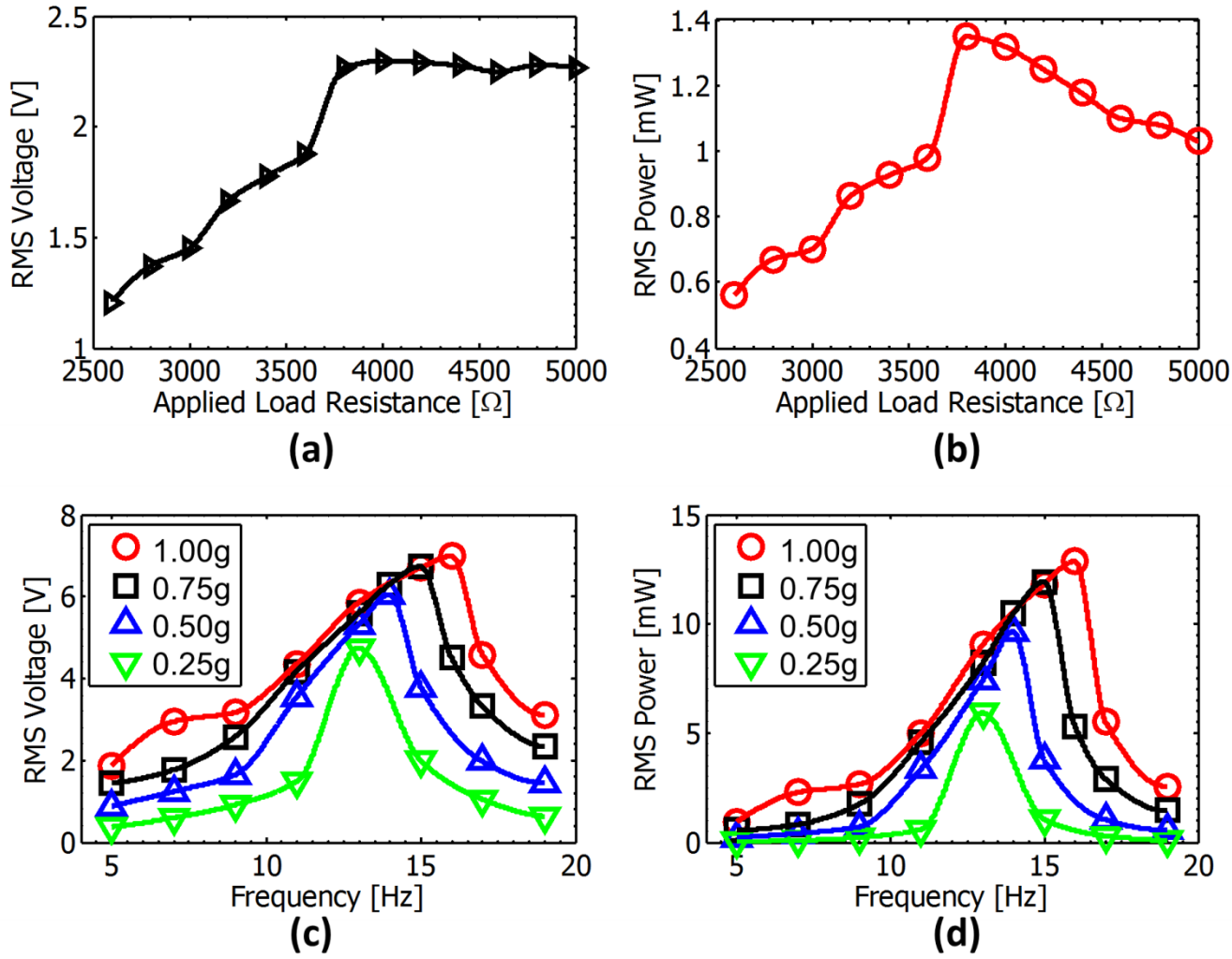

Figure 32: Experimental results. (a) RMS voltage as a function of the applied load resistance at 11Hz (off resonance) and 0.25g (b) RMS power as a function of the applied load resistance at 11Hz (off resonance) and 0.25g, (c) RMS voltage response of the LIVE harvester across different base excitations as a function of frequency (at peak load of 3800Ω), (d) RMS power response of the LIVE harvester across different base excitations as a function of frequency (at peak load of 3800Ω).

From the plots of the closed circuit RMS voltage and power variations shown in Figure 32c & d, the harvester exhibited a broadband response across a wide range of base accelerations. The resonance frequencies were approximately 13Hz at 0.25*g*, 14.03Hz at 0.5*g*, 15.05Hz at 0.75*g*, and 16Hz at 1*g*. Thus the increase in base acceleration causes a slight

increase in the resonance frequency. Also, the RMS voltage output values were approximately 4.7V at 0.25*g*, 6.1V at 0.5*g*, 6.75V at 0.75*g*, and 7V at 1*g*. The voltage response was therefore significantly greater than the 1.5V produced at peak non-depleted performance by a standard AA-battery. In comparison with the modeling results shown in Figure 31b, the experimental voltage response at 0.25g is consistently within 7% error. The only exception is at resonance where the sharp voltage peak in the model was not captured experimentally. The experimental RMS power response as shown in behaves in the same way as the voltage response. The harvester produced a RMS power output of 5.9mW at 0.25*g*, 9.7mW at 0.5*g*, 12mW at 0.75*g*, and 12.9mW at 1*g*.

The LIVE harvester was also compared with current state of the art electromagnetic harvesters as shown in Table 10. For low frequency energy harvesting, the harvester exhibits comparatively high power output with increasing base excitation (12.9mW at 1*g* and 16Hz). However, the normalized power density is significantly higher than similar electromagnetic harvesters, especially at low base excitation (15.33mWcm$^{-3}g^{-2}$ at 0.25*g* and 13Hz).

4.3.3 Charging a Cellphone

To provide insight into the capability of the harvester for energy harvesting from human motion (such as running, walking, and hand movements), the harvester was shaken by hand to generate the voltage. The harvester was first tested by connecting it to the SigLab setup (Figure 33a) and the voltage response was recorded as shown in Figure 33b. The raw alternating voltage from the harvester had maximum amplitude of 14 V and the overall waveform corresponded to a frequency of approximately 7.4 Hz and RMS voltage of 4.7V. It can be seen therefore that despite being shaken below resonance frequency (~ 16Hz), the

harvester's broadband nature enabled significant voltage response. The exhibited frequency (when compared with Figure 32c) occurred slightly above 1g acceleration and was slightly higher than observed in a human sprinter's motion (approximately 4 - 5Hz). Figure 33c shows the external charging circuit designed for the harvester. It was built and used to supply constant 5V DC and 500mA to charge a cellphone via hand motion as shown in Figure 33d. The circuit was designed to convert AC to DC voltage, and supply the DC voltage to the cellphone when it is within the range of $5\text{V} \pm 0.4\text{V}$.

Table 10: Comparison of reported power densities in electromagnetic harvesters

Researcher	Frequency (Hz)	Base excitation (g)	Power (mW)	Normalized power density ($\text{mWcm}^{-3}.g^{-2}$)
Cepnik *et al.* (2011)	50	1	20.6	1.01
Byung-Chul *et al.* (2012)	16	0.2	1.52	1.07
Hatipoglu *et al.* (2009)	24.4	15	0.4	0.017
Ching *et al.* (2002)	110	9.74	0.83	0.0087
Shuo *et al.* (2010)	9.2	0.8	0.55	0.023
Saha, O'Donnell [8]	2.75	1	2.46	0.194
Beeby, Torah [29]	52	0.06	0.005	4.5×10^{-8}
Marin *et al.* (2013)	50	0.2	25.5	0.541
Marin *et al.* (2012)	168	0.7	19	0.347
von Büren *et al.* (2007)	20	-	0.025	0.0096
Wang, Liu [89]	280	0.82	0.00212	0.101
Pan *et al*. (2006)	60	-	0.1	0.86
This work	13	0.25	5.9	15.33
This work	16	1	12.9	2.09

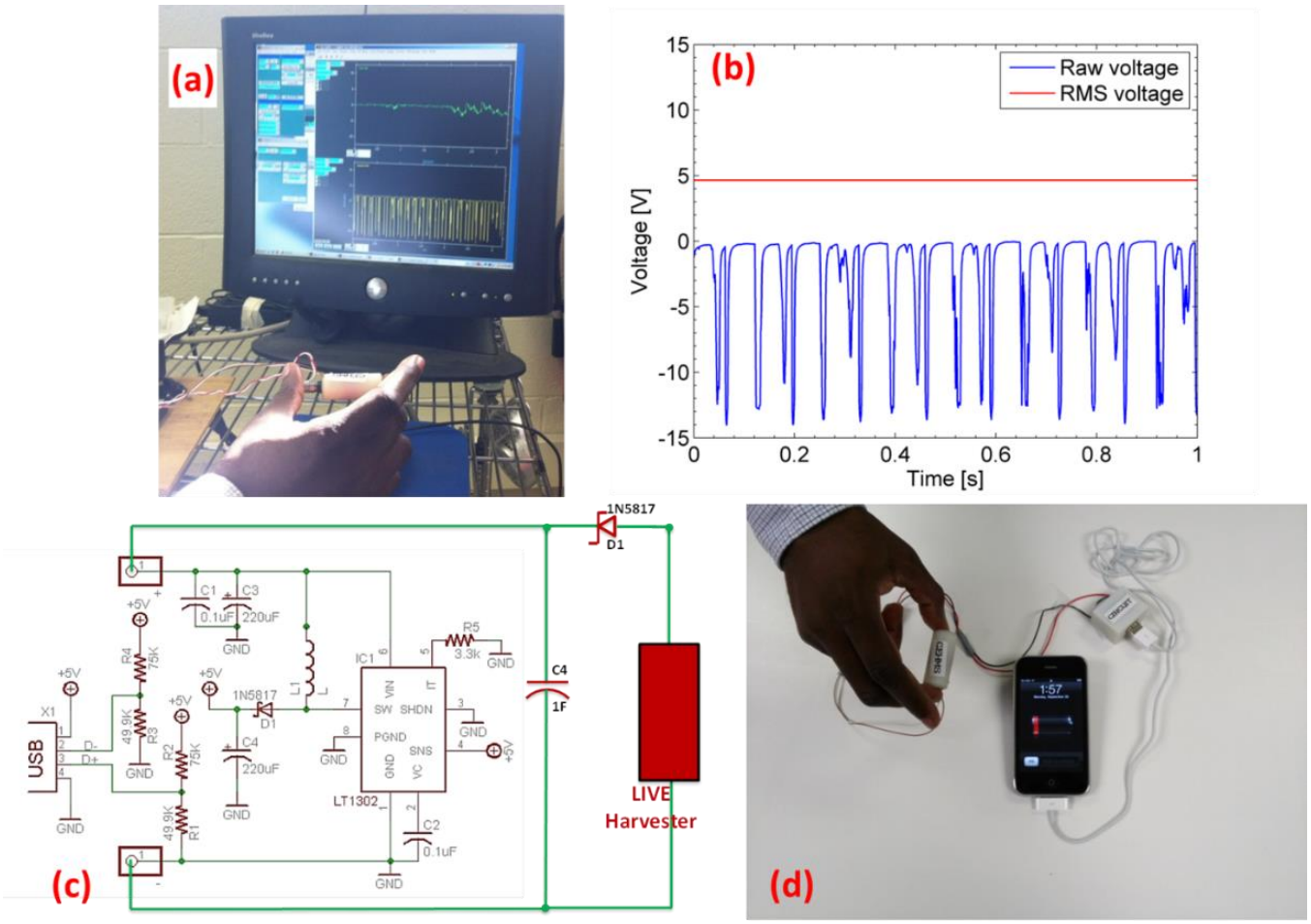

Figure 33: Harvester demonstration. (a) Hand-controlled harvester in voltage testing setup (b) Voltage response from the harvester being shaken by hand at a frequency of 7.4Hz (c) External charging circuit for the harvester (d) Harvester being used to charge a cellphone.

4.4 Chapter Conclusion

An AA battery-sized harvester was modeled, fabricated and tested. The harvester employed a double-repulsion configuration in the moving magnet composite which allowed for easy coil/magnet optimization. The double-repulsion configuration exhibited the lowest frequency, the highest displacement amplitudes and the largest velocity when compared to the no-repulsion and single-repulsion configurations. Furthermore, the double-repulsion

configuration exhibited two strong regions of high magnetic flux which enabled efficient coil placement and significant voltage output. The double-repulsion LIVE harvester was found to exhibit RMS power output values of 5.9mW at 0.25g and 12.9mW at 1g. The harvester was also used to power a cellphone by supplying constant 4.7V when shaken by hand.

5 Chapter 5:

LIVE Harvester Scaling Analysis and Micro LIVE Harvester Characterization

5.1 LIVE Harvester Scaling Analysis

In the past decade, magnetic levitation systems which are based on electromagnetic induction have been shown to provide a promising solution for low frequency-low excitation vibration energy harvesting [78, 91]. The power densities exhibited by these systems have also been shown to be significantly higher than other forms of energy harvesting such as piezoelectric cantilevers at length scales larger than the micro scale. The harvesters also exhibit a nonlinear stiffness profile due to the repulsive force between magnetic poles that varies as the square of the distance between them. This leads to a broadband behavior which reduces the energy harvesting dependence on the resonance frequency.

Based on reported literature, a very promising form of energy harvesting from magnetic levitation involves the levitation of a magnet or magnet composite between two stationary magnets [8, 76, 77]. We previously reported (in chapter 4) a highly efficient form of this concept by modeling, fabricating, and testing a harvester with a double-repulsion configuration in the levitated magnet composite [92]. The harvester exhibited better dynamics (displacement and velocity) and output response (voltage) than other analyzed harvester configurations.

The analysis carried out in this section focuses on scaling analysis based on the previously reported harvester. Four harvesters were varied in height across three orders of magnitude based on the distance between stationary magnets (0.36mm, 3.6mm, 36mm, and 360mm), and were analyzed based on their magnetic field, dynamics and energy output responses to a scaled range of applied base accelerations ($0.01g$, $0.1g$, $1g$, and $10g$), where $1g = 9.8\text{m/s}^2$. The magnetic flux density, which impacts the output response of the harvester, was shown to be similar across all analyzed length scales. However, the increased scaling was shown to impact the magnetic force field in two different ways: the linear stiffness coefficient increased while the nonlinear stiffness decreased. Furthermore, the velocity and resonance frequency were shown to decrease with increased scaling by size. The resonance frequency however increased with increased scaling of the applied acceleration. The voltage and power responses were shown to increase with increasing acceleration and increasing length scale.

5.1.1 Design and Modeling

The designs of the harvesters in this section are based on a previously reported experimentally characterized (and modeled) harvester that generated 13mW power output in response to applied base acceleration of $1g$ [92]. The design involves placing a magnet composite between two stationary magnets which repel it. The uniqueness of the harvester is in the double-repulsion configuration of its moving magnet composite as shown in Figure 34. The moving magnet composite is comprised of three permanent magnets separated by two steel dividers (discs). This configuration was shown to limit electrical damping due to

the coils, increase the velocity and displacement, and lower the resonance frequency. Furthermore, the configuration allowed effective coil placement in the harvester. The overall effect was observed in the improved energy response (voltage and power) of the harvester.

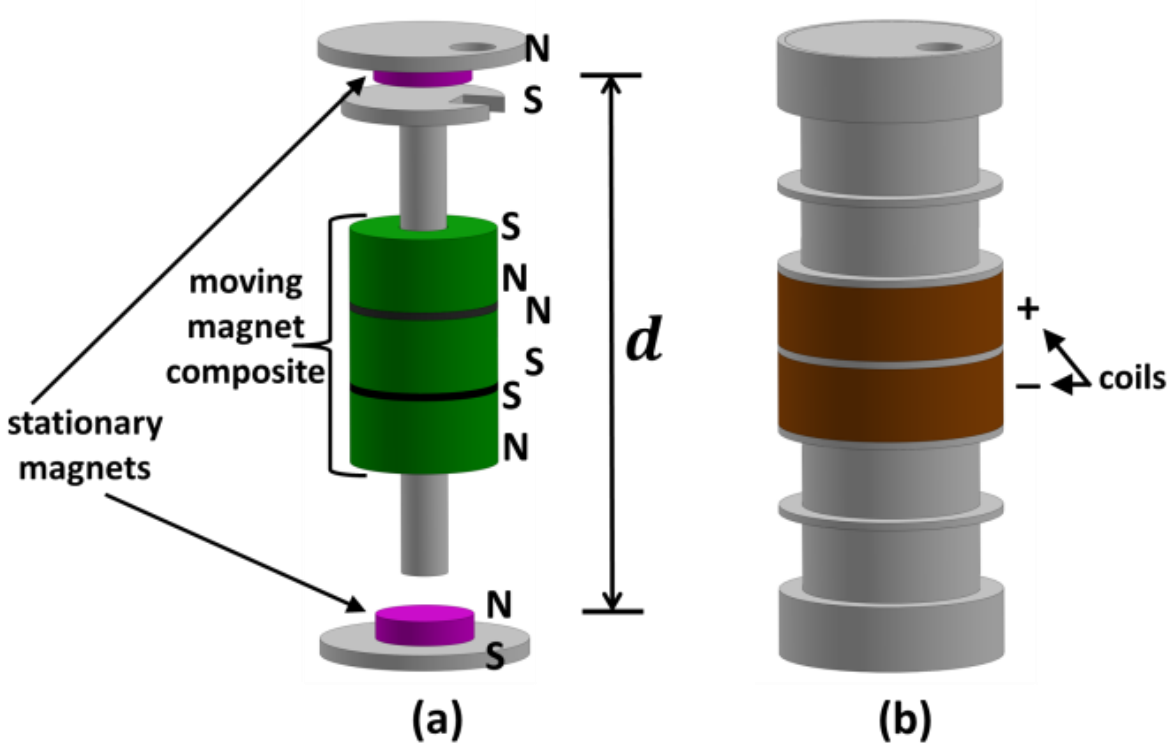

Figure 34: Double-repulsion LIVE harvester configuration: (a) magnet configuration with three magnet discs and two steel discs in the moving magnet composite, and (b) harvester casing and coils.

The spacing between the stationary magnets, d, in the experimental harvester was 36mm. The other properties and details of this harvester (modeling and experiments) are detailed in chapter 4 and Apo *et al.* [92]. The four harvesters modeled in this study have spacing equal to $d = 0.36\text{mm}, 3.6\text{mm}, 36\text{mm}, \text{and } 360\text{m}$ respectively. Therefore the harvesters are separated by increasing order of magnitude in size: the harvesters and all their components (coils, magnets, casing, etc.) are also scaled uniformly by increasing order of magnitude.

The harvester modeling is same as detailed in the previously reported harvester model – a nonlinear spring-mass-damper mechanical system with an externally applied base excitation:

$$m\ddot{z}(t) + c_m\dot{z}(t) + c_e(t)\dot{z}(t) + k_1 z(t) + k_3 z(t)^3 = -m\ddot{y}(t) - mg \tag{86}$$

where m is the moving magnet composite mass, c_m is the mechanical damping constant, $c_e(t)$ is the instantaneous electrical damping, k_1 is the linear stiffness constant of the spring, k_3 is the nonlinear stiffness constant of the spring, z̈(t) is the relative acceleration between the base of the structure ÿ(t) and the vibrating mass ẍ(t), g is the gravitational constant, $\dot{z}$ and z are the velocity and displacement of the moving magnet composite respectively. The acceleration of the vibrating mass ẍ(t) includes the moving magnet and the base of the structure also, i.e. $z(t) = x(t) - y(t)$. Thus the value of z defines the vibration of the moving magnet only. Equation (86) depicts the behavior of a typical Duffing oscillator with an added time-dependent electrical damping term. The full model is robust enough to capture the time and frequency-based dynamics and energy outputs of the harvesters.

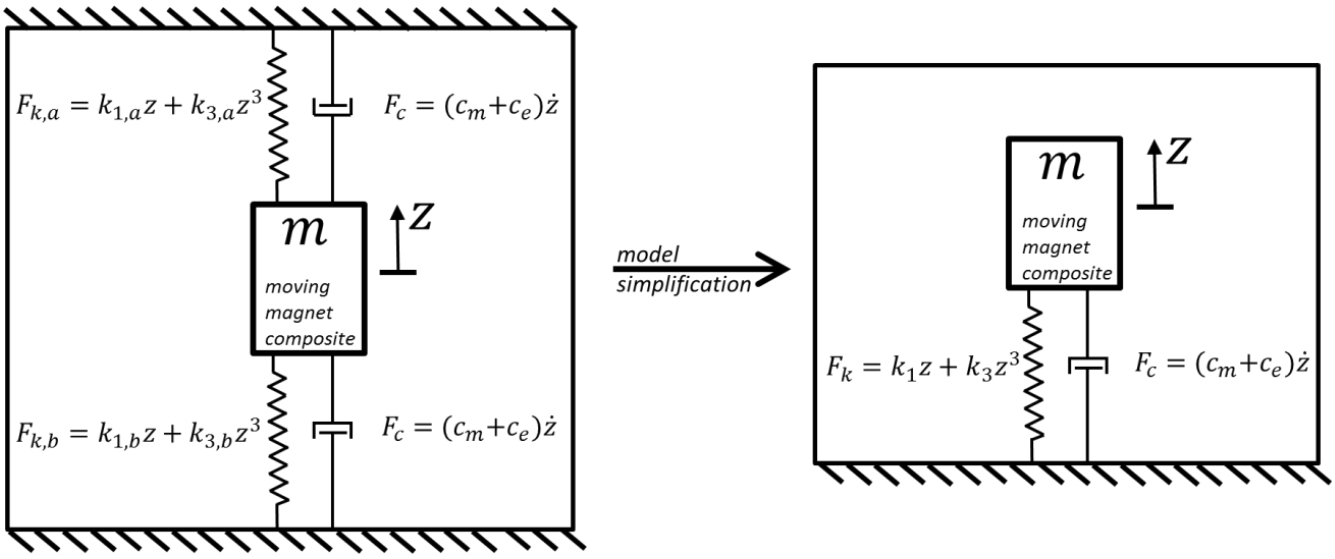

Figure 35: Dynamic modeling schematic of the LIVE harvesters

Figure 35 shows the dynamic modeling schematic of the harvester which is described using the magnetic and damping forces present. The magnetic repulsion of the moving magnet composite towards the stationary magnets is modeled as a force, F_k, dependent on a nonlinear spring. The repulsion forces of both stationary magnets towards the moving magnet composite are similar. Thus, they can be combined (taking into account cancelation effects) into a single spring to form a simplified model. The mechanical damping, c_m, is not dependent on the repulsion forces, but on the ambient air conditions and friction from the harvester materials. Therefore, the mechanical damping is constant as seen in the full and simplified models. The time-dependent electrical damping, $c_e(t)$, which is due to the feedback from the coils (not shown in the schematic) indirectly impacts the dynamics of the moving magnet composite when it passes through the coils.

5.1.2 Magnetic fields and Dynamics

It is important to understand the effects of scaling on the magnetic flux and force fields to help better understand harvester behavior. The magnetic flux field impacts the electrical damping which in turn affects the harvester dynamics since

$$c_e(t) \propto B(t) \tag{87}$$

where $B(t)$ is the instantaneous magnetic flux density. However, as previously explained, the electrical damping in the case of the double-repulsion configuration is almost negligible. Furthermore, the magnetic flux field also impacts the energy response of the harvester since

$$V \propto B \quad \text{and} \quad P \propto B^2 \tag{88}$$

where V is the voltage response and P is the power response. As shown in Figure 36a, the magnetic flux densities (B-field) are very similar across different scales. There are two important design factors which ensure this result: the uniformly scaled steel divider height between the magnets in the moving composite, and the uniformly scaled radial distance between the moving composite and coil. Therefore it is important to understand the magnetic pole saturation conditions in the harvesters [93]. Since the $d = 36$mm configuration has the optimum steel divider height, the magnetic flux profiles imply the smaller harvesters ($d = 0.36$mm and 3.6mm) have saturated poles in the moving magnet composite while the largest harvester ($d = 360$mm) has unsaturated poles. Also, the reduced radial distance in the smaller harvesters means the coils are closer to the moving magnet composites and this causes an increase in the B-field to the point of matching the B-

field of the $d = 36$mm harvester. The $d = 360$mm harvester can therefore exhibit a stronger B-field profile if the steel divider height is reduced (until saturation) and the radial distance between the moving composite and coil is reduced.

The magnetic force profiles shown in Figure 36b show a linear response to scaling. The linear stiffness coefficient (k_1) increases by order of magnitude with increasing order of magnitude of d. However, the nonlinear stiffness coefficient (k_3) decreases by order of magnitude with increasing order of magnitude of d.

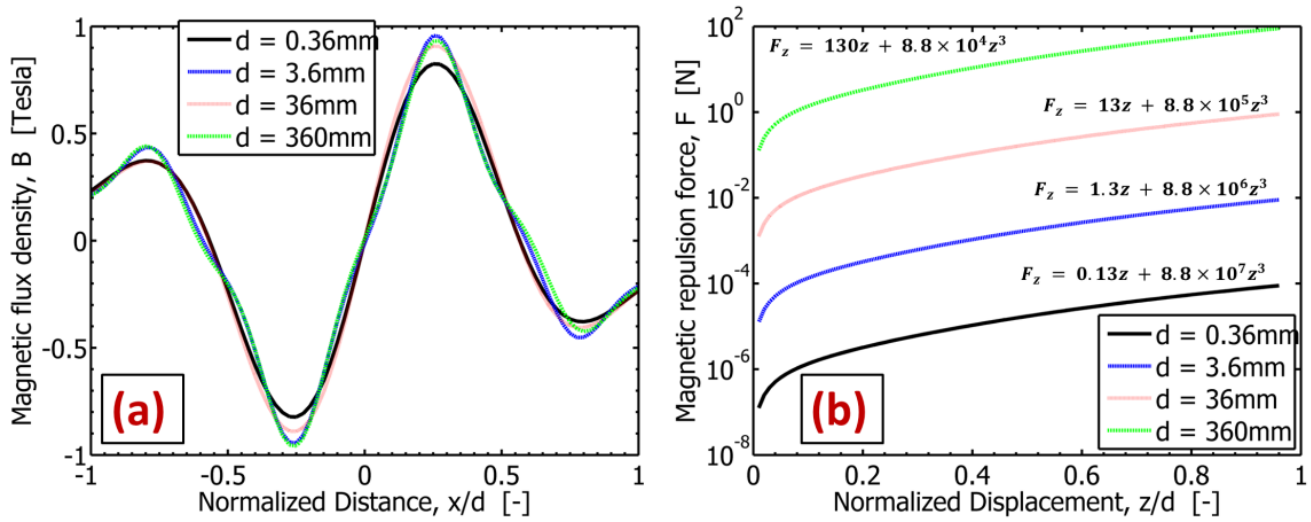

Figure 36: Magnetic field characteristics of the harvesters: (a) magnetic flux density as a function of normalized distance within the harvester with the moving magnet composite at its rest position, and (b) magnetic force field as a function of normalized displacement in the upward ($+z$) direction.

The effect of the magnetic force fields and the mass of the moving magnet composite can be observed as shown in Figure 37. Despite the increase in linear stiffness with increasing length scale, the concurrent increase in the mass of the moving magnet composite ensures the resonance frequency decreases with increasing length scale regardless of the applied base acceleration. The peak velocity also decreases with increasing scale as expected due to

the decreased spacing between stationary magnets. As the applied base acceleration is increased by order of magnitude (from $0.01g$ to $10g$), the velocities also increase roughly by order of magnitude. Scaling the applied acceleration also causes a slight increase in the resonance frequencies of the harvesters as well as increased nonlinear behavior leading to increased bandwidth available for energy harvesting.

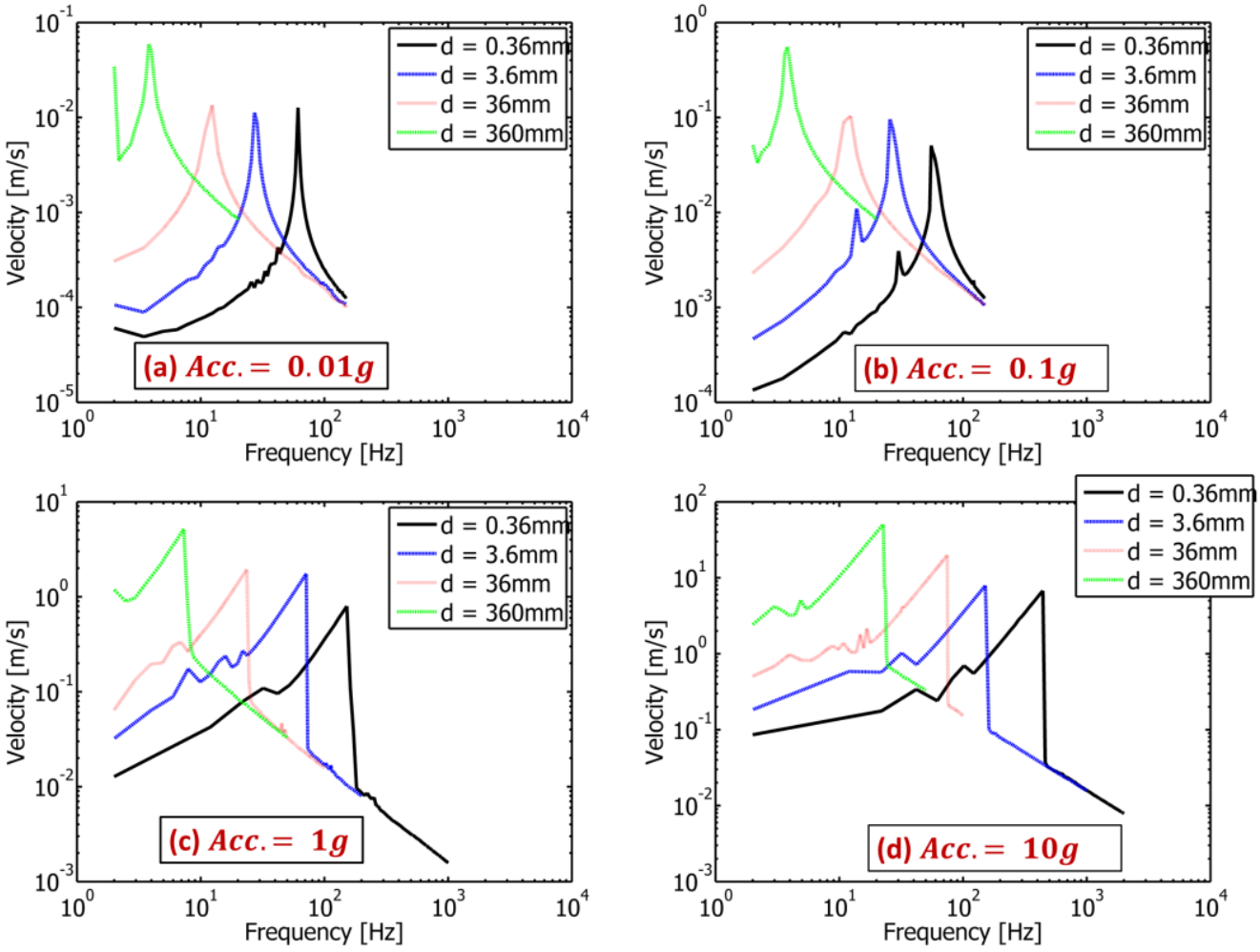

Figure 37: Dynamic (velocity) response of the harvesters to applied base acceleration as a function of frequency ($1g$ = 9.8m/s^2).

It should be noted that the extreme accelerations have obvious disadvantages. At $0.01g$, the friction within the harvester may overcome or severely dampen the motion of the moving magnet composite. At $10g$, the kinetic force due to the motion of the moving magnet composite is likely to overcome the magnetic repulsion force and thus cause the moving magnet composite to hit the stationary magnets during operation of the harvester.

5.1.3 Energy Output

The energy responses of the harvesters are dependent on the coil and optimum resistances ($\boldsymbol{R_e}$ and $\boldsymbol{R_l}$) as well as the dynamics and $\boldsymbol{B}$-fields. The values of voltage and power and voltage and power can be estimated from:

$$V = \frac{Bl\dot{z}}{R_L+R_e}R_L, \qquad V_{rms} = \sqrt{\frac{1}{n}\sum_{i=1}^{n} V_i^2} \tag{89}$$

$$P = \left(\frac{Bl\dot{z}}{R_L+R_e}\right)^2 R_L \qquad P_{rms} = \sqrt{\frac{1}{n}\sum_{i=1}^{n} P_i^2} \tag{90}$$

where $\boldsymbol{l}$ is the length of the coil, $\boldsymbol{n}$ is the number of discrete time-based points applied, and RMS is the root-mean-square value.

The voltage response predictably increases with increasing base acceleration as shown in Figure 38. However, the smaller harvesters ($\boldsymbol{d} = \mathbf{0.36}$mm and $\mathbf{3.6}$mm) constantly exhibit very low voltage output. This result follows the commonly reported trend of low energy response from micro scale electromagnetic harvesters [47]. This poor response is mostly due to the small length of coil combined with limited space for motion (displacement and velocity of the moving magnet composite) within the micro scale harvesters. The larger harvesters

($\boldsymbol{d} = \mathbf{36}$mm and $\mathbf{360}$mm) however exhibit appreciable voltage responses even at extremely low accelerations due to appreciable velocity and coil length.

Furthermore, the resonance values of RMS voltage for any given acceleration decreases by 3 to 4 orders of magnitude as the value of $\boldsymbol{d}$ is scaled by one order of magnitude. In comparison with the experimental harvester ($\boldsymbol{d} = \mathbf{36}$mm), the model slightly overestimates the natural frequency (19Hz vs. 16Hz) mainly due to increased friction in the experimental harvester, but it accurately estimates the RMS voltage response.

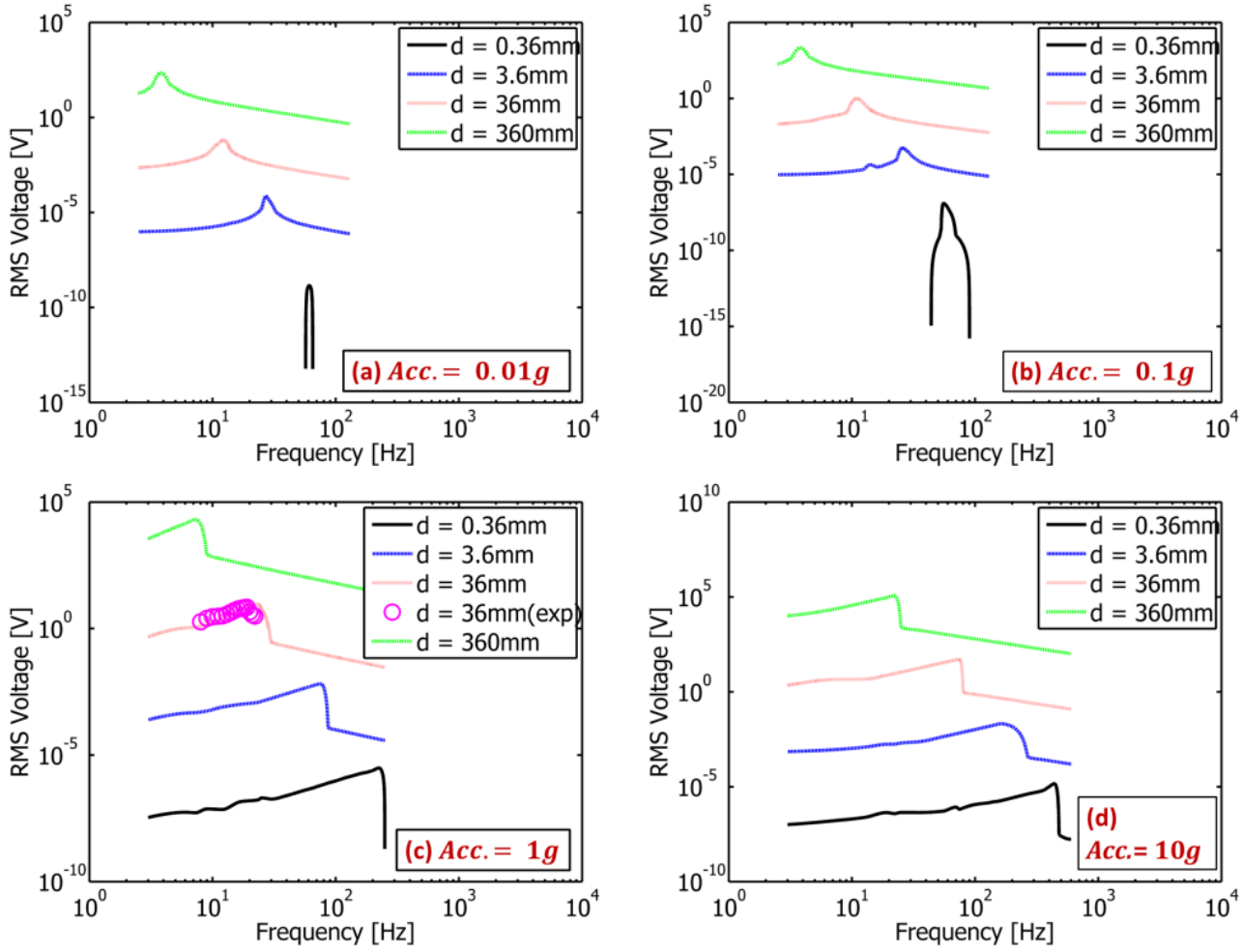

Figure 38: RMS Voltage response of the harvesters to applied base acceleration as a function of frequency ($1g$ = 9.8m/s²). exp = experimental results.

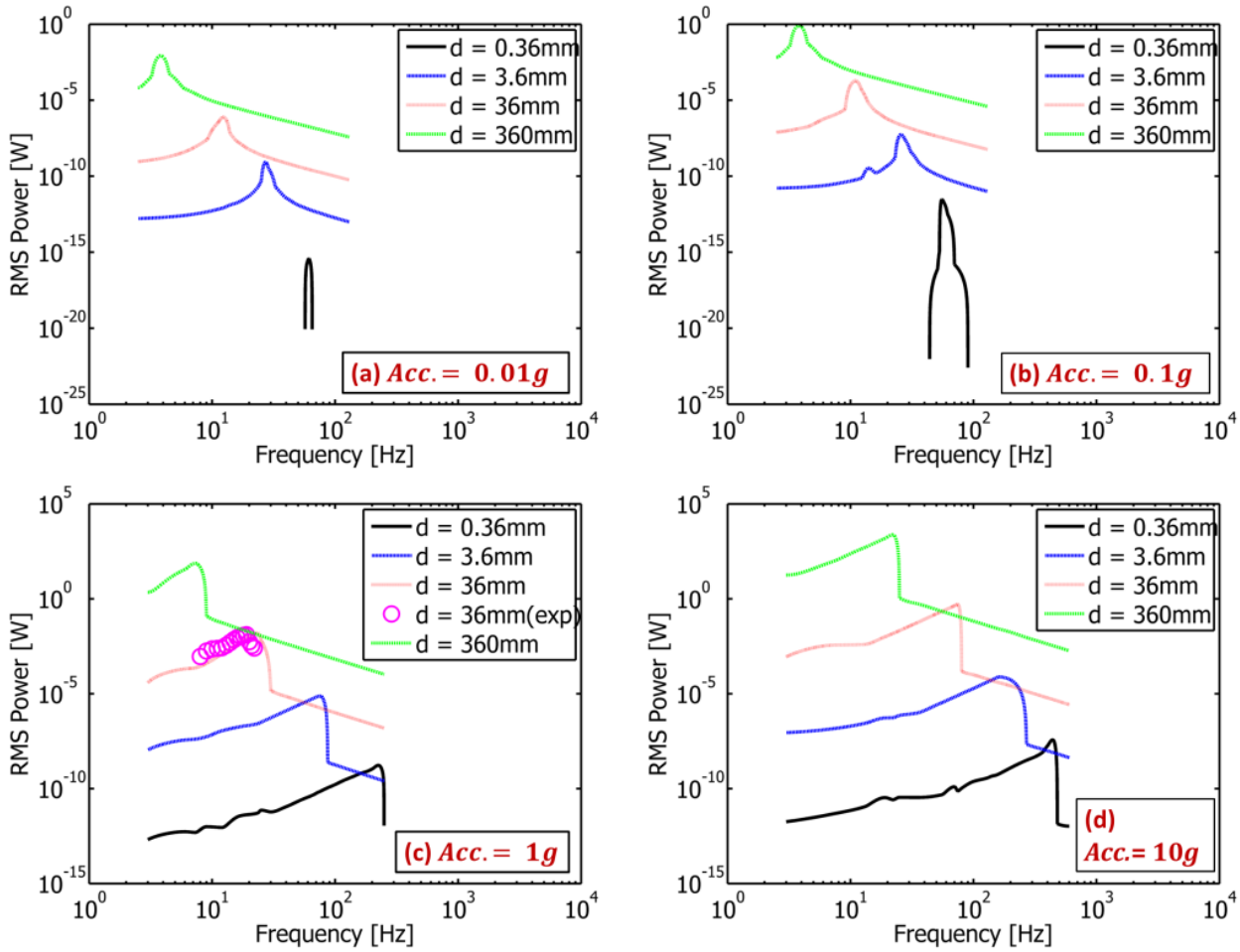

Figure 39: RMS Power response of the harvesters to applied base acceleration as a function of frequency ($1g$ = 9.8m/s^2). exp = experimental results.

The useful power output of the harvesters depends on the useful voltage response as well as the coil and optimum resistances. Therefore the largest harvester (d = 360mm) is mostly impacted due to the high resistances present. The RMS power for any given acceleration decreases by 2 or 4 orders of magnitude as the value of d is scaled by one order of magnitude, with the difference of 2 orders of magnitude only occurring between the two largest harvesters. In comparison with the experimental harvester (d = 36mm), the model

accurately predicts the RMS power response. As expected, the useful power response for all harvesters increases with increasing base acceleration.

5.2 MEMS Levitation-Induced Vibration Energy Harvester with Nonlinear Inflection Profile

In this section, a MEMS electromagnetic harvester was designed with high permeability material (metglas) being used as coil guides (and magnetic field amplifier). The geometric design of the magnet composite and coil is similar to the AA battery-sized harvester discussed in chapter 4. The analysis covers the characteristics of this harvester and compares it with a similar design which is devoid of the guides.

5.2.1 Concept

The design configurations of the harvesters are shown in Figure 40 depicting the harvester structure and the two variations that were characterized. As shown in Figure 41 and Table 11, the characterized LIVE MEMS electromagnetic harvesters were designed to fit within a space restriction of 10mm x 10mm x 10mm.

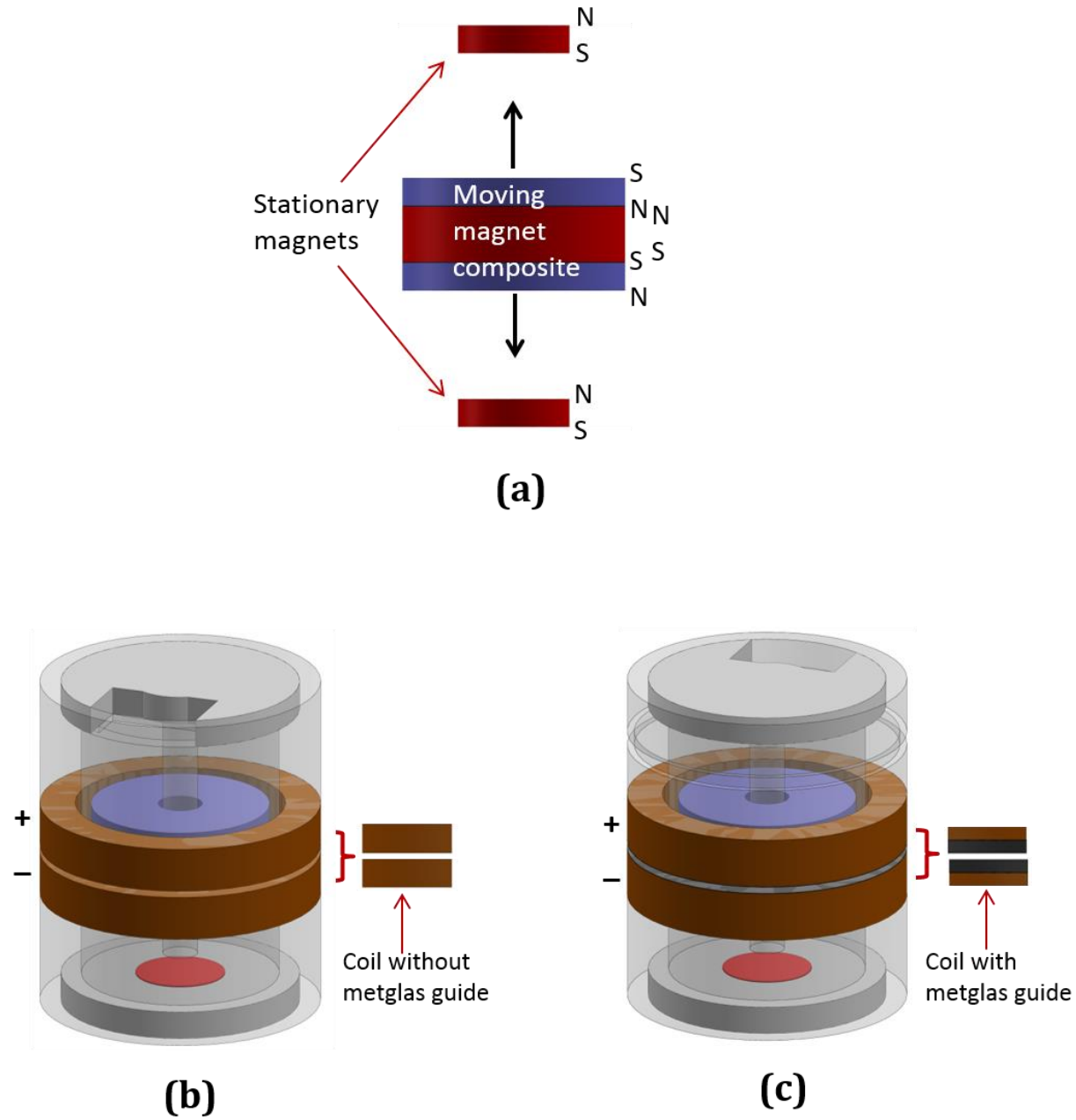

Figure 40: Harvester design: (a) magnet configuration, (b) harvester without coil guides, and (c) harvester with coil guides.

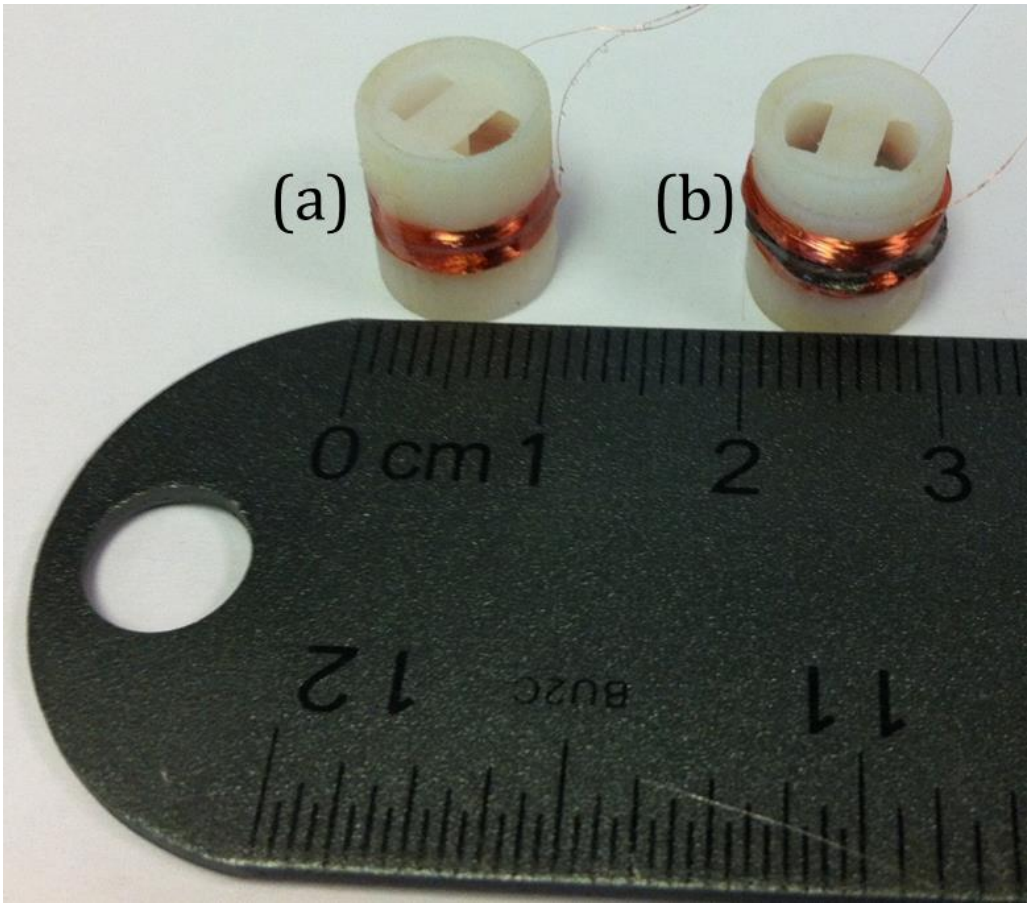

Figure 41: Fabricated harvester casings: (a) harvester without coil guides, and (b) harvester with coil guides.

Table 11: Dimension and materials of the LIVE harvester components (all configurations)

Component	Properties
Harvester casing dimensions (mm)	10 od x 7.1 id x 10 long
Magnet material	NdFeB N52
Moving magnet composite dimensions (mm)	6.4 od x 1.6 id x 3.2 thick
Metglas spacer dimensions (mm)	6.4 od x 1.6 id x 0.025 thick
Metglas guide dimensions (mm)	10 od x 7.5 id x 0.025 thick
Stationary magnet dimensions (mm)	3.2 od x 0.8 thick
Coil material	copper
Each coil segment (mm)	10 od x 7.5 id x 1.5 thick
Coil resistance	14.43 ohm/m
Coil diameter (mm)	44μm

5.2.2 Modeling

The dynamics of the oscillating moving magnet composite has been modified to include a magnetic damping (or eddy current damping) term. Again, the harvester was mathematically modeled by using a nonlinear spring-mass-damper mechanical system with an external applied base excitation given as:

$$m\ddot{z}(t) + \left(c_m + c_{mag} + c_e\right) \times \dot{z}(t) + kz(t) + k_3 z(t)^3 = -m\ddot{y}(t) - mg \tag{91}$$

where m is the moving magnet composite mass, c_m is the mechanical damping constant, c_{mag} is the newly added magnetic damping term, $c_e(t)$ is the instantaneous electrical damping, k is the linear stiffness constant of the spring, k_3 is the nonlinear stiffness constant of the spring, z̈(t) is the relative acceleration between the base of the structure ÿ(t) and the vibrating mass ẍ(t), g is the gravitational constant, $\dot{z}$ and z are the velocity and displacement of the moving magnet composite respectively.

5.2.3 Results

The magnetic force field of the MEMS electromagnetic harvester shows a softening spring behavior as shown in Figure 42. This profile is a major departure from the usually observed magnetic force fields in similar harvesters (usually hardening springs). As shown in Figure 43, the presence of metglas guides creates spikes in the magnetic flux field profile, thereby suggesting an increase in the overall power response of the harvester. From Figure 44 and Figure 45, the dynamics of the harvester is not affected by the metglas guides. However, as observed in Figure 46 and Figure 47, the metglas guides caused a significant

increase in the voltage and power response of the harvester giving 0.32V peak voltage and 0.27 mW peak power responses at resonance (16Hz).

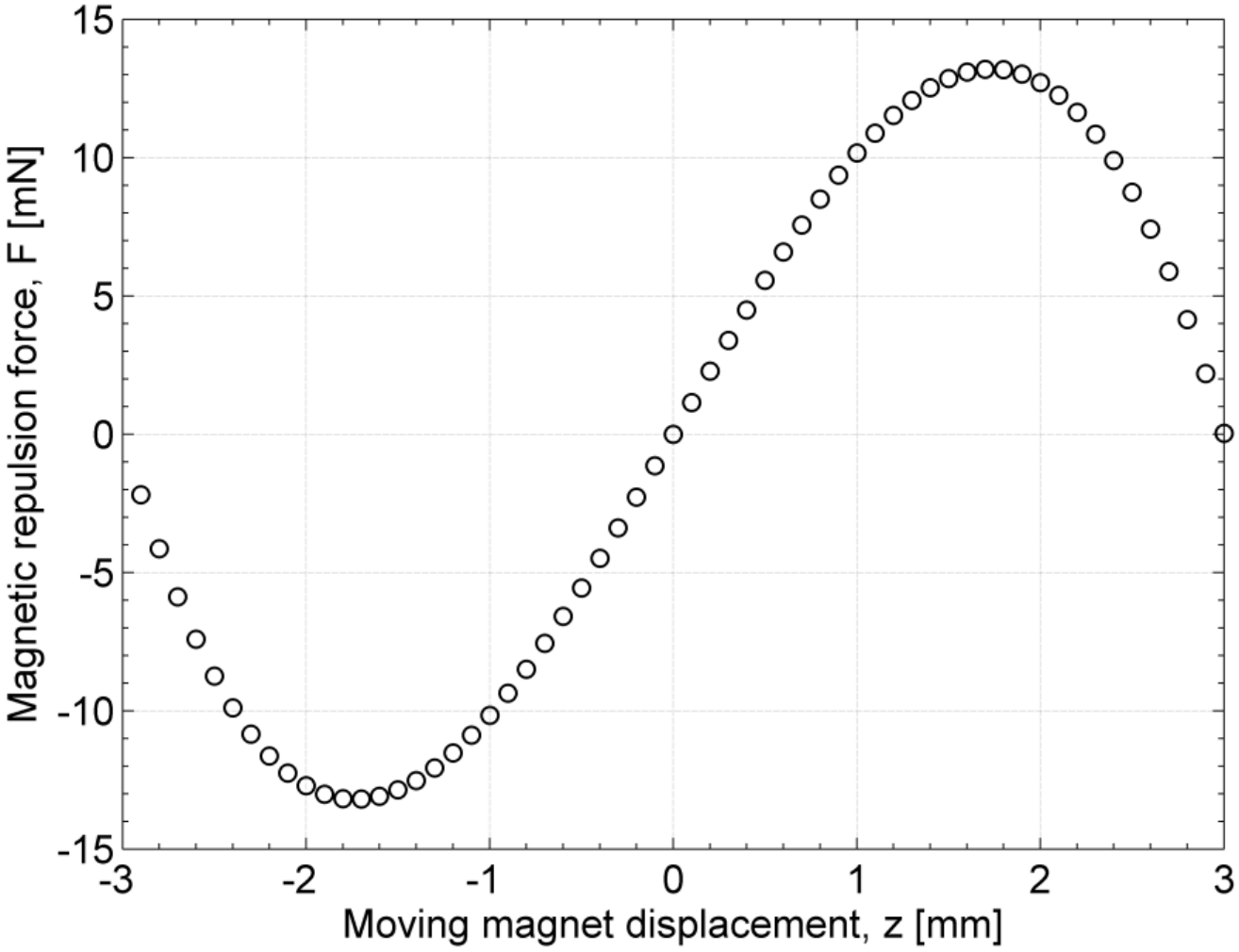

Figure 42: Predicted magnetic force field. The spring is a nonlinear softening spring ($F = 11z - 1 \times 10^6 z^3$). The distance between the magnet composite and each stationary magnet is assumed to be 3.9mm.

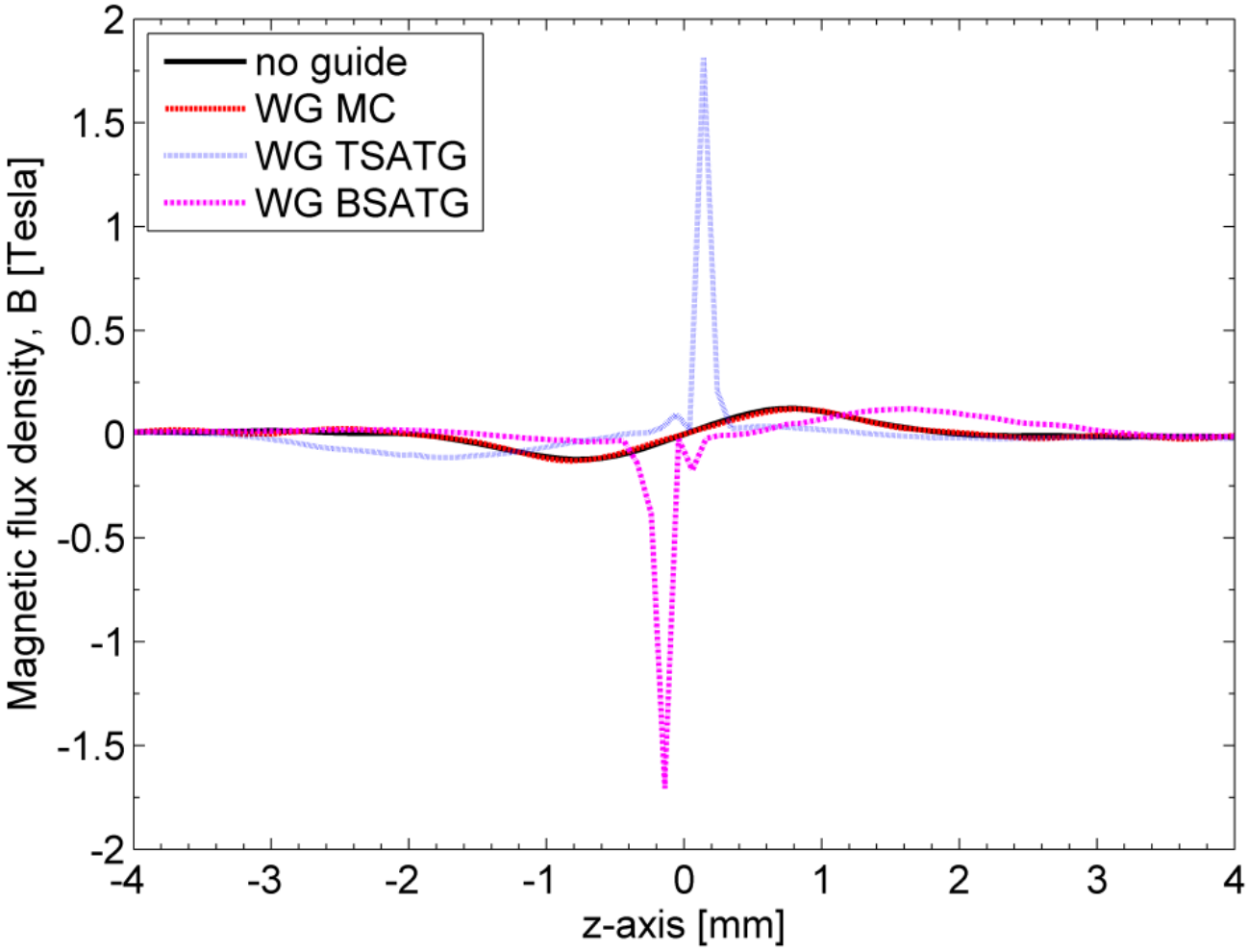

Figure 43: Predicted magnetic flux densities. WG = with guides, MC = Magnet is Centered, TSATG = top spacer adjacent to guides, BSATG = bottom spacer adjacent to guides.

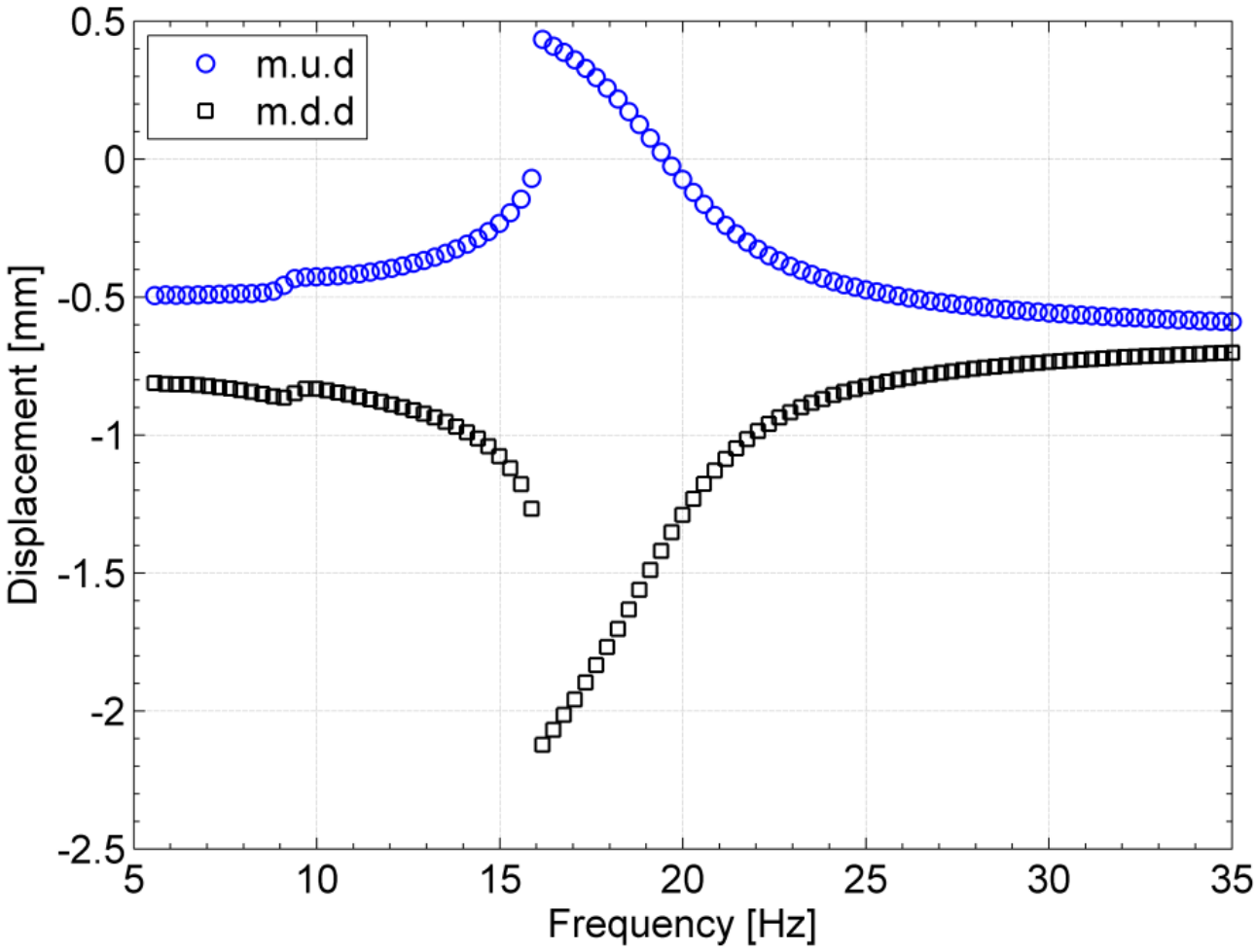

Figure 44: Predicted displacement amplitudes for both harvesters (with and without guides) at 0.2*g*. N.B: magnetic damping not yet accounted for. m.u.d = maximum upward displacement, m.d.d = maximum downward displacement.

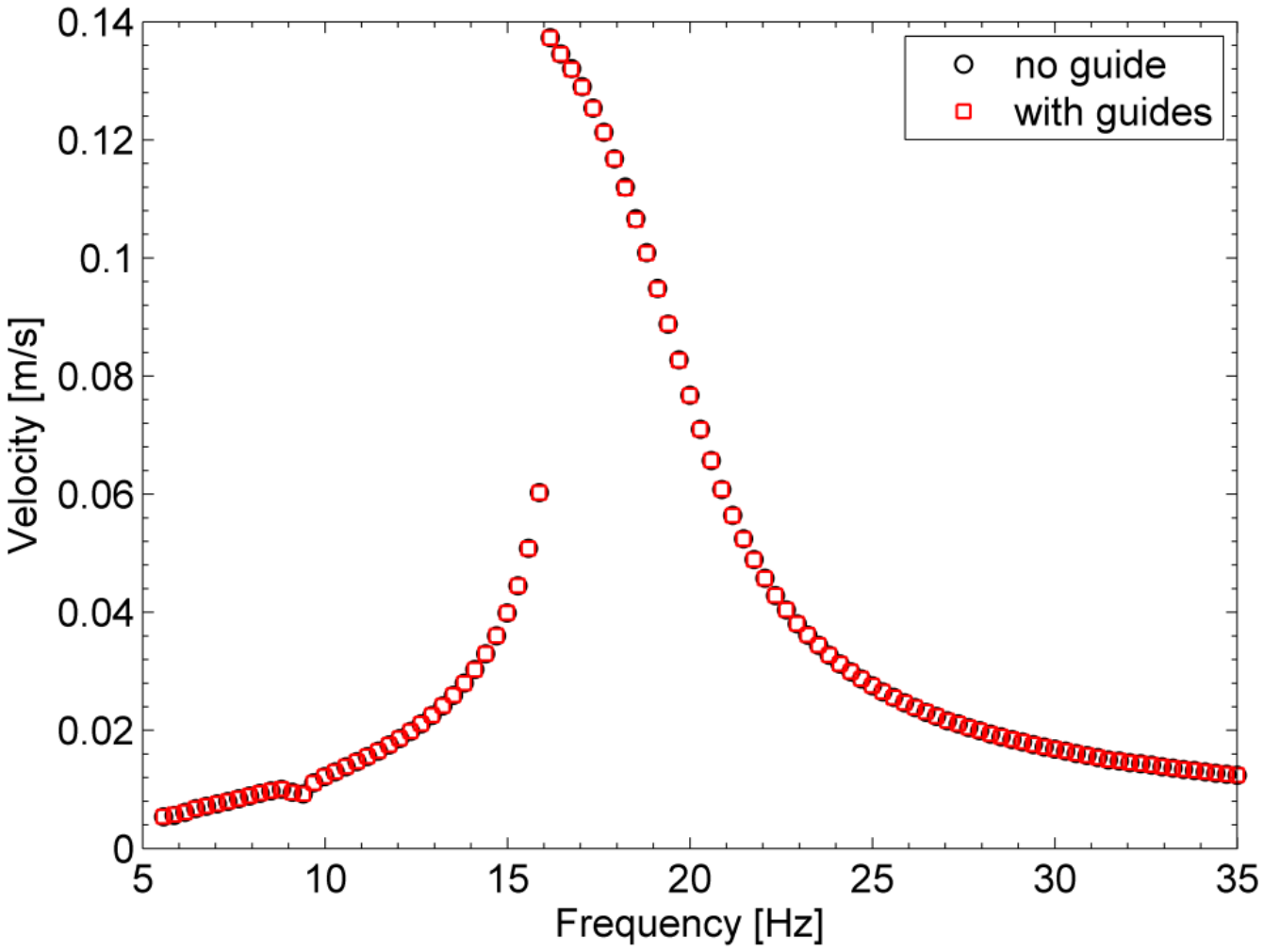

Figure 45: Predicted velocities for both harvesters (with and without guides) at 0.2*g*. N.B: magnetic damping not yet accounted for.

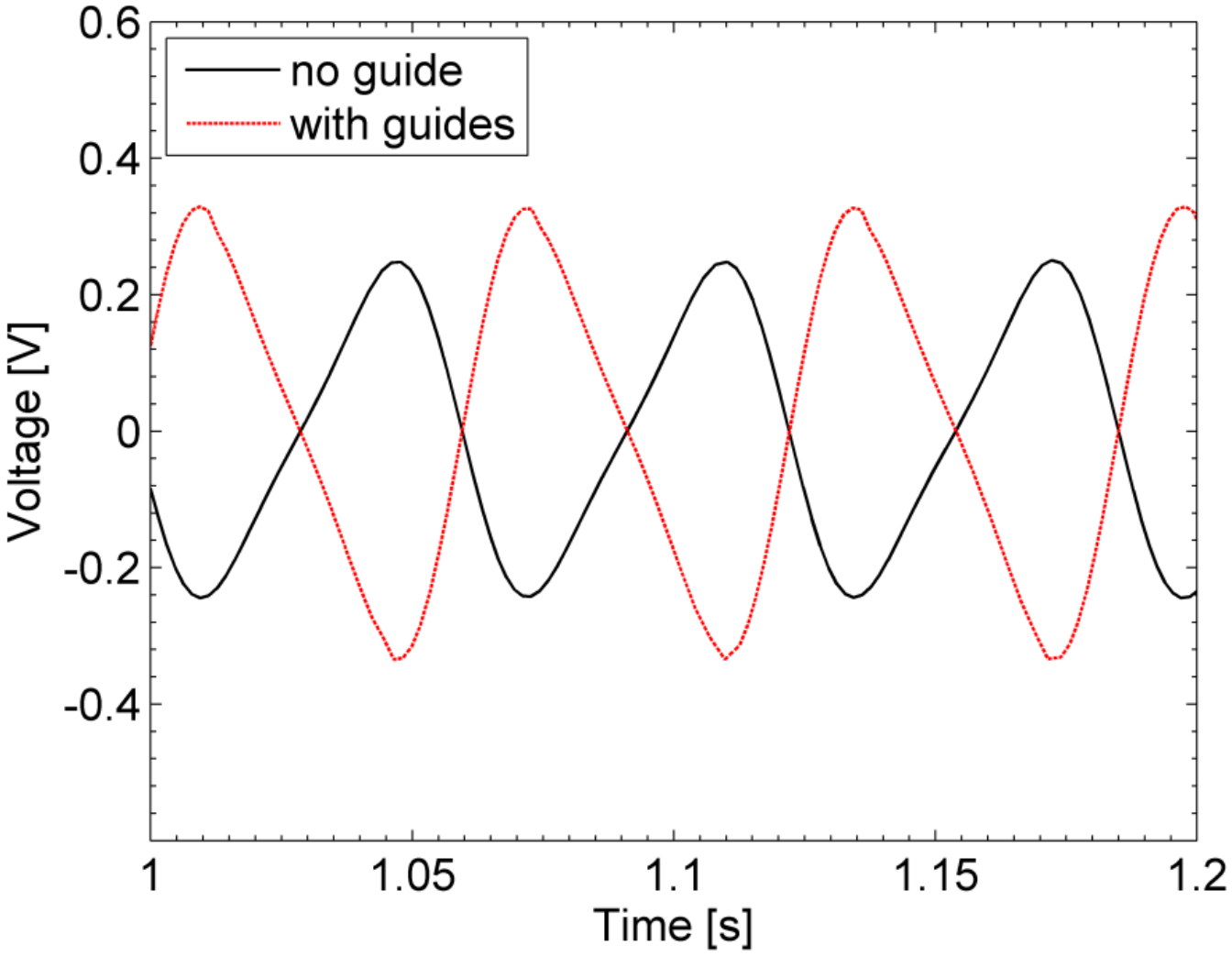

Figure 46: Resonance (16Hz) voltage response for both harvesters at 0.2*g*.

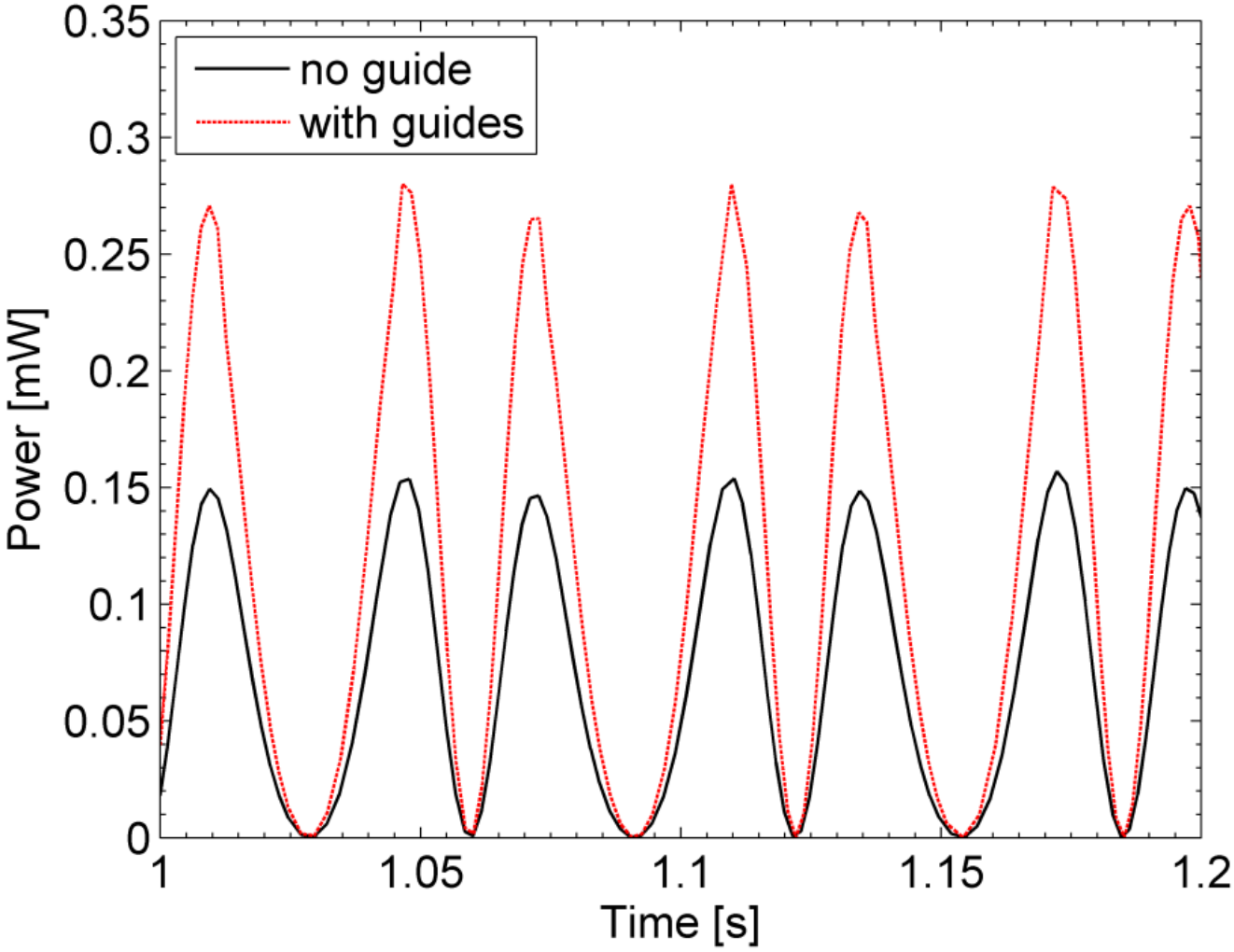

Figure 47: Resonance (16Hz) power response for both harvesters at 0.2*g*.

5.3 Nonlinear Inflection in Magnetically-Levitated Electromagnetic Systems

5.3.1 Theory

The idea is to estimate the nonlinear inflection point in magnetically-levitated electromagnetic systems similar to those in chapter 4 and chapter 5. The nonlinear inflection point is the point at which the nonlinear spring constant (k_3) changes sign (+ve to –ve or vice-versa). The spring thus changes from hardening to softening spring or vice-versa. This is an interesting phenomenon which suggests the nonlinearities in these systems do not necessarily vanish as spacing between magnets is decreased (usually, as the spacing is decreased, the nonlinear stiffness reportedly vanishes and the linear spring onstant k increases, thus increasing the natural frequency of the system).

5.3.2 Estimating the nonlinear inflection point

The inflection point is dependent on a number of factors including the reduction in size ratio of moving magnet to stationary magnet (Vol_{mm}/Vol_{sm}). It also occurs as the distance between the moving magnet and stationary magnet (d) decreases. For the device in section 6.1, the nonlinear inflection point occurs between 7mm $< d >$ 10mm as shown in Figure 48 since the nonlinear spring constant is -ve for d = 7mm and +ve for d = 10mm.

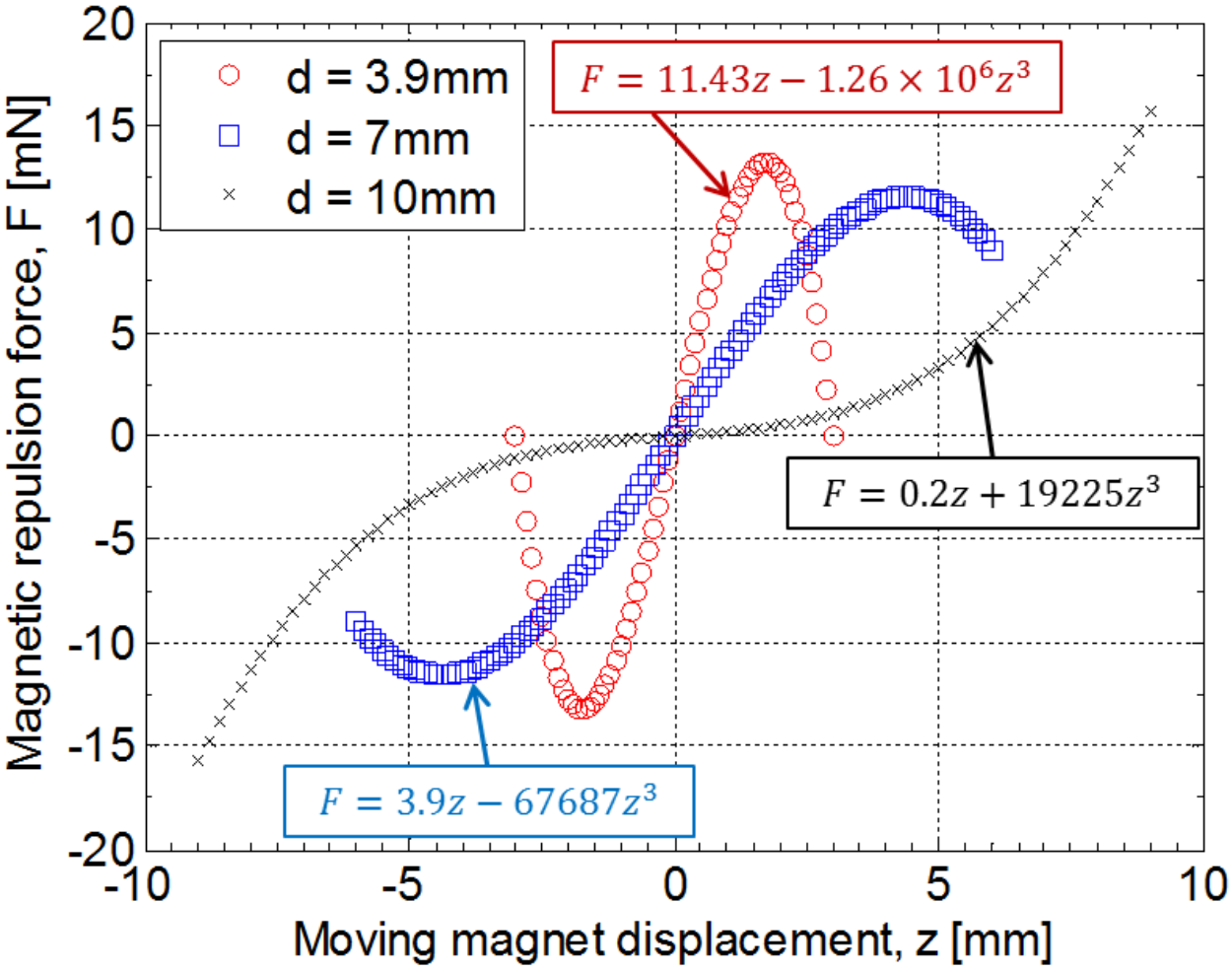

Figure 48: Predicted magnetic force fields for different values of *d* for the device in section 5.2. Note the –ve or +ve sign of the nonlinear stiffness (coefficient of z^3).

5.4 Chapter Conclusion

Scaling analysis was carried out on four harvesters differentiated by increasing order of magnitude of the distance between stationary magnets. The analysis was based on a previously reported experimental harvester which exhibited high power density due to an

efficient double-repulsion configuration in the moving magnet composite. The distance between magnets for the harvesters were 0.36mm, 3.6mm, 36mm, and 360mm while the applied base accelerations were 0.01g, 0.1g, 1g, and 10g. The magnetic field results showed a similar flux profile across all length scales. However, the force field showed an increase in the linear stiffness coefficient and a decrease in the nonlinear stiffness coefficient as the length scale was increased. The resonance frequency decreased with increasing length scale while the maximum velocity also decreased with increasing length scale due to the decreased spacing between the stationary magnets. The resonance frequencies and bandwidth available for energy harvesting however increased as the applied acceleration increased. The voltage response of the harvesters scaled by 3-4 orders of magnitude while the power response scaled by 2-4 orders of magnitude as the distance between stationary magnets was scaled by one order of magnitude. The model was compared with the experimental harvester and the results were in close agreement for the energy response.

A MEMS electromagnetic harvester with metglas guides installed was designed, modeled, fabricated and tested. From the analysis of the results, the inclusion of the metglas guides led to an increase in the voltage and power response providing up to 0.27mW peak power response at resonance of 16Hz. The harvester was also shown to exhibit a unique softening spring in the magnetic force field leading to an analysis of the nonlinear inflection present in the harvester design.

6 Chapter 6:

MEMS Energy Harvester with Coupled Electromagnetic and Piezoelectric Components

6.1 Concept

In this chapter, a combination of piezoelectric cantilever and electromagnetic induction is attempted at the MEMS scale. A coupled harvester was modeled, fabricated and tested with following attributes:

- It combined piezoelectric cantilever and electromagnetic magnetic induction concepts
- The cantilever part provided low stiffness (low frequency), good displacement and velocity. It also provided pure bending vibration around the first mode.
- The magnetic induction part provided nonlinearity (and thus broadband behavior), increases strain (there's also prestress) and thus power response from the piezoelectric. It also strains the center part of the arc-based cantilever by longitudinal magnetically-induced stretching (constant DC field due to attached magnet).

The harvester properties are detailed in Table 12. As with the other MEMS harvesters reported in this thesis, the harvester was restricted to within a form factor of 10mm × 10mm × 10mm. The harvester design details are shown in Figure 50. As depicted, the arc-based cantilever holds the moving magnet concentrically within the harvester tube. The metglas

layer of the arc-based cantilever was included to ensure proper bonding to the moving magnet composite due to magnetic attraction.

The total stiffness in the coupled harvester can be obtained by the adding the linear stiffness due to the cantilever and the nonlinear stiffness due to magnetic repulsion.

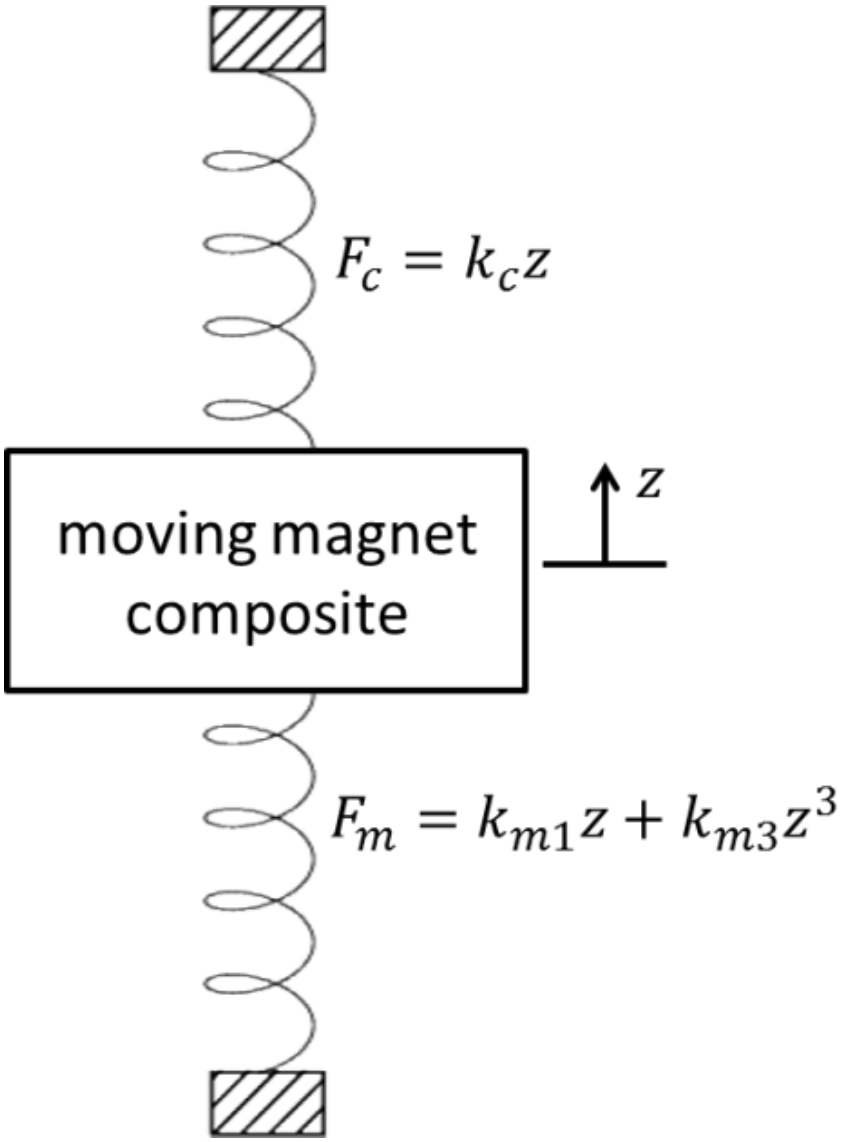

Figure 49: Schematic of the dynamic model of the harvester.

The cantilever modeling follows after the concepts discussed in chapter 3 while the electromagnetic modeling is similar to that provided in chapter 4. The stiffness of the

cantilever was estimated at 2.27 N/m. In addition to the nonlinear stiffness from the electromagnetic part (2×10^6 N/m^3), the harvester becomes a low frequency coupled system with a nonlinear and broadband response.

6.2 Fabrication

The fabrication step discussed here focuses on the cantilever part. The electromagnetic portion was fabricated similar to the harvester in chapter 4. Firstly, brass was cut into a square shape of 2" x 2". Then, a tool path was designed in NX Unigraphics software into the intended harvester shape. This tool path was fed into a CNC machine computer and was used by the CNC machine to cut the desired shape. Then, the polymer piezoelectric (PVDF) of size 2" by 2" was bonded onto the top of the already machined structure. The machined shape was used as a guide for the PVDF during the next step (laser cutting). An Aerosol Jet printing system (Optomec) equipped with an 830 nm continuous wave Yb-fiber laser was used to make the desired pattern on the PVDF attached on the already cut structure. The current in the laser source can be varied from 0.2-2 Amp maximum. The PVDF sample was kept on a stage capable of moving in XYZ directions with speed in the range of 0.01-15 mm/s. The speed and current were also optimized to get nice clean patterned surface of PVDF. Then, metglas (size 5.4" diameter) was epoxy-bonded to the center of the harvester (the circle portion).

Table 12: Properties of the coupled harvester

Property	Value
Cantilever piezoelectric layer	PVDF
Cantilever magnetostrictive layer	metglas
Cantilever flexible support layer	brass
Cantilever diameter (mm)	9
Width of each arc in the cantilever ($R_o - R_i$) (mm)	0.7
Spacing or via in the cantilever (mm)	0.2
PVDF, brass, or metglas thickness (μm)	25
Electrode thickness (μm)	1.5
Harvester casing dimensions (mm)	10 od x 7.1 id x 10 long
Magnet material	NdFeB N52
Moving magnet composite dimensions (mm)	6.4 od x 1.6 id x 3.2 thick
Connecting magnet dimensions (mm)	4.8 od x 1.6 id x 3.2 thick
Metglas spacer dimensions (mm)	6.4 od x 1.6 id x 0.025 thick
Metglas guide dimensions (mm)	10 od x 7.5 id x 0.025 thick
Stationary magnet dimensions (mm)	3.2 od x 0.8 thick
Coil material	copper
Each coil segment (mm)	10 od x 7.5 id x 1.5 thick
Coil resistance	14.43 ohm/m
Coil diameter (mm)	44μm

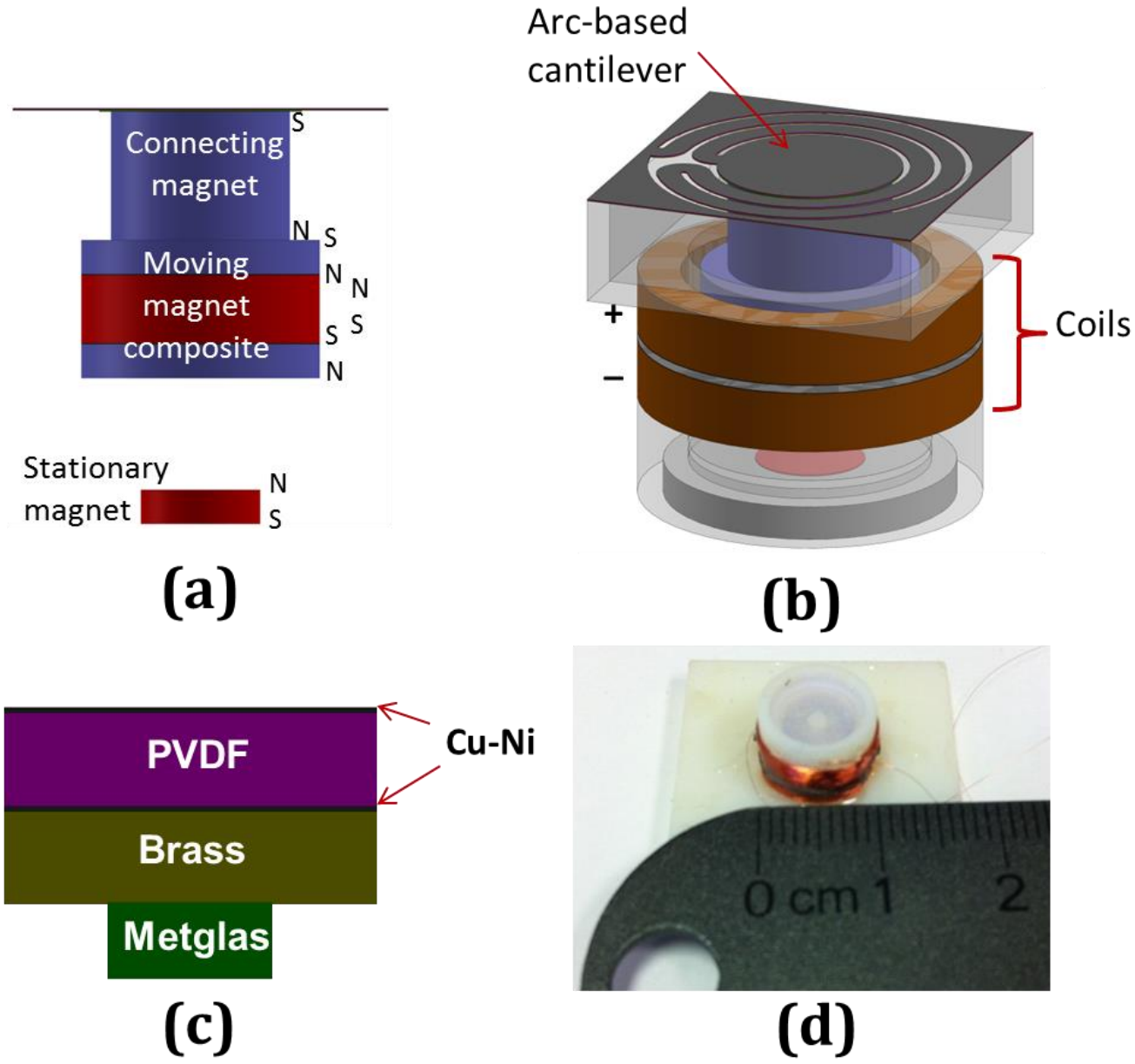

Figure 50: Coupled harvester design: (a) magnet configuration, (b) full design, (b) cantilever layer design, and (d) fabricated harvester casing.

6.3 Results

The coupled harvester was shown to resonate at 21.8 Hz as shown in Figure 51. The magnet (and thus the piezoelectric cantilever) was shown to exhibit significant displacement

which is favorable for high strain in the piezoelectric cantilever and high velocity in the electromagnetic system. Both of these effects typically lead to an increase in the power response. As shown in Figure 52 and Figure 53, the output response of the harvester's electromagnetic part was significantly higher than observed for the MEMS electromagnetic harvester presented in chapter 5.2. The power response was increased by about least an order of magnitude when compared with the MEMS electromagnetic harvester.

As shown in Figure 54, the piezoelectric part was tested as part of the coupled harvester and outside of it (i.e. cantilever alone). There was a 31% reduction in the resonance frequency from testing outside the coupled harvester (31.8Hz) to testing as part of it (21.8Hz). Also, there was 30 times increase in the power response due to the presence of the magnetic system which significantly increased the effective moving mass within the coupled harvester and caused the cantilever part to strain much more than it would in a standalone design.

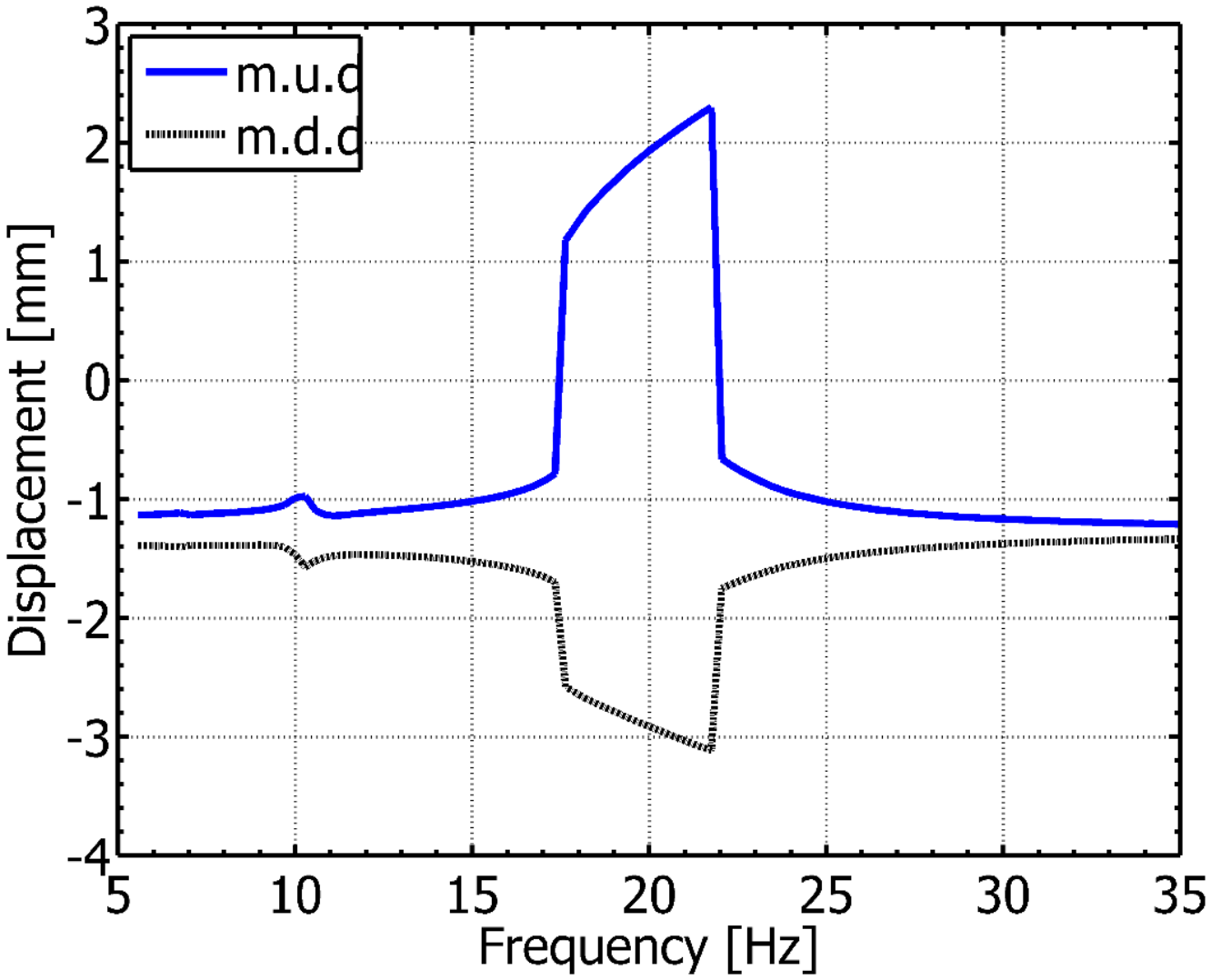

Figure 51: Displacement amplitude profile of the moving magnet composite (and thus the center of the arc-based cantilever) in the coupled harvester showing resonance at 21.8 Hz (at applied acceleration of 0.2 g). m.u.d = maximum upward displacement, m.d.d = maximum downward displacement.

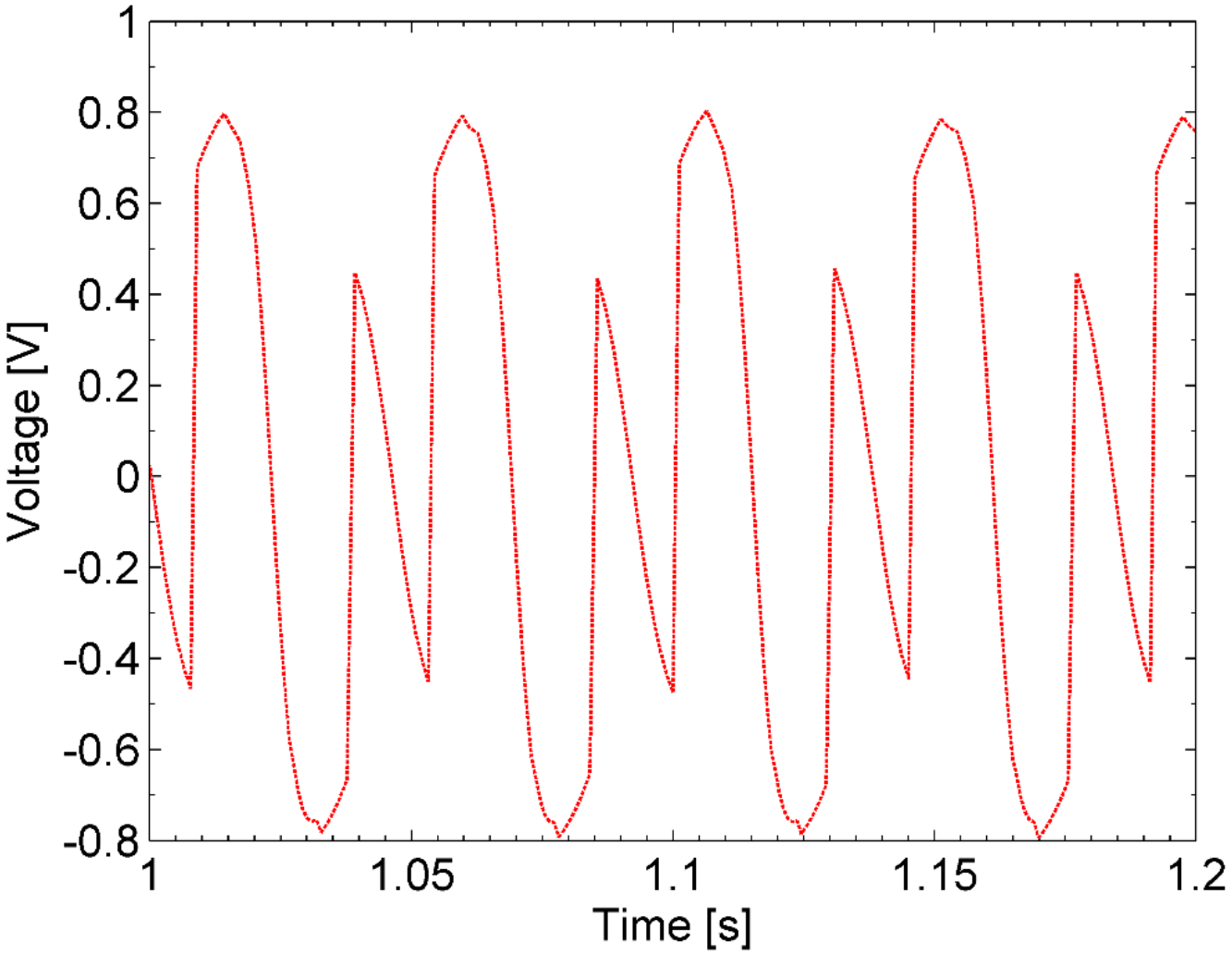

Figure 52: Voltage response of the electromagnetic part at resonance (and applied acceleration of 0.2 *g*).

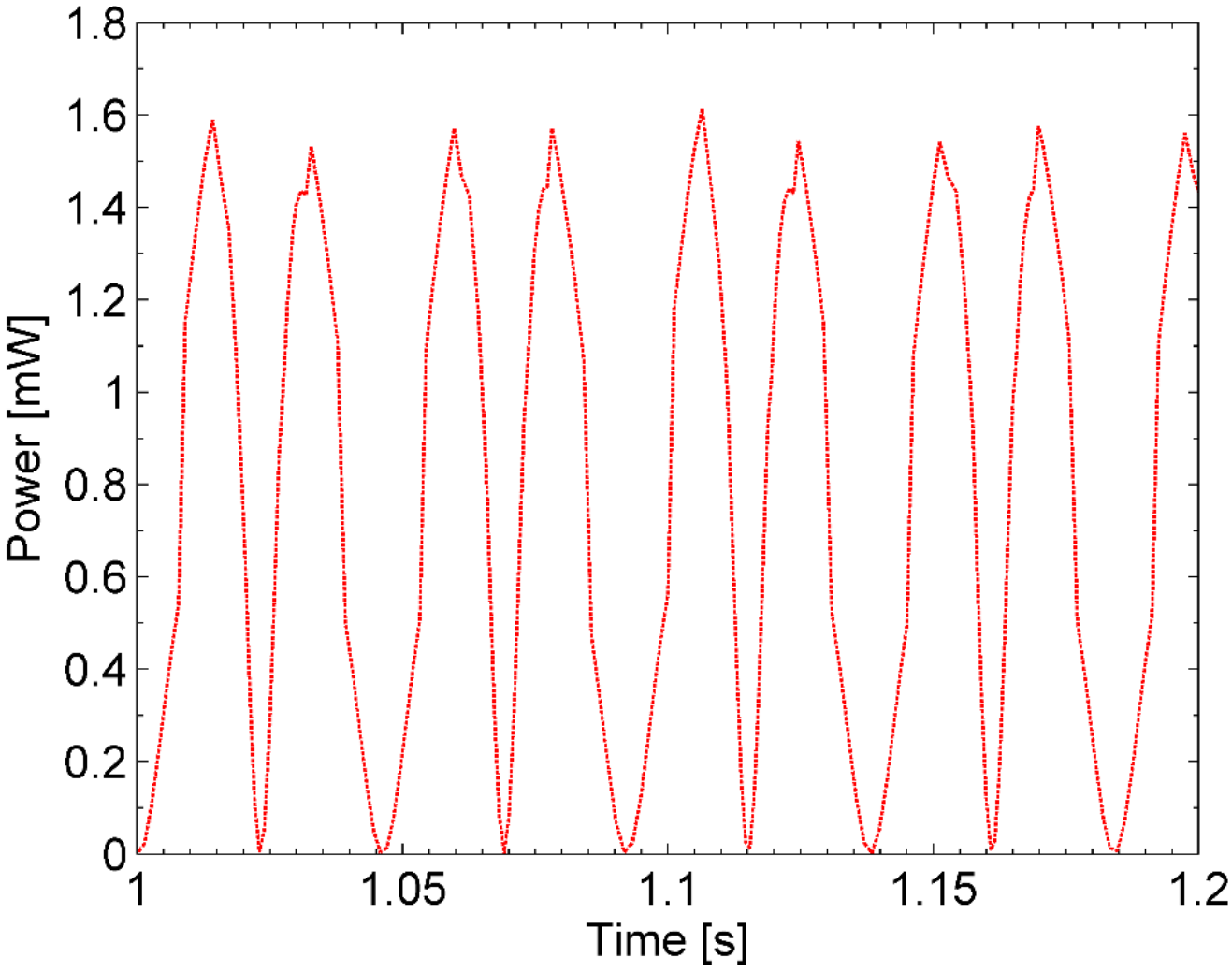

Figure 53: Power response of the electromagnetic part at resonance (and applied acceleration of 0.2 g). The RMS response was 1.1 mW.

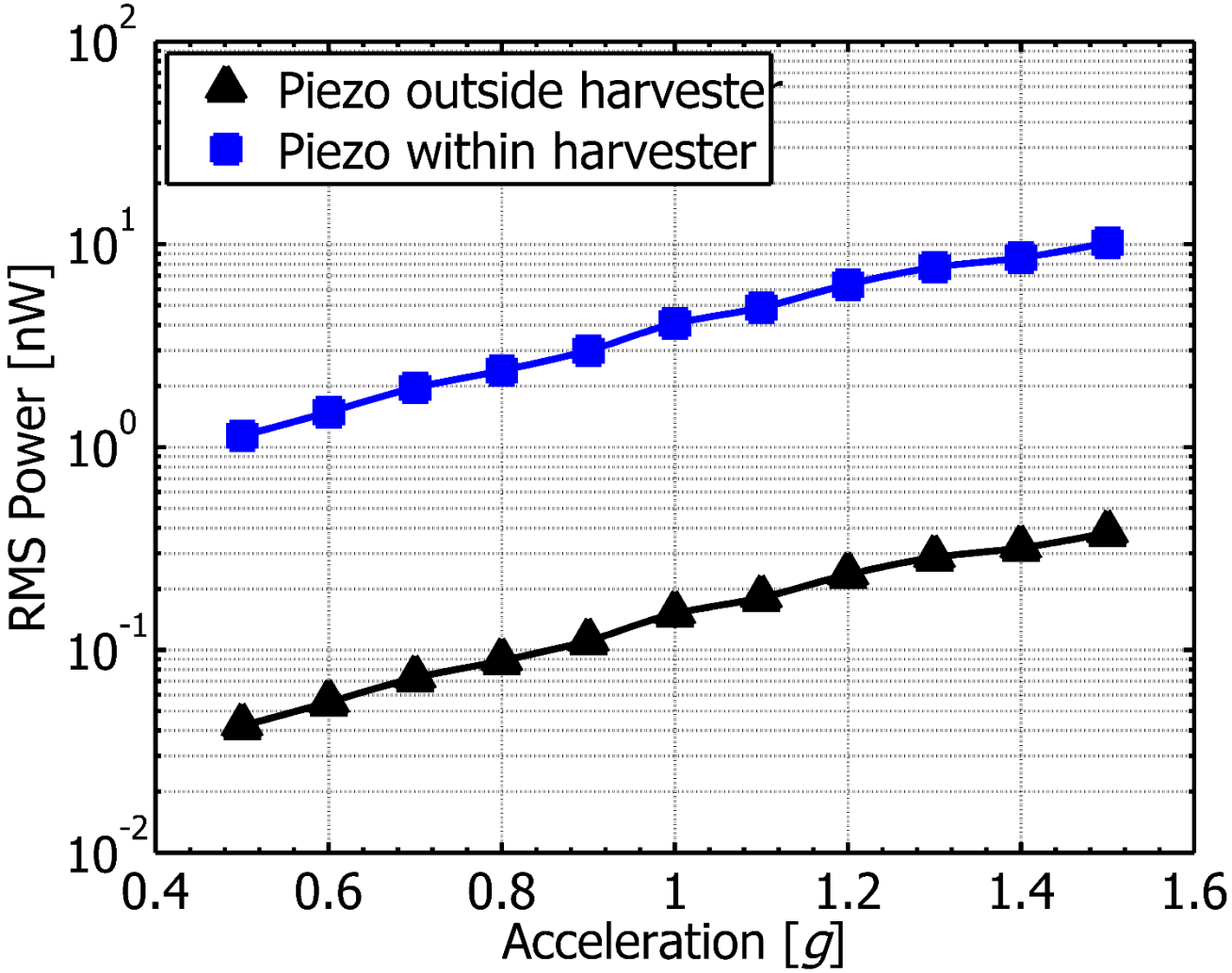

Figure 54: Power response of the piezoelectric component as part of the coupled harvester system and outside of the coupled harvester (cantilever alone). The resonance frequency within the coupled harvester was 21.8Hz, while it was 31.8Hz for the standalone piezoelectric cantilever.

6.4 PIEZOCAP Harvester

In this section, modeling and experimental verification of a novel concept for vibration energy harvesting is presented. In this design, piezoelectric microfiber composites (MFCs) with magnets attached on top and bottom form a chamber where another magnet is levitated. We refer to this configuration as PiezoCap which allows harvesting energy at frequencies much lower than the natural frequencies of the MFCs. The natural frequency of the PiezoCap device was found to be 245Hz. It was also found that significant strains can be induced in the MFCs leading to high power output. Scaling analysis showed that reduction in the distance between the MFCs increases the power output. The numerical model was shown to agree with experimental results.

Energy harvesting via micro-electro-mechanical systems (MEMS) is a developing technology which currently depends on energy sources such as vibrations, heat and light. For energy harvesting from vibrations, piezoelectric transduction is currently the preferred energy harvesting technique at the MEMS scale [47]. Power generation via piezoelectric transduction is highly dependent on surface area [94]. Therefore, an improvement in power performance can be obtained by the development of device configurations which optimize the piezo surface area available for energy harvesting.

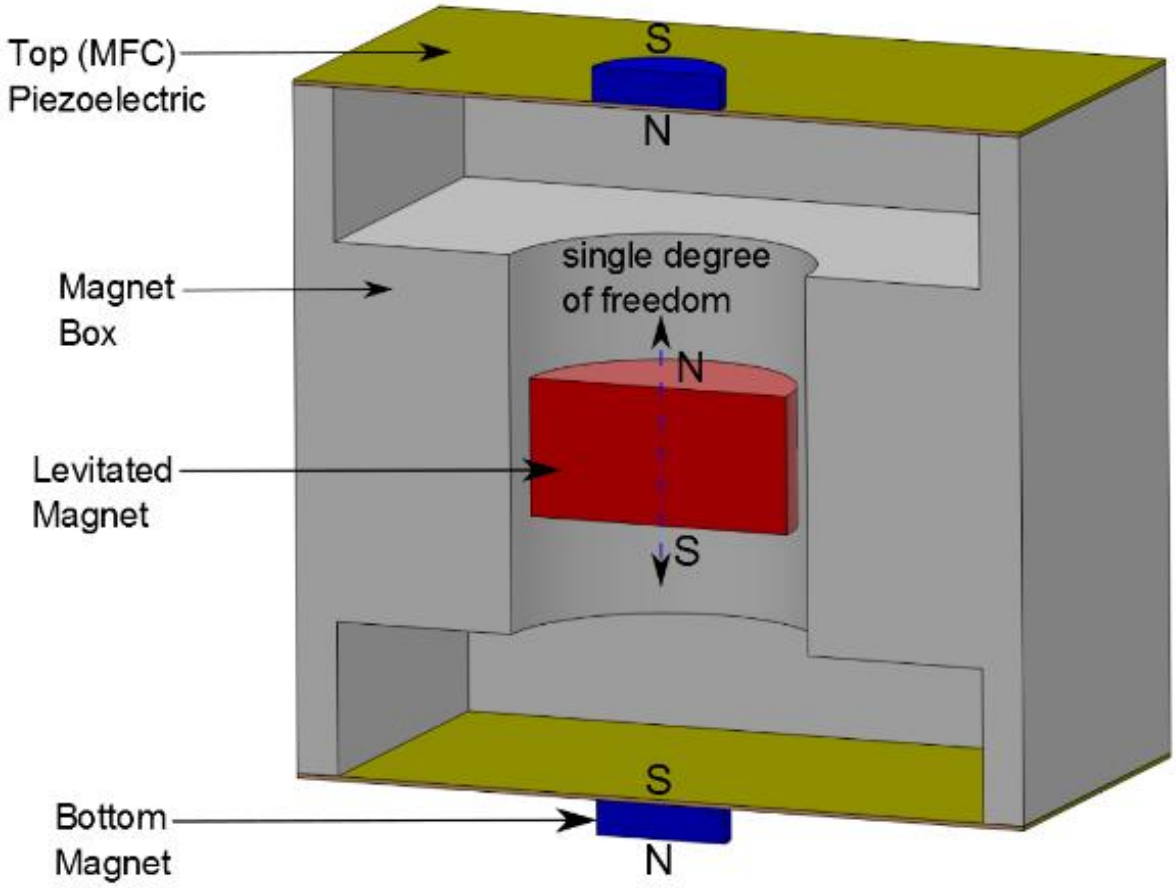

Figure 55: Section view of the PiezoCap model

We present a novel concept (PiezoCap) for piezoelectric energy harvesting that relies on magnetic field induced strain in piezoelectric microfiber composites (MFCs) [95]. The PiezoCap device consists of one magnetic layer on the top and bottom of the MFCs with a levitating magnet in the middle of the device (Figure 55). The top and bottom magnets (attached to MFCs) were aligned to create repulsive force on the levitating magnet. As the device is excited through external vibrations (vertically), the levitating magnet vibrates and repels the attached magnets on the MFCs, thus inducing strain in the MFCs. When clamped

on all four sides, the MFCs exhibit natural frequencies in the kHz range. However, the PiezoCap device enables the development of significant power output at low frequencies, thus addressing the problem of off-resonance energy harvesting.

6.4.1 PIEZOCAP Model

The PiezoCap model incorporates a nonlinear magnetic system and the resultant harmonic displacements of the MFCs. The vibration of the levitated magnet is based on the mass-spring-damper system [77], and is governed by a summation of forces as:

$$\boldsymbol{m\ddot{z}(t) + c\dot{z}(t) + mg + F_{MAG} + F_D = 0} \tag{92}$$

where m is the mass of the levitating magnet, c is an empirically derived mechanical damping constant, z is the vertical displacement of the levitating magnet, t is the time, and g is the acceleration due to gravity. F_{MAG} is the nonlinear magnetic repulsion force and is defined as:

$$\boldsymbol{F_{MAG} = kz(t) + k_3 z(t)^3} \tag{93}$$

where k and k_3 are spring constants with units of N/m and N/m^3 respectively. F_D is the driving force from base excitation of the harvester and is defined by a cosine waveform as:

$$\boldsymbol{F_D = F_0 cos\omega t} \tag{94}$$

where F_0 is the amplitude of the driving force and ω is the driving frequency. Overall, the governing equation for the nonlinear magnetic system is a modified form of the Duffing equation [76].

F_{MAG} was obtained via finite element modeling (FEM) using ANSYS solid 236 element. The set of F_{MAG} versus z values obtained from FEM were was curve-fitted to obtain the spring constants k and k_3. Equations 92-94 were solved numerically and the damped natural frequency (ω_d) of the magnetic vibrating system was obtained as the value of the driving frequency (ω) which corresponds to the peak value of velocity ($\dot{z}$).

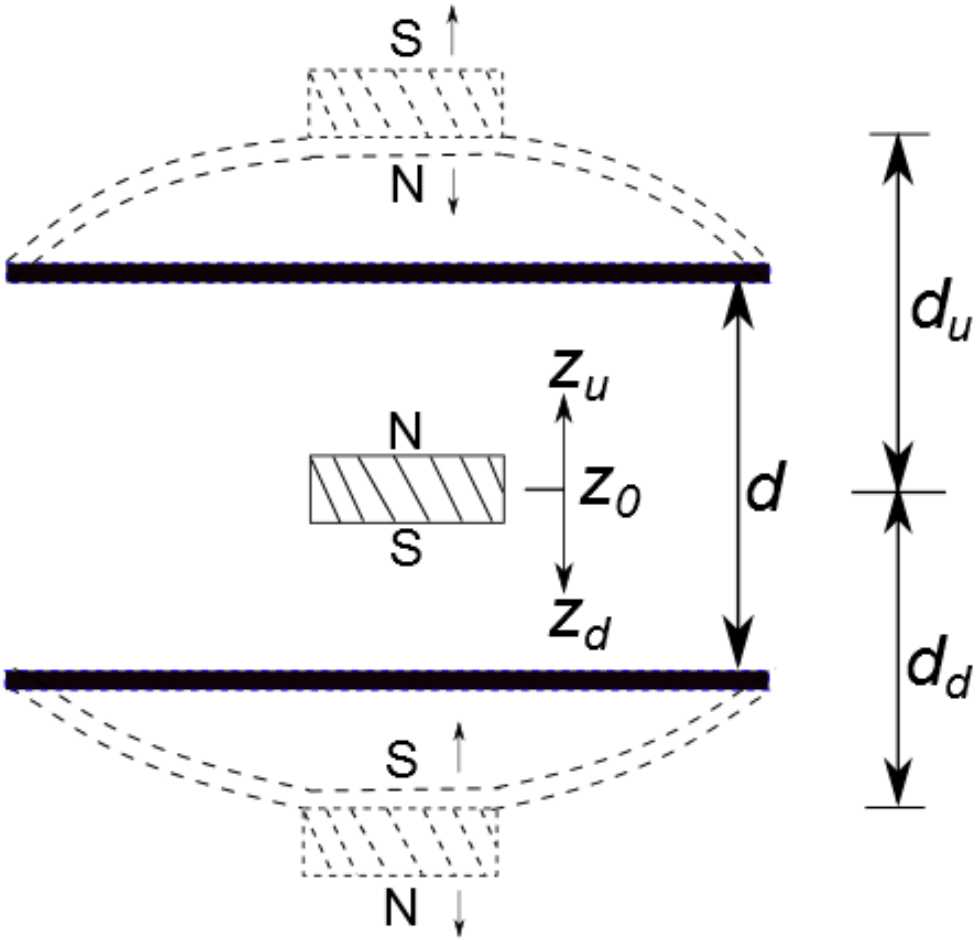

Figure 56: Schematic description of PiezoCap.

A schematic diagram of the PiezoCap device is shown in Figure 56. In the absence of the attached magnets, the distance between the MFCs is d. The distance between the levitated magnet and the top magnet is d_u and the distance between the levitated magnet and the bottom magnet is d_d. As the levitated magnet vibrates, it is displaced by a distance z_u upwards and downwards z_d from its rest position z_0. The top and bottom MFCs are displaced harmonically during vibration due to the repulsion of the attached magnets towards the levitating magnet. Therefore the PiezoCap device is modeled iteratively since the distances between the magnets (d_u and d_d) are initially unknown.

To find the output power of a PiezoCap device, (1) F_{MAG} is obtained based on d and equations 92-94 are solved. (2) Next, the F_{MAG} values which correspond to the maximum displacements (up and down) of the levitating magnet are used to perform FEM harmonic analyses on the MFCs using ANSYS solid 186 element. (3) The center displacements of the MFCs are obtained and steps 1 and 2 are repeated until the solution converges.

The values which define the PiezoCap device in this preliminary study are given in Table 13. The levitated and attached magnets are of the same dimensions and are made of NdFeB material. The MFCs (small and big) have the same MFC and piezo thicknesses thickness (H and H_p). The small MFC is in d_{31} mode while the big MFC is in d_{33} mode.

Table 13: Important values for the PiezoCap device

Magnet diameter	3/8 inch
Magnet thickness	1/32 inch
Magnet material	NdFeB
Magnet mass (m)	0.424g
Small MFC (L_s x B_s)	27mm x 13mm
Big MFC (L_b x B_b)	28mm x 16mm
d_{33} constant (big MFC)	4×10^{-10} C/N
d_{31} constant (small MFC)	1.7×10^{-10} C/N
g_{33} constant (big MFC)	22.2×10^{-3} Vm/N
g_{31} constant (small MFC)	10.9×10^{-3} Vm/N
Total MFC thickness (H)	305µm
Piezo thickness (H_p)	185µm
MFC piezo material	PZT 5A1
MFC elastic modulus	30.336GPa
MFC density	5.55g/cm^3
MFC Poisson's ratio	0.31
Distance between MFCs in the absence of magnets (d)	3.2mm

6.4.2 Results and Discussion

The magnetic force (F_{MAG}) profile obtained from FEM (Figure 57) is nonlinear as expected and the spring constants were obtained as $\boldsymbol{k = 1007}$ N/m and $\boldsymbol{k_3 = 4.374 \times 10^8}$N/m^3. The F_{MAG} profile is an important determinant of the natural frequency: As the device becomes less nonlinear (i.e as k/k_3 increases), the frequency increases.

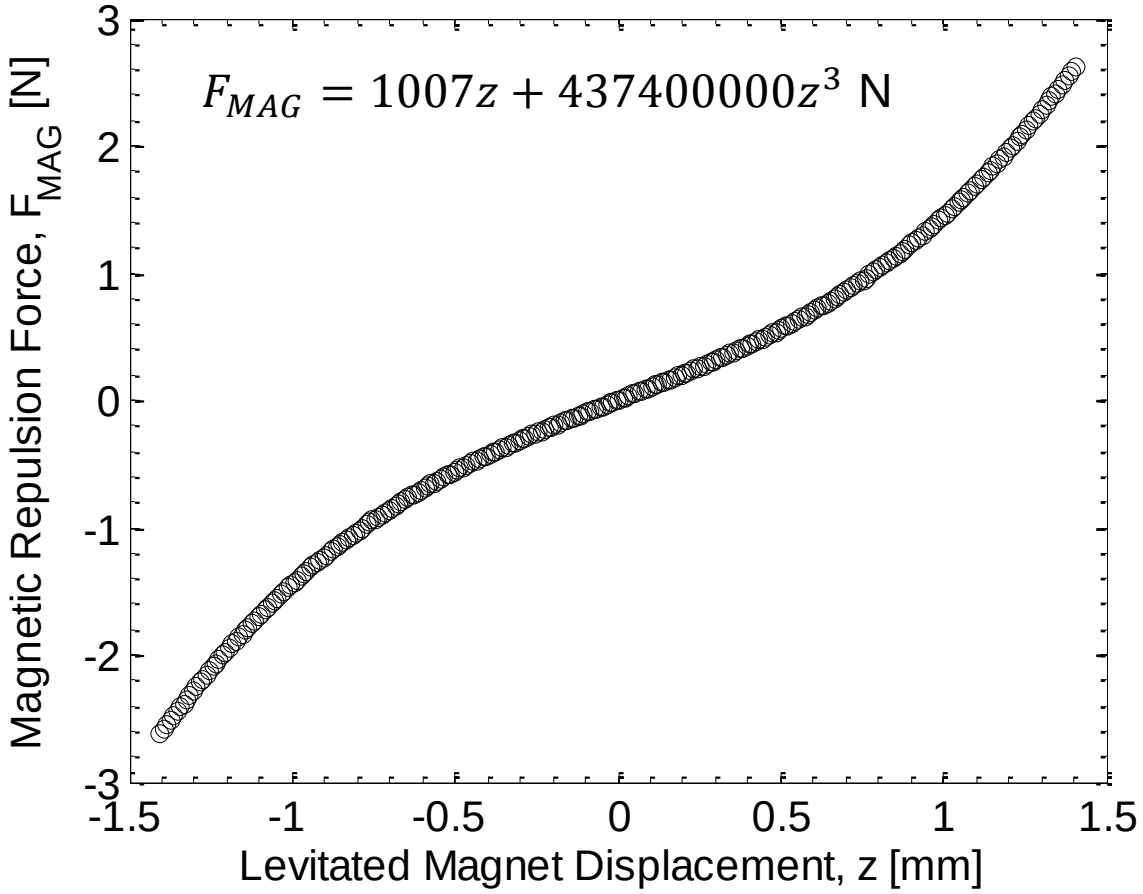

Figure 57: The magnetic repulsion force on the levitating magnet as a function of its displacement.

The velocity and maximum displacements of the levitating magnet as a function of frequency are shown in Figure 58. The dynamics of the levitating magnet was modeled for two cases:

A. With small MFC on top and big MFC at the bottom; and

B. With big MFC on top and small MFC at the bottom.

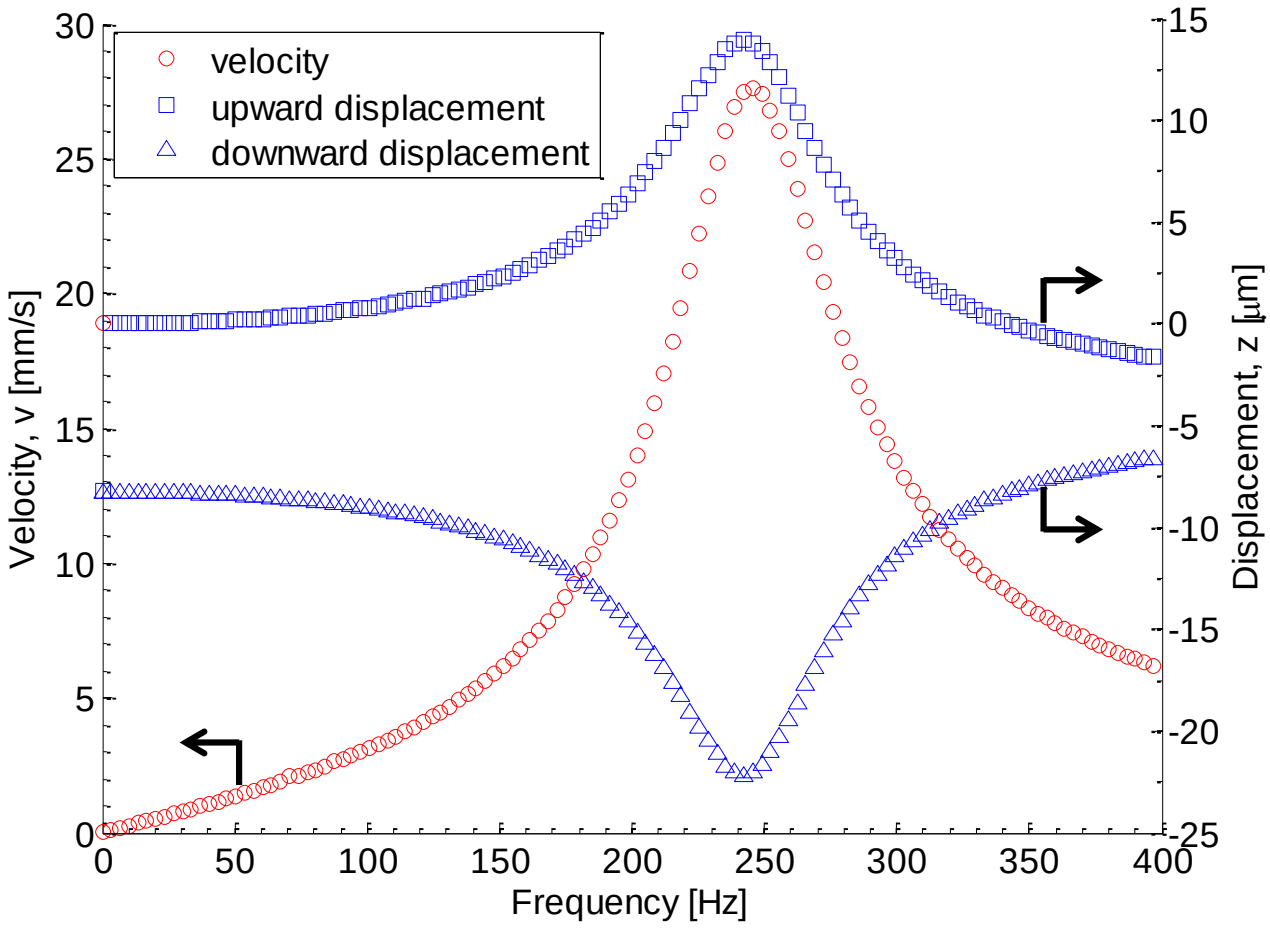

Figure 58: Dynamics of the levitating magnet as a function of frequency (values of velocity (v) and maximum values of the upward (z_u) and downward (z_d) displacements).

In both cases, the results are similar except with respect to the displacement of the MFCs. This is mainly because the natural frequencies of the MFCs are in the kHz range while the magnetic system has a natural frequency less than 300Hz. Since the base excitation frequency is varied below 1000Hz, the governing frequency of the PiezoCap device is that of the magnetic system.

The maxima (or minima) values of velocity and displacement correspond to the resonance

of the system. Therefore, the natural frequency of the PiezoCap system was 245 Hz. The maximum velocity was 27.62mm/s, while the upward (z_u) and downward (z_d) displacements (relative to the center of the PiezoCap device) were 13.92μm and -22.17μm respectively. This shows the actual rest position of the levitating magnet (z_0 = -4.13μm) was influenced by gravity.

Table 14: Maximum displacements of the MFCs at resonance

	Max. upward displacement (μm)	Max. downward displacement (μm)	Total piezo displacement at center (μm)
Small piezo on top	68.96	397.70	466.66
Big piezo on top	297.95	54.07	352.02

The natural frequency and displacement values indicate that the device in this study is quite stiff (large values of k and k_3). However, despite the low displacement values of the levitating magnet, the displacements induced in the MFCs (at resonance) were quite significant as shown in Table 14.

Due to the weight of the levitating magnet, the PiezoCap device favors the small-MFC-on-top configuration as indicated by the 32.6% increase in total piezo displacement above the case with big MFC on top. The piezo displacement results are particularly crucial for power output calculations since power is dependent on the strain rate.

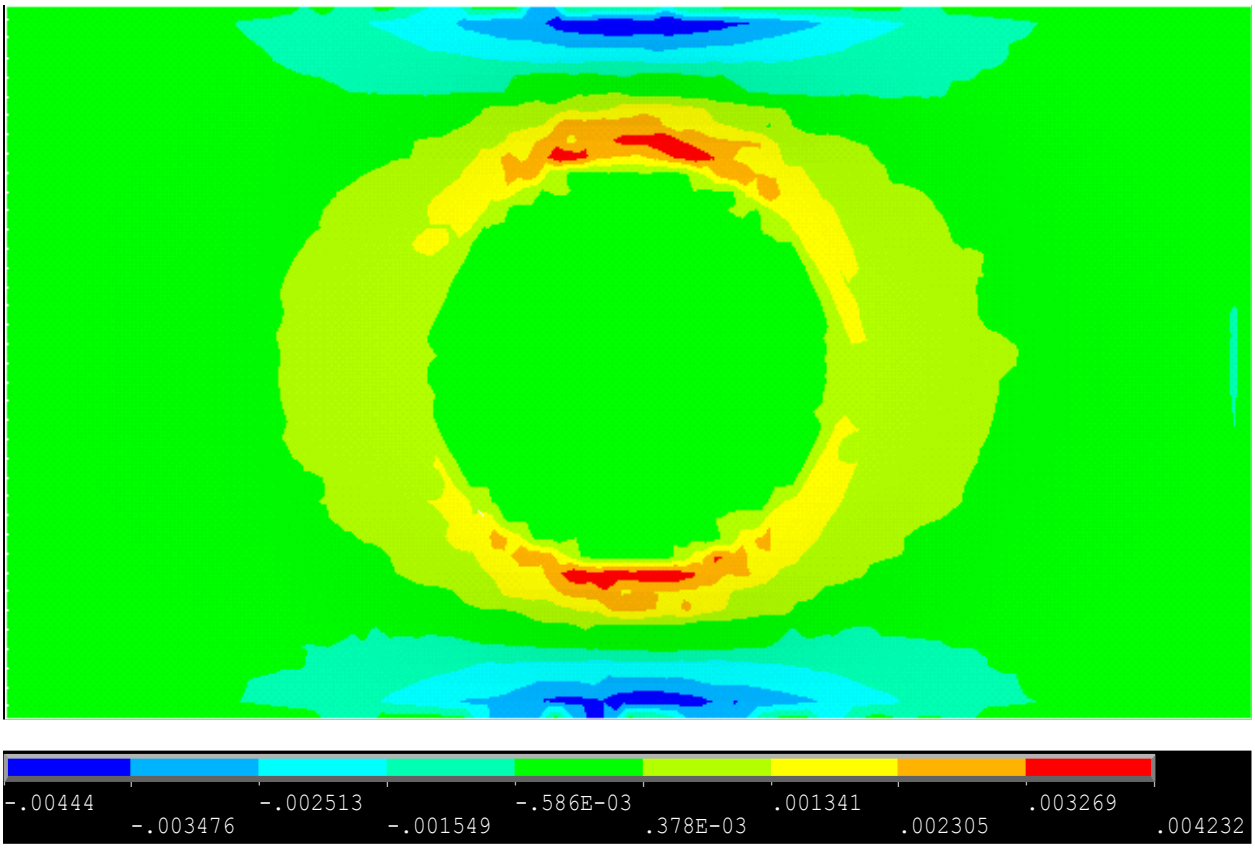

Figure 59: Resonance strain profile of the big MFC in the small-MFC-on-top configuration.

The maximum power output will be obtained by placing the big MFC at the bottom of the PiezoCap device. As seen in Figure 59, the strain profile of the MFC indicates that maximum strain occurs around the edge of the attached magnet placed under the MFC. Otherwise, the strain is uniform for most of the MFC.

The average stresses on the MFCs in the small-MFC-on-top configuration were obtained from ANSYS FEM harmonic analysis as $\boldsymbol{\sigma_{big}} = \mathbf{1.7} \times \mathbf{10^5}\mathrm{N/m^2}$ and $\boldsymbol{\sigma_{small}} = \mathbf{1.5} \times \mathbf{10^5}\mathrm{N/m^2}$. Therefore maximum power estimates for the device can be calculated for the MFCs at resonance as [94]

$$\boldsymbol{P_{big} = \sigma_{big}^2 g_{33} d_{33} L_b B_b H_p f_r = 5.39\ \mu W},\ \textit{and} \tag{95}$$

$$\boldsymbol{P_{small} = \sigma_{small}^2 g_{31} d_{31} L_s B_s H_p f_r = 0.71\ \mu W} \tag{96}$$

where f_r is the resonance frequency. Overall, the maximum power density of the PiezoCap device (MFC volume only) is estimated at resonance as

$$\textbf{Power density} = \frac{P_{big}+P_{small}}{(L_s B_s + L_b B_b)H} = 25\ \mu W/cm^3 \tag{97}$$

6.4.3 MEMS Scaling Analysis

Scaling analysis was carried out to show the effects of reducing the spacing between MFCs (d) as depicted in Figure 60. Reduction in d reduces nonlinearity (k/k_3 increases) and leads to an increase in resonance frequency. The pressure on the bottom MFC also increases with reduced d, leading to more strain and energy harvesting potential at the MEMS scale. However, the decrease in nonlinearity implies that peak performance may occur close to resonance only as the device bandwidth is reduced.

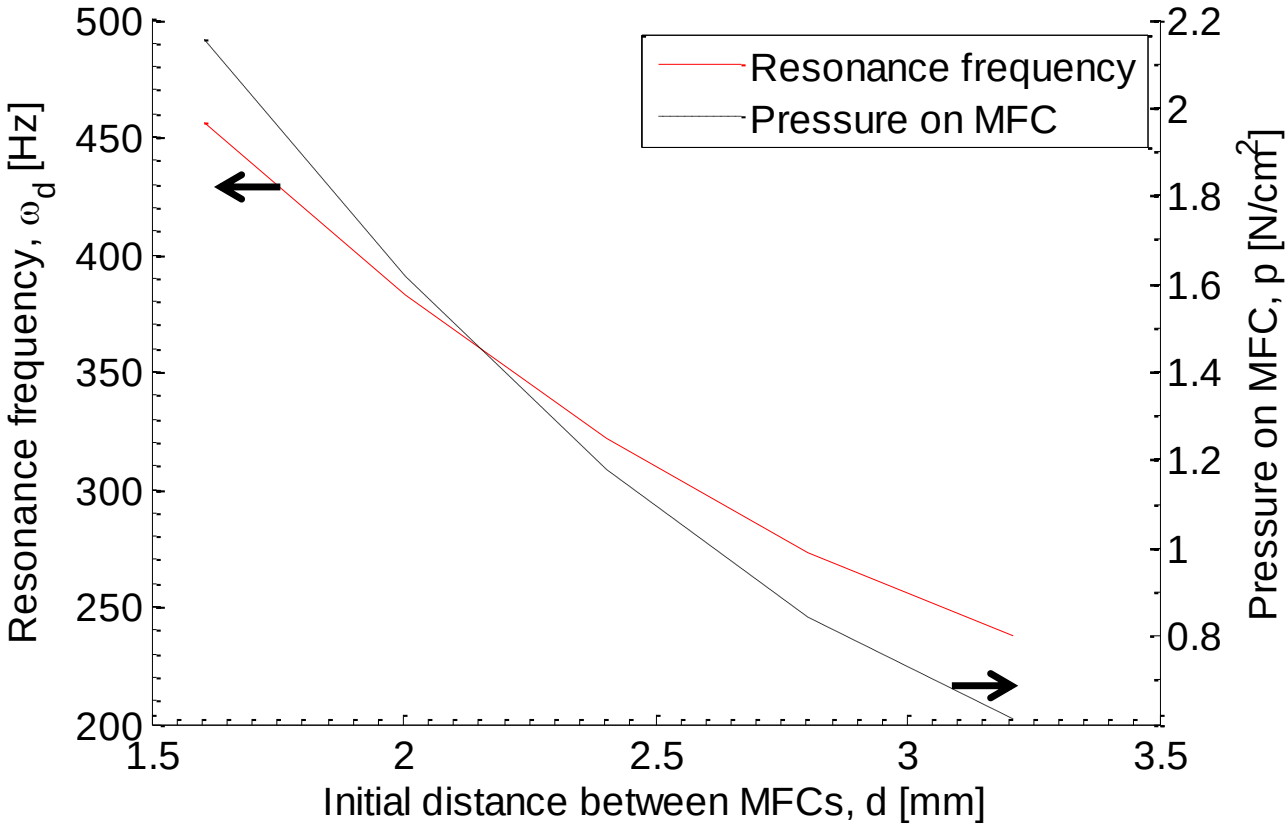

Figure 60: Scaling analysis of the PiezoCap device: The effect of initial distance between the levitating magnet and the MFC (d) on the resonance frequency, and the maximum force impacting the bottom MFC.

6.4.4 Experimental Verification

The numerical model for the PiezoCap device was experimentally verified by vibrating the device with an accelerometer attached at its base and recording the response of the top

and bottom MFCs. The experimental setup had an initial MFC separation distance d = 2mm. The results were compared to the numerical displacement calculations with the same value of d as shown in Figure 61.

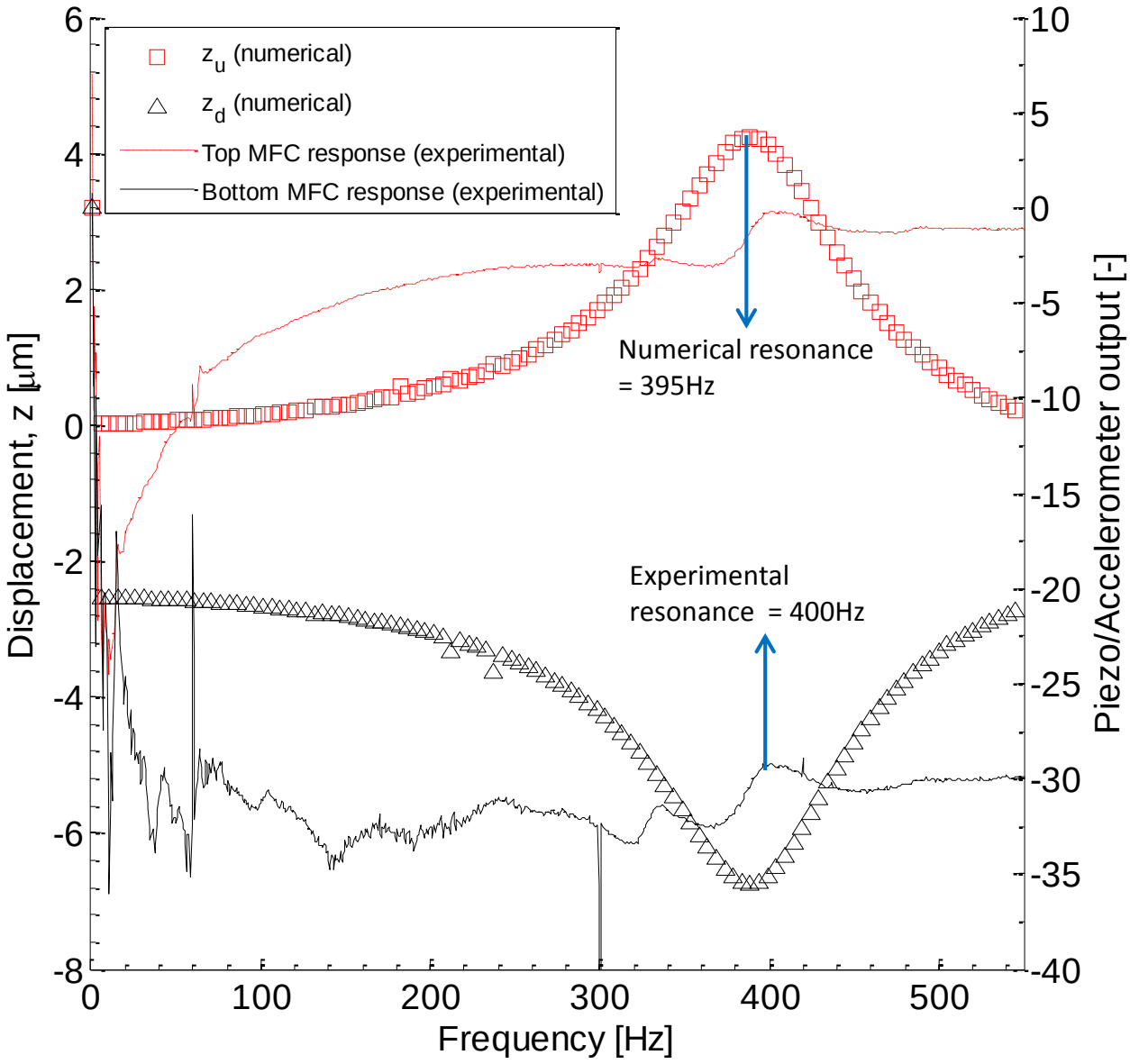

Figure 61: Results for PiezoCap setup with d = 2mm. Magnet and MFC dimensions remain the same as in Table 13.

From these results, the error in predicting the natural frequency was 1.3%. The under-prediction of the frequency may be due to the measured value of *d*, since any slight variation in the value of *d* (especially at the MEMS scale) will have a significant effect on the natural frequency (see Figure 60).

6.5 Chapter Conclusion

A coupled harvester has been presented to show the combination of piezoelectric cantilever and electromagnetic concepts. From the results, the coupled harvester is less stiff and exhibits significant displacements and velocities leading to an order of magnitude increase in the power response of the electromagnetic part (up to 1.1mW at 0.2 *g*) when compared with the previously reported LIVE MEMS electromagnetic harvester. Also, vibration testing showed a 31% decrease in the resonance frequency of the piezoelectric part (31.8Hz vs. 21.8Hz) as a result of its inclusion within the coupled harvester system. The power response response was also shown to amplify 30 times as a result of the inclusion.

Modeling of a PiezoCap device was also conducted. The model involved iterative analysis of the magnetic levitation system and the resulting piezo response. The natural frequency of the device was 245Hz. Despite low displacement values of the levitating magnet, the MFCs exhibited significant strain, and thus significant power output potential. The small-MFC-on-top configuration produced the best displacement results due to the effect of gravity on the levitated magnet's rest position. MEMS scaling analysis showed that a reduction in the distance between the MFCs increases the power output, but increases the frequency and

reduces nonlinearity. The numerical modeling error was shown to be 1.3% when compared with experimental results.

7 Chapter 7:

Conclusion

7.1 Summary

A general out-of-plane vibration model for continuous arc based cantilevers which includes the effects of shear and rotary inertia and also considers the multiple layers of different materials has been developed for the determining the natural frequency and mode shapes. Based on the Timoshenko beam theory, an eigenvalue problem was developed which enables the analysis of multidirectional continuous beams. Expressions for effective properties of multilayered beams were obtained based on calculation of the distances of the layers from the neutral axes and reordering of the layers by decreasing thicknesses. An example cantilever beam was analyzed to illustrate the application of the model and the potential for achieving low frequency resonance in arc-based beams at the micro scale. As indicated by the results, the fundamental mode was 38Hz for 100μm thick silicon substrate. The mode shapes showed the behavior of the centerline of the beams and indicated that the important fundamental mode exhibited a dominant bending behavior which is favorable for many micro-scale applications. Modal experiments were performed on an aluminum arc-based cantilever and the results showed close agreement with the numerical model.

Arc-based cantilever geometries were designed, modeled and compared with their linear counterparts to show their operational capability at low frequency and their response to external excitation. The results obtained show that arc-based cantilevers offer significant

frequency reduction for MEMS scale harvesters. The reduction in frequency becomes more significant when the effective mass and/or volume of the cantilevers are taken into account. Furthermore, the vibration characteristics of arc-based cantilevers (such as mode shapes) can be predetermined thereby simplifying the design and modeling process. Furthermore, different configurations of MEMS ABCs were characterized via modeling and experiments. Then, experimental ABC structures were developed to harvest energy from vibrations and magnetic fields.

An AA battery-sized harvester was modeled, fabricated and tested. The harvester employed a double-repulsion configuration in the moving magnet composite which allowed for easy coil/magnet optimization. The double-repulsion configuration exhibited the lowest frequency, the highest displacement amplitudes and the largest velocity. Furthermore, the double-repulsion configuration exhibited two strong regions of high magnetic flux which enabled efficient coil placement and significant voltage output. The double-repulsion LIVE harvester was found to exhibit RMS power output values of 5.9mW at 0.25G and 12.9mW at 1G. The AA battery-sized harvester was also used to charge a cell phone. A micro electromagnetic harvester was also developed which exhibited softening nonlinear spring behavior, thus leading to the discovery of nonlinear inflection in magnetically-levitated electromagnetic harvesters. The nonlinear inflection theory was then presented to show its causal parameters.

Finally, a coupled harvester was presented which combines the piezoelectric cantilever and electromagnetic induction mechanisms. The advantages of each mechanism were transferred positively to each to other. The cantilever provided low stiffness, low frequency, and pure bending, while the magnetic system provided nonlinearity, broadband

response, and increased strain (and thus voltage). A novel PIEZOCAP concept was then introduced to show the effects of magnetic field repulsion on increased performance of piezoelectric membranes (or caps).

7.2 Performances of the MEMS Harvesters and Future Outlook

7.2.1 Harvester Performance

The harvesters reported in this study have been shown to exhibit significantly improved energy harvesting potential in comparison to most reported MEMS harvesters. They are easy to fabricate, are structurally stable, and they exhibit low frequencies (below 35Hz) despite their miniaturized sizes.

One way of measuring the effectiveness of the reported harvesters is to rate their power responses as a way of predicting the potential for commercial deployment or optimization research. Based on the modification of a model obtained from the work of Mitcheson et al [47], the maximum theoretical RMS power output from a vibration-based harvester can be derived using the $1/\sqrt{2}$ root-mean-square rule, as

$$P_{\max} = \frac{1.4\mathrm{Y}_0\mathrm{Z}_0(2\pi f)^3\mathrm{m}}{\pi} \tag{98}$$

where Y_0 is the displacement amplitude of the base shaker, Z_0 is the displacement amplitude of the harvester, f is the resonance frequency (in Hz), and m is the mass of the moving part

of the harvester. The harvester performance (H.P) can therefore be estimated as a value between 0 and 1 thus:

$$\text{H. P} = \frac{P_{actual}}{P_{\max}} \tag{99}$$

where P_{actual} is the actual RMS power output from the harvester. Based on this performance rating, the values for each harvester's performance (at the harvester's resonance) were obtained as shown in Table 15. All values used in the calculations were obtained experimentally.

It should be noted that the analysis of the harvester performances does not account for the material limitations (especially PVDF piezoelectric properties). As a result, some room is left available for improvement in designing the harvesters as well as in developing highly efficient energy harvesting materials.

Table 15: Performance rating for the experimentally characterized harvesters in this thesis

Harvester Name	**Acc. (g)**	**Y_0 (mm)**	**Z_0 (mm)**	**f (Hz)**	**m (g)**	**P_{max} (μW)**	**P_{actual} (μW)**	**H.P (%)**
MEMS ABC Bimorph	1	0.59	2.2	23	1.1e-2	23.2	1.24e-3	0.053
MEMS ABC Unimorph	1	0.57	1.1	33	2.5e-2	62.2	1.71e-3	0.027
LIVE Harvester	0.25	3.5	15	13	7.29	95300	6000	6.3
MEMS LIVE Harvester	0.2	1	1.25	16	0.72	419.4	191	45.54
Coupled MEMS (Piezo part)	1	0.53	2	22	0.72	20.95	4.1e-3	0.19
Coupled MEMS (Electromagnetic part)	0.2	1.6	1.8	22	0.72	2400	1100	46

From the performance results obtained, it can be seen that the electromagnetic harvesters outperform the piezoelectric/magnetoelectric harvesters. The main reason for this difference is the poor piezoelectric properties of the PVDF used. Since the performance equation does not account for material limitations, the effect of the PVDF is not estimated. It is therefore obvious that that cantilever-based harvesters can be optimized further (from a materials standpoint). For the electromagnetic harvesters, more room for improvement only seems reasonable for larger sizes (slightly greater than MEMS scale), since the MEMS electromagnetic harvesters are already performing at about half of their maximum capacities.

7.2.2 Future Outlook

From the performance calculations, it can be concluded that further work should be carried out on the cantilever-based harvesters and the LIVE harvester. For the cantilever-based harvesters (both piezoelectric and magnetoelectric), the power response can be significantly improved by carrying out MEMS-based fabrication using thin PZT (< 1μm thick) as the piezoelectric material. This would also enable the production of several harvesters on a wafer, thereby speeding up the fabrication process. Furthermore, interdigitated electrodes (IDEs) can be applied to improve the d_{33} energy harvesting potential in magnetic field environment.

For the LIVE harvester, more work can be done to minimize friction within the harvester. However, this is difficult to do so, since the requirement of magnetic pole alignment within the tube means that a center pole is always required. Furthermore, it is obvious from the coupled harvester results that electromagnetic harvesters benefit significantly when a

different vibration-based mechanism is present within the same device. Therefore, more research should be carried out to incorporate a voltage mechanism that would match the output response of the electromagnetic part (piezoelectric additions currently produce several orders of magnitude less power) and therefore increase the overall output power.

More research can still be done in MEMS energy harvesting. For cantilever-based harvesters, unique geometries which exhibit low natural frequencies and significant power response should continue to be developed in the MEMS and NEMS scale as opposed to the use of tip masses. Also, other voltage generation mechanisms (e.g. electrochemical) should be incorporated to aid the desired increase in power output (up to mW) which has seemed so elusive thus far at the MEMS scale.

Bibliography

1. Zorlu, Ö. and H. Külah, *A MEMS-based energy harvester for generating energy from non-resonant environmental vibrations.* Sensors and Actuators A: Physical, 2013. **202**(0): p. 124-134.

2. Boisseau, S., et al., *Cantilever-based electret energy harvesters.* Smart Materials and Structures, 2011. **20**(10): p. 105013.

3. Karami, M.A. and D.J. Inman, *Analytical Modeling and Experimental Verification of the Vibrations of the Zigzag Microstructure for Energy Harvesting.* Journal of Vibration and Acoustics, 2011. **133**(1): p. 011002-10.

4. Timoshenko, S., *On the correction factor for shear of the differential equation for transverse vibrations of prismatic bars.* Philosophical Magazine, 1921. **41**: p. 744-746.

5. Timoshenko, S. and D.H. Young, *Elements of strength of materials*1968, Princeton, N.J.: Van Nostrand.

6. Erturk, A. and D.J. Inman, *An experimentally validated bimorph cantilever model for piezoelectric energy harvesting from base excitations.* Smart Materials and Structures, 2009. **18**(2): p. 025009.

7. Erturk, A. and D.J. Inman, *A Distributed Parameter Electromechanical Model for Cantilevered Piezoelectric Energy Harvesters.* Journal of Vibration and Acoustics, 2008. **130**(4): p. 041002-15.

8. Saha, C.R., et al., *Electromagnetic generator for harvesting energy from human motion.* Sensors and Actuators A: Physical, 2008. **147**(1): p. 248-253.

9. Tsutsumino, T., et al. *Seismic Power Generator Using High-Performance Polymer Electret*. in *Micro Electro Mechanical Systems, 2006. MEMS 2006 Istanbul. 19th IEEE International Conference on*. 2006.

10. Arakawa, Y., Y. Suzuki, and N. Kasagi. *Micro Seismic Power Generator Using Electret Polymer Film*. in *Proc. PowerMEMS*. 2004. Kyoto, Japan.

11. Tsutsumino, T., et al. *High-Performance Polymer Electret for Micro Seismic Generator*. in *Proc. PowerMEMS 2005*. 2005. Tokyo.

12. Tsutsumino, T., Y. Suzuki, and N. Kasagi. *Electromechanical Modeling of Micro Electret Generator for Energy Harvesting*. in *Solid-State Sensors, Actuators and Microsystems Conference, 2007. TRANSDUCERS 2007. International*. 2007.

13. Lo, H.-W. and Y.-C. Tai, *Parylene-based electret power generators.* Journal of Micromechanics and Microengineering, 2008. **18**(10).

14. Choi, W., et al., *Energy harvesting MEMS device based on thin film piezoelectric cantilevers.* Journal of Electroceramics, 2006. **17**(2): p. 543-548.

15. Liu, J.-Q., et al., *A MEMS-based piezoelectric power generator array for vibration energy harvesting.* Microelectronics Journal, 2008. **39**(5): p. 802-806.

16. Aktakka, E.E., R.L. Peterson, and K. Najafi. *Thinned-PZT on SOI process and design optimization for piezoelectric inertial energy harvesting*. in *Solid-State Sensors, Actuators and Microsystems Conference (TRANSDUCERS), 2011 16th International*. 2011.

17. Hajati, A. and S.-G. Kim, *Ultra-wide bandwidth piezoelectric energy harvesting.* Applied Physics Letters, 2011. **99**(8): p. 083105-3.

18. Huicong, L., et al., *Piezoelectric MEMS Energy Harvester for Low-Frequency Vibrations With Wideband Operation Range and Steadily Increased Output Power.* Microelectromechanical Systems, Journal of, 2011. **20**(5): p. 1131-1142.

19. Tang, G., et al., *Piezoelectric MEMS low-level vibration energy harvester with PMN-PT single crystal cantilever.* Electronics Letters, 2012. **48**(13): p. 784-786.

20. Xu, R., et al., *Fabrication and characterization of MEMS-based PZT/PZT bimorph thick film vibration energy harvesters.* Journal of Micromechanics and Microengineering, 2012. **22**(9): p. 094007.

21. Jackson, N., et al. *CMOS compatible low-frequency aluminium nitride MEMS piezoelectric energy harvesting device*. 2013.

22. Kim, D., et al., *A spring-type piezoelectric energy harvester.* RSC Advances, 2013. **3**(10): p. 3194-3198.

23. Tsujiura, Y., et al. *Lead-free piezoelectric MEMS energy harvesters of stainless steel cantilevers*. in *Solid-State Sensors, Actuators and Microsystems (TRANSDUCERS & EUROSENSORS XXVII), 2013 Transducers & Eurosensors XXVII: The 17th International Conference on*. 2013.

24. Tsujiura, Y., et al. *Modeling of metal-based piezoelectric MEMS energy harvesters*. in *Micro-NanoMechatronics and Human Science (MHS), 2013 International Symposium on*. 2013.

25. Jackson, N., et al., *Evaluation of low-acceleration MEMS piezoelectric energy harvesting devices.* Microsystem Technologies, 2014. **20**(4-5): p. 671-680.

26. Janphuang, P., et al., *Vibrational piezoelectric energy harvesters based on thinned bulk PZT sheets fabricated at the wafer level.* Sensors and Actuators A: Physical, 2014. **210**(0): p. 1-9.

27. Liu, W., et al., *Low frequency wide bandwidth MEMS energy harvester based on spiral-shaped PVDF cantilever.* Science China Technological Sciences, 2014. **57**(6): p. 1068-1072.

28. Ching, N.N.H., et al., *A laser-micromachined multi-modal resonating power transducer for wireless sensing systems.* Sensors and Actuators A: Physical, 2002. **97–98**(0): p. 685-690.

29. Beeby, S.P., et al., *A micro electromagnetic generator for vibration energy harvesting.* Journal of Micromechanics and Microengineering, 2007. **17**(7): p. 1257.

30. Wang, P., W. Li, and L. Che, *Design and fabrication of a micro electromagnetic vibration energy harvester.* Journal of Semiconductors, 2011. **32**(10): p. 104009.

31. Cepnik, C. and U. Wallrabe. *A micro energy harvester with 3D wire bonded microcoils*. in *Solid-State Sensors, Actuators and Microsystems Conference (TRANSDUCERS), 2011 16th International*. 2011.

32. Huicong, L., et al., *Feasibility study of a 3D vibration-driven electromagnetic MEMS energy harvester with multiple vibration modes.* Journal of Micromechanics and Microengineering, 2012. **22**(12): p. 125020.

33. Bang, D.-H. and J.-Y. Park, *Bulk Micromachined Vibration Driven Electromagnetic Energy Harvesters for Self-sustainable Wireless Sensor Node Applications.* Journal of Electrical Engineering and Technology, 2013. **8**(6): p. 1320-1327.

34. Li, M., et al., *A resonant frequency self-tunable rotation energy harvester based on magnetoelectric transducer.* Sensors and Actuators A: Physical, 2013. **194**(0): p. 16-24.

35. Liu, H., Y. Qian, and C. Lee, *A multi-frequency vibration-based MEMS electromagnetic energy harvesting device.* Sensors and Actuators A: Physical, 2013. **204**(0): p. 37-43.

36. Shih-Jui, C., W. Jia-Yin, and L. Shu-Yu. *Electromagnetic energy harvester with an in-phase vibration bandwidth broadening technique*. in *Micro Electro Mechanical Systems (MEMS), 2014 IEEE 27th International Conference on*. 2014.

37. Mengdi, H., et al. *Springless cubic harvester for converting three dimensional vibration energy*. in *Micro Electro Mechanical Systems (MEMS), 2014 IEEE 27th International Conference on*. 2014.

38. Lei, Y., Z. Wen, and L. Chen, *Simulation and testing of a micro electromagnetic energy harvester for self-powered system.* AIP Advances, 2014. **4**(3): p. -.

39. Miki, D., et al. *Large-amplitude MEMS electret generator with nonlinear spring*. in *Micro Electro Mechanical Systems (MEMS), 2010 IEEE 23rd International Conference on*. 2010.

40. Triches, M., et al., *A MEMS Energy Harvesting Device for Vibration with Low Acceleration.* Procedia Engineering, 2012. **47**(0): p. 770-773.

41. Andrea, C., W. Fei, and H. Ole, *An electret-based energy harvesting device with a wafer-level fabrication process.* Journal of Micromechanics and Microengineering, 2013. **23**(11): p. 114010.

42. Yu, J., et al., *Parametrically excited MEMS vibration energy harvesters with design approaches to overcome the initiation threshold amplitude.* Journal of Micromechanics and Microengineering, 2013. **23**(11): p. 114007.

43. Minakawa, Y., C. Rui, and Y. Suzuki. *X-shaped-spring enhanced MEMS electret generator for energy harvesting*. in *Solid-State Sensors, Actuators and Microsystems (TRANSDUCERS & EUROSENSORS XXVII), 2013 Transducers & Eurosensors XXVII: The 17th International Conference on*. 2013.

44. Wang, F. and O. Hansen, *Electrostatic energy harvesting device with out-of-the-plane gap closing scheme.* Sensors and Actuators, A: Physical, 2014. **211**: p. 131-137.

45. Cottone, F., et al. *Electrostatic generator with free micro-ball and elastic stoppers for low-frequency vibration harvesting*. in *Micro Electro Mechanical Systems (MEMS), 2014 IEEE 27th International Conference on*. 2014.

46. Tao, K., et al. *A three-dimensional electrostatic/electret micro power generator for low acceleration and low frequency vibration energy harvesting*. in *Micro Electro Mechanical Systems (MEMS), 2014 IEEE 27th International Conference on*. 2014.

47. Mitcheson, P.D., et al., *Performance limits of the three MEMS inertial energy generator transduction types.* Journal of Micromechanics and Microengineering, 2007. **17**(9): p. S211.

48. Ojalvo, I.U., *Coupled twist-bending vibrations of incomplete elastic rings.* International Journal of Mechanical Sciences, 1962. **4**(1): p. 53-72.

49. Culver, C.G. and D.J. Oestel, *Natural frequencies of multispan curved beams.* Journal of Sound and Vibration, 1969. **10**(3): p. 380-389.

50. Philipson, L.L., *On the role of extension in the flexural vibrations of rings.* Journal of Applied Mechanics, 1956. **23**: p. 364-366.

51. Seidal, B.S. and E.A. Erdelyi, *On the vibrations of a thick ring in its own plane.* Journal of Engineering for Industry, 1964. **86**: p. 240-244.

52. Rao, S.S. and V. Sundararajan, *In-Plane Flexural Vibrations of Circular Rings.* Journal of Applied Mechanics, 1969. **36**(3): p. 620-625.

53. Rao, S.S., *Effects of transverse shear and rotatory inertia on the coupled twist-bending vibrations of circular rings.* Journal of Sound and Vibration, 1971. **16**(4): p. 551-566.

54. Wang, T.M., R.H. Nettleton, and B. Keita, *Natural frequencies for out-of-plane vibrations of continuous curved beams.* Journal of Sound and Vibration, 1980. **68**(3): p. 427-436.

55. Tung-Ming, W., A.J. Laskey, and M.F. Ahmad, *Natural frequencies for out-of-plane vibrations of continuous curved beams considering shear and rotary inertia.* International Journal of Solids and Structures, 1984. **20**(3): p. 257-265.

56. Howson, W. and A. Jemah, *Exact Out-of-Plane Natural Frequencies of Curved Timoshenko Beams.* Journal of Engineering Mechanics, 1999. **125**(1): p. 19-25.

57. Lee, S.Y. and J.C. Chao, *OUT-OF-PLANE VIBRATIONS OF CURVED NON-UNIFORM BEAMS OF CONSTANT RADIUS.* Journal of Sound and Vibration, 2000. **238**(3): p. 443-458.

58. Rao, S.S., *Vibration of continuous systems*2007, Hoboken, N.J.: Wiley.

59. Blevins, R.D., *Formulas for natural frequency and mode shape*1979, New York: Van Nostrand Reinhold Co.

60. Apo, D.J., M. Sanghadasa, and S. Priya, *Vibration modeling of arc-based cantilevers for energy harvesting applications.* Energy Harvesting and Systems, 2014. **1**(1): p. 1-12.

61. Zhou, Y., D.J. Apo, and S. Priya, *Dual-phase self-biased magnetoelectric energy harvester.* Applied Physics Letters, 2013. **103**(19): p. -.

62. Liu, H., et al., *Piezoelectric MEMS-based wideband energy harvesting systems using a frequency-up-conversion cantilever stopper.* Sensors and Actuators A: Physical, 2012. **186**(0): p. 242-248.

63. Wang, Z., et al. *Large power amplification of a piezoelectric energy harvester excited by random vibrations*. in *Micro Electro Mechanical Systems (MEMS), 2013 IEEE 26th International Conference on*. 2013.

64. Deterre, M., et al. *Micromachined piezoelectric spirals and ultra-compliant packaging for blood pressure energy harvesters powering medical implants*. in *Micro Electro Mechanical Systems (MEMS), 2013 IEEE 26th International Conference on*. 2013.

65. Apo, D.J., M. Sanghadasa, and S. Priya. *Low frequency arc-based MEMS structures for vibration energy harvesting*. in *Nano/Micro Engineered and Molecular Systems (NEMS), 2013 8th IEEE International Conference on*. 2013.

66. Polytec. Available from: www.polytec.com.

67. PCB-Piezotronics. Available from: www.pcb.com.

68. SigLab. Available from: www.spectraldynamics.com.

69. MathWorks. Available from: www.mathworks.com.

70. ANSYS, *Element Reference v15.* ANSYS Inc, 2013.

71. Hitachi-Metals. Available from: www.hitachimetals.com.

72. Measurement-Specialties. Available from: www.meas-spec.com.

73. Optomec. Available from: www.optomec.com.

74. Singh, S.P., et al., *Measurement and Analysis of Vibration and Temperature Levels in Global Intermodal Container Shipments on Truck, Rail and Ship.* Packaging Technology and Science, 2012. **25**(3): p. 149-160.

75. Marin, A., S. Bressers, and S. Priya, *Multiple cell configuration electromagnetic vibration energy harvester.* Journal of Physics D: Applied Physics, 2011. **44**(29): p. 295501.

76. Mann, B.P. and N.D. Sims, *Energy harvesting from the nonlinear oscillations of magnetic levitation.* Journal of Sound and Vibration, 2009. **319**(1–2): p. 515-530.

77. Dallago, E., M. Marchesi, and G. Venchi, *Analytical Model of a Vibrating Electromagnetic Harvester Considering Nonlinear Effects.* Power Electronics, IEEE Transactions on, 2010. **25**(8): p. 1989-1997.

78. Tornincasa, S., et al., *Optimization of magneto-mechanical energy scavenger for automotive tire.* Journal of Intelligent Material Systems and Structures, 2012. **23**(18): p. 2055-2064.

79. Marin, A., et al. *Improved pen harvester for powering a pulse rate sensor*. 2012. San Diego, California, USA: SPIE.

80. Marin, A., et al., *Multimodal Vibration Harvester Using Inductive and Magnetostrictive Mechanisms.* Integrated Ferroelectrics, 2011. **125**(1): p. 111-122.

81. Marin, A., Y. Yongke, and S. Priya. *Combinatory piezoelectric and inductive vibration energy harvesters*. in *Applications of Ferroelectrics held jointly with 2012 European Conference on the Applications of Polar Dielectrics and 2012 International Symp Piezoresponse Force Microscopy and Nanoscale Phenomena in Polar Materials (ISAF/ECAPD/PFM), 2012 Intl Symp*. 2012.

82. Zavodney, L.D. and A.H. Nayfeh, *The non-linear response of a slender beam carrying a lumped mass to a principal parametric excitation: Theory and experiment.* International Journal of Non-Linear Mechanics, 1989. **24**(2): p. 105-125.

83. Cepnik, C., et al., *Effective optimization of electromagnetic energy harvesters through direct computation of the electromagnetic coupling.* Sensors and Actuators A: Physical, 2011. **167**(2): p. 416-421.

84. Byung-Chul, L., et al., *Low frequency driven electromagnetic energy harvester for self-powered system.* Smart Materials and Structures, 2012. **21**(12): p. 125024.

85. Hatipoglu, G. and H. Urey, *FR4-based electromagnetic energy harvester for wireless tyre sensor nodes.* Procedia Chemistry, 2009. **1**(1): p. 1211-1214.

86. Shuo, C. and P.A. David, *A study of a multi-pole magnetic generator for low-frequency vibrational energy harvesting.* Journal of Micromechanics and Microengineering, 2010. **20**(2): p. 025015.

87. Marin, A., et al., *Broadband electromagnetic vibration energy harvesting system for powering wireless sensor nodes.* Smart Materials and Structures, 2013. **22**(7): p. 075008.

88. von Büren, T. and G. Tröster, *Design and optimization of a linear vibration-driven electromagnetic micro-power generator.* Sensors and Actuators A: Physical, 2007. **135**(2): p. 765-775.

89. Wang, P., et al., *Design, simulation, fabrication and characterization of a micro electromagnetic vibration energy harvester with sandwiched structure and air channel.* Microelectronics Journal, 2012. **43**(2): p. 154-159.

90. Pan, C.T., et al., *Fabrication and analysis of a magnetic self-power microgenerator.* Journal of Magnetism and Magnetic Materials, 2006. **304**(1): p. e394-e396.

91. Wang, X.Y., et al., *A magnetically levitated vibration energy harvester.* Smart Materials and Structures, 2013. **22**(5): p. 055016.

92. Apo, D.J. and S. Priya, *High Power Density Levitation-Induced Vibration Energy Harvester.* Energy Harvesting and Systems, 2014.

93. Vokoun, D., et al., *Magnetostatic interactions and forces between cylindrical permanent magnets.* Journal of Magnetism and Magnetic Materials, 2009. **321**(22): p. 3758-3763.

94. Ramsay, M.J. and W.W. Clark, *Piezoelectric energy harvesting for bio-MEMS applications.* 2001: p. 429-438.

95. Apo, D.J., et al. *PIEZOCAP: A high power density vibration energy harvester*. in *PowerMEMS*. 2012. Atlanta, U.S.A.

Appendix A:

Published Work

Journal Publications

1. Apo, Daniel J. and Priya, Shashank; “Review of Low Frequency MEMS Energy Harvesting”. *In Preparation*
2. Apo, Daniel J.; Zhou, Yuan; Maurya, Deepam, Sanghadasa, Mohan; Priya, Shashank; “MEMS hybrid harvester with electromagnetic and piezoelectric components”. *In Preparation*
3. Apo, Daniel J. and Priya, Shashank; “MEMS electromagnetic energy harvester with nonlinear inflection profile”. *In Preparation*
4. Apo, Daniel J.; Zhou, Yuan; Maurya, Deepam, Sanghadasa, Mohan; Priya, Shashank; “Magnetoelectric MEMS device for low-frequency dual-phase energy harvesting independent of magnetic DC field”. *In Preparation*
5. Apo, Daniel J.; Zhou, Yuan; Sanghadasa, Mohan; Priya, Shashank; “Vibration characteristics of low frequency arc-based microcantilevers"; *AIP Advances,* Submitted June 2014.
6. Apo, Daniel J. and Shashank Priya. "High Power Density Levitation-Induced Vibration Energy Harvester" *Energy Harvesting and Systems*, 1.1-2 (2014): 79-88. doi:10.1515/ehs-2013-0005
7. Apo, Daniel J., Mohan Sanghadasa and Shashank Priya. "Vibration Modeling of Arc-Based Cantilevers for Energy Harvesting Applications" *Energy Harvesting and Systems*, 1.1-2 (2014): 57-68. doi:10.1515/ehs-2013-0002
8. Zhou, Yuan; Apo, Daniel J.; Priya, Shashank, “Dual-phase self-biased magnetoelectric energy harvester," *Applied Physics Letters*, vol.103, no.20, Nov 2013
9. Zhou, Yuan; Chul Yang, Su; Apo, Daniel J.; Maurya, Deepam; Priya, Shashank, "Tunable self-biased magnetoelectric response in homogenous laminates," *Applied Physics Letters* , vol.101, no.23, pp.232905,232905-5, Dec 2012

Patent Disclosure

10. Daniel J. Apo, Shashank Priya, Mohan Sanghadasa. "Arc-Based Structures for Low Frequency Vibration Energy Harvesting". U.S. Patent Application No: 61/808,841 (File Date: 4/5/2013). *Provisional Patent.*

Conference Proceedings

11. Daniel J. Apo and Shashank Priya, "Levitation-induced vibration energy harvesting," *Motion and Vibration Control, 2014 12th International Conference on*, 4-6 August 2014
12. Daniel J. Apo, Mohan Sanghadasa, and Shashank Priya, "Low Frequency Arc-Based MEMS Structures for Vibration Energy Harvesting," *Nano/Micro Engineered and Molecular Systems (NEMS), 2013 8th IEEE International Conference on*, 7-10 April 2013
13. Patrick Kirchen, Daniel J. Apo, Anton Hunt, Ahmed F. Ghoniem, *A novel ion transport membrane reactor for fundamental investigations of oxygen permeation and oxy-combustion under reactive flow conditions*, Proceedings of the Combustion Institute, Volume 34, Issue 2, 2013, Pages 3463-3470, ISSN 1540-7489, 10.1016/j.proci.2012.07.076.
14. Apo, D.J.; Varghese, R.; Sanghadasa, M.; Priya, S.; PIEZOCAP: A High Power Density Vibration Energy Harvester, Proceedings Power MEMS, 2012.

Book Chapters

15. Cary Baur, Daniel J. Apo, Deepam Maurya, and Shashank Priya. "*Advances in Piezoelectric Polymer Composites for Vibrational Energy Harvesting*" in "Polymer Composites for Energy Harvesting, Conversion, and Storage", Book chapter submitted Jan 2014.
16. Zhou, Yuan; Apo, Daniel J.; Bichurin, Mirza; Priya, Shashank; "*Magnetoelectric Energy Harvester*"; Book chapter submitted June 2014.
17. Daniel J. Apo, Jungho Ryu, Shuxiang Dong, Shashank Priya, "*Applications of Magnetoelectrics";* Book chapter submitted June 2014

Theses

18. Daniel J. Apo; *Low Frequency Microscale Energy Harvesting;* Doctor of philosophy (PhD) thesis; Virginia Polytechnic Institute and State University (Virginia Tech), June 2014.
19. Daniel J. Apo; *Experimental characterization of an Ion Transport Membrane (ITM) reactor for methane oxyfuel combustion;* Master of Science (S.M) thesis; Massachusetts Institute of Technology, Feb 2012.

Appendix B:

Method of Microcantilever Fabrication

The method used in this work for fabricating MEMS cantilevers is unique and is dissimilar to conventional MEMS fabrication techniques. This unique method will be presented here to provide an alternative when MEMS fabrication techniques become too expensive, lengthy or difficult to carry out.

The process involves epoxy bonding, material micromilling and laser processing of the micromilled material. Firstly, the individual material layers (except the polymer materials) are cut into square shapes of 2" x 2". Then, the layers are bonded together under applied pressure with Loctite® epoxy and left to completely bond for two days. Thereafter, a tool path based on the intended harvester shape is designed using a CAD software (e.g. Unigraphics or SolidWorks). This tool path is fed into a CNC machine computer and is used by the CNC machine to cut the desired shape. Then, the polymer piezoelectric (PVDF) of size 2" by 2" is bonded under applied pressure with Loctite® epoxy onto the already machined structure. The machined shape is used as a guide for the PVDF during the next step (laser cutting). An Aerosol Jet printing system (Optomec) equipped with an 830 nm continuous wave Yb-fiber laser is used to make the desired pattern on the PVDF attached on the already cut structure. The current in the laser source can be varied from 0.2-2 Amp maximum. The PVDF sample is kept on a stage capable of moving in XYZ directions with speed in the range

of 0.01-15 mm/s. The speed and current are also optimized to get nice clean patterned surface of PVDF.

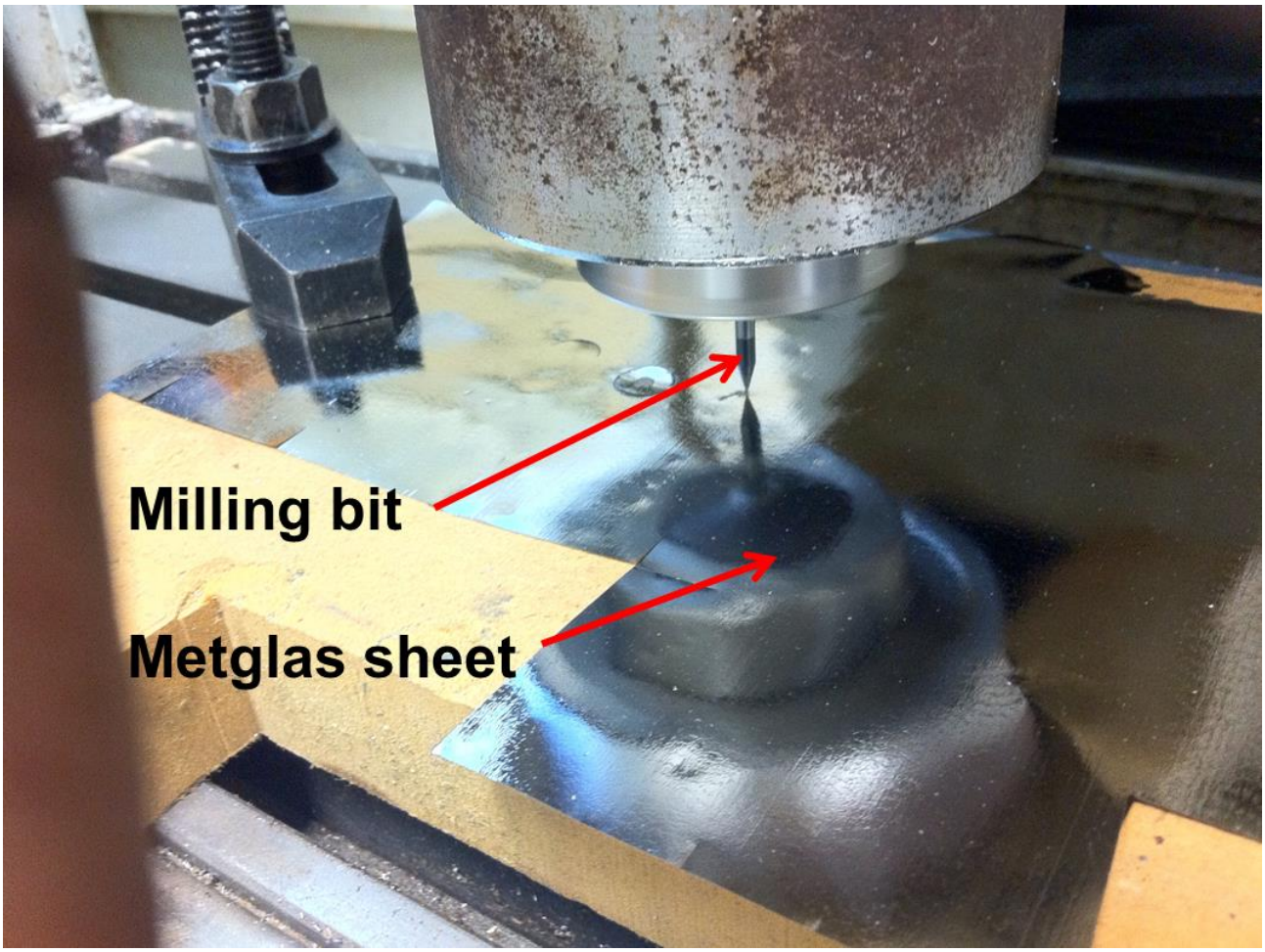

Figure 62: Micromilling of the base metglas structure

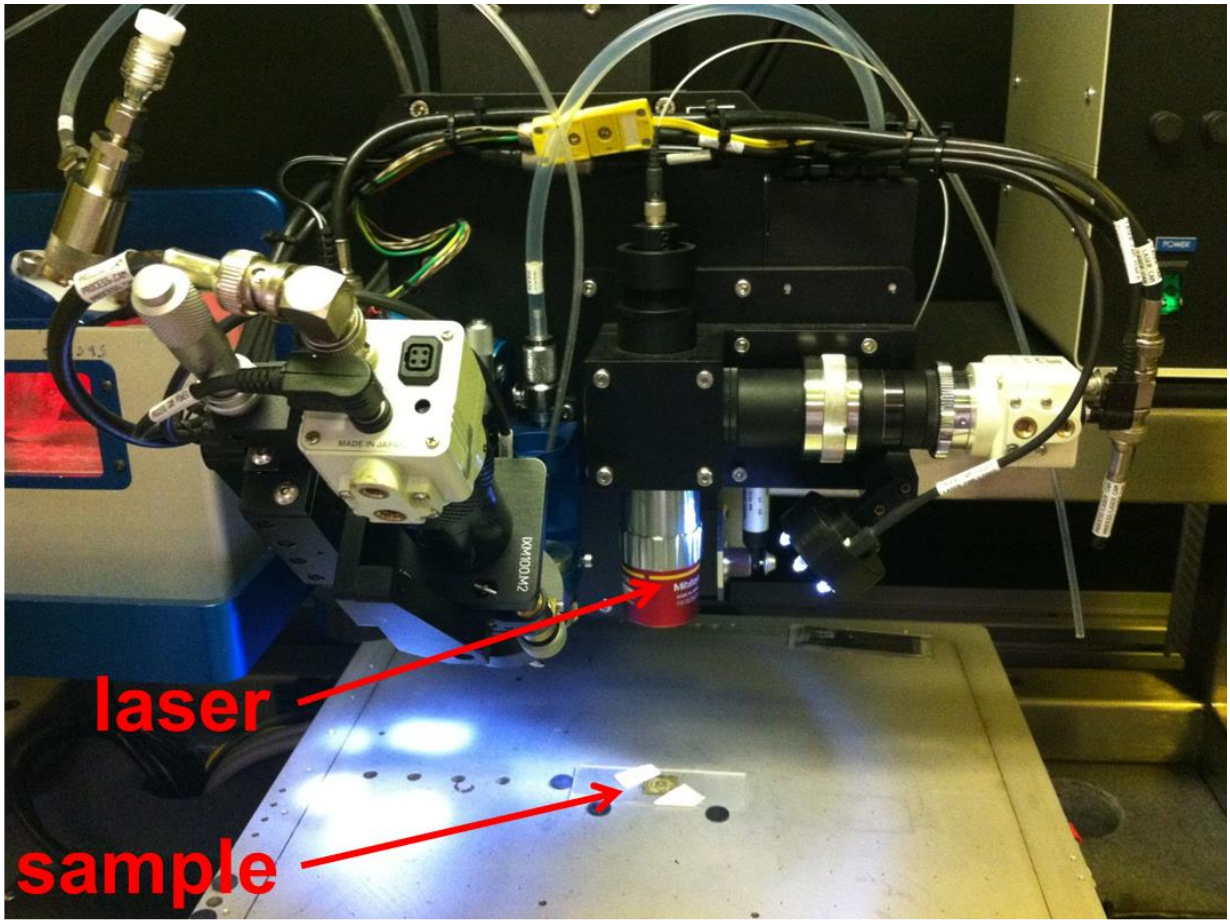

Figure 63: Laser cutting of the PVDF layer

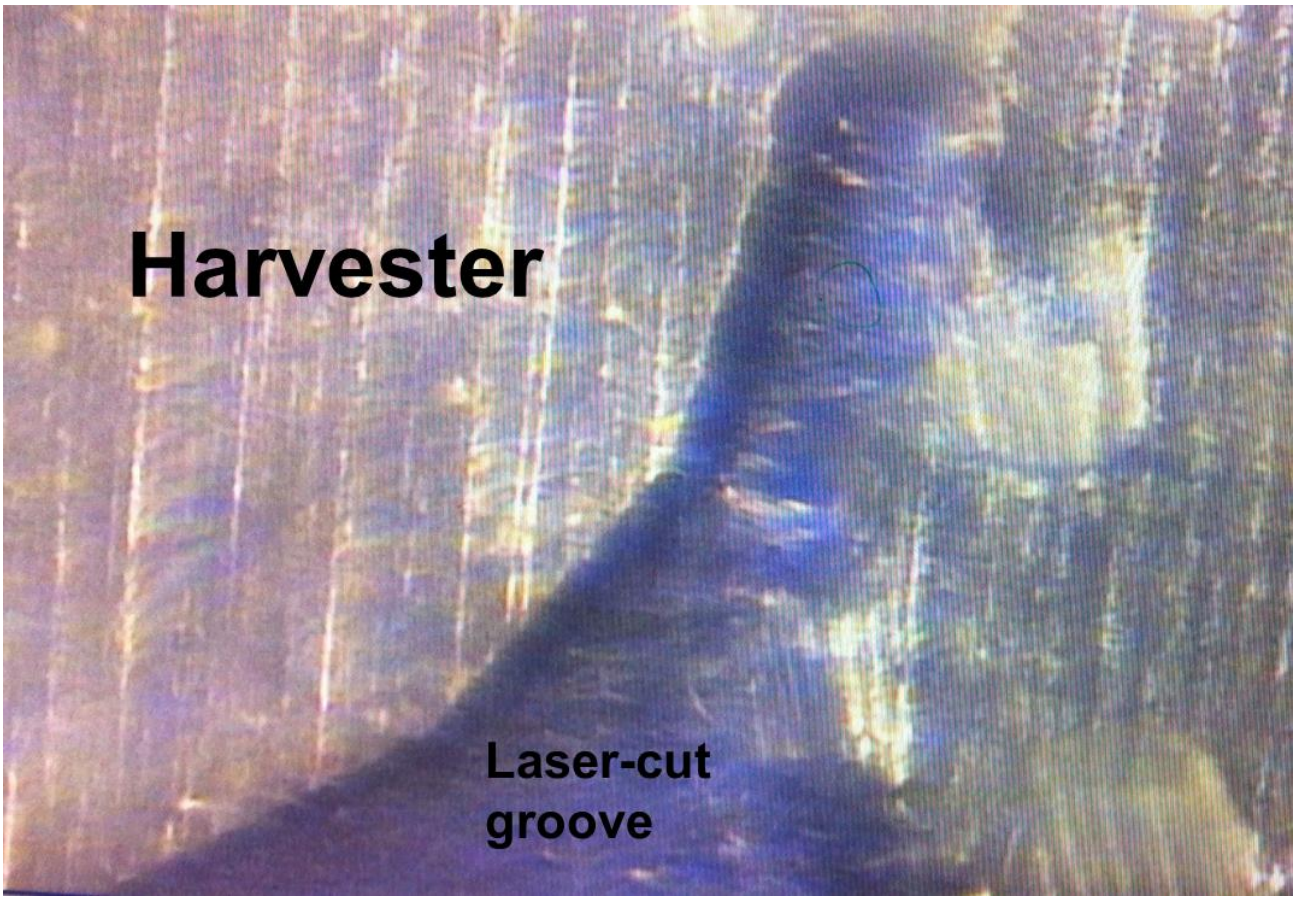

Figure 64: Laser-cut groove

Appendix C:

Modeling Code

Matlab codes for modeling of an arc-based cantilever and for the LIVE harvester are provided here. Also, finite element codes (ANSYS) for estimating the magnetic flux and force fields for the LIVE harvester are presented. These sections serve as the modeling framework used for developing the modeling code for the other harvesters/structures in this work.

C.1 Matlab code for the arc-based cantilever in chapter 2.2

```
%% Script for vibration modeling of an arc-based cantilever


%%%%%%%%%%%%%%%%%%%%%%%%%%%%%%
% Daniel Apo (11/01/2012)
%%%%%%%%%%%%%%%%%%%%%%%%%%%%%%


W = 10e-3;   %width of each member

DETMMlist = [];
div =1e1;
for omega = 2*pi*10:2*pi/div:2*pi*800; %frequency in rad/s
%Micro beam = 2*pi*43.064156422487
%% Individual beam characteristics

%beam 1
th1 = 90*pi/180;
[BeamS1 BeamSC1 BeamE1 BeamEC1] = ModelProp(omega,th1,W);

%beam 2
th2 = 180*pi/180;
[BeamS2 BeamSC2 BeamE2 BeamEC2] = ModelProp(omega,th2,W);

%beam 3
th3 = 135*pi/180;
[BeamS3 BeamSC3 BeamE3 BeamEC3] = ModelProp(omega,th3,W);
```

```
%% Matrices

%Clamped end matrix
BEa = [BeamE1(1,:);BeamE1(2,:);BeamE1(3,:)];

%Free end matrix
BEb = [BeamS3(4,:);BeamS3(5,:);BeamS3(6,:)];

%Continuity matrices
CE1 = BeamS1;
CS2 = BeamSC2;
CE2 = BeamE2;
CS3 = BeamEC3;
CSE = (CS3\CE2)*(CS2\CE1);

CSEE = BEb*CSE;
MM = vertcat(BEa,CSEE);


DETMM = det(MM);
DETMMlist = [DETMMlist; [omega/(2*pi) DETMM]];
disp('omega is complete')
disp(omega)
end

VV = real(DETMMlist(:,2));
UU = find(VV==0);
xxxx = min(DETMMlist(:,2));

plot(DETMMlist(:,1),abs(DETMMlist(:,2)).^-1)


%% Mode shapes

MMre = [MM(:,1), MM(:,2), MM(:,3), MM(:,4), MM(:,5)]; %first 5 columns of MM
MMred = [MMre(1,:); MMre(2,:); MMre(3,:); MMre(4,:); MMre(5,:)]; %first 5
rows of MMre
MMc = -MM(:,6); %the 6th column of MM moves to the RHS
MMcon = [MMc(1); MMc(2); MMc(3); MMc(4); MMc(5)]; %MMc is reduced to the same
size as MMred
A1red = MMred\MMcon; %mode shape vector of arc 1 without the 6th entry (A16)
A1 = [A1red;1]; %complete mode shape vector of arc 1
A1r = abs(A1);
A1n = sum(A1);

A2 = (CS2\CE1)*A1;
A2r = abs(A2);
A2n = sum(A2);

A3 = (CS3\CE2)*A2;
A3r = abs(A3);
A3n = sum(A3);
```

```
function [BeamS BeamSC BeamE BeamEC] = ModelProp(omega,th,W)

% General Properties
H = 0.4064e-3;       %adjustable thickness of cantilever
Y = 70E9;      %Young's modulus
rho = 2700;     %density
nu = 0.35; %Poisson's ratio
G = Y/(2*(1+nu));     %shear modulus
Rc = 10e-3; %Center radius of all arcs

I = W*H^3/12;   %area moment of inertia about x-axis
%Iy = H*W^3/12;   %area moment of inertia about y-axis
J = W*H^3/16*((16/3)-3.36*H/W*(1-(H^4/(W^4*12))));        %polar moment of
inertia
A = W*H;        %cross-sectional area
%mu = rho*A;     %mass per unit length
k = G*J/(Y*I);  %stiffness parameter
eta = 10*(1+nu)/(12+11*nu); %shear coefficient (pg 173 of Blevins text & In
cowper article)
% Ro = Rc+W/2;
% Ri = Rc-W/2;
R = Rc; %sqrt((Ro-Ri)*(Ro+Ri));


u = rho*R^2*omega^2/G;
m = 2;
n = 1-rho*A*R^4*omega^2/(Y*I);
q = rho*A*R^4*omega^2/(G*J);

% g represents gamma
% th represents theta

poly = [1 0 m 0 n 0 q];
g = roots(poly);

b1 = (1/R)*(g(1)+u/(eta*g(1)));
b2 = (1/R)*(g(2)+u/(eta*g(2)));
b3 = (1/R)*(g(3)+u/(eta*g(3)));
b4 = (1/R)*(g(4)+u/(eta*g(4)));
b5 = (1/R)*(g(5)+u/(eta*g(5)));
b6 = (1/R)*(g(6)+u/(eta*g(6)));
b = [b1 b2 b3 b4 b5 b6];

c1 = b1*g(1)*((1+k)/(1-k*u-g(1)^2*k));
c2 = b2*g(2)*((1+k)/(1-k*u-g(2)^2*k));
c3 = b3*g(3)*((1+k)/(1-k*u-g(3)^2*k));
c4 = b4*g(4)*((1+k)/(1-k*u-g(4)^2*k));
c5 = b5*g(5)*((1+k)/(1-k*u-g(5)^2*k));
c6 = b6*g(6)*((1+k)/(1-k*u-g(6)^2*k));
c = [c1 c2 c3 c4 c5 c6];
```

```
BeamS = [ones(1,6);    b;     c;
    (c1-b1*g(1))/R (c2-b2*g(2))/R,...
    (c3-b3*g(3))/R (c4-b4*g(4))/R,...
    (c5-b5*g(5))/R (c6-b6*g(6))/R;
    (b1+c1*g(1))/R (b2+c2*g(2))/R,...
    (b3+c3*g(3))/R (b4+c4*g(4))/R,...
    (b5+c5*g(5))/R (b6+c6*g(6))/R;
    g(1)/R-b(1)  g(2)/R-b(2),...
    g(3)/R-b(3)  g(4)/R-b(4),...
    g(5)/R-b(5)  g(6)/R-b(6)];

BeamSC = [ones(1,6);    b;     c;
    -(c1-b1*g(1))/R -(c2-b2*g(2))/R,...
    -(c3-b3*g(3))/R -(c4-b4*g(4))/R,...
    -(c5-b5*g(5))/R -(c6-b6*g(6))/R;
    -(b1+c1*g(1))/R -(b2+c2*g(2))/R,...
    -(b3+c3*g(3))/R -(b4+c4*g(4))/R,...
    -(b5+c5*g(5))/R -(b6+c6*g(6))/R;
    -(g(1)/R-b(1))  -(g(2)/R-b(2)),...
    -(g(3)/R-b(3))  -(g(4)/R-b(4)),...
    -(g(5)/R-b(5))  -(g(6)/R-b(6))];

BeamE = [exp(g(1)*th)  exp(g(2)*th)  exp(g(3)*th),...
    exp(g(4)*th)  exp(g(5)*th)  exp(g(6)*th);
    b1*exp(g(1)*th)  b2*exp(g(2)*th)  b3*exp(g(3)*th),...
    b4*exp(g(4)*th)  b5*exp(g(5)*th)  b6*exp(g(6)*th);
    c1*exp(g(1)*th)  c2*exp(g(2)*th)  c3*exp(g(3)*th),...
    c4*exp(g(4)*th)  c5*exp(g(5)*th)  c6*exp(g(6)*th);
    (c1-b1*g(1))*exp(g(1)*th)/R   (c2-b2*g(2))*exp(g(2)*th)/R,...
    (c3-b3*g(3))*exp(g(3)*th)/R   (c4-b4*g(4))*exp(g(4)*th)/R,...
    (c5-b5*g(5))*exp(g(5)*th)/R   (c6-b6*g(6))*exp(g(6)*th)/R;
    (b1+c1*g(1))*exp(g(1)*th)/R   (b2+c2*g(2))*exp(g(2)*th)/R,...
    (b3+c3*g(3))*exp(g(3)*th)/R   (b4+c4*g(4))*exp(g(4)*th)/R,...
    (b5+c5*g(5))*exp(g(5)*th)/R   (b6+c6*g(6))*exp(g(6)*th)/R;
    (g(1)/R-b(1))*exp(g(1)*th)   (g(2)/R-b(2))*exp(g(2)*th),...
    (g(3)/R-b(3))*exp(g(3)*th)   (g(4)/R-b(4))*exp(g(4)*th),...
    (g(5)/R-b(5))*exp(g(5)*th)   (g(6)/R-b(6))*exp(g(6)*th)];

BeamEC = [exp(g(1)*th)  exp(g(2)*th)  exp(g(3)*th),...
    exp(g(4)*th)  exp(g(5)*th)  exp(g(6)*th);
    b1*exp(g(1)*th)  b2*exp(g(2)*th)  b3*exp(g(3)*th),...
    b4*exp(g(4)*th)  b5*exp(g(5)*th)  b6*exp(g(6)*th);
    c1*exp(g(1)*th)  c2*exp(g(2)*th)  c3*exp(g(3)*th),...
    c4*exp(g(4)*th)  c5*exp(g(5)*th)  c6*exp(g(6)*th);
    -(c1-b1*g(1))*exp(g(1)*th)/R   -(c2-b2*g(2))*exp(g(2)*th)/R,...
    -(c3-b3*g(3))*exp(g(3)*th)/R   -(c4-b4*g(4))*exp(g(4)*th)/R,...
    -(c5-b5*g(5))*exp(g(5)*th)/R   -(c6-b6*g(6))*exp(g(6)*th)/R;
    -(b1+c1*g(1))*exp(g(1)*th)/R   -(b2+c2*g(2))*exp(g(2)*th)/R,...
    -(b3+c3*g(3))*exp(g(3)*th)/R   -(b4+c4*g(4))*exp(g(4)*th)/R,...
    -(b5+c5*g(5))*exp(g(5)*th)/R   -(b6+c6*g(6))*exp(g(6)*th)/R;
    -(g(1)/R-b(1))*exp(g(1)*th)   -(g(2)/R-b(2))*exp(g(2)*th),...
    -(g(3)/R-b(3))*exp(g(3)*th)   -(g(4)/R-b(4))*exp(g(4)*th),...
    -(g(5)/R-b(5))*exp(g(5)*th)   -(g(6)/R-b(6))*exp(g(6)*th)];
```

C.2 Matlab code for the LIVE harvester in chapter 4

```
%% Script for solving the Battery harvester system


%%%%%%%%%%%%%%%%%%%%%%%%%%%%%
% Daniel Apo (07/16/2013)
%%%%%%%%%%%%%%%%%%%%%%%%%%%%%


%% Magnetic field strength(s)

% relevant z regions
dic = 0.2e-3; %coil (and B*L vector) discretizing thickness (-12mmm to 12mm
displacement)
za = -60*dic:dic:60*dic; %do not modify
zb = za;
zc = za;

[Ba Bb Bc] = BattBField(za, zb, zc);
%% Resistance Values

cf = 0.53; %coil factor for all configurations
wd = 44e-6; %wire diameter for all configurations
HHa = 0.0152875; %height of center magnet in no opposing config
HHb = 7.39375e-3; %height of one center magnet in single opposing config
HHc = 4.7625e-3; %height of one center magnet in single opposing config
Mod = 9.525e-3; %center magnet outer diameter
Mid = 3.175e-3; %center magnet internal diameter
HHs = 0.5e-3; %height of steel divider

crpm = 14.43; %coil resistance per meter
cod = 14e-3; %coil outer diameter
cid = 11e-3; %coil internal diameter



%a
LLc = cf*pi*((cod^2-cid^2)/4)*dic/(pi*wd^2/4); %length of coil occupying dic
mm thickness
Rec = crpm*LLc*2*HHc/dic; %total coil resistance
Rlc = 5600;    %optimum load resistance

%b
LLb = LLc;
Reb = Rec;
Rlb = 5600;

%c
LLa = LLc;
Rea = Rec;
Rla = 5600;
```

```
%% Solving the dynamic system(s)

% displacement and time inputs
xo=[0;0];
axo = xo;
bxo = xo;
cxo = xo;

ts=[0 5];

% Ambient excitation
Fo = 9.8*0.25;
Foa = Fo;
Fob = Fo;
Foc = Fo;

massA = 7.2706e-3; % mass of center magnet in no opposing config
massB = 3.5164e-3; % mass of one center magnet in single opposing config
massC = 2.2650e-3; % mass of one center magnet in double opposing config
massS = 7850*HHs*pi*(Mod^2-Mid^2)/4; % density of mild/carbon steel

global w

% (a)
ffa = 20; % edit this 31.08
wta=ffa:(2*pi*ffa-ffa)/100:2*pi*ffa;
ma=massA;
ka = 42.84;
k3a = 2.006e+006;
    avelocity=zeros;
    aposition=zeros;
    apositionlow=zeros;
for i = 1:length(wta)
    w=wta(i);
    [ta,xa]=ode45(@(ta,xa)
BattDynam(ta,xa,ma,ka,k3a,Foa,mean(Ba),Rea,Rla,crpm),ts,axo);
    dispa = xa(:,1);
    vela = xa(:,2);
    avelocity(i)=min(xa(0.8*length(xa):0.9*length(xa),2));
    aposition(i)=max(xa(0.8*length(xa):0.9*length(xa),1));
    apositionlow(i)=(min(xa(0.8*length(xa):0.9*length(xa),1)));
    axo=[(aposition(i)+apositionlow(i))/2;avelocity(i)];
end


% (b)
ffb = 20;% edit this 22.27
wtb=ffb:(2*pi*ffb-ffb)/100:2*pi*ffb;
mb=2*massB + massS;
kb = 30.99;
k3b = 1.124e+006;
    bvelocity=zeros;
    bposition=zeros;
```

```
    bpositionlow=zeros;
for i = 1:length(wtb)
    w=wtb(i);
    [tb,xb]=ode45(@(tb,xb)
BattDynam(tb,xb,mb,kb,k3b,Fob,mean(Bb),Reb,Rlb,crpm),ts,bxo);
    dispb = xb(:,1);
    velb = xb(:,2);
    bvelocity(i)=min(xb(0.8*length(xb):0.9*length(xb),2));
    bposition(i)=max(xb(0.8*length(xb):0.9*length(xb),1));
    bpositionlow(i)=(min(xb(0.8*length(xb):0.9*length(xb),1)));
    bxo=[(bposition(i)+bpositionlow(i))/2;bvelocity(i)];
end


%(c)
ffc = 20; % edit this 17.43
wtc=ffc:(2*pi*ffc-ffc)/100:2*pi*ffc;
mc=3*massC + 2*massS;
kc = 12.82;
k3c = 8.776e+005;
    cvelocity=zeros;
    cposition=zeros;
    cpositionlow=zeros;
for i = 1:length(wtc)
    w=wtc(i);
    [tc,xc]=ode45(@(tc,xc)
BattDynam(tc,xc,mc,kc,k3c,Foc,mean(Bc),Rec,Rlc,crpm),ts,cxo);
    dispc = xc(:,1);
    velc = xc(:,2);
    cvelocity(i)=min(xc(0.8*length(xc):0.9*length(xc),2));
    cposition(i)=max(xc(0.8*length(xc):0.9*length(xc),1));
    cpositionlow(i)=(min(xc(0.8*length(xc):0.9*length(xc),1)));
    cxo=[(cposition(i)+cpositionlow(i))/2;cvelocity(i)];
end


%% Induction Coil(s)
%%full coil vectors (using a wide range of vibration (241points))

xlc = -120*dic:dic:120*dic; %do not modify values
% Lc=zeros;
% for i = 1:121
%     Lc(i) = 0;
%     if xlc(i) >= -TTa/2 + mean(dispa) && xla(i) <= TTa/2 + mean(dispa)
%         Lc(i) = LLa;
%     else
%         Lc(i) = 0;
%     end
% end

% Lc=zeros;
% for i = 1:241
%     Lc(i) = 0;
%     if xlc(i) >= -HHc-HHs/2  && xlc(i) <= -HHs/2
%         Lc(i) = LLc;
%     elseif xlc(i) >= HHs/2  && xlc(i) <= HHc+HHs/2
```

```
%         Lc(i) = LLc;
%     else
%         Lc(i) = 0;
%     end
% end
%
% La = Lc;
% Lb = Lc;

%% The F = B X L vector: Modify the input B values accordingly

%Current range is for 121 displacement terms,
%so pls check min and max of disp!!!

% Fa = BattBLvector(Ba,La,dispa,dic);
% Fb = BattBLvector(Bb,Lb,dispb,dic);
% Fc = BattBLvector(Bc,Lc,dispc,dic);
%
% FFa = BattBLvector(Ba,La,aposition,dic);
% FFb = BattBLvector(Bb,Lb,bposition,dic);
% FFc = BattBLvector(Bc,Lc,cposition,dic);



%% Essential output values

% [Vola Volrmsa VolVa Pa Prmsa PPa] =
BattOutput(Fa,vela,Rla,Rea,dispa,FFa,avelocity);
% [Volb Volrmsb VolVb Pb Prmsb PPb] =
BattOutput(Fb,velb,Rlb,Reb,dispb,FFb,bvelocity);
% [Volc Volrmsc VolVc Pc Prmsc PPc] =
BattOutput(Fc,velc,Rlc,Rec,dispc,FFc,cvelocity);

%% Plotting

%% (bbb) All B fields

% figure
% hold on
% plot(za*1e3,Ba,'or')
% title('B-Field for config a')
% xlabel('z-axis, [mm]')
% ylabel('Magnetic flux density, B [Tesla]')
% formatFig(gcf, 'thesis');
% hold off
%
% figure
% hold on
% plot(zb*1e3,Bb,'or')
% title('B-Field for config b')
% xlabel('z-axis, [mm]')
% ylabel('Magnetic flux density, B [Tesla]')
% formatFig(gcf, 'thesis');
% hold off
%
```

```
% figure
% hold on
% plot(zc*1e3,Bc,'or')
% title('B-Field for config c')
% xlabel('z-axis, [mm]')
% ylabel('Magnetic flux density, B [Tesla]')
% formatFig(gcf, 'thesis');
% hold off

% figure
% hold on
% plot(za*1e3,Ba,'-k',zb*1e3,Bb,'--b',zc*1e3,Bc,':r')
% %title('B-Field for config c')
% xlabel('z-axis, [mm]')
% ylabel('Magnetic flux density, B [Tesla]')
% legend('no repulsion','single repulsion','double repulsion',2)
% %ylim([-0.601 0.6])
% formatFig(gcf, 'slideLS')
% grid off
% hold off


%% (a)
% velocity vs freq
% figure
% hold on
% title('Vel vs Freq (config a)')
% plot(wta/(2*pi),avelocity*-1,'o')
% ylabel('Velocity [m/s]')
% xlabel('Frequency of center magnet [Hz]')
% %xlim([5 30])
% hold off
%
%position vs freq
% figure
% hold on
% %title('disp vs Freq (config c)')
% plot(wta/(2*pi),aposition*1e3,'-b',wta/(2*pi),apositionlow*1e3,':k')
% ylabel('Displacement [mm]')
% xlabel('Frequency [Hz]')
% legend('m.u.d','m.d.d',2)
% ylim([-10 10])
% formatFig(gcf, 'slide')
% grid off
% hold off
%
% % position
% figure
% hold on
% plot(ta,dispa)
% ylabel('disp [m]')
% xlabel('time [s]')
% hold off

% % Voltage
% figure
```

```
% hold on
% plot(ta,Vola)
% %title('Voltage for config a')
% xlabel('Time [s]')
% ylabel('Voltage')
% %xlim([0 0.5])
% hold off
%% (b)
% velocity vs freq
% figure
% hold on
% title('Vel vs Freq (config b)')
% plot(wtb/(2*pi),bvelocity*-1,'o')
% ylabel('Velocity [m/s]')
% xlabel('Frequency of center magnet [Hz]')
% %xlim([5 30])
% hold off
%
%position vs freq
% figure
% hold on
% %title('disp vs Freq (config c)')
% plot(wtb/(2*pi),bposition*1e3,'-b',wtb/(2*pi),bpositionlow*1e3,':k')
% ylabel('Displacement [mm]')
% xlabel('Frequency [Hz]')
% legend('m.u.d','m.d.d',2)
% ylim([-10 10])
% formatFig(gcf, 'slide')
% grid off
% hold off
%
% % position
% figure
% hold on
% plot(tb,dispb)
% ylabel('disp [m]')
% xlabel('time [s]')
% hold off

% % Voltage
% figure
% hold on
% plot(tb,Volb)
% %title('Voltage for config b')
% xlabel('Time [s]')
% ylabel('Voltage')
% %xlim([0 0.5])
% hold off

%% (c)
%velocity vs freq
% figure
% hold on
% %title('Vel vs Freq (config c)')
% plot(wta/(2*pi),avelocity*-1,'-k',wtb/(2*pi),bvelocity*-1,'--
b',wtc/(2*pi),cvelocity*-1,':r')
```

```
% ylabel('Velocity [m/s]')
% xlabel('Frequency [Hz]')
% legend('no repulsion','single repulsion','double repulsion',2)
% %ylim([-0.6 0.6])
% formatFig(gcf, 'slide')
% grid off
% hold off

%position vs freq
% figure
% hold on
% %title('disp vs Freq (config c)')
% plot(wtc/(2*pi),cposition*1e3,'-b',wtc/(2*pi),cpositionlow*1e3,':k')
% ylabel('Displacement [mm]')
% xlabel('Frequency [Hz]')
% legend('m.u.d','m.d.d',2)
% ylim([-10 10])
% formatFig(gcf, 'slide')
% grid off
% hold off
%
% % velocity
% figure
% hold on
% plot(tc,velc)
% ylabel('velocity [m/s]')
% xlabel('time [s]')
% hold off
%
% % position
% figure
% hold on
% plot(tc,dispc)
% ylabel('disp [m]')
% xlabel('time [s]')
% hold off
%
% Voltage
% figure
% hold on
% plot(ta,Vola)
% %title('Voltage for config c')
% xlabel('Time [s]')
% ylabel('Voltage')
% xlim([1 1.5])
% hold off
% formatFig(gcf, 'thesis');
%
% figure
% hold on
% plot(tb,Volb)
% %title('Voltage for config c')
% xlabel('Time [s]')
% ylabel('Voltage')
% xlim([1 1.5])
% hold off
% formatFig(gcf, 'thesis');
```

```
%
% figure
% hold on
% plot(tc,Volc)
% title('Voltage for double-repulsion')
% xlabel('Time [s]')
% ylabel('Voltage')
% xlim([1 1.5])
% hold off
% formatFig(gcf, 'thesis');

% % Power
% figure
% hold on
% plot(tc,Pc)
% %title('Power (config c)')
% ylabel('Power')
% xlabel('Time [s]')
% %xlim([0 0.5])
% hold off
%
% Peak Voltage vs freq
% figure
% hold on
% plot(wtc/(2*pi),VolVc)
% ylabel('Peak Voltage [V]')
% xlabel('Frequency [Hz]')
% hold off

% % Peak Power vs freq
% figure
% hold on
% plot(wtc/(2*pi),PPc)
% %title('Power (config c)')
% ylabel('Peak Power')
% xlabel('Frequency [Hz]')
% %xlim([0 0.5])
% hold off



function [Ba Bb Bc] = BattBField(za, zb, zc)

Ba = BField_a(za);
Bb = BField_b(zb);
Bc = BField_c(zc);



function Ba = BField_a(za)
%%
% General model Sin5:
%      f(x) =
%                     a1*sin(b1*x+c1) + a2*sin(b2*x+c2) + a3*sin(b3*x+c3) +
%                     a4*sin(b4*x+c4) + a5*sin(b5*x+c5)
```

```
%Coefficients (with 95% confidence bounds):
       a1 =      0.1553; %(-0.3054, 0.616)
       b1 =       203.5; %(-107, 514.1)
       c1 =       3.103; %(2.867, 3.339)
       a2 =     0.04071; %(0.0146, 0.06681)
       b2 =       623.7; %(437.9, 809.6)
       c2 =    -0.01505; %(-0.2139, 0.1838)
       a3 =     0.01972; %(0.009054, 0.03038)
       b3 =         998; %(864.9, 1131)
       c3 =      -3.136; %(-3.556, -2.716)
       a4 =      0.0169; %(-0.4994, 0.5332)
       b4 =       298.1; %(-122.7, 718.9)
       c4 =     -0.4209; %(-11.55, 10.71)
       a5 =    0.009873; %(0.001042, 0.01871)
       b5 =        1449; %(1313, 1585)
       c5 =    -0.03949; %(-0.8288, 0.7499)

% Goodness of fit:
%   SSE: 0.01609
%   R-square: 0.9721
%   Adjusted R-square: 0.9623
%   RMSE: 0.02006



Ba = a1*sin(b1*za+c1) + a2*sin(b2*za+c2) + a3*sin(b3*za+c3) +...
                    a4*sin(b4*za+c4) + a5*sin(b5*za+c5);


function Bb = BField_b(zb)
%%
% General model Sin5:
%      f(x) =
%                     a1*sin(b1*x+c1) + a2*sin(b2*x+c2) + a3*sin(b3*x+c3) +
%                     a4*sin(b4*x+c4) + a5*sin(b5*x+c5)
% Coefficients (with 95% confidence bounds):
       a1 =      0.2056; %(0.192, 0.2193)
       b1 =       220.4; %(208.3, 232.5)
       c1 =      -1.556; %(-1.627, -1.485)
       a2 =      0.1704; %(0.1565, 0.1844)
       b2 =       497.3; %(482.5, 512)
       c2 =      -1.567; %(-1.649, -1.485)
       a3 =     0.05694; %(0.04274, 0.07113)
       b3 =       907.9; %(866.6, 949.2)
       c3 =       -1.52; %(-1.758, -1.282)
       a4 =     0.05264; %(0.03891, 0.06637)
       b4 =        1258; %(1208, 1307)
       c4 =      -1.455; %(-1.718, -1.192)
       a5 =     0.02731; %(0.01348, 0.04114)
       b5 =        1629; %(1544, 1714)
       c5 =      -1.451; %(-1.942, -0.9593)

% Goodness of fit:
%   SSE: 0.208
%   R-square: 0.9535
```

```
%   Adjusted R-square: 0.9461
%   RMSE: 0.04834



Bb = a1*sin(b1*zb+c1) + a2*sin(b2*zb+c2) + a3*sin(b3*zb+c3) +...
                    a4*sin(b4*zb+c4) + a5*sin(b5*zb+c5);


function Bc = BField_c(zc)
%%
% General model Sin5:
%      f(x) =
%                     a1*sin(b1*x+c1) + a2*sin(b2*x+c2) + a3*sin(b3*x+c3) +
%                     a4*sin(b4*x+c4) + a5*sin(b5*x+c5)
% Coefficients (with 95% confidence bounds):
       a1 =      0.1417; %(0.06235, 0.221)
       b1 =       402.9; %(343.8, 462)
       c1 =     0.02516; %(-0.06567, 0.116)
       a2 =      0.1455; %(0.1117, 0.1793)
       b2 =       613.6; %(463.2, 764)
       c2 =   -0.002951; %(-0.09005, 0.08414)
       a3 =     0.01951; %(0.006439, 0.03258)
       b3 =        1542; %(1396, 1688)
       c3 =      -2.822; %(-3.459, -2.185)
       a4 =     0.02556; %(0.012, 0.03912)
       b4 =        1836; %(1738, 1935)
       c4 =      -3.097; %(-3.586, -2.609)
       a5 =     0.05715; %(-0.03011, 0.1444)
       b5 =       831.2; %(644.4, 1018)
       c5 =    -0.03337; %(-0.2516, 0.1848)

% Goodness of fit:
%   SSE: 0.3285
%   R-square: 0.9206
%   Adjusted R-square: 0.9116
%   RMSE: 0.05147



Bc =  a1*sin(b1*zc+c1) + a2*sin(b2*zc+c2) + a3*sin(b3*zc+c3) +...
                    a4*sin(b4*zc+c4) + a5*sin(b5*zc+c5);




function F = BattBLvector(B,L,disp,dic)
```

```
%N.B: This code is designed to discretize the B*L vector into 121 points only
F=zeros;
for i = 1:length(disp)
    F(i) = 0;
    for j=1:length(B)
        if disp(i)>= dic*-60 && disp(i)< dic*-59
            F(i) = sum(B(j).*L(1:length(B)+1));
        elseif disp(i)>= dic*-59 && disp(i)< dic*-58
            F(i) = sum(B(j).*L(2:length(B)+2));
        elseif disp(i)>= dic*-58 && disp(i)< dic*-57
            F(i) = sum(B(j).*L(3:length(B)+3));
        elseif disp(i)>= dic*-57 && disp(i)< dic*-56
            F(i) = sum(B(j).*L(4:length(B)+4));
        elseif disp(i)>= dic*-56 && disp(i)< dic*-55
            F(i) = sum(B(j).*L(5:length(B)+5));
        elseif disp(i)>= dic*-55 && disp(i)< dic*-54
            F(i) = sum(B(j).*L(6:length(B)+6));
        elseif disp(i)>= dic*-54 && disp(i)< dic*-53
            F(i) = sum(B(j).*L(7:length(B)+7));
        elseif disp(i)>= dic*-53 && disp(i)< dic*-52
            F(i) = sum(B(j).*L(8:length(B)+8));
        elseif disp(i)>= dic*-52 && disp(i)< dic*-51
            F(i) = sum(B(j).*L(9:length(B)+9));
        elseif disp(i)>= dic*-51 && disp(i)< dic*-50
            F(i) = sum(B(j).*L(10:length(B)+10));
        elseif disp(i)>= dic*-50 && disp(i)< dic*-49
            F(i) = sum(B(j).*L(11:length(B)+11));
        elseif disp(i)>= dic*-49 && disp(i)< dic*-48
            F(i) = sum(B(j).*L(12:length(B)+12));
        elseif disp(i)>= dic*-48 && disp(i)< dic*-47
            F(i) = sum(B(j).*L(13:length(B)+13));
        elseif disp(i)>= dic*-47 && disp(i)< dic*-46
            F(i) = sum(B(j).*L(14:length(B)+14));
        elseif disp(i)>= dic*-46 && disp(i)< dic*-45
            F(i) = sum(B(j).*L(15:length(B)+15));
        elseif disp(i)>= dic*-45 && disp(i)< dic*-44
            F(i) = sum(B(j).*L(16:length(B)+16));
        elseif disp(i)>= dic*-44 && disp(i)< dic*-43
            F(i) = sum(B(j).*L(17:length(B)+17));
        elseif disp(i)>= dic*-43 && disp(i)< dic*-42
            F(i) = sum(B(j).*L(18:length(B)+18));
        elseif disp(i)>= dic*-42 && disp(i)< dic*-41
            F(i) = sum(B(j).*L(19:length(B)+19));
        elseif disp(i)>= dic*-41 && disp(i)< dic*-40
            F(i) = sum(B(j).*L(20:length(B)+20));
        elseif disp(i)>= dic*-40 && disp(i)< dic*-39
            F(i) = sum(B(j).*L(21:length(B)+21));
        elseif disp(i)>= dic*-39 && disp(i)< dic*-38
            F(i) = sum(B(j).*L(22:length(B)+22));
        elseif disp(i)>= dic*-38 && disp(i)< dic*-37
            F(i) = sum(B(j).*L(23:length(B)+23));
        elseif disp(i)>= dic*-37 && disp(i)< dic*-36
            F(i) = sum(B(j).*L(24:length(B)+34));
        elseif disp(i)>= dic*-36 && disp(i)< dic*-35
            F(i) = sum(B(j).*L(25:length(B)+35));
        elseif disp(i)>= dic*-35 && disp(i)< dic*-34
            F(i) = sum(B(j).*L(26:length(B)+26));
```

```
elseif disp(i)>= dic*-34 && disp(i)< dic*-33
    F(i) = sum(B(j).*L(27:length(B)+27));
elseif disp(i)>= dic*-33 && disp(i)< dic*-32
    F(i) = sum(B(j).*L(28:length(B)+28));
elseif disp(i)>= dic*-32 && disp(i)< dic*-31
    F(i) = sum(B(j).*L(29:length(B)+29));
elseif disp(i)>= dic*-31 && disp(i)< dic*-30
    F(i) = sum(B(j).*L(30:length(B)+30));
elseif disp(i)>= dic*-30 && disp(i)< dic*-29
    F(i) = sum(B(j).*L(31:length(B)+31));
elseif disp(i)>= dic*-29 && disp(i)< dic*-28
    F(i) = sum(B(j).*L(32:length(B)+32));
elseif disp(i)>= dic*-28 && disp(i)< dic*-27
    F(i) = sum(B(j).*L(33:length(B)+33));
elseif disp(i)>= dic*-27 && disp(i)< dic*-26
    F(i) = sum(B(j).*L(34:length(B)+34));
elseif disp(i)>= dic*-26 && disp(i)< dic*-25
    F(i) = sum(B(j).*L(35:length(B)+35));
elseif disp(i)>= dic*-25 && disp(i)< dic*-24
    F(i) = sum(B(j).*L(36:length(B)+36));
elseif disp(i)>= dic*-24 && disp(i)< dic*-23
    F(i) = sum(B(j).*L(37:length(B)+37));
elseif disp(i)>= dic*-23 && disp(i)< dic*-22
    F(i) = sum(B(j).*L(38:length(B)+38));
elseif disp(i)>= dic*-22 && disp(i)< dic*-21
    F(i) = sum(B(j).*L(39:length(B)+39));
elseif disp(i)>= dic*-21 && disp(i)< dic*-20
    F(i) = sum(B(j).*L(40:length(B)+40));
elseif disp(i)>= dic*-20 && disp(i)< dic*-19
    F(i) = sum(B(j).*L(41:length(B)+41));
elseif disp(i)>= dic*-19 && disp(i)< dic*-18
    F(i) = sum(B(j).*L(42:length(B)+42));
elseif disp(i)>= dic*-18 && disp(i)< dic*-17
    F(i) = sum(B(j).*L(43:length(B)+43));
elseif disp(i)>= dic*-17 && disp(i)< dic*-16
    F(i) = sum(B(j).*L(44:length(B)+44));
elseif disp(i)>= dic*-16 && disp(i)< dic*-15
    F(i) = sum(B(j).*L(45:length(B)+45));
elseif disp(i)>= dic*-15 && disp(i)< dic*-14
    F(i) = sum(B(j).*L(46:length(B)+46));
elseif disp(i)>= dic*-14 && disp(i)< dic*-13
    F(i) = sum(B(j).*L(47:length(B)+47));
elseif disp(i)>= dic*-13 && disp(i)< dic*-12
    F(i) = sum(B(j).*L(48:length(B)+48));
elseif disp(i)>= dic*-12 && disp(i)< dic*-11
    F(i) = sum(B(j).*L(49:length(B)+49));
elseif disp(i)>= dic*-11 && disp(i)< dic*-10
    F(i) = sum(B(j).*L(50:length(B)+50));
elseif disp(i)>= dic*-10 && disp(i)< dic*-09
    F(i) = sum(B(j).*L(51:length(B)+51));
elseif disp(i)>= dic*-09 && disp(i)< dic*-08
    F(i) = sum(B(j).*L(52:length(B)+52));
elseif disp(i)>= dic*-08 && disp(i)< dic*-07
    F(i) = sum(B(j).*L(53:length(B)+53));
elseif disp(i)>= dic*-07 && disp(i)< dic*-06
    F(i) = sum(B(j).*L(54:length(B)+54));
elseif disp(i)>= dic*-06 && disp(i)< dic*-05
```

```
    F(i) = sum(B(j).*L(55:length(B)+55));
elseif disp(i)>= dic*-05 && disp(i)< dic*-04
    F(i) = sum(B(j).*L(56:length(B)+56));
elseif disp(i)>= dic*-04 && disp(i)< dic*-03
    F(i) = sum(B(j).*L(57:length(B)+57));
elseif disp(i)>= dic*-03 && disp(i)< dic*-02
    F(i) = sum(B(j).*L(58:length(B)+58));
elseif disp(i)>= dic*-02 && disp(i)< dic*-01
    F(i) = sum(B(j).*L(59:length(B)+59));
elseif disp(i)>= dic*-01 && disp(i)< dic*00
    F(i) = sum(B(j).*L(60:length(B)+60));



elseif disp(i)< dic*60 && disp(i)>= dic*59
    F(i) = sum(B(j).*L(120:length(B)+120));
elseif disp(i)< dic*59 && disp(i)>= dic*58
    F(i) = sum(B(j).*L(119:length(B)+119));
elseif disp(i)< dic*58 && disp(i)>= dic*57
    F(i) = sum(B(j).*L(118:length(B)+118));
elseif disp(i)< dic*57 && disp(i)>= dic*56
    F(i) = sum(B(j).*L(117:length(B)+117));
elseif disp(i)< dic*56 && disp(i)>= dic*55
    F(i) = sum(B(j).*L(116:length(B)+116));
elseif disp(i)< dic*55 && disp(i)>= dic*54
    F(i) = sum(B(j).*L(115:length(B)+115));
elseif disp(i)< dic*54 && disp(i)>= dic*53
    F(i) = sum(B(j).*L(114:length(B)+114));
elseif disp(i)< dic*53 && disp(i)>= dic*52
    F(i) = sum(B(j).*L(113:length(B)+113));
elseif disp(i)< dic*52 && disp(i)>= dic*51
    F(i) = sum(B(j).*L(112:length(B)+112));
elseif disp(i)< dic*51 && disp(i)>= dic*50
    F(i) = sum(B(j).*L(111:length(B)+111));
elseif disp(i)< dic*50 && disp(i)>= dic*49
    F(i) = sum(B(j).*L(110:length(B)+110));
elseif disp(i)< dic*49 && disp(i)>= dic*48
    F(i) = sum(B(j).*L(109:length(B)+109));
elseif disp(i)< dic*48 && disp(i)>= dic*47
    F(i) = sum(B(j).*L(108:length(B)+108));
elseif disp(i)< dic*47 && disp(i)>= dic*46
    F(i) = sum(B(j).*L(107:length(B)+107));
elseif disp(i)< dic*46 && disp(i)>= dic*45
    F(i) = sum(B(j).*L(106:length(B)+106));
elseif disp(i)< dic*45 && disp(i)>= dic*44
    F(i) = sum(B(j).*L(105:length(B)+105));
elseif disp(i)< dic*44 && disp(i)>= dic*43
    F(i) = sum(B(j).*L(104:length(B)+104));
elseif disp(i)< dic*43 && disp(i)>= dic*42
    F(i) = sum(B(j).*L(103:length(B)+103));
elseif disp(i)< dic*42 && disp(i)>= dic*41
    F(i) = sum(B(j).*L(102:length(B)+102));
elseif disp(i)< dic*41 && disp(i)>= dic*40
    F(i) = sum(B(j).*L(101:length(B)+101));
elseif disp(i)< dic*40 && disp(i)>= dic*39
    F(i) = sum(B(j).*L(100:length(B)+100));
```

```
elseif disp(i)< dic*39 && disp(i)>= dic*38
    F(i) = sum(B(j).*L(99:length(B)+99));
elseif disp(i)< dic*38 && disp(i)>= dic*37
    F(i) = sum(B(j).*L(98:length(B)+98));
elseif disp(i)< dic*37 && disp(i)>= dic*36
    F(i) = sum(B(j).*L(97:length(B)+97));
elseif disp(i)< dic*36 && disp(i)>= dic*35
    F(i) = sum(B(j).*L(96:length(B)+96));
elseif disp(i)< dic*35 && disp(i)>= dic*34
    F(i) = sum(B(j).*L(95:length(B)+95));
elseif disp(i)< dic*34 && disp(i)>= dic*33
    F(i) = sum(B(j).*L(94:length(B)+94));
elseif disp(i)< dic*33 && disp(i)>= dic*32
    F(i) = sum(B(j).*L(93:length(B)+93));
elseif disp(i)< dic*32 && disp(i)>= dic*31
    F(i) = sum(B(j).*L(92:length(B)+92));
elseif disp(i)< dic*31 && disp(i)>= dic*30
    F(i) = sum(B(j).*L(91:length(B)+91));
elseif disp(i)< dic*30 && disp(i)>= dic*29
    F(i) = sum(B(j).*L(90:length(B)+90));
elseif disp(i)< dic*29 && disp(i)>= dic*28
    F(i) = sum(B(j).*L(89:length(B)+89));
elseif disp(i)< dic*28 && disp(i)>= dic*27
    F(i) = sum(B(j).*L(88:length(B)+88));
elseif disp(i)< dic*27 && disp(i)>= dic*26
    F(i) = sum(B(j).*L(87:length(B)+87));
elseif disp(i)< dic*26 && disp(i)>= dic*25
    F(i) = sum(B(j).*L(86:length(B)+86));
elseif disp(i)< dic*25 && disp(i)>= dic*24
    F(i) = sum(B(j).*L(85:length(B)+85));
elseif disp(i)< dic*24 && disp(i)>= dic*23
    F(i) = sum(B(j).*L(84:length(B)+84));
elseif disp(i)< dic*23 && disp(i)>= dic*22
    F(i) = sum(B(j).*L(83:length(B)+83));
elseif disp(i)< dic*22 && disp(i)>= dic*21
    F(i) = sum(B(j).*L(82:length(B)+83));
elseif disp(i)< dic*21 && disp(i)>= dic*20
    F(i) = sum(B(j).*L(81:length(B)+81));
elseif disp(i)< dic*20 && disp(i)>= dic*19
    F(i) = sum(B(j).*L(80:length(B)+80));
elseif disp(i)< dic*19 && disp(i)>= dic*18
    F(i) = sum(B(j).*L(79:length(B)+79));
elseif disp(i)< dic*18 && disp(i)>= dic*17
    F(i) = sum(B(j).*L(78:length(B)+78));
elseif disp(i)< dic*17 && disp(i)>= dic*16
    F(i) = sum(B(j).*L(77:length(B)+77));
elseif disp(i)< dic*16 && disp(i)>= dic*15
    F(i) = sum(B(j).*L(76:length(B)+76));
elseif disp(i)< dic*15 && disp(i)>= dic*14
    F(i) = sum(B(j).*L(75:length(B)+75));
elseif disp(i)< dic*14 && disp(i)>= dic*13
    F(i) = sum(B(j).*L(74:length(B)+74));
elseif disp(i)< dic*13 && disp(i)>= dic*12
    F(i) = sum(B(j).*L(73:length(B)+73));
elseif disp(i)< dic*12 && disp(i)>= dic*11
    F(i) = sum(B(j).*L(72:length(B)+72));
elseif disp(i)< dic*11 && disp(i)>= dic*10
```

```
            F(i) = sum(B(j).*L(71:length(B)+71));
        elseif disp(i)< dic*10 && disp(i)>= dic*09
            F(i) = sum(B(j).*L(70:length(B)+70));
        elseif disp(i)< dic*09 && disp(i)>= dic*08
            F(i) = sum(B(j).*L(69:length(B)+69));
        elseif disp(i)< dic*08 && disp(i)>= dic*07
            F(i) = sum(B(j).*L(68:length(B)+68));
        elseif disp(i)< dic*07 && disp(i)>= dic*06
            F(i) = sum(B(j).*L(67:length(B)+67));
        elseif disp(i)< dic*06 && disp(i)>= dic*05
            F(i) = sum(B(j).*L(66:length(B)+66));
        elseif disp(i)< dic*05 && disp(i)>= dic*04
            F(i) = sum(B(j).*L(65:length(B)+65));
        elseif disp(i)< dic*04 && disp(i)>= dic*03
            F(i) = sum(B(j).*L(64:length(B)+64));
        elseif disp(i)< dic*03 && disp(i)>= dic*02
            F(i) = sum(B(j).*L(63:length(B)+63));
        elseif disp(i)< dic*02 && disp(i)>= dic*01
            F(i) = sum(B(j).*L(62:length(B)+62));
        elseif disp(i)< dic*01 && disp(i)>= dic*00
            F(i) = sum(B(j).*L(61:length(B)+61));
        end
    end
end
```

```
function v=BattDynam(t,x,m,k,k3,Fo,aveB,Re,Rl,crpm)
global w

dr = 0.047; %damping ratio
c=2.*dr.*sqrt(k.*m);
coilL = Re./crpm;
ce =((aveB.*coilL).^2)/(Re+Rl);

% ce=0.029;
Fg=-9.8;
% v=[x(2);x(1).*-k/m+(x(1).^3).*-k3/m+(x(1).^5).*-k5/m+x(2).*-
c/m+(piecewise1(x(1))*(x(2).*-ce/m))-Fo*cos(w*t)+Fg];
v=[x(2);
    x(1).*-k./m  +  (x(1).^3).*-k3./m  +  x(2).*-c./m ...
    + (piecewise(x(1)).*(x(2).*-ce./m))  -  Fo.*cos(w.*t)  +  Fg];
```

```
function em=piecewise(x)

HHc = 0.0047625; %height of one center magnet in single opposing config
```

```
HHs = 0.5e-3; %height of steel divider

if x >= -HHc-HHs/2 && x <= -HHs/2
    em = 1;
elseif x >= HHs/2 && x <= HHc+HHs/2
    em = 1;
elseif x <= -HHc-HHs/2 && x >= -2*HHc
    em = 0.5;
elseif x >= HHc+HHs/2 && x <= 2*HHc
    em = 0.5;
else
    em = 0;
end
```

```
function [Vol Volrms VolV P Prms PP] =
BattOutput(F,vel,Rl,Re,disp,FF,velocity)

% Rl = load resistance range
% RlC = optimum load resistance

%%Output vs time
Vol = zeros;
P = zeros;
for i = 1:length(disp)
    Vol(i) = 0;
    P(i) = 0;
    Vol(i) = Rl*F(i)*vel(i)./(Rl+Re);
    P(i) = (Vol(i)).^2/Rl;
    Volrms = sqrt(mean(Vol(i).^2)); %to optimize load and for values at diff
frequencies
    Prms = sqrt(mean(P(i).^2)); %to optimize load and for values at diff
frequencies
end

%%Peak output vs frequency
VolV = zeros;
PP = zeros;
for i = 1:length(velocity)
    VolV(i) = 0;
    PP(i) = 0;
    VolV(i) = Rl*FF(i)*velocity(i)./(Rl+Re);
    PP(i) = (VolV(i)).^2/Rl;
end
```

C.3 ANSYS code for magnetic flux field in the LIVE harvester in chapter 4

```
fini
/cle,nostar

/TITLE, Magnetic flux density (LIVE Battery, double opposing)

! Filter out unneeded options in the GUI:
KEYW,PR_SET,1
KEYW,PR_ELMAG,1
KEYW,MAGNOD,1

/PREP7
EMUNITS,MKS

T = 0.009525/2              ! Moving (center) magnet outer radius
r = 0.003175/2              ! Moving (center) magnet inner radius
B = 0.0047625               ! Moving magnet height
h = 0.00079375              ! Stationary magnet height
sr = 0.00635/2              ! Stationary magnet radius
d = 0.0364125               ! Distance between the two stationary magnets
st = 0.5e-3                 ! Height of steel divider
                !Dimensions


!! Material properties:
ET,1,SOLID96          ! Element for all materials
MP,MURX,1,1           ! Air: Material #1 (Rel. Permeability = 1)
MP,MURX,2,1           ! SN magnets : Material #2 (Rel. Permeability = 1)
MP,MGZZ,2,875270  ! (Coercive force component, Z direction)
MP,MURX,3,1           ! NS magnets: Material #3 (Rel. Permeability = 1)
MP,MGZZ,3,-875270          ! (Coercive force component, Z direction)
MP,MURX,4,100        ! Steel Divider: Material #4 (Rel. Permeability = 100)


!! Geometries:
CYLIND,0,sr,-d/2,-(d/2+h),0,360,    ! 1: bottom stationary magnet
CYLIND,r,T,-(B*3/2+st),-(B/2+st),0,360,    ! 2: bottom of moving magnet composite
CYLIND,r,T,-(B/2+st),-(B/2),0,360, ! 3: Steel divider 1
CYLIND,r,T,-B/2,B/2,0,360,            ! 4: center of moving magnet composite
CYLIND,r,T,(B/2+st),(B/2),0,360,    ! 5: Steel divider 2
CYLIND,r,T,(B*3/2+st),(B/2+st),0,360,      ! 6: top of moving magnet composite
CYLIND,0,sr,d/2,(d/2+h),0,360,              ! 7: top stationary magnet
```

```
SPHERE,0,(d/2+h)*3,0,90
SPHERE,0,(d/2+h)*3,90,180
SPHERE,0,(d/2+h)*3,180,270
SPHERE,0,(d/2+h)*3,270,360
SPHERE,0,(d/2+h)*6,0,90
SPHERE,0,(d/2+h)*6,90,180
SPHERE,0,(d/2+h)*6,180,270
SPHERE,0,(d/2+h)*6,270,360        ! Air composite

vovlap,all


!! Assign Volume attributes:  !vlist !vplot,18,21
vsel,s,,,16,19,,1
vatt,1,1,1
vsel,s,,,48,51,,1
vatt,1,1,1                ! Air composite

vsel,s,,,20,23,,1
vatt,2,1,1
vsel,s,,,24,27,,1
vatt,2,1,1                ! stationary magnets

vsel,s,,,28,31,,1
vatt,3,1,1
vsel,s,,,36,39,,1
vatt,2,1,1
vsel,s,,,44,47,,1
vatt,3,1,1                ! moving magnets

vsel,s,,,32,35,,1
vatt,4,1,1
vsel,s,,,40,43,,1
vatt,4,1,1                ! steel dividers


!! Mesh:
ALLSEL
SMRT,1
MSHAPE,1,3D
MSHKEY,0
VSEL,ALL
VMESH,ALL

!! Refine the region of interest for better calculations
```

```
nsel,all
nsel,s,loc,x,-0.007,0.007
nsel,r,loc,y,-0.007,0.007
nsel,r,loc,z,-0.015,0.015
nrefine,all,,,2
allsel
finish


!! Solve and plot magnetic field vectors:
/SOLU
magsolv,3,,,,,1
finish
/POST1
!PLVECT,B, , , ,VECT,ELEM,ON,0

nsel,all

WPOFFS,0,0,0          ! Offset the working plane for cross-section view
wprota,0,90,0         ! Rotate the working plane
/cplane,1             ! Cutting plane defined to use the WP
sucr,djapo,cplane,,,,,
SUMAP,xflux,B,X
/GO
SUPL,djapo,xflux,0
SUPR,djapo,xflux
```

C.4 ANSYS code for magnetic force field in the LIVE harvester in chapter 4

```
fini
/cle,nostar

/CWD,'C:\Users\djapo'

/TITLE, Magnetic force field (LIVE Battery, double opposing)

npts=200
*dim,dist,table,npts
*dim,F,table,npts,1
d=0.001


*do,ii,1,npts

parsave,all
/clear,nostart
parres

/PREP7
EMUNITS,MKS

T = 0.009525/2              ! Moving (center) magnet outer radius
r = 0.003175/2              ! Moving (center) magnet inner radius
B = 0.0047625               ! Big magnet height
h = 0.00079375              ! Stationary magnet height
sr = 0.00635/2              ! Stationary magnet radius
!dd = 0.0364125             ! Distance between the two stationary magnets
st = 0.5e-3                 ! Height of steel divider
a = 4*(d+h+3*B+2*st)        ! air box length


!! Material properties:
ET,1,SOLID236         ! Element for all materials
MP,MURX,1,1           ! Air: Material #1 (Rel. Permeability = 1)
MP,MURX,2,1           ! SN Magnets: Material #2 (Rel. Permeability = 1)
MP,MGZZ,2,-875270 ! (Coercive force component, Z direction)
MP,MURX,3,1           ! NS magnets: Material #3 (Rel. Permeability = 1)
MP,MGZZ,3,875270  ! (Coercive force component, Z direction)
MP,MURX,4,100         ! Steel Divider: Material #4 (Rel. Permeability = 100)
```

```
!! Geometries:
CYLIND,0,sr,-(d/2+h/2),-d/2,0,360,                  ! 1: bottom stationary magnet
CYLIND,,T,d/2,(d/2+B),0,360,                        ! 2: bottom of moving magnet composite
CYLIND,,T,(d/2+B),(d/2+B+st),0,360,                 ! 3: Steel divider 1
CYLIND,,T,(d/2+B+st),(d/2+2*B+st),0,360,            ! 4: center of moving magnet composite
CYLIND,,T,(d/2+2*B+st),(d/2+2*B+2*st),0,360,        ! 5: Steel divider 2
CYLIND,,T,(d/2+2*B+2*st),(d/2+3*B+2*st),0,360,      ! 6: top of moving magnet
composite

BLOCK,-a,a,-a,a,-a,a                    ! 7: air box

vovlap,all


!! Mesh:
keyop,1,7,1             ! condense forces to the corner nodes
SMRT,1
MSHAPE,1,3D
MSHKEY,0
VSEL,ALL
VMESH,ALL


!! Assign Volume attributes:  !vlist !vplot,1
vsel,s,,,1,,,1
emod,all,mat,2                  ! bottom stationary magnet

vsel,s,,,8,,,1
emod,all,mat,4
vsel,s,,,10,,,1
emod,all,mat,4                  ! Steel dividers

vsel,s,,,2,,,1
emod,all,mat,3
vsel,s,,,9,,,1
emod,all,mat,2
vsel,s,,,11,,,1
emod,all,mat,3                  ! moving magnets

vsel,s,,,12,,,1
emod,all,mat,1                  ! air box

allsel


!! Solve and plot magnetic field vectors:
```

```
esel,s,mat,,2,3
eplot
allsel
fini

/SOLU
solve
fini

/POST1
vsel,s,,,1,,,1              ! select lower magnet along with the
                  ! associated elements and nodes
esln
EMFT                        ! sum up magnetic forces
allsel

esel,s,mat,,2,3
allsel
fini

dist(ii)=d
F(ii,1)=_fzsum              ! FX sum calculated by EMFT

d=d+0.0001                        ! upper magnet displacement update

*enddo

/axlab,x,Distance d (m)
/axlab,y,Forces acting on the magnet (N)
/gcol,1,Fz

*vplot,dist(1),F(1,1)



!!!!! RUN THE CODE BELOW ONLY AFTER THE ABOVE SECTIONS ARE COMPLETE!!!

!! Collect Output (do the same for distance too)

*CREATE,ansuitmp
*CFOPEN,'force','txt',' '
*VWRITE,F(1), , , , , , , , ,
(e13.4)
*CFCLOS
*END
/INPUT,ansuitmp
```